

Florida State University Libraries

2015

Structural Elucidation in Biomolecules by Nanometal Surface Energy Transfer Contact Points

Rachel Elizabeth Armstrong



FLORIDA STATE UNIVERSITY
COLLEGE OF ARTS AND SCIENCES

STRUCTURAL ELUCIDATION IN BIOMOLECULES BY NANOMETAL SURFACE
ENERGY TRANSFER CONTACT POINTS

By

RACHEL ELIZABETH ARMSTRONG

A Dissertation submitted to the
Department of Chemistry and Biochemistry
in partial fulfillment of the
requirements for the degree of
Doctor of Philosophy

2015

Rachel Elizabeth Armstrong defended this dissertation on October 27, 2015.

The members of the supervisory committee were:

Geoffrey Strouse
Professor Directing Dissertation

Piotr Fajer
University Representative

Ken Knappenberger
Committee Member

Al Stiegman
Committee Member

Steven Lenhart
Committee Member

The Graduate School has verified and approved the above-named committee members, and certifies that the dissertation has been approved in accordance with university requirements.

For my family and my teachers - you're the reason I got this far.

TABLE OF CONTENTS

List of Tables	vi
List of Figures	vii
Abstract	xvi
CHAPTER 1 - INTRODUCTION	1
1.1 Nucleic acid secondary structures	1
1.2 Aptamer sensors	2
1.3 G-quadruplexes and disease state implications	7
1.3.1 The role of G-quadruplexes in cancer	10
1.3.1a C-Myc function and cancer	10
1.3.1b Telomeres and cancer	11
1.3.2 The role of G-quadruplexes in Type I Diabetes	12
1.4 Summary of chapters	15
CHAPTER 2 – METHODS FOR MONITORING NUCLEIC ACID STRUCTURES	16
2.1 Introduction	16
2.1.1 NMR spectroscopy	16
2.1.2 EPR	17
2.1.3 X-ray crystallography	18
2.1.4 Optical tweezers	18
2.1.5 Circular dichroism (CD)	20
2.1.6 Förster Resonance Energy Transfer	21
2.2 Nanometal Surface Energy Transfer (NSET) for structural elucidation	23
2.2.1 Biophysical research with NSET	26
2.3 Contact distance distributions in labeled systems (EPR, FRET, and NSET)	29
CHAPTER 3 – AN NSET APTAMER BEACON FOR ATP DETECTION	32
3.1 Introduction	32
3.2. Experimental section	34
3.2.1 Aptamer beacon construction	34
3.2.2 Absorption and photoluminescence measurements	36
3.3 Results & discussion	37
3.4 Conclusion	49
CHAPTER 4 – STRUCTURES OF TELOMERIC G-QUADRUPLEXES	51
4.1 Introduction	51
4.2 Experimental and section	54
4.2.1 NSET beacon construction	54
4.2.2 Absorption and photoluminescence experiments	56

4.2.3 NSET distance calculations	56
4.3 Results & discussion.....	58
4.4 Conclusion.....	63
 CHAPTER 5 – G-QUADRUPLEX POPULATIONS IN HUMAN TELOMERES	65
5.1 Introduction	65
5.2 Experimental section	68
5.2.1 Tel22 NSET beacon construction	68
5.2.2 Temperature-dependent optical experiments	70
5.4 Results & discussion.....	71
5.5 Conclusion.....	78
 CHAPTER 6 – COOPERATIVE BEHAVIOR OF ILPR QUADRUPLEXES	80
6.1 Introduction	80
6.3 Experimental section	82
6.3.1 ILPR one-, two-, and non-quadruplex NSET beacon construction	82
6.3.2 Absorption and photoluminescence experiments	83
6.3.3 Fluorescein-AuNP NSET distance calculations	84
6.4 Results & discussion.....	85
6.5 Conclusion.....	93
 CHAPTER 7 – A MULTIFACETED OPTICAL ENERGY TRANSFER SYSTEM	95
7.1 Introduction	95
7.3 Experimental section	97
7.3.1 NSET-FRET beacon construction	97
7.3.2 Absorption and photoluminescence experiments	98
7.3.3 Lifetime experiments	100
7.4 Results & discussion.....	100
7.5 Conclusion.....	105
 References	106
 Biographical Sketch.....	132

LIST OF TABLES

3.1	Stemloop aptamer beacon sequences used in this study. Red, italicized text is indicative of the conserved 25-base-pair ATP aptamer sequence. A dotted underline represents the loop portion in the stemloop structure while a bold underline represents the 6-base-pair stem. Amine-terminated 15-base-pair linkers are listed below the sequence, aligned at the appropriate complementary positions	35
3.2	Intensity values and the extracted distance between the FAM moiety and the AuNP surface at I_0 (no ATP added) and I_{\max} (saturation with ATP) for each of the NSET beacon sequences	40
3.3	K_{d1} and K_{d2} of AMP and ATP binding to sequence <i>iii</i> (circles) and sequence <i>iv</i> . Similarity in binding affinities indicate the NSET stemloop beacons have no affect on ATP and AMP's mechanism of binding to the aptamer sequence	41
3.4	Table of the K_d values with the reported 95% confidence limits (2σ) extracted from equation 3.1, the Hill coefficients (h) extracted from equation 3.4 and the F-test and AIC values extracted from equation statistical analyses described in equation 3.3.....	46
3.5	Percent double-stranded portion of the aptamer sequence (% d.s), the melting temperature of the hairpin (T_{hairpin}), the Gibbs free energy of the hairpin ($\Delta G_{\text{hairpin}}$), and the Gibbs free energy of the duplexed aptamer sequence (ΔG_{duplex}) in each NSET stemloop beacon. The ΔG values are calculated from IDT Oligoanalyzer software [237].....	48
4.1	Variables used in this chapter to extract the appropriate d_0 values for a 5.3 ± 0.6 nm, 6.6 ± 0.6 nm, 9.0 ± 0.6 nm, and 10.0 ± 1.1 nm AuNP and DL680, as expressed in eqn. 3.1 and 3.2	58
4.2	Table of the extracted distances from the NSET theorem based up the T14 DL680 emission intensities observed for the 5nm, 7nm, 9nm, and 10nm Tel26 and wtTel26 NSET beacons	63
6.1	Table of the non-, one-, and two-quadruplex sequences, the universal 12mer linker, and the one- and two-quadruplex block sequences utilized in this chapter. ILPR G-quadruplex sequences are underlined in the one- and two-quadruplex sequences. The terminal 5' C ₆ thiol and terminal 3' fluorescein modifications are shown in each sequence	82
7.1	Table listing the four sequences used in these energy transfer studies. The labeled basepair in the dROX donor strand is bold, italicized, and underlined. Sequences complementary to the dROX sequence, aDL680 and dROX-comp, are listed in the 3' to 5' direction.....	98
7.2	Table of the extracted NSET, FRET, and FRET-NSET values using experimental ROX lifetimes (τ') and eqn. 7.6 and 7.7	104

LIST OF FIGURES

- 1.1 Schematic illustration of the cell-SELEX process used to select aptamer sequences specific to one cell type. Reproduced from Reference [68] with permission of The Royal Society of Chemistry 3
- 1.2 (Left) Schematic of the “aptamer beacon” mechanism outlined by Ellington, et al [38] where a change in aptamer sequence structure from hairpin to target-bound induces a decrease in FRET. (Right) Successful “aptamer beacon” (labeled “G15D5d” in the image) in that the emission intensity increases with increasing target (thrombin) concentration. Reprinted from *Analytical Chemistry*, Vol. 294/Issue 2, Hamaguchi, N., Ellington, A., and Stanton, M., “Aptamer Beacons for the Direct Detection of Proteins,” pages 128 (Left) and 129 (Right), 2001, with permission from Elsevier [38] 4
- 1.3 Illustration of (a) an antibody-based electronic sensor and (b) an aptamer-based electronic sensor where the clear advantage in the use of aptamer is the shortening of the Debye length, positioning of the target near the electrode surface, and increase in observed voltage per target molecule bound. Reprinted with permission from Maehashi, K.; Katsura, T.; Kerman, K.; Takamura, Y.; Matsumoto, K., Tamiya, E. Label-free protein biosensor based on aptamer-modified carbon nanotube field-effect transistors. *Anal. Chem.* **2007**, *79*, 782-787 [86]. Copyright 2007 American Chemical Society 5
- 1.4 Data set plotting the fraction of aptamer bound to its target molecule vs. target concentration. The data is fit to the binding curve described in eqn 1.1. The data points were obtained from a GraphPad PRISM example data set for a one-site binding curve [92] 6
- 1.5 (Left) Bird’s eye view down the center of a G-quadruplex, depicting the stabilizing guanine hydrogen bonds encircling a metal cationic center. (Right) A DNA sequence in the G-quadruplex secondary structure with two metal cations located in between guanine planes, represented as flat rectangles [105]. Ambrus, A.; Chen, D.; Dai, J.; Bialis, T.; Jones, R.A.; Yang, D. Human telomeric sequence forms a hybrid-type intramolecular G-quadruplex structure with mixed parallel/antiparallel strands in potassium solution, *Nucleic Acids Research*, 2006, *34*, 2723–2735, by permission of Oxford University Press [105] 8
- 1.6 Adenocarcinoma cell nuclei (left) in G0/G1 phase and (middle) in S phase stained with the BG4 fluorescent DNA quadruplex-binding antibody (red) and DAPI blue nuclei stain (blue). Scale bars at 20 μM . An increase in G-quadruplex concentration per nuclei in S phase is indicative of the life cycle-dependent nature of G-quadruplexes and their roles in cell metabolism. (Right) Chromosomes stained with BG4 quadruplex-binding antibody (red) and DAPI blue (blue). High BG4 intensity observed at the chromosomal tips verifies a high density of quadruplex folding in telomeres [117]. Scale bars at 2.5 μM [117]. Adapted by permission from Macmillan Publishers Ltd: *Nature* (Biffi, G.; Tannahill, D.; McCafferty, J.; Balasubramanian, S. Quantitative visualization of DNA G-

	quadruplex structures in human cells. <i>Nat. Chem.</i> 2013 , <i>5</i> , 182-186), copyright 2013 [117]	9
1.7	(Left) Representation of the normal, G-quadruplex-induced repression of the c-Myc gene stemming from G-quadruplex formation in the promoter region. (Right) Protein-bound duplex DNA inducing c-Myc gene transcription by a promoter region binding site. The absence of the G-quadruplex in the promoter region permits protein binding and subsequent c-Myc upregulation commonly observed in malignant cells. Adapted with permission from Reference 127 and Reference 132 [127, 132]	10
1.8	(Top) Cartoon of a chromosome terminated in a string of protective G-quadruplex structures, as predicted by researchers [139]. From Xu, X., “Consecutive formation of G-quadruplexes in human telomeric-overhang DNA: a protective capping structure for telomere ends,” <i>Angewandte Chemie International Edition</i> . Copyright © 2009 by John Wiley & Sons, Inc. Reprinted by permission of John Wiley & Sons, Inc [120]. (Bottom) Single molecule experiments that elucidate the unfolding of telomere G-quadruplexes by two POT1 proteins, monitored by the change going from a high FRET efficiency (quadruplex-folded state) to a low FRET efficiency (POT1 unwound state) [140]. Ying, L.; Green, J.J.; Haitao, L.; Klenerman, D.; Balasubramanian, S. Studies on the structure and dynamics of the human telomeric G quadruplex by single-molecule fluorescence resonance energy transfer. <i>Proc. Natl Acad. Sci. USA</i> 2003 , <i>100</i> , 14629–14634. Copyright 2003 National Academy of Sciences, USA [140]	12
1.9	Schematic of the ILPR region located upstream from the INS gene. It is speculated that the length and/or quadruplex-forming behavior of allele 3 contribute to the higher transcriptional activity of INS relative to the shortened, mutated allele 1, which consequently, results in a predisposition for T1D [152-155]	14
2.1	Short double stranded DNA sequence labeled terminally with triarylmethyl (TAM) radicals to monitor room temperature distant-dependent magnetic coupling via pulsed EPR spectroscopy [173]. Adapted with permission from Shevelev, G.Y.; Krumkacheva, O.A.; Lomzov, A.A.; Kuzhelev, A.A.; Rogoshnikova, O.Y.; Trukhin, D.V.; Troitskaya, T.I.; Tormushev, V.M.; Fedin, M.V.; Pyshnyi, D.P.; Bagryansjaya, E.G. Physiological-temperature distance measurement in nucleic acid using triarylmethyl-based spin labels and pulsed dipolar EPR spectroscopy. <i>J. Am. Chem. Soc.</i> 2014 , <i>136</i> , 9874-9877. Copyright 2014 American Chemical Society [174]	17
2.2	(Left) Illustration of the optical tweezer experimental setup in the forced unfolding a G-quadruplex. Blue 3D circles represent the beads located within the focus of the optical laser responsible for the opposing directional motion. (Right) Force (in picoNewtons, pN) exerted on the quadruplex structure vs. the distance extension between the beads. A jump in the extension (orange line to blue line at ~1200nm) indicates a quadruplex unfolding event [129]. Adapted with permission from Yu, Z.; Schonhoff, J.D.; Dhakal, S.; Bajracharya, R.; Hegde, R.; Soumitra, B.; Mao, H. ILPR G-quadruplexes formed in seconds demonstrate high mechanical stabilities. <i>J. Am Chem. Soc.</i> 2009 , <i>131</i> , 1876-1882. Copyright 2009 American Chemical Society [129]	19

- 2.3 Circular dichroism (CD) spectra of (left) a fully parallel G-quadruplex and (right) an antiparallel G-quadruplex. Notable differences between the spectra are the negative valley at 250nm in the parallel structure and more pronounced 290nm peak in the antiparallel quadruplex spectra. Hybrid telomere quadruplexes, which have a (3+1) mixture of parallel to antiparallel strands in their quadruplex, exhibit a CD spectra intermediate of those shown above [182]. Reprinted from *Methods*, 43, Paramasivan, S., Rujan, I., and Bolton, P.H., “Circular dichroism of quadruplex DNAs: applications to structure, cation effects and ligand binding, pages 324–331, Copyright 2007, with permission from Elsevier [182]..... 20
- 2.4 (Left) Illustration of the condensed RNA hairpin structures littered with three dyes, fluorescein (green), Cy3 (yellow), and ROX (red), which act as a FRET waterfall system where one excitation wavelength (488nm) produces three emission peaks (510nm, 555nm and 600nm). (Right) Emission spectra of the FRET waterfall where various dyes are omitted from the system, as denoted by the binary representation in the top right corner. The binary legend is listed as left to right, fluorescein, Cy3, and ROX, respectively. From Hu, R., “DNA Nanoflowers for Multiplexed Cellular Imaging and Traceable Targeted Drug Delivery,” *Angewandte Chemie International Edition*. Copyright © 2014 by John Wiley & Sons, Inc. Reprinted by permission of John Wiley & Sons, Inc [195]..... 22
- 2.5 (Left) Depiction of the size-dependent NSET energy transfer measurements between various AuNP sizes (changing “r” values) and dye-labeled double-stranded DNA (of lengths “d”) [178]. (Right) Quenching efficiency (Q_{eff}) curves describing the efficiency of energy transfer versus distance for a FRET pair with an $R_0=65 \text{ \AA}$ (solid line), a 5nm AuNP with fluorescein dye where $d_0=136 \text{ \AA}$ (dotted line), and a 10nm AuNP with fluorescein dye where $d_0=221 \text{ \AA}$ (dashed line). It is clear from the efficiency curves and the R_0 , d_0 values that incorporation of an AuNP as the acceptor in the energy transfer increases the distance to which energy transfer from donor to acceptor occurs [176-178, 191]..... 25
- 2.6 (Left) Scheme of aptamer “nano-flare” technology on AuNPs developed in the Mirkin lab, where target binding to the aptamer sequence releases a dye-labeled “flare” strand. (Right) Flow cytometry graph demonstrating the increased dye (Cy5) intensity observed in cells laced with high target concentrations. In this instance, the target is ATP [39]. Adapted with permission from Zheng, D.; Seferos, D.S.; Giljohann, D.A.; Patel, P.C.; Mirkin, C.A. Aptamer nano-flares for molecular detection in living cells. *Nano Lett.* **2009**, 9, 3258–3261 [50]. Copyright 2007 American Chemical Society..... 26
- 2.7 (Left) Scheme of AuNP-gene/DNA uptake and subsequent cargo release from the AuNP surface within the cell. The intracellular surface release is tracked by the sudden emission of a fluorescein dye appended to the gene/DNA that was initially quenched by the AuNP. The gene, which codes for a red fluorescent protein, is then transcribed/translated into protein as marked by red emission post-translation [204]. (Right) The evolution of an RNA hammerhead complex tracked by NSET after substrate annealing and preliminary cleavage steps with the addition of Mg^{2+} . Dye to AuNP distances derived from the dye’s

	variable quenched lifetime/emission intensity are indicative of the two heammerhead states, annealed and active hammerhead [179]	28
2.8	(Left) Example nitroxide EPR spin label with a methanethiosulfonate linker, displaying the rotational potential of the linker's bonds [207]	29
2.9	FRET and NSET construct demonstrating the dynamic rotational potential of the organic fluorophore modifications (green and red) and of the thiol-modified linker at the AuNP surface (purple). Gray dots represent 10,000 possible locations generated by accounting for the motion of each label. These distributions stem from the size distribution of the AuNP ($10\text{nm} \pm 0.5\text{nm}$) and a randomized 3D Gaussian point distribution with one sigma defined as 90% of the fluorophore's linker length [216]	30
2.10	Percentage of the measured distance comprised by the linker vs. the experimental distance measured (red), assuming the linker's distributed distance due to rotational freedom is 14 \AA . Vertical lines denote the measureable distances of a FRET dye pair with an $R_0=65 \text{ \AA}$ (black solid line), a dye-small AuNP pair with a $d_0=136 \text{ \AA}$ (black dotted line), and a dye-large AuNP pair with a $d_0=221 \text{ \AA}$. The measureable distances of the FRET and NSET methods (vertical lines) were calculated by assuming the distance at which 10% energy transfer occurs is the longest experimentally measureable distance ..	31
3.1	Illustration of the movement of the ATP aptamer sequence around the circumference of the NSET stemloop beacon, the effect of which on the binding affinity of ATP is studied in this chapter	33
3.2	UV-Vis (left), TEM (middle) and gel electrophoresis (right) of the NSET stemloop beacons. Sample iii represents the final purified NSET beacon and contains features from its separate components, free FAM-labeled aptamer sequences (i) and free 3 nm AuNPs (ii). A DNA absorption peak at 260nm and FAM feature at 494nm are observed in sample i, though due to it's low absorption cross-section relative to the AuNP, the FAM feature is not observed in the final purified NSET beacon (iii). TEM of the final NSET beacon indicates a size distribution of $3\text{nm} \pm 0.6$. Retardation of the NSET beacon's movement through the gel (iii) relative to the unlabeled DHLA-coated AuNPs (ii) is indicative of DNA attachment to the AuNP surface via EDC coupling reaction.....	36
3.3	Scheme of the NSET stemloop beacons and their response tp ATP. The red bars in the stemloop structures are indicative of the aptamer sequence location in the stemloop architecture. Sequences <i>i</i> , <i>ii</i> , <i>iii</i> , <i>iv</i> , and <i>vi</i> remain a single construct upon ATP binding whereas sequence <i>v</i> contains enough aptamer sequence overlap in the stem to induce displacement of the flare strand upon ATP binding.....	37
3.4	Quenching efficiency of FAM on a 3nm AuNP versus distance (left) and the calculated distribution in NSET R_0 values for FAM on a 3nm AuNP stemming from the distribution in AuNP diameter, $3.0\text{nm} \pm 0.6$ (right).....	38

3.5	Saturation curves of sequence <i>ii</i> without excess AuNPs (circles) and in the presence of 2x [AuNPs] (triangles). Similar saturation behavior indicates no adverse affects of free AuNPs in solution.....	39
3.6	Saturation curves of sequence <i>ii</i> , sequence <i>iii</i> , and sequence <i>iv</i> with ATP (circles), UTP (triangles), and GTP (squares.) The specificity of the aptamer for ATP is unchanged despite movement around the hairpin circumference.....	41
3.7	Raw PL data of the NSET stemloop beacons increasing ATP concentrations. Each sample is at a concentration of ~1nM beacon. Hairpin sequences (sequence <i>i</i> , <i>ii</i> , <i>iii</i> , <i>iv</i> , and <i>v</i>) increase in intensity with increasing ATP concentration whereas sequence <i>vi</i> , a non-hairpin structure, decreases in intensity with increasing ATP concentration	42
3.8	ATP binding curves of the five NSET stemloop beacons fit to equation 3.1. The curves display the relationship between ΔPL and micromolar ATP concentration. The sequence <i>vi</i> saturation curve is fit to a single-event model described in equation. 3.2.....	43
3.9	Log plot of the two-site binding model (one-site binding model is employed for sequence <i>vi</i>) fit to the NSET beacon saturation with ATP, demonstrating the range of detection for each sequence	44
3.10	(Left) Correlation between the aptamer Gibbs free energy of the duplex region vs. experimentally measured K_{d1} (circles) and K_{d2} (triangles) values of the aptamer. (Right) The region of duplex sequence utilized for the $-\Delta G_{duplex}$ calculation, depicting sequence <i>iv</i> as an example.....	49
3.11	Log plots of the NSET beacon binding curves as a demonstration of their range of ATP detection across six orders of magnitude.....	50
4.1	Scheme of Hybrid-1 and Hybrid-2 G-quadruplexes folded on AuNP surfaces of various sizes and the distinct position of thymine 14 (T14) between the two structures. Theoretical distances between the AuNP surface and the dye labels at T8 and T14 were extracted from proton NMR structures of the two conformers.	51
4.2	(Left) UV-Vis absorption spectra of DL680-labelled wtTel26 sequence (i), 5nm BSPP-coated AuNPs (ii), and a purified NSET wtTel26 beacon after appendage of the DNA to the AuNP surface via thiol reduction (iii). (Right) Gel electrophoresis of the BSPP-coated AuNPs prior to DNA appendage (lane 1: 5nm, lane 3: 7nm, lane 5: 9nm, and lane 7: 10nm), and after attachment of the wtTel26 beacon complex to the AuNP surface (lane 2: 5nm, lane 4: 7nm, lane 6: 9nm, and lane 8: 10nm.)	55
4.3	(Left) Theoretical NSET quenching efficiency versus distance of a 5.3 ± 0.6 nm, 6.6 ± 0.6 nm, 9.0 ± 0.6 nm, and 10.0 ± 1.1 nm AuNP (sliding from left to right) and DL680. (Right) First derivative of the quenching efficiency curve which depicts the distance at which the maximum slope of the quenching efficiency curve is incurred.....	59

4.4	Normalized PL intensities of Tel26 (left column) and wtTel26 (right column) NSET beacons. The beacons are listed from top to bottom increasing in AuNP size. Each plot contains the normalized DL680 intensity of free DL680-DNA (dotted line), an initial, 0mM K ⁺ concentration (solid line), and at high 75-100mM K ⁺ concentration (dashed lined).....	60
4.5	Normalized PL data of the T8 DL680 emission intensities for the 5nm, 7nm, 9nm, and 10nm NSET beacons upon K ⁺ addition. Each plot depicts the emission intensity of free DL680-DNA (dotted line), an initial, 0mM K ⁺ concentration (solid line), and at high 75-100mM K ⁺ concentration (dashed lined).....	61
4.6	Plots of the AuNP-T8 (left) and AuNP-T14 (right) separation distances extracted from the DL680 emission intensities using the NSET theorem (eqn. 4.1, 4.2, and Table 4.1). Horizontal lines denote the theoretical separation distances exhibited by Hybrid-1 (Tel26) and Hybrid-2 (wtTel26) folding, as calculated from reported (3+1) Hybrid NMR structures.....	64
5.1	A schematic showing the two predicted G-quadruplex folding conformations and contact distances for Tel22 in an NSET ruler containing a T14 DyLight680 (DL680) fluorolabel on a 5.3 + 0.6 nm AuNP at the 5' end of the sequence. The structures are based upon calculations from previously reported NMR structures of Hybrid-1 and Hybrid-2 conformers [105,165,166]	66
5.2	(Left) Gel electrophoresis of the NSET ruler versus BSPP-coated 5.3nm ± 0.6 AuNPs. Retardation of the NSET ruler band (left-hand well) in comparison to the BSPP-coated AuNPs (right-hand well) indicates appendage of DNA to the AuNP surface. (Center) TEM of the BSPP- coated 5.3nm ± 0.6 AuNPs and (Right) the AuNP size distribution. TEM size distribution analysis reports an AuNP size of 5.3nm ± 0.6	68
5.3	Dissolution of the AuNPs by NaCN and serial dilutions allow the measurement of DNA:AuNP ratios by UV-Vis absorption and Beer's Law correlation. A 10μL aliquot of 100mM NaCN was added to a concentrated (0.48 μM) 50μL Tel26-AuNP construct. To track the disappearance of the AuNP features upon CN ⁻ addition, dilutions of the sample are tracked via (A) UV-Vis and (B) PL spectroscopy. The concentrated sample blocks all incident light and is incapable of optical monitoring before dilutions. After 30 minutes, a UV-Vis and PL spectra (solid line) of the concentrated sample reveal complete digestion of the AuNP and a final [DNA] of 1.6μM. It should be noted that the absorption cross-sections of the DNA ($\epsilon_{260} = 3.97 \cdot 10^5 \text{ LM}^{-1} \text{ cm}^{-1}$) and DL680 ($\epsilon_{680} = 1.40 \cdot 10^5 \text{ LM}^{-1} \text{ cm}^{-1}$) are drastically lower than that of the AuNP ($\epsilon_{520} = 9.97 \cdot 10^7 \text{ LM}^{-1} \text{ cm}^{-1}$) and therefore the typical DNA:AuNP ratios utilized in the PL studies (~1-4:1) do not produce noticeable absorption features for the DL680-labeled DNA sequences, as observed in the 37.5x dilution (dotted line) spectra.....	69
5.4	To ensure changes in Tel22 quenching arise from dynamic Hybrid-2/Hybrid-1 ratios, the temperature dependence in DL680 (left) and fluorescein (right) is shown. The photoluminescence of a Tel22 NSET beacon sample was divided into four 50μL aliquots,	

	each taken to a different temperature, 4°C, 15°C, 25°C, and 37°C. It is clear the DL680 emission intensity is unchanged by the temperature range explored in this study.....	72
5.5	Time dependent quenching of Tel26, wtTel26, and Tel22, demonstrating an equilibrium is reached in each sequence within 2 hours of the K ⁺ addition	72
5.6	(Left) Gel electrophoresis of 10nm BSPP-coated AuNP (left lane) and 10nm AuNPs after Tel22 sequence appendage (right lane). (Right) PL monitoring DL680 emission intensity before (solid line) and after (dotted line) addition of excess reduced dihydrolipoic acid (DHLA)	73
5.7	PL of T14 DL680 (left) and T14 fluorescein (right) emission intensities at 25°C for the Tel26 beacon (“H-1” solid line), the wtTel26 beacon (dotted line), the saturated (100mM K ⁺) Tel22 beacon (dashed line) and the pre-salt (0mM K ⁺) Tel22 beacon gray line. The “H-2 _{theory} ” solid line represents the theoretical 100% Hybrid-2 conformation, extracted from the wtTel26 data which is known to form 75% Hybrid-2 and 25% Hybrid-1	74
5.8	Tel22 T14 DL680 (left) and T14 fluorescein (right) emission intensity at 0mM K ⁺ (solid line) and at 100mM K ⁺ (dashed line). The dotted line is indicative of the emission intensity without appending the Tel22 sequence to an AuNP.....	75
5.9	(Top left) Temperature-dependent PL measurements for the DL680 Tel22 beacon at 4°C (purple), 15°C (blue), 25°C (red), and 37°C (black). (Top right) The calculated fractional population of Hybrid-1 and Hybrid-2 as a function of temperature, extracted from NSET model calculations. (Bottom left) Temperature-dependent PL measurements for the fluorescein Tel22 beacon at 4°C (purple), 15°C (blue), 25°C (red), and 37°C (black). (Bottom right) The calculated fractional population of Hybrid-1 and Hybrid-2 as a function of temperature. The dotted line in both PL spectra represents the initial (0mM K ⁺) state normalized to 1	76
5.10	The observation of each flanked telomere sequence, Tel26 and wtTel26, to fold under the temperature range studied is essential to ensuring the observed quenching of Tel22 is due to a Hybrid-1/Hybrid-2 mixture, rather than an alternate temperature-dependent structure. (Top left) The DL680-T8 emission of Tel26 and (Top right) the DL680-T14 emission of wtTel26 are similarly quenched at all temperatures (4°C, 15°C, 25°C, and 35°C) at 100mM K ⁺ . (Bottom left) The fluorescein-T14 Tel26 emission and (Bottom right) the fluorescein-T14 wtTel26 emission are also similarly quenched at the temperature range studied. This is indicative of native folding behavior across the temperature range explored in this Tel22 study. For simplicity, the free-DNA fluorescein emission peak is not shown in the fluorescein-T14 (bottom) samples	78
6.1	Scheme of the variable length (and variable quadruplex number) ILPR NSET beacons used in this chapter. The one, two, and non-quadruplex systems are named for the respective number of putative quadruplexes that can form from the ILPR 14mer repeats comprising the beacons’ sequences.....	81

6.2	CN ⁻ etch of the 5nm one-quadruplex ILPR NSET beacon. The relative change in intensity represents the degree of quenching in the initial, pre-K ⁺ state of the NSET beacons, where Q _{eff} = 0.41. Averaging of all three 5nm NSET beacons (one-, two-, and non-quadruplex) and conversion to a distance utilizing the NSET theorem results in an initial AuNP-fluorescein distance of 145 ± 19 Å prior to G-quadruplex folding. Identical distances were extracted in CN ⁻ analysis of the 10nm ILPR NSET beacons.....	84
6.3	(Left column) Raw fluorescein PL data upon increase in [K ⁺] of the 5nm NSET beacon non-, one-, and two-quadruplex strands (top to bottom). (Right column) Integration of the normalized fluorescein PL peaks with respect to [K ⁺] concentration fit to a linear equation in the non-quadruplex system and eqn. 6.1 in the one- and two-quadruplex systems	87
6.4	(Left column) Raw fluorescein PL data upon increase in [K ⁺] of the 10nm NSET beacon one-, two-, and non-quadruplex strands (top to bottom). (Right column) Integration of the fluorescein PL peaks with respect to [K ⁺] concentration fit to eqn. 6.1 in the one- and two-quadruplex system and fit to a linear equation in the non-quadruplex system	88
6.5	Quenching efficiency curve of 5nm and 10nm AuNPs with fluorescein (blue lines) which describes the fluorescein-AuNP separation distance relationship monitored in the ILPR quadruplex beacons. The d ₀ values are 136 Å for the 5nm NSET beacon and 221 Å for the 10nm NSET beacon. The initial distance (calculated from the CN ⁻ etch experiments outlined in section 6.2 and Figure 6.2), 145 ± 19 Å, is depicted as a black vertical solid line. Final saturated, G-quadruplex-folded distances extracted from the NSET theorem are shown as black dotted (one-quadruplex) and dashed (two-quadruplex) lines, at 100 ± 9 Å and 72 ± 11 Å, respectively. Likewise the theoretical values are shown as red dotted (one-quadruplex) and dashed (two-quadruplex) lines, at 103 Å and 70 Å, respectively ..	89
6.6	Scheme of the folded ILPR quadruplex behavior of the one- and two-quadruplex sequences with and without the pre-annealed 40mer “block” sequence	90
6.7	(Left column) Raw PL data of the one-quadruplex (top) and two-quadruplex block sequences with K ⁺ additions. (Right column) Linear fit of the (top) one-quadruplex and K _d curve fit to eqn. 6.1 of the (bottom) two-quadruplex block sequence saturation extracted from the raw intensity data	92
6.8	Plots of the theoretical two-quadruplex, two-site binding curve (dotted line) assuming a quadruplex-uncoupled system and the experimental two-quadruplex binding curve (solid line). The theoretical plot is fit to eqn. 6.2 where K _{d1} = 3.5 mM and K _{d2block} = 4.7 mM, and B _{max(1)} and B _{max(2)} are assumed to be 0.475 to match the maximum y-value in the experimental plot (0.95). The experimental plot is fit to a one-site binding model, eqn. 6.1, as the two-site model produces ambiguous values for K _{d1} and K _{d2} , commonly observed in highly positively cooperative systems [260].....	93
6.9	Graph of the synthetic disadvantage of G-quadruplex design plotted as a function of % yield (from a 200 nmole synthesis) vs. the number of putative quadruplexes incorporated	

into the sequence. It is worth noting that the terminal fluorescein and thiol modifications in the one-, two-, and non-quadruplex sequences are also detrimental to DNA yields when compared to unmodified DNA sequences of the same length (69mer). The three-quadruplex sequence contains more basepairs (111mer) to accommodate the inclusion of the third ILPR quadruplex sequence, which is also inhibitory to its synthesis 94

7.1	Scheme of the NSET-FRET beacon where a donor dye, ROX, is separated from a 10nm AuNP by 42 basepairs, and separated from an acceptor dye, DL680 by 18 basepairs. The NSET $d_0=137 \text{ \AA}$ for ROX with a 10nm AuNP and the $R_0=67 \text{ \AA}$ for an ROX-DL680 FRET pair 96
7.2	Absorption spectra of (black line) 10nm BSPP-AuNPs, (orange dotted line) dROX, (red dotted line) aDL680, and emission spectra of (orange solid line) aROX, and (red solid line) aDL680..... 99
7.3	Raw PL data of the (Left) FRET-based beacons and the (Right) NSET-based beacons. (Left) The orange dotted line represents free dROX-complement strand, the red dotted line represents the small DL680 population directly excited by $\lambda_{ex}=550 \text{ nm}$, and the solid black represents the FRET spectra after subtracting the directly excited DL680 contribution..... 102
7.4	Lifetime decay data of the (top left) free dROX sequence ($\tau_0 =4.4 \pm 0.1\text{ns}$), (top right) the dROX-aDL680 FRET complex ($\tau'=2.8 \pm 0.1\text{ns}$), (bottom left) the dROX-complement-AuNP beacon ($\tau'=2.1 \pm 0.1\text{ns}$), and (bottom right) the NSET-FRET beacon ($\tau'=1.9 \pm 0.1\text{ns}$). Residuals of the AuNP-based fits (ROX NSET and FRET-NSET) are shown below the corresponding lifetime plots 103

ABSTRACT

Optical technology in biophysics has seen significant growth with development of high resolution techniques, like single-molecule FRET, to investigate biological structures under native conditions. Additionally, with the rise in gold nanoparticle use in drug delivery, bioassays, and intracellular tracking, Nanometal surface energy transfer (NSET) applications have also improved since its limited beginnings on 2nm gold nanoparticles. This dissertation aims to further exploit the surface plasmon – organic dye coupling properties by investigating a series of nucleic acid secondary structures with modified gold nanoparticles and fluorophores as structural contact points.

Chapter 1 and Chapter 2 introduce the importance of tracking nucleic acid structures by describing their essential roles in biology as well as state-of-the-art techniques to monitor various conformers. In Chapter 3, gold nanoparticle-based aptamer sensors are investigated and manipulated to detect a multi-magnitude range of target concentrations. It is observed that the aptamer's degree of exposure to the target predictably decreases the limit of detection in optical aptasensors. In sequential Chapters 4-6, a variety of G-quadruplex structures are investigated for their structural characteristics as well as their more global, cooperative relationships. The gold nanoparticle acts as a distant-dependent quencher for these surface-appended, dynamic nucleic acid sequences, in which the intensity of a DNA-functionalized dye distinguishes the specific G-quadruplex structure. In Chapter 7, NSET is pushed to further limits, by adding a distant-dependent contact point to the gold nanoparticle surface in the form of a FRET pair, to build a theorem for an NSET-FRET hybrid system for optical triangulation. The observed quenching of the donor lifetime in the presence of additional decay pathways confirms the efficacy of the NSET-FRET hybrid system and lays the groundwork for a mathematically predictable distance dependence model.

CHAPTER 1

INTRODUCTION

1.1 Nucleic acid secondary structures

With structural elucidation of double helix DNA by James Watson, Francis Crick, and Rosalind Franklin in 1953, a new series of nucleic acid investigations began [1]. Their initial discovery explained the conformational status of double-stranded DNA at rest in the nucleus, but soon after, additional researchers began to discover alternate conformers under different conditions – organic solvents, cationic ions, salt concentration, pH, temperature, etc. [2,3,4]. Even a new basepairing mechanism was observed, Hoogsteen basepairing, that takes advantage of misaligned hydrogen bonding interactions, including non-AT or CG basepairs [5]. Simultaneously, research into the roles of short ribonucleic acid (RNA) sequences was also on the rise. It became evident that secondary and tertiary structures of t-RNA, m-RNA (including introns), and r-RNA are essential to RNA functions in protein production, small molecule binding, and immunological response [6-15]. Fast forward to the early 2000's; past the discoveries of B- and Z-DNA, DNA helicases, genome sequencing and siRNAs [16-32]. Now, new classes of nucleic acid secondary structures are dominating the direction of genetic research. Not only have complex structures of non-Watson-Crick nucleic acids been identified, their structural stability is being explored in connection with biological processes and exploited for new bioanalytical assays [6-12,18,28,33-43].

The motivation of this dissertation is to explore relevant nucleic acid secondary structures using analytical methods. Not only is the understanding of nucleic acid folding crucial to understanding biological function, but the potential to use nucleic acids in sensor applications also depends on this knowledge [36,41,42,44-49]. Section **1.2** of this chapter describes the incorporation of DNA and RNA aptamers into sensing applications, which leads to systematic study of improving DNA aptamer sensor design in Chapter 3. Section **1.3** investigates the biological relevance of the G-quadruplex nucleic acid structure. More specifically, the importance of determining specific G-quadruplex structures is discussed, which explains the reasoning for human telomere and ILPR G-quadruplex investigations in Chapters 4, 5, and 6. In Chapter 2, common analytical techniques used for exploring nucleic acid secondary structures

are discussed, highlighting their strengths and weaknesses for structural elucidation under biological conditions. The need for improved techniques to monitor DNA and RNA structures drives the goals in Chapter 7, where advances in Nanometal Surface Energy Transfer (NSET) are explored.

1.2 Aptamer sensors

Exploitation of favorable nucleic acid structures came about with the incorporation of “aptamers,” which are oligonucleotide sequences capable of binding to target molecules, into small-molecule binding assays [33,50]. While a DNA sequence binding to the human protein thrombin was the first and has certainly been the “guinea pig” aptamer sequence for biotechnologists, the discovery of new molecule-binding nucleic acids has spiraled with the development of library-style aptamer detection methods [33,50-57]. SELEX (systematic evolution of ligands by exponential enrichment), for instance, takes advantage of exponential amounts of random nucleic acid sequences (up to 10^{20} sequences) to determine potential aptamer-bound motifs with minimal experimentation [33,50,52-57]. Pull-down assays of the aptamer-target assembly determines the most stable bound oligonucleotides to the target molecule (ligand) in question. The ligand can be biomolecules such as peptides, cell surfaces (and receptors), proteins, small molecules, ions, other oligonucleotides, and enzymes [34,35,58-60]. In several instances, the target-aptamer construct is stable enough to crystallize and an X-ray crystallography structure is acquireable [51,62-65]. In an aptamer-target interaction, crystallography elucidates the stabilizing mechanisms. The target molecule is stabilized by hydrogen-bonding between single-stranded basepairs where the target hydrogen bonds with the oligo itself or is stabilized by a positional pocket in the oligo secondary structure where basepair hydrogen-bonding is responsible for maintaining the target-bound state [51,62-65].

Since the optimization of SELEX, more applicable methods have been developed that elucidate sequence-dependent aptamer-target constructs in biologically relevant environments. For instance, Cell-SELEX replicates the combinatorial library technique of SELEX, yet incorporates one specific cell type as the target molecule to distinguish aptamers specific to the target cell [37,66-68]. A schematic of the Cell-SELEX process is shown in Figure 1.1 [68]. Cell-SELEX has served as an effective springboard for aptamer use as cancer cell markers and cell-specific, drug delivery mechanisms [37,68-72].

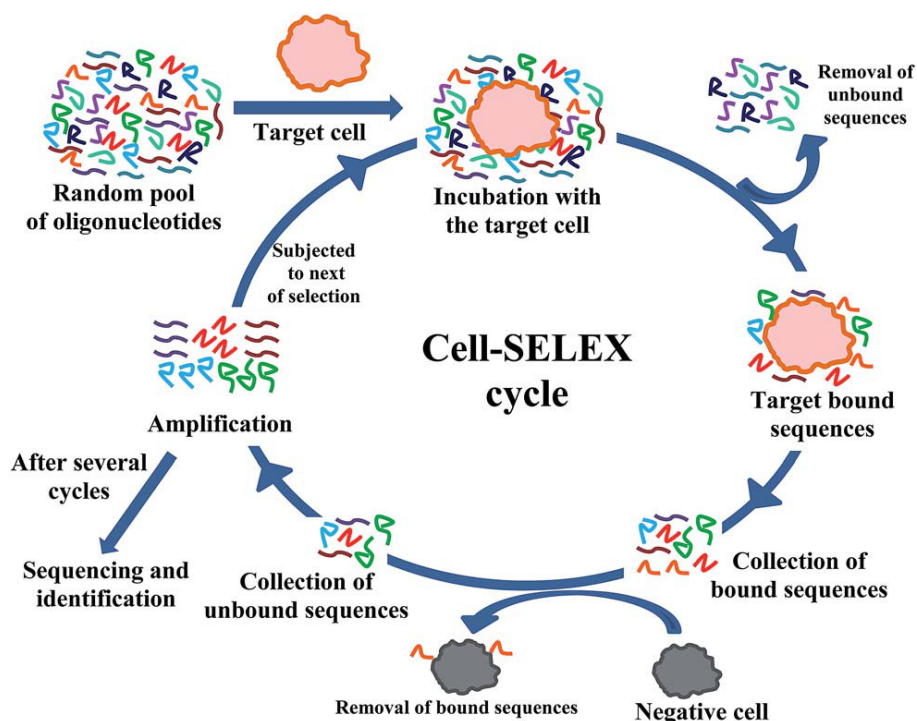


Figure 1.1: Schematic illustration of the cell-SELEX process used to select aptamer sequences specific to one cell type. Reproduced from Reference [68] with permission of The Royal Society of Chemistry.

Intriguingly, once purified, the aptamer target sequence is incredibly specific, where single basepair modifications, even those modifications away from the known binding site, inhibit target binding to the aptamer, presumably due to hydrogen-bond disruption within the target-stabilized nucleic acid secondary structure. The degree of inhibition with single basepair replacement/omission range from slight decreases in the binding affinity to complete impotence of ligand-aptamer formation [73-75].

Binding of the analyte molecule to its sequence specific aptamer is traceable by observation of the structural adjustment from the single-stranded sequence into its stable, target-bound secondary structure [38,41,64]. Under this premise, as well as the sequence specificity of the target molecule, the aptamer is an obvious biophysical target for biomolecular assays and a broad variety of sensors. In fact, aptamers are a potential replacement for immunoassay technologies which rely on antigen-antibody interactions [76].

Antibody-based sensors frequently incur nonspecific interactions [76-78]. Thus, aptamers have arisen as a good alternative to antibodies in detection systems where sensitive target-

aptamer permits appendage to surfaces, electrodes, nanoparticles, fluorophores, magnetic components, etc. [42-45,81-89]. For instance, significant steps in electrochemical sensing of molecular binding have been made in recent years. In these instances, the target, often an unlabeled small ligand, can induce a measurable change in voltage when the aptamer sequence positions the target near the electrode [44,83-85]. The electrochemical aptamer sensor represents useful replacement technology for antibody-based electrochemical sensors, as aptamers are smaller and the Debye length, or the distance between the target and the electrode surface, is significantly decreased as depicted in Figure 1.3 [86]. Other electronic aptasensors incur voltage changes from redox reactions triggered by the aptamer's structural change when target-bound [45,87-89].

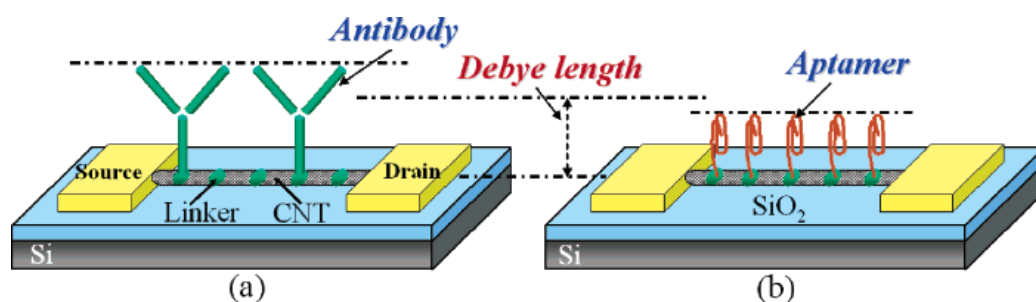


Figure 1.3: Illustration of (a) an antibody-based electronic sensor and (b) an aptamer-based electronic sensor where the clear advantage in the use of aptamer is the shortening of the Debye length, positioning of the target near the electrode surface, and increase in observed voltage per target molecule bound. Reprinted with permission from Maehashi, K.; Katsura, T.; Kerman, K.; Takamura, Y.; Matsumoto, K., Tamiya, E. Label-free protein biosensor based on aptamer-modified carbon nanotube field-effect transistors. *Anal. Chem.* **2007**, *79*, 782-787 [86]. Copyright 2007 American Chemical Society.

With aptasensor development on the rise, it is necessary to determine the aptamer properties that influence their detection capabilities. Previous groups have explored the importance of sequence mutations, sequence length, and environmental conditions most optimal for aptamer-target binding [46-49,90,91]. A common measure of the aptamer-target interaction is the binding dissociation constant (K_d), which is the reciprocal of the binding association constant (K_a) and an equilibrium constant describing the ratio of bound to unbound target concentrations. K_d is represented as

$$K_d = \frac{[A] \times [T]}{[AT]} \quad (\text{eqn. 1.1})$$

where [A], [T], and [AT] represent the concentrations of the aptamer, target, and aptamer-target complex, respectively. Naturally, a lower K_d value is indicative of stronger aptamer-target interaction. Typical K_d values reported for individual aptamers necessarily report the aptamer concentration with respect to the K_d or the K_d at a common, 1nM aptamer concentration [39,41,47]. A model aptamer-target binding curve with an extracted K_d is shown in Figure 1.4.

It is speculated that changes in K_d between aptasensors, even those that employ identical aptamer sequences, occur because the sensor conditions affect aptamer-target binding [39,41,47,58]. Efforts to modulate the K_d have been reasonably successful by modifying the aptamer sequence *away* from the ligand-binding site, ensuring that binding between the target and aptamer can still occur, though a destabilization of the aptamer-ligand secondary structure occurs. In addition, the use of duplex sequences away from the binding site show a similar, inhibitory affect on the aptamer's K_d value [36].

In examples where the identical aptamer sequence is utilized, optical aptasensors with “flare” strands report a wide range of K_d values. Though it has not been explored systematically, this particular change in K_d is attributed to varying degrees of aptamer sequence blockage by the complement “flare” strand [39,41]. The suggestion that modifications made to the sensor design

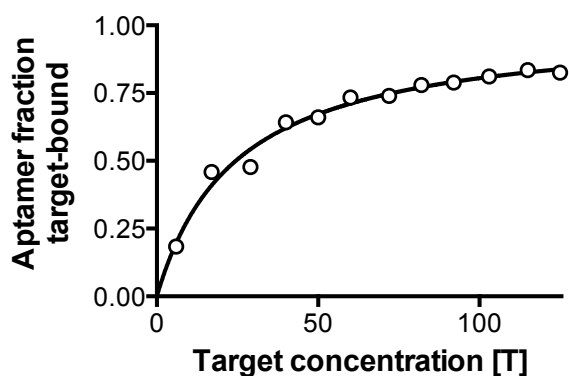


Figure 1.4: Data set plotting the fraction of aptamer bound to its target molecule vs. target concentration. The data is fit to the binding curve described in eqn 1.1. The data points were obtained from a GraphPad PRISM example data set for a one-site binding curve [92].

(rather than the aptamer sequence itself) are capable of tuning the K_d is powerful, as changing the sequence itself is risky and can result in the loss of ligand binding altogether [73]. K_d modulation is an essential biophysical tool in sensing, as target molecule concentrations vary greatly depending on the medium [46-48,75]. In order to continue pushing aptamer sensor applications forward to near-patient or implanted sensors, further investigation into control over aptamer K_d modification is necessary. In Chapter 3, the capability to “tune” concentration-dependent binding in molecular beacon style aptamer sensors is studied.

1.3 G-quadruplexes and disease state implications

G-quadruplexes, an RNA and/or DNA conformation stabilized by guanine Hoogsteen basepair interactions, have dominated much of the genetic and biological literature over the past two decades [93]. Since their characterization in 1962 as a “Helix formation by guanylic DNA,” G-quadruplexes have proven to be pivotal mechanistic regulators in the genome [93-96].

Hoogsteen basepairing between multiple stacked planes of 4-guanine complexes comprise the G-quadruplex structure and can be structurally stable with as little as two guanine stacks maintaining the box-like formation [97,98]. Formation of a single-stranded G-quadruplex requires four total repetitive guanine runs, whereas multi-strand quadruplexes can form with less consecutive guanine runs per strand, as long as the sum of the total guanine tracts contributing to the structure is four [94-96]. The formation of G-quadruplexes shortens the DNA run from $\sim 72\text{\AA}$ to $\sim 21\text{\AA}$, reflecting a box-like formation. It is suggested that longer guanine repeats or more stacked guanine planes equate to more energetically favorable structures (i.e. a TATG₄ quadruplex will have a higher melting temperature (T_m) than TATG₃), though this effect is difficult to quantify as the number of total guanine runs in the sequence negates this inherent stability [98].

G-quadruplexes exhibit exceptional stability relative to other DNA secondary structures as well. A single telomere quadruplex composed of a 3-guanine stack, has a Gibbs free energy value that rivals a 4-basepair Watson-Crick double strand sequence ($\Delta G_{\text{Quad}} = -7.3$ kcal/mole vs. $\Delta G_{\text{Watson-Crick}} = -9.2$ kcal/mole) [99-102]. This quadruplex stability is heavily reliant on the presence of cationic salts, particularly low valence metal ions, that sit in the guanine plane or in between planes to stabilize the guanine hydrogen bond interactions (Figure 1.5) [97-101,103,104]. This trait alludes to the G-quadruplex’s capability to fold under biologically

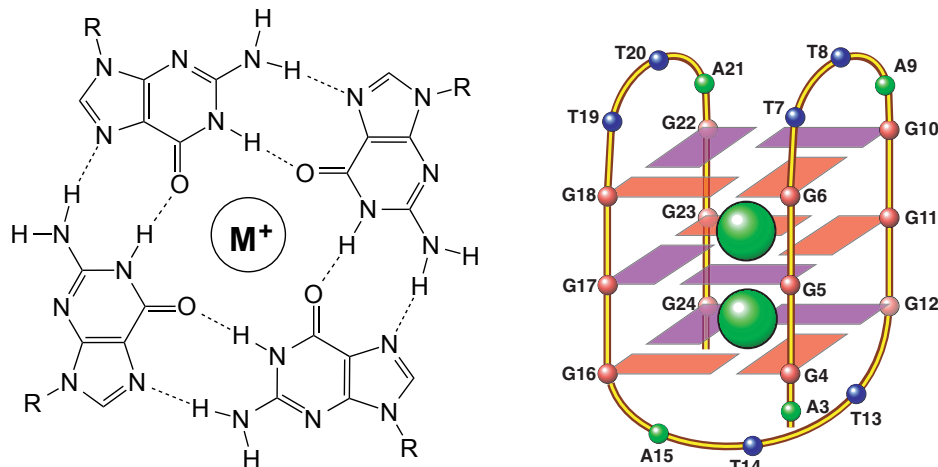


Figure 1.5: (Left) Bird's eye view down the center of a G-quadruplex, depicting the stabilizing guanine hydrogen bonds encircling a metal cationic center. (Right) A DNA sequence in the G-quadruplex secondary structure with two metal cations located in between guanine planes, represented as flat rectangles [105]. Ambrus, A.; Chen, D.; Dai, J.; Bialis, T.; Jones, R.A.; Yang, D. Human telomeric sequence forms a hybrid-type intramolecular G-quadruplex structure with mixed parallel/antiparallel strands in potassium solution, *Nucleic Acids Research*, 2006, 34, 2723–2735, by permission of Oxford University Press [105].

relevant conditions, as intracellular and intranuclear alkaline concentrations can reach 100mM Na^+ and 200mM K^+ , with notable concentrations of other divalent metal ions also present (Mg^{2+} , Ca^{2+} , etc.) [106-108].

Assumption of biological relevance eventually led to observation, with groups reporting G-quadruplex structures in promoter regions, short RNAs, and telomeres [109-118]. In an attempt to gain quantitative insight into genetic/genomic DNA quadruplex relevance, the Balasubramanian group verified the genetic versatility of quadruplex locations in the genome via chromosomal imaging with a highly specific, optical antibody probe, BG4, as seen in Figure 1.6 [117]. Additional work in imaging RNA quadruplex structures within the cytoplasm by the Balasubramanian group further verifies the biological relevance of G-quadruplexes in native nucleic acids [118]. Furthermore, genetic sequencing alludes to potentially up to 40% of promoters containing G-quadruplex sequences [116,117]. Some researchers argue that *double* the number of putative quadruplexes exist versus previous sequencing-based calculations due to stable RNA/DNA hybrid quadruplexes capable of formation. These hybrid structures only require 2 guanine tracts per RNA and DNA strand to induce a quadruplex conformation [94-96].

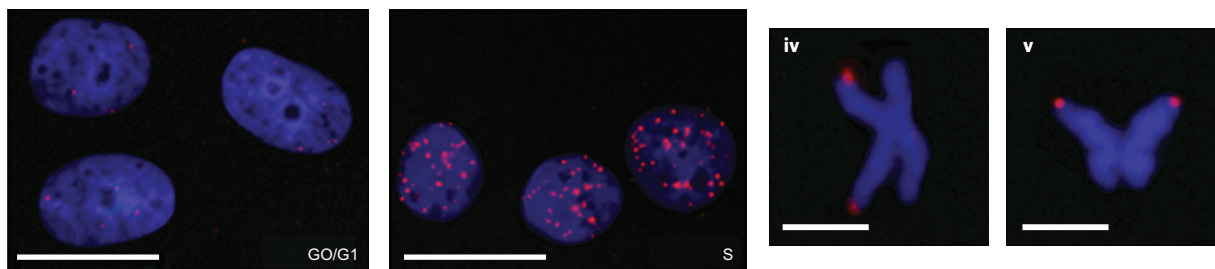


Figure 1.6: Adenocarcinoma cell nuclei (left) in G₀/G₁ phase and (middle) in S phase stained with the BG4 fluorescent DNA quadruplex-binding antibody (red) and DAPI blue nuclei stain (blue). Scale bars at 20 μ M. An increase in G-quadruplex concentration per nuclei in S phase is indicative of the life cycle-dependent nature of G-quadruplexes and their roles in cell metabolism. (Right) Chromosomes stained with BG4 quadruplex-binding antibody (red) and DAPI blue (blue). High BG4 intensity observed at the chromosomal tips verifies a high density of quadruplex folding in telomeres [117]. Scale bars at 2.5 μ M [117]. Adapted by permission from Macmillan Publishers Ltd: *Nature* (Biffi, G.; Tannahill, D.; McCafferty, J.; Balasubramanian, S. Quantitative visualization of DNA G-quadruplex structures in human cells. *Nat. Chem.* **2013**, *5*, 182-186), copyright 2013 [117].

Interestingly, oncogenic promoters demonstrate a higher incidence of putative quadruplex sequences, linking G-quadruplexes to disease-state metabolisms [114,116,117,119]. The majority of these oncogenic sites contain single quadruplex sequences, but also of medical interest are long repeat guanine tracts in the human genome, only two of which are known: the telomere and insulin-linked polymorphic regions (ILPR) [74,99,101,114,120,121]. Summaries of these G-quadruplex-littered repeat sequences are provided in sections **1.3.1b** and **1.3.2**, respectively.

G-quadruplex relevance in cell function and medicine presumably stem from protein-quadruplex interactions, examples of which have been reported in recent years [122-127]. Intriguingly, both stabilization and destabilization effects of quadruplexes are observed with specific proteins, endorsing the versatility of quadruplexes in biological function. While some G-quadruplexes are assigned the role of transcriptional upregulators, others are reported as repressors, varying only by genetic location [128]. Moreover, G-quadruplex stability and destabilization effects by proteins that are linked to specific disease states support observations that G-quadruplexes could also be considered a “resting” conformation of DNA in addition to duplex, histone-coiled, DNA [129]. The metabolic function and disease state implications of G-

quadruplexes in DNA are quite remarkable. Notable examples are summarized below in sections 1.3.1 and 1.3.2.

1.3.1 The role of G-quadruplexes in cancer

1.3.1a C-Myc function and cancer

The Myc family of transcription factors plays important roles in DNA replication, apoptosis, and cell transformation [130,131]. Within this group of similarly structured proteins exists c-Myc, a protein that acts as both a transcriptional activator and suppressor via its DNA-binding mechanism. Misregulation of the c-Myc gene is linked to a variety of human

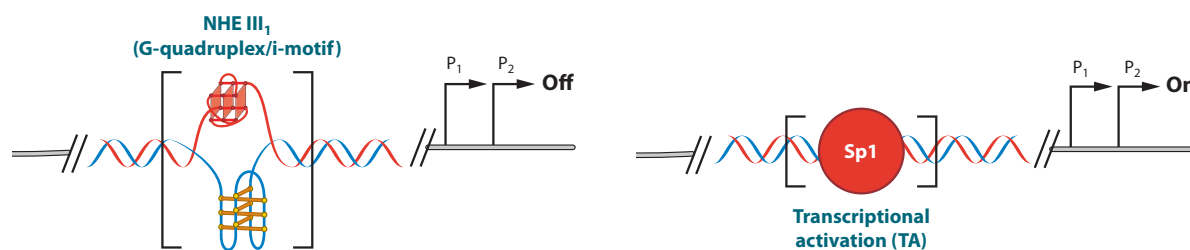


Figure 1.7: (Left) Representation of the normal, G-quadruplex-induced repression of the c-Myc gene stemming from G-quadruplex formation in the promoter region. (Right) Protein-bound duplex DNA inducing c-Myc gene transcription by a promoter region binding site. The absence of the G-quadruplex in the promoter region permits protein binding and subsequent c-Myc upregulation commonly observed in malignant cells. Adapted with permission from Reference 127 and Reference 132 [127, 132].

malignancies and, more specifically, a short, G-quadruplex folding region of its promoter, NHE III₁, accrues the blame for c-Myc's inconsistent expression [127,130-132]. Studies comparing healthy cell and tumor cell c-Myc transcript levels indicate a general upregulation of c-Myc transcription in malignant tumors, with strong evidence suggesting that single-stranded, non-quadruplex folded DNA, or protein-bound duplex DNA induces c-Myc transcription. A representation of this quadruplex-based protein regulation is shown in Figure 1.7. Small-molecule drugs effective in binding and stabilizing NHE III₁'s parallel quadruplex are being explored as a potential treatment to repress c-Myc expression [132-135].

1.3.1b Telomeres and cancer

Telomeres, non-coding overhangs at the 3'-end of chromosomes, are considered a protective mechanism against genome degradation and genetic mutations during the DNA replication process [136-138]. Existing at lengths out to 300,000bp, telomere sequences provide

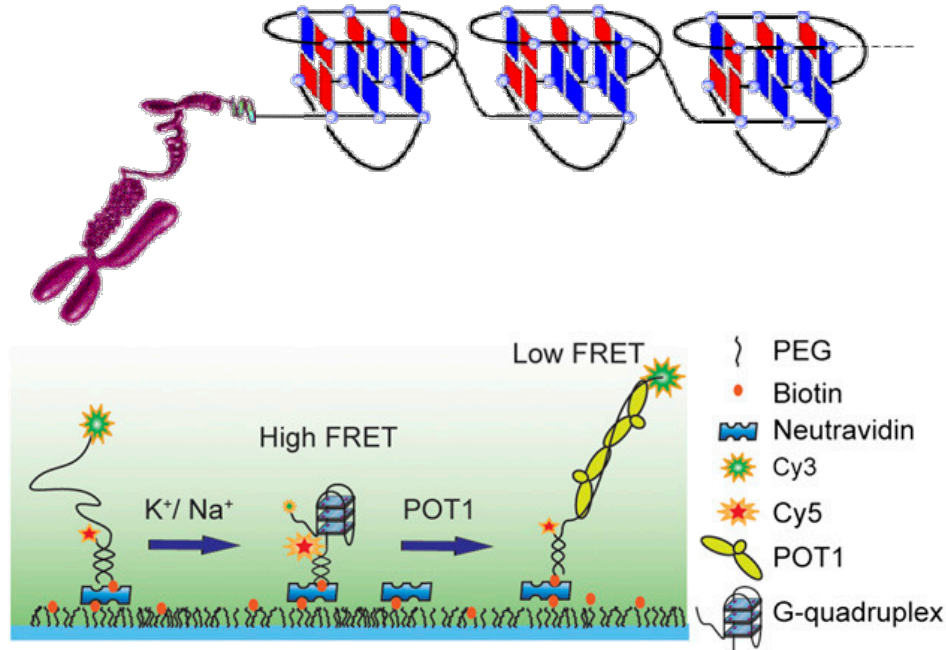


Figure 1.8: (Top) Cartoon of a chromosome terminated in a string of protective G-quadruplex structures, as predicted by researchers [139]. From Xu, X., “Consecutive formation of G-quadruplexes in human telomeric-overhang DNA: a protective capping structure for telomere ends,” *Angewandte Chemie International Edition*. Copyright © 2009 by John Wiley & Sons, Inc. Reprinted by permission of John Wiley & Sons, Inc [120]. (Bottom) Single molecule experiments that elucidate the unfolding of telomere G-quadruplexes by two POT1 proteins, monitored by the change going from a high FRET efficiency (quadruplex-folded state) to a low FRET efficiency (POT1 unwound state) [140]. Ying, L.; Green, J.J.; Haitao, L.; Klenerman, D.; Balasubramanian, S. Studies on the structure and dynamics of the human telomeric G quadruplex by single-molecule fluorescence resonance energy transfer. *Proc. Natl Acad. Sci. USA* **2003**, *100*, 14629–14634. Copyright 2003 National Academy of Sciences, USA [140].

healthy cells with an inherent senescence by way of gradual shortening with every DNA replication that eventually results in a cease of the replicative process when no protective single-stranded overhang remains. They are heavily researched in the aging process for their dictation

of an individual cell's lifetime [136-138]. The telomere sequence is a repeat of guanine-infused tracts (dTTAGGG) known to form a number of stable G-quadruplex conformations. Of all the calculated and observed structures in solution, only one conformation, the (3+1) Hybrid (which can be subdivided into two, inverse structures, Hybrid-1 and Hybrid-2), is observed both intracellularly and in multi-quadruplex telomere sequences [139,141-143].

In non-senescent tumor cells, a telomere lengthening mechanism is employed, utilizing the enzyme telomerase to bypass the natural senescence of the cell [136-138]. By encouraging never-ending cell replication, cancer cells dominate tissue locale over the properly aging healthy cells [144,145]. Thus, a number of research groups are identifying telomere and telomerase targets in anti-cancer investigations [125,135,136,144-148]. Use of quadruplex-binding small molecules consistently results in inhibition of telomerase, which indicates either unfolding of the quadruplex is necessary for telomerase binding/lengthening or the small molecule prevents telomerase binding to the occupied quadruplex [147,148].

Other telomere-binding proteins, such as TPP1 and Pot1, exhibit an important directional dependence (3' vs. 5' movement) in the single-stranded telomere sequence [124,140,149]. For instance, Pot1 can bind single stranded DNA independently, but is capable of movement along the strand only in the 5' → 3' direction. When complexed with TPP1, the new dual-protein formation is capable of sliding in both directions along the telomere single-strand. The protein complex is known to fold and unfold quadruplex sequences in a stepwise fashion, as shown by single-molecule FRET experiments, alluding to their potential as a priming step for other telomere-relevant events, such as elongation by telomerase [124,140,149]. The directionality is intriguing and indicates an importance in distinguishing Hybrid-1 from Hybrid-2 formation in telomeres, because the only structural distinction between the inverse Hybrids is the directionality of a single parallel arm in the quadruplex "box" [101,141]. In Chapters 4 and 5, NSET-based human telomere probes are utilized to determine the specific G-quadruplex structures forming under biologically relevant conditions.

1.3.2 The role of G-quadruplexes in Type I Diabetes

The second known G-quadruplex repeat sequence in the genome is the insulin-linked polymorphic region (ILPR), also known as the hypervariable tandem repeat (HVR), the variable nucleotide tandem repeat (VNTR), and the insulin diabetes mellitus loci (IDDM)

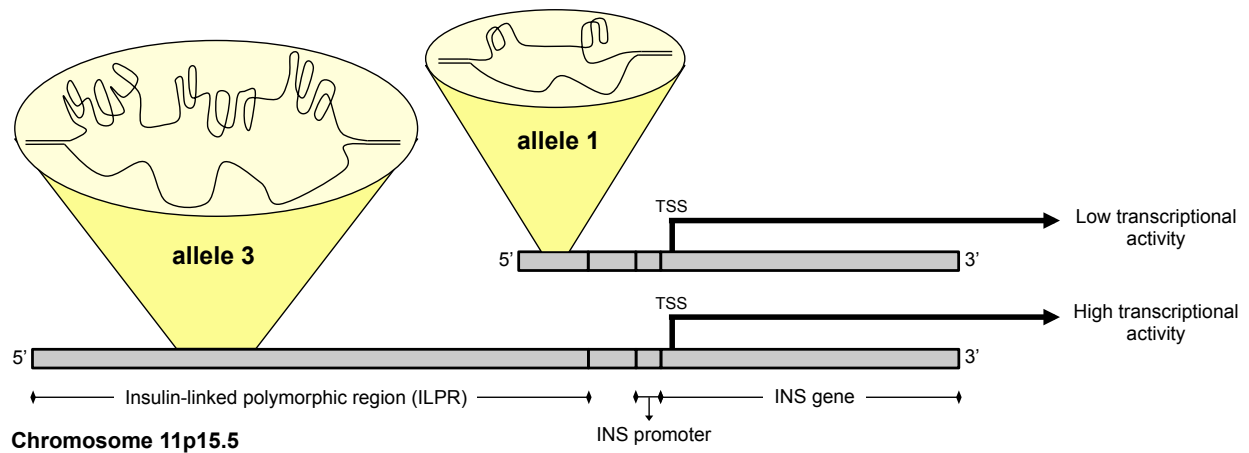


Figure 1.9: Schematic of the ILPR region located upstream from the INS gene. It is speculated that the length and/or quadruplex-forming behavior of allele 3 contribute to the higher transcriptional activity of INS relative to the shortened, mutated allele 1, which consequently, results in a predisposition for T1D [152-155].

[121,129,150,151]. Containing anywhere from 60-200 sequence repeats (dACAG₄TGTG₄), the ILPR is located 365 basepairs upstream from the insulin gene (INS) promoter region. The consecutive guanine tracts are potentially capable of forming anywhere from 30 to 100 G-quadruplex structures with high stability, as 4bp guanine stacks are involved [121,129,150-153]. The ILPR's role in INS regulation and subsequent Type 1 Diabetes (T1D) predisposition is complex and not well understood. In fact, it requires the merging of multiple disciplines in biology to fully grasp the complexity of ILPR's T1D mechanistic participation.

Geneticists have observed that large deletions within the ILPR cause a 40% increase in late-onset T1D development [150-154,156]. Whereas several examples of single-nucleotide mutations in G-quadruplex structures have been shown to completely inhibit quadruplex formation *and* those types of mutations are present in the ILPR, single-nucleotide deletions are not to blame for the malfunction in the ILPR [121,129,151]. Rather, deletions of hundreds of basepairs, creating clear phenotypic differences in healthy versus T1D predisposed patients, led to categorization of three genotypes (allele I, II, and III) based solely on ILPR length. Allele III patients (135-200 ILPR 14bp repeats) exhibit normal phenotypes and are therefore not likely to develop T1D in their lifetime, while allele I patients (26-65 14bp repeats) incur a 40%

predisposition rate [152-154,156]. Allele II ILPR length is rarely observed (65-135 14bp repeats) and lies in between the categories of healthy and T1D predisposed. Biologists have correlated allele I's genotype to low levels of INS transcripts in fetal thymus development [155,157]. This is important because unlike Type 2 Diabetes, T1D is an autoimmune disease, where insulin-producing beta cells are healthy, but are attacked by the body's own immune system as foreign entities [155,157].

Biochemists and biophysicists simultaneously went on to discover important protein-quadruplex interactions in the ILPR that are potentially driving the misregulation of INS transcript levels. While several proteins have been shown to be effective ILPR binders (IGF-2 and even insulin itself) [158-160], only one is specific to thymal cells, namely the autoimmune regulator (AIRE) [155,157,161]. In synthetic ILPR-INS constructs, it was observed that the level of AIRE protein is directly proportional to the level of INS transcription. Moreover, the number of quadruplexes preceding the INS promoter (i.e. – allele I vs. allele III) is directly proportional to the level of INS transcription [155,157]. Both of these observations were only relevant with the native INS 365bp promoter, and a significant decrease in INS transcription is observed when a generic promoter is introduced between the ILPR and INS gene [155].

In summary, the dominant regulator of the INS gene is the ILPR region preceding the INS promoter. Playing an important role in this regulation is the length of the ILPR (allele I vs. allele III) and potentially the number of quadruplexes forming in the region (Figure 1.9) [121,150-157,161]. AIRE, a known thymus-specific protein and ILPR quadruplex binder, assists in the ILPR-based transcription of the INS gene, possibly through a quadruplex-binding mechanism in early stage thymal development; low levels of which encourage T1D development later in life [155].

The role of quadruplex formation in the ILPR's INS regulation differs from those observed in the c-Myc cancer mechanism and telomere function. More specifically, it has not proven helpful or necessary to study ILPR quadruplexes on a structure-specific basis [151,159]. Whereas c-Myc's function is attributed to a single parallel quadruplex formation [127,130-135] and telomeres are identified solely as Hybrid conformers [139,141-143], the ILPR's large deletions and resulting T1D phenotype is more global. Therefore, less attention is paid to the individual quadruplex structures within the region, but rather the relationship and cooperativity between ILPR quadruplexes becomes relevant [162]. Experiments described in Chapter 6 begin

to bridge the biophysics-genetics gap by studying the interactions of multiple, sequential ILPR quadruplexes using an NSET-based probe. Furthermore, the capabilities of future work incorporating more than three sequential quadruplexes is discussed.

1.4 Summary of chapters

This dissertation is directed towards exploring the applicability of NSET in elucidating biological structures via optical sensing mechanisms. In Chapter 2, state-of-the-art techniques in tracking nucleic acid conformations are discussed, including the techniques utilized in this dissertation. In Chapter 3, the sequence-dependent modification of effective aptamer sensors is described using off-to-on ATP aptamer NSET beacons. Chapter 4 investigates 1) the capability of NSET to distinguish biologically relevant nucleic acid structures (flanked human telomere G-quadruplexes) and 2) the size limits of gold nanoparticles (AuNPs) as quenching molecules for these types of biophysical probes. In Chapter 5, relevant biological information is attained when the same NSET probes from Chapter 4 are applied to determine structural populations the native telomere sequence, Tel22. Continuing with the theme of investigating important G-quadruplex properties, Chapter 6 describes NSET beacons to track long-range ILPR quadruplex folding. The cooperativity of these quadruplexes is investigated by extracting biophysical constants from the NSET-quenching saturation curves. Last, Chapter 7 explores the next steps in structural elucidation with NSET contact points by establishing a mathematical model for an NSET-FRET hybrid system. In this system, the capability to explore long-range (NSET) and short-range (FRET) distances simultaneously is investigated.

CHAPTER 2

METHODS FOR MONITORING NUCLEIC ACID STRUCTURES

2.1 Introduction

Rosalind Franklin revealed the helical DNA structure via X-ray diffraction, but since her discovery, great strides have been made in employing other techniques to characterize nucleic acid conformations [1]. Summarized below are various relevant experimental methods, their strengths and weaknesses, and examples of their usefulness in the field of nucleic acid research. The techniques described in sections 2.4.1-2.4.6 (NMR, EPR, X-ray Crystallography, Optical Tweezers, CD, and FRET) are alternative methodologies used in the field of biophysics for conformational analysis. In section 2.4.7, NSET is described, which is the *primary* method utilized to study DNA secondary structures in this dissertation.

2.1.1 NMR spectroscopy

The benefits of NMR spectroscopy in nucleic acid research are vast. Stemming from early characterizations such as DNA-intercalating drugs [163,164], NMR can be used to monitor a variety of conformers because of the distinct ppm shift attributed to changes in local atom environments. For example, parallel telomere G-quadruplex sequences are easily identifiable from Hybrid quadruplexes based solely on ¹H NMR, where significant changes in the guanine-specific hydrogens' low-field ppm values are observed due to differences in the structures' hydrogen-bonding interactions [105,164-168]. Moreover, site-specific basepair labeling with NMR-active isotopes like ¹⁵N in synthetic nucleic acid sequences permits easy tracking of specific basepair/protein interactions [169-171].

With the benefits of NMR, also come various downsides. High sample concentrations not only make experiments expensive but also introduce unwanted, non-native intermolecular interactions. Also, nucleic acid folding has a heavy reliance on high salt concentrations, which cause broadening of NMR signals difficult to fully deconvolute [165,167,168]. Attempts to verify optical results with NMR in this dissertation failed, due to low sample concentrations.

2.1.2 EPR

EPR tracking of nucleic acids has developed in recent years with progress in synthesis of effective spin-labels [172,173]. Specifically, DEER-EPR (also known as PELDOR) calculates the distance between two spin-labels based on the strength of their magnetic coupling. The two spin-labeled basepairs act as contact points in an oligonucleotide sequences, the intermolecular distance of which is extractable based upon the observed resonant coupling [142,143,172-174].

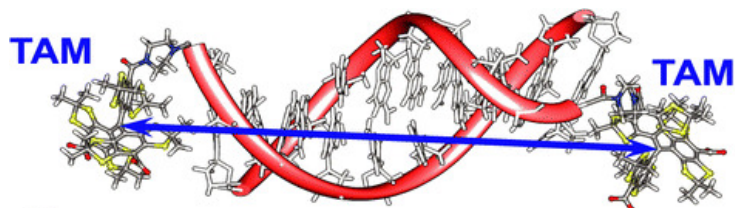


Figure 2.1: Short double stranded DNA sequence labeled terminally with triarylmethyl (TAM) radicals to monitor room temperature distant-dependent magnetic coupling via pulsed EPR spectroscopy [173]. Adapted with permission from Shevelev, G.Y.; Krumkacheva, O.A.; Lomzov, A.A.; Kuzhelev, A.A.; Rogoshnikova, O.Y.; Trukhin, D.V.; Troitskaya, T.I.; Tormushev, V.M.; Fedin, M.V.; Pyshnyi, D.P.; Bagryansjaya, E.G. Physiological-temperature distance measurement in nucleic acid using triarylmethyl-based spin labels and pulsed dipolar EPR spectroscopy. *J. Am. Chem. Soc.* **2014**, *136*, 9874-9877. Copyright 2014 American Chemical Society [174].

In terms of experimental accuracy and versatility, EPR is arguably the most effective short-range contact-point tool for nucleic acid conformations, as it is effective in solution, at low concentrations, and has also been used for intracellular measurements [142]. Maximum EPR contact measurements of ~ 90 Å have been reported [175].

EPR's primary pitfall is the inability to track distances at biologically relevant temperatures. Measurements are performed at 0°C or below [142,143,172,173] to attain observable resonance between labels, which potentially alters the structure of the nucleic acid under observation. Recently though, a group reported the synthesis of trityl spin labels capable of room temperature measurement of short dsDNA basepair distances (<13 basepairs, 45 Å) [174]. A schematic image of sample under investigation is shown in Figure 2.1 [174]. If spin labels with strong resonance at room temperature continue to be developed, EPR may be an experimental method difficult to beat in nucleic acid research. While EPR was not utilized in this

dissertation, EPR studies from others have appeared that confirm the results obtained with optical techniques described in Chapters 4 and 5.

2.1.3 X-ray crystallography

The best structural resolution in oligonucleotide structures, without contest, is X-ray crystallography. X-ray diffraction of planes in the crystallized DNA structure is resolvable to sub-angstrom levels, and produces definitive, inarguable details of the conformer under investigation [5,7,15,51,61-66]. In the development of NSET (described in section 2.2), X-ray crystal structures of nucleic acids were crucial to analyze the relevance of the observed structure [176-179].

Examples of DNA/RNA structures solved by crystallography are numerous, but an excellent use of crystallography (which also conveniently identifies its shortcomings) is the telomeric G-quadruplex sequence. Under K^+ rich conditions, a single parallel G-quadruplex crystallizes and is characterizable by crystallographic analysis [180]. Under Na^+ conditions, however, the parallel structure does not crystallize, and is observed as part of a mixed population of quadruplex structures by other methods [101,105,141,143,164-166]. In this case, crystallographic data is unattainable, highlighting the sensitivity of crystal formation to sample purity. Moreover, solution-based methods, such as Förster resonance energy transfer (FRET), EPR, NMR, and circular dichroism (CD), characterize the human telomere sequence in K^+ rich *solution* conditions as a mixture of conformers [101,105,140-143, 164-166,181,182]. This demonstrates that crystallographic methods, while attaining exceptional resolution, lack the capability of replicating biological conditions for ideal nucleic acid structural mapping.

2.1.4 Optical tweezers

Apparatuses built to “trap” single molecules were initially limited to applications in physics [159]. Upon slowly filtering into the biological sciences, however, optical traps have become an exciting asset in monitoring environmentally-sensitive molecules, sorting phenotypically diverse cells, and measuring biomolecular properties [183-188]. Molecules studied via optical trapping techniques range in size from small molecules to living cells [184-187]. It is important to note that optical traps, which utilize focused lasers at optical wavelengths to control the 3D position of nano-objects, are not ideal for determining structures. Therefore,

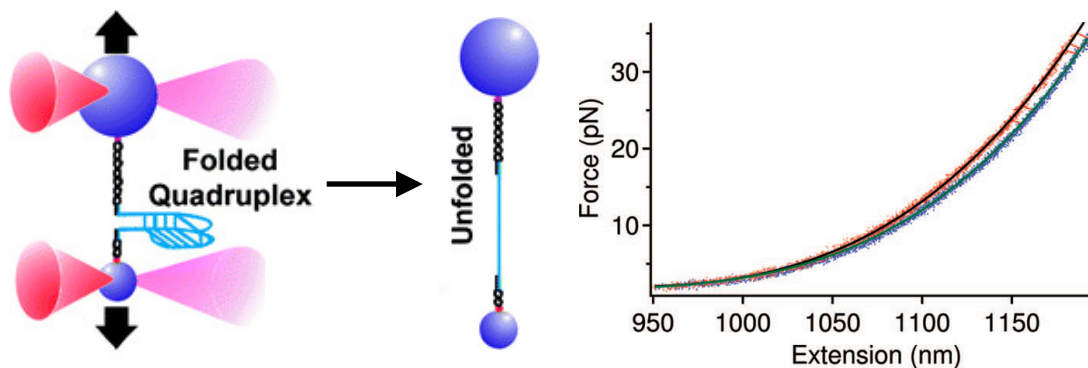


Figure 2.2: (Left) Illustration of the optical tweezer experimental setup in the forced unfolding a G-quadruplex. Blue 3D circles represent the beads located within the focus of the optical laser responsible for the opposing directional motion. (Right) Force (in picoNewtons, pN) exerted on the quadruplex structure vs. the distance extension between the beads. A jump in the extension (orange line to blue line at ~1200nm) indicates a quadruplex unfolding event [129]. Adapted with permission from Yu, Z.; Schonhoft, J.D.; Dhakal, S.; Bajracharya, R.; Hegde, R.; Soumitra, B.; Mao, H. ILPR G-quadruplexes formed in seconds demonstrate high mechanical stabilities. *J. Am Chem. Soc.* **2009**, *131*, 1876-1882. Copyright 2009 American Chemical Society [129].

their usefulness in nucleic acid research is limited to determining biophysical constants, as shown in the Force (pN) vs. Extension (nm) curve in Figure 2.2 [129]. However biophysical constants are often sufficient to distinguish amongst known structures; perhaps structures pre-selected by X-ray crystallography or molecular dynamics calculations.

Pertinent G-quadruplex information, for instance, has been unlocked by analyzing the structural properties of individual and sequential structures in an optical (or magnetic) tweezer system [129,162]. The force required (in pico-Newtowns (pN)) to unwind a single quadruplex, as well as the average distance change in transitioning from the folded G-quadruplex to single-stranded DNA state, are directly related to the entropic, enthalpic, and free energy forces maintaining the hydrogen-bond stabilized G-quadruplex (Figure 2.2) [129,162]. Using optical tweezer measurements to compare the unwinding force of one quadruplex to two quadruplexes in sequence, elucidated an additional force that stabilizes the two-quadruplex system, verifying an interaction (at least in the folded state) between neighboring G-quadruplex structures [120,162]. What these optical trapping techniques lack in obtaining structural information and replicating native conditions, they regain in sensitivity at the single molecule level.

2.1.5 Circular dichroism (CD)

The differential absorption of right-handed versus left-handed circular polarized light represents a potent characteristic of chiral molecules. In addition, Applied Photophysics Ltd., designer of highly sensitive spectroscopic instrumentation, notes that “a primary use [of CD] is in analysing the secondary structure or conformation of macromolecules,” which naturally explains the popularity of utilizing CD in nucleic acid structural analysis [189].

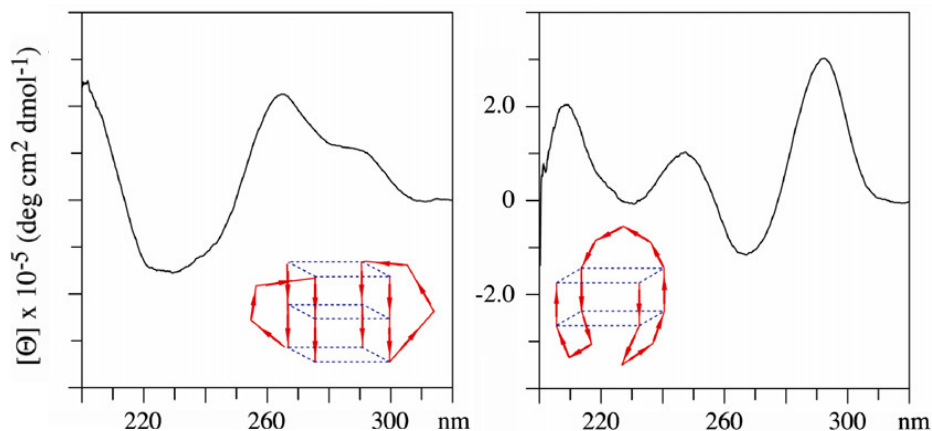


Figure 2.3: Circular dichroism (CD) spectra of (left) a fully parallel G-quadruplex and (right) an antiparallel G-quadruplex. Notable differences between the spectra are the negative valley at 250nm in the parallel structure and more pronounced 290nm peak in the antiparallel quadruplex spectra. Hybrid telomere quadruplexes, which have a (3+1) mixture of parallel to antiparallel strands in their quadruplex, exhibit a CD spectra intermediate of those shown above [182]. Reprinted from *Methods*, 43, Paramasivan, S., Rujan, I., and Bolton, P.H., “Circular dichroism of quadruplex DNAs: applications to structure, cation effects and ligand binding, pages 324–331, Copyright 2007, with permission from Elsevier [182].

The human telomere structures, for instance, which each contain a different combination of parallel and antiparallel directional arms that comprise the overall G-quadruplex structure, are no exception in that they contain distinguishable absorptive traits in CD spectroscopy [181,182,190]. While fully parallel and fully antiparallel telomere conformers have distinct CD spectra in the UV region, the (3+1) hybrid structures are, as one would expect, intermediate in relative CD spectral features. These differences in spectra, noted primarily by clear positive or negative peaks at 250nm and 290nm, render the parallel (“propeller”), the anti-parallel

(“basket”), and hybrid structures distinguishable, as shown in Figure 2.3 [181,182,190]. Unfortunately, the two most biologically relevant telomere structures, Hybrid-1 and Hybrid-2, produce identical spectra, as they both contain the same ratio of antiparallel/parallel strands [101,181,182,190]. While CD is useful in tracking most biomolecules with a secondary or tertiary folded structure, its applicability for structurally similar biomolecules is limited. In Chapters 5 and 6, CD is utilized as a secondary technique to verify quadruplex folding, though the specific G-quadruplex structures under investigation are indeterminable.

2.1.6 Förster Resonance Energy Transfer (FRET)

FRET describes the dipole coupling interaction of two fluorophores in close proximity (<100 Å), observable by the decrease in emission intensity from the high energy donor and subsequent appearance of emission intensity from the low energy acceptor [191,192]. This non-radiative downhill transfer of energy follows a distant-dependent efficiency model where the R_0 , or distance as which 50% energy transfer occurs is described as,

$$R_0 = \left[\frac{9000(\ln 10)\kappa^2\Phi_{dye}J(\lambda)}{128\pi^5N_A n^4} \right]^{1/6} \quad \text{eqn. 2.1}$$

where κ is the orientation factor, Φ_{dye} is the quantum yield of the donor, N_A is Avogadro’s number, n is the refractive index of the medium, and $J(\lambda)$ is the overlap integral between the donor emission and acceptor absorption, calculated from the donor emission spectra and acceptor extinction spectra. As seen in the theory, values that increase the likelihood of effective energy transfer (large R_0 values) are a large overlap integral and high quantum yield of the donor [191,192].

FRET systems are easily predictable, adaptable to a variety of dye combinations, and reliable in regards to their correlation to theory. Thus, the popularity of FRET systems for monitoring a wide-range of biomolecular events, especially changes in nucleic acid structures, is no surprise. The simplest nucleic acid FRET system is likely the molecular beacon, noted earlier in section 1.1 in the form of an “aptamer beacon,” where a change in nucleic acid structure from a hairpin (high FRET state) to an extended double stranded DNA (low FRET state) is tracked [38,193]. The loss of FRET signal (decrease in acceptor emission), then, is attributed to the presence of a complement target strand.

With the availability of a full optical spectrum of organic dyes, FRET systems can become drastically more complicated, as groups look to incorporate multi-wavelength markers in an attempt to eliminate the need to deconvolute auto-fluorescence and background noise. Three-color FRET is a useful triangulation system where the distant-dependent quenching of multiple donors/acceptors can elucidate 3D structural information. In devices designed to mimic electron transfer systems, such as those used to convert solar energy, representation of energy flow in DNA origami-based devices is easily observable via optical energy in multi-dye FRET, and subsequent structural changes in the origami structures can be tested for their reliability in energy transfer [194]. When structure is less important, as in the instance of multi-wavelength biomarkers, a FRET waterfall system is employed. FRET waterfall constructs have one clear benefit: one excitation wavelength results in up to three emission wavelengths [195]. This concept is represented further in Figure 2.4 [195].

It is important to note that even FRET dye pairs with the highest $J(\lambda)$ are limited in distance. Theory and experiment both support the observation that the maximum efficient FRET

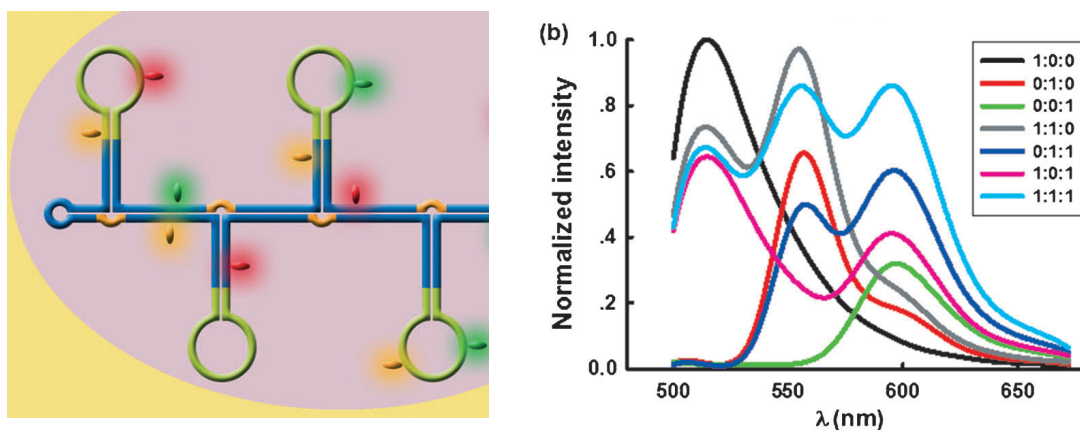


Figure 2.4: (Left) Illustration of the condensed RNA hairpin structures littered with three dyes, fluorescein (green), Cy3 (yellow), and ROX (red), which act as a FRET waterfall system where one excitation wavelength (488nm) produces three emission peaks (510nm, 555nm and 600nm). (Right) Emission spectra of the FRET waterfall where various dyes are omitted from the system, as denoted by the binary representation in the top right corner. The binary legend is listed as left to right, fluorescein, Cy3, and ROX, respectively. From Hu, R., “DNA Nanoflowers for Multiplexed Cellular Imaging and Traceable Targeted Drug Delivery,” *Angewandte Chemie International Edition*. Copyright © 2014 by John Wiley & Sons, Inc. Reprinted by permission of John Wiley & Sons, Inc [195].

coupling is ~ 100 Å as, FRET R_0 's max out at 65 Å [191-193]. Some researchers are looking to push the FRET R_0 limit by placing the dye pairs within the near-field of a large metal nanoparticle in an effort to take advantage of plasmonic enhancement effects observed when metal nanoparticles exceed 30nm in diameter [196-198]. Large increases in the FRET R_0 value have been observed with this technique though it is without predictability. Systematic studies of FRET systems coupled to plasmonic systems are necessary before the FRET R_0 enhancement tactic can be reliably controlled. The majority of the contact distances under investigation in this dissertation fall outside of measurable FRET distances, thus FRET is not used in this dissertation.

2.2 Nanometal Surface Energy Transfer (NSET) for structural elucidation

The Strouse group has developed an additional energy transfer model over the past decade incorporating a metal nanoparticle acceptor (rather than the FRET organic dye acceptor) in an effort to break the 100 Å distance barrier in optical energy transfer experiments. Derived from the original work of Kuhn and Chance, Prock, & Silbey for gold and silver surfaces, the Strouse group has developed an empirical model of Nanometal Surface Energy Transfer (NSET) between small spherical nanometals and organic fluorophores [199,200]. In NSET, the small (<20nm diameter) nanometal acts as the acceptor, providing an additional non-radiative decay pathway for the organic fluorophore, in analogy to a FRET acceptor. NSET extends the distance of interaction between the donor fluorophore and energy transfer acceptor well beyond the 100 Å seen in FRET, out to distances greater than 350 Å [176-178]. The NSET model has been shown to be empirically valid for gold nanoparticles with diameters smaller than 20nm and is strictly valid only for particles that have negligible nearfield intensities compared to their absorptivity [178]. Whereas previous groups successfully described the plasmonic oscillatory effects of bulk and nanometals, none have effectively constructed an energy transfer theory describing the interaction between a metal nanoparticle and molecular dye confirmable by experimentation. In fact, the most notable theories commonly over-predicted the metal's quenching behavior when considering small metal nanoparticles (~ 2 nm) [200].

Equation 2.2 outlines the size-dependent NSET model, written as the d_0 value, or the distance at which 50% energy transfer between the donor and nanoparticle acceptor occurs,

$$d_0 = \frac{\alpha\lambda}{n_m} (A\phi)^{1/4} \left[\frac{n_r}{2n_m} \left(\frac{1+\varepsilon_1^2}{\varepsilon_2^2} \right) \right]^{1/4} \quad \text{eqn. 2.2}$$

where α is the orientation of the donor treated as an average vector equal to $\frac{\left(\frac{9}{2}\right)^{1/4}}{4\pi}$, and A (eqn. 2.3) is the absorptivity of the nanoparticle.

$$A = 10^3 \ln 10 \left[\frac{\varepsilon_\lambda \left(2r_{cm} \left(\frac{2r_{cm}}{\gamma_{skin}} \right) \right)}{N_A V_{cm}^3} \right] \quad \text{eqn 2.3}$$

In equation 2.2, λ is the emission wavelength of the donor, n_m is the refractive index of water, n_r is the refractive index of the metal, Φ is the quantum yield of the donor, ε_1 is the dielectric constant of water, and ε_2 is the dielectric constant of the metal. In the subsequent equation (eqn. 2.4), N_A is Avogadro's number, ε_λ is the extinction coefficient as a function of λ , r_{cm} is the radius of the nanoparticle in centimeters, γ_{skin} is the skin depth of the nanoparticle, and V_{cm} is the volume of the nanoparticle in cm^3 [178].

It is important to first note the distance factor's mathematical powers in FRET and NSET, which are $1/d^6$ versus $1/d^4$, respectively. This stems from the coupling interaction in FRET occurring between two dipole interactions (between the donor, F_A , and acceptor, F_D) described as $F_A * F_D$ or $(1/d^3) * (1/d^3) \approx (1/d^6)$. On the other hand, the conduction electrons in the oscillatory metal nanoparticle increase the resonant coupling, which is best represented by a $F_A * F_{Dm}$ model of $(1/d^3) * (1/d) \approx (1/d^4)$ [175,190]. This 4th power dependence for small AuNPs has been confirmed by several groups but is in contrast to the d^6 distance dependence seen in larger particles (stemming from derivations of the Gersten-Nitzan model), which is a consequence of the large nearfields observed in larger nanoparticles (diameter >20 nm) [201-203]. The large particle interactions leading to the d^6 interaction can be successfully modeled as a point dipole at the center of the particle (in analogy to FRET) [201].

In development of the size-dependent NSET theory, correlation to the absorptive properties of nanoparticles required treatment of the surface absorption term with a volume absorption term, A, as shown in equations 2.2 and 2.3. In general, two terms in the NSET model, the absorptivity, A, and the dielectric constant of the metal, ε_2 , are size-dependent and are

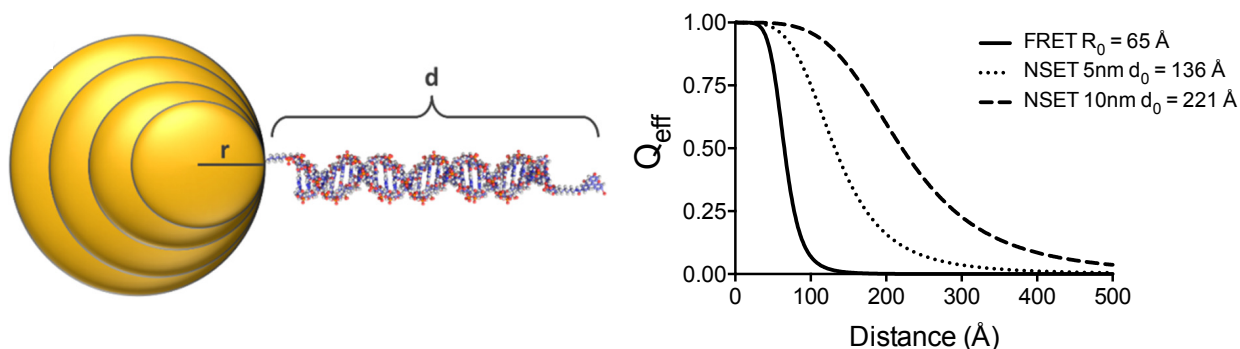


Figure 2.5: (Left) Depiction of the size-dependent NSET energy transfer measurements between various AuNP sizes (changing “r” values) and dye-labeled double-stranded DNA (of lengths “d”) [178]. (Right) Quenching efficiency (Q_{eff}) curves describing the efficiency of energy transfer versus distance for a FRET pair with an $R_0=65 \text{ \AA}$ (solid line), a 5nm AuNP with fluorescein dye where $d_0=136 \text{ \AA}$ (dotted line), and a 10nm AuNP with fluorescein dye where $d_0=221 \text{ \AA}$ (dashed line). It is clear from the efficiency curves and the R_0 , d_0 values that incorporation of an AuNP as the acceptor in the energy transfer increases the distance to which energy transfer from donor to acceptor occurs [176-178, 191].

necessarily adjusted as larger nanoparticles are employed (up to 20 nm in diameter). With the increase in nanoparticle size, a larger d_0 is also observed, indicating that the fluorophore can participate in energy transfer out to distances significantly farther from the nanoparticle surface [178].

The NSET theorem’s correlation to experiment has been demonstrated with multiple sizes of AuNPs coupled to dye-labeled, double-stranded DNA of variable lengths [176-178]. Duplexed DNA acts as a rigid rod molecule out to exceptional distances, making it the perfect “ruler” for exploring NSET’s distant dependent behavior. Initial studies confirmed that 1) AuNPs up to 16nm in diameter and 2) dyes with different optical wavelengths correlate well to the NSET theorem. Intriguingly, the verification of the mathematical theory also confirmed the drastic increase in distances to which energy transfer is still observable, $\sim 400 \text{ \AA}$ [178]. A depiction of this AuNP size and distance dependence is depicted in Figure 2.5. These initial studies on duplex DNA opened the door for the utilization of NSET as a viable tool in biophysics.

2.2.1 Biophysical research with NSET

The quenching behavior of metal nanoparticles has been known long before the mathematical modeling of its capabilities were compiled into NSET. Where the NSET theorem describes the applicability of energy transfer molecular “rulers,” simple off-to-on optical systems also rely on metal nanoparticle-based quenching. These turn-on optical systems have proven to be exceptionally compatible in intracellular environments [39,40,204].

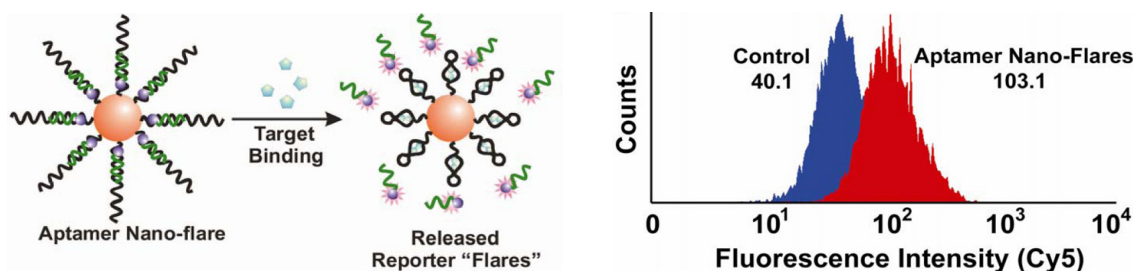


Figure 2.6: (Left) Scheme of aptamer “nano-flare” technology on AuNPs developed in the Mirkin lab, where target binding to the aptamer sequence releases a dye-labeled “flare” strand. (Right) Flow cytometry graph demonstrating the increased dye (Cy5) intensity observed in cells laced with high target concentrations. In this instance, the target is ATP [39]. Adapted with permission from Zheng, D.; Seferos, D.S.; Giljohann, D.A.; Patel, P.C.; Mirkin, C.A. Aptamer nano-flares for molecular detection in living cells. *Nano Lett.* **2009**, *9*, 3258–3261 [50]. Copyright 2007 American Chemical Society.

Mirkin, et al utilized the basic quenching properties in AuNPs to track ATP binding to its aptamer in living cells. The aptamer sequence, complexed to the previously described, dye-labeled nano-“flare,” is appended to the AuNP surface until ATP binding releases the “flare” reporter, resulting in a sudden increase in dye emission intensity (Figure 2.6) [39,40]. Dye intensities are then correlated to intracellular ATP concentrations. The Strouse group has also taken advantage of intracellular off-to-on mechanisms using NSET in recent years. In studies to investigate and calibrate the process of gene release from nanoparticle-based delivery systems, fluorescent dyes were appended to gene constructs near the nanoparticle surface [204]. A “turn-on” event, or increase in dye emission tracked through confocal microscopy, is indicative of gene release from the nanoparticle surface (Figure 2.7). Through these NSET-based constructs, it was discovered that time-dependent intracellular cargo release from the nanoparticle surface is linked

to gene/DNA sequence size, providing valuable data to the field of controlled intracellular release [204].

Ray, et al has transformed NSET technology into an effective marker for photothermal destruction of malignant cells by combining aptamer-based cell selectivity with fluorescent “flare” turn-on. Dye-labeled aptamers coating AuNP nanocages select and bind to cancer cells expressing the aptamer’s target receptor, PSMA. Simultaneous near-IR excitation (785nm) of the aptamer-AuNP nanocage during incubation results in a heat-induced release of the dye-labeled aptamer “flare” from the AuNP nanocage surface, fluorescently marking the affected cells. Absorption of the near-IR radiation by the AuNP nanocages results in a strong plasmonic heating effect, leading to cell death. Coupling of nanotechnologies (i.e. aptamers, photothermal therapy, and NSET) has proven an effective concept in the development of new potential nanomedicines [205].

NSET’s use as a molecular “ruler,” taking advantage of the distant dependent modeling, is also used by the biophysical community. Tan, et al in particular utilized size-dependent NSET rulers prior to the mathematical model development by empirically measuring the width of individual receptors at a cell surface [206]. By appending AuNPs and dyes to opposing sides of a cell receptor, the emission intensity and the change in optical quenching repeated with varying AuNP sizes was tracked. The change in distance between the dye and AuNP surface related solely to the increasing AuNP radius with each experiment (as both energy transfer entities are bound to the same cell receptor) producing a static distal value which corresponds to the cell receptor’s width [206].

The Strouse group elucidated relevant structural information of RNA hammerhead complexes via optical tracking and NSET molecular ruler calculations. Lifetime and photoluminescent measurements of a dye appended terminally to the substrate, with a 2nm AuNP appended to a RNA hammerhead arm, reveal two different structures when the substrate is bound and in the presence Mg^{2+} [179]. Differences in quenching, correlated to distances via the NSET theorem, reveal two distinct states in the hammerhead complex – one structure prior to substrate activity, and a subsequent structure in the presence of Mg^{2+} revealing an active hammerhead complex [179]. A representation of the hammerhead complex is shown in Figure 2.7.

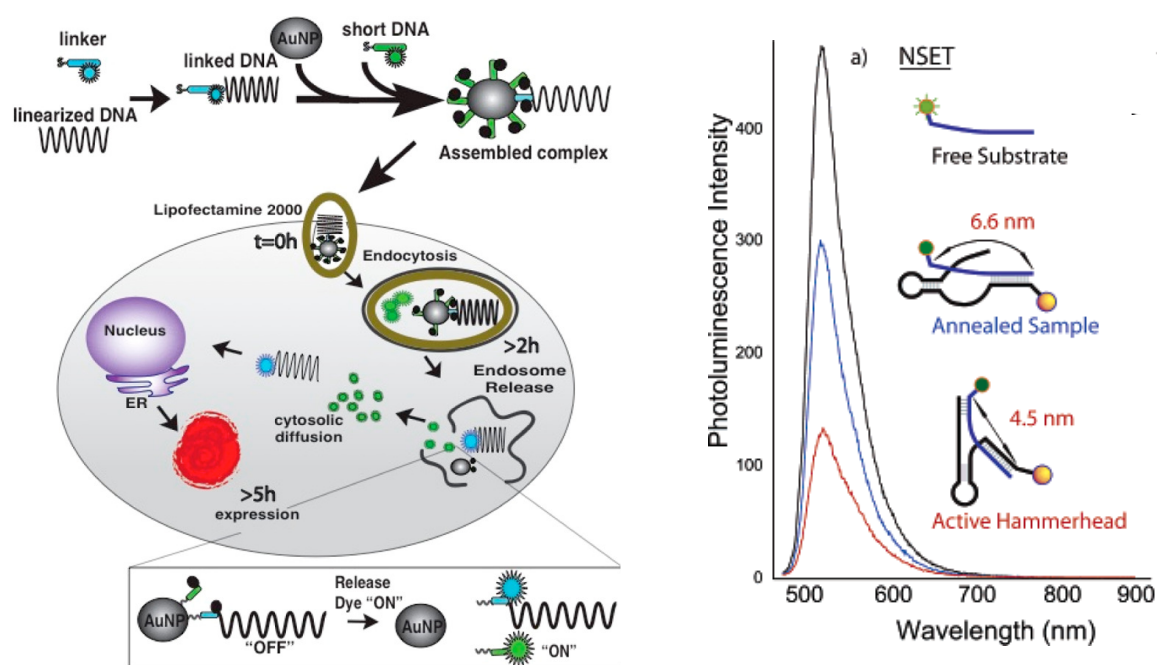


Figure 2.7: (Left) Scheme of AuNP-gene/DNA uptake and subsequent cargo release from the AuNP surface within the cell. The intracellular surface release is tracked by the sudden emission of a fluorescein dye appended to the gene/DNA that was initially quenched by the AuNP. The gene, which codes for a red fluorescent protein, is then transcribed/translated into protein as marked by red emission post-translation [204]. (Right) The evolution of an RNA hammerhead complex tracked by NSET after substrate annealing and preliminary cleavage steps with the addition of Mg^{2+} . Dye to AuNP distances derived from the dye's variable quenched lifetime/emission intensity are indicative of the two hammerhead states, annealed and active hammerhead [179].

NSET's versatility in nanoparticle size, metal composition, dye wavelength, and range of distances for which it can measure make its potential uses in biology and biophysics vast. The remainder of this dissertation aims to use NSET to improve new technologies and investigate properties of relevant biomolecular structures previously limited by obstacles in experimental design. Likewise, in Chapter 7, additions to the molecular ruler capabilities of NSET are made in a FRET-NSET hybrid system capable of triangulating three relative points in space.

2.3 Contact distance distributions in labeled systems (EPR, FRET, and NSET)

Before demonstrating the application of SET and FRET for biomolecular distance measurements in the upcoming chapters, it is essential to discuss the effects of dye/spin label-based methods to measure nanometer-scale distances. Inherent in any molecule, including non-native dye or spin-label modifications used in FRET, NSET, and EPR, are rotational degrees of freedom about the chemical bonds [207-209]. Multiple computational methods have been employed to account for the spin label's likely rotational space, though molecular dynamics calculations of the side-chain labels on peptides, proteins, and/or nucleic acids, derived from the rotamer states' free energy minima, have provided the best predictability of the label's potential conformers stemming from the statistically relevant bond rotations and atomic locations [207-213]. More importantly, the calculated populations of the conformer states from molecular dynamics simulations elucidate the inherent distance distribution incurred by dynamic movement of the labeled molecule [207,212,213]. With information about the label's distributive movement in 3D space, experimental design accounting for the measurement's error is simpler and is discussed for EPR, FRET, and SET here.

Pulsed EPR spin labels for distance extraction have evolved over the years to include nitroxide, triaryl methyl, and, more recently, Gd^{3+} -DOTA derivatives [175,210,214,215]. The coupling distances of these labels naturally rely on the strength of their paramagnetic resonance, and the accuracy of the reported contact distance between coupled labels relies on the length of

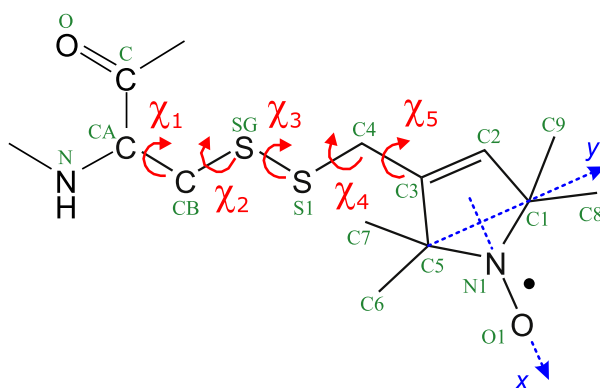


Figure 2.8: (Left) Example nitroxide EPR spin label with a methanethiosulfonate linker, displaying the rotational potential of the linker's bonds [207].

the labels' linker structures [207,210-214]. Figure 2.8 shows the potential bond rotations of a common nitroxide spin label's linker, methanethiosulfonate [207,208,211,212]. Reviews of nitroxide spin label dynamics report EPR techniques capable of measuring spin label contact distances within 3 Å [207]. While this reported distribution is impressive, it is important to note the relationship between length, favorable free energy structures and distance distributions of the spin labels [207,210,211,212]. All labels do not produce this level of accuracy and analysis of the spin label's conformer states ought to be strongly considered in experimental design [207,211,212,215]. In fact, more recent molecular dynamics analyses of common EPR spin labels at varying protein amino acid positions note a patternless distribution of single, dual, and multipartite conformer populations amongst label sites. The overall distance between conformers of individual spin labels, however, varied by as much as 16 Å [212].

Similarly, FRET and NSET organic fluorophore labels incur rotational bond disorder depending on the linker length and structure to the biomolecule [216-219]. As concluded in the instances of EPR, it is essential to design experiments that account for these unavoidable distributions in distance. Figure 2.9 presents a dual FRET-NSET system containing two organic dyes appended to complement DNA strands, with the duplex DNA strands attached to a 10nm AuNP. To account for the rotamer disorder in the dye labels and the change in energy transfer rates stemming from nanoparticle size distribution, gray dots represent 10,000 possible label positions generated from the linker length, with probabilities dictated by a Gaussian distribution [216]. In instances of short distances measurements with FRET and NSET, distance extraction

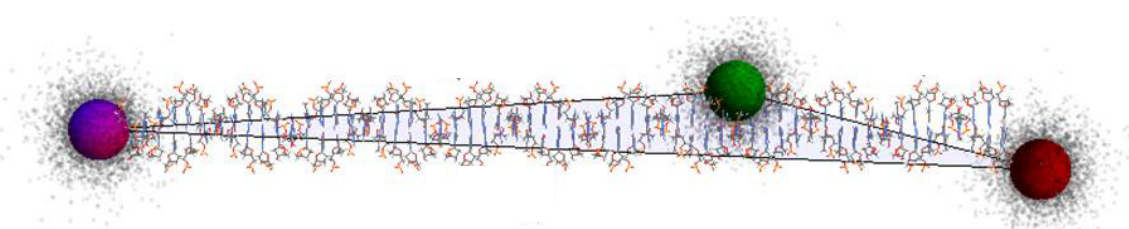


Figure 2.9: FRET and NSET construct demonstrating the dynamic rotational potential of the organic fluorophore modifications (green and red) and of the thiol-modified linker at the AuNP surface (purple). Gray dots represent 10,000 possible locations generated by accounting for the motion of each label. These distributions stem from the size distribution of the AuNP ($10\text{nm} \pm 0.5\text{nm}$) and a randomized 3D Gaussian point distribution with one sigma defined as 90% of the fluorophore's linker length [216].

from these labels is more largely affected by the linker length distribution, in that the overall uncertainty in length constitutes a higher percentage of the measured separation distance, as shown in Figure 2.10. In longer distances, however, the distribution of the dye label is small

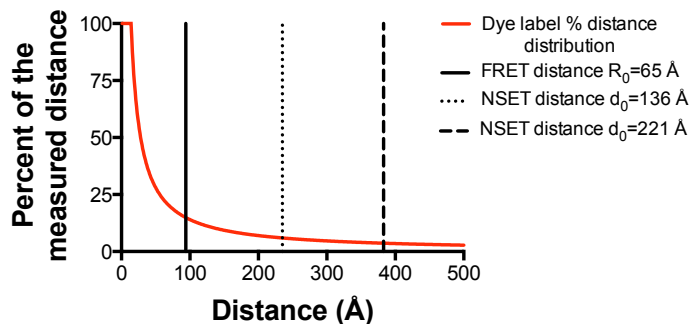


Figure 2.10: Percentage of the measured distance comprised by the linker vs. the experimental distance measured (red), assuming the linker’s distributed distance due to rotational freedom is 14 Å. Vertical lines denote the measureable distances of a FRET dye pair with an $R_0=65 \text{ \AA}$ (black solid line), a dye-small AuNP pair with a $d_0=136 \text{ \AA}$ (black dotted line), and a dye-large AuNP pair with a $d_0=221 \text{ \AA}$. The measureable distances of the FRET and NSET methods (vertical lines) were calculated by assuming the distance at which 10% energy transfer occurs is the longest experimentally measureable distance.

percentage to the measured contact distance. While FRET demonstrates higher resolution than NSET measurements at short distances, dye label error is substantially less relevant in long-range NSET studies (Figure 2.10) [216,217]. These considerations are important in implementing optical energy transfer methods into biomedical applications.

CHAPTER 3

AN NSET APTAMER BEACON FOR ATP DETECTION

3.1 Introduction

Nucleic acid sequences can form non-canonical structures by folding in the presence of small molecule ligands or following the binding of a protein [45,86,89,179,220]. The realization that single-stranded DNA forms unique, complex, nucleic acid structures in response to ligand binding has led to the development of synthetic, single-stranded DNA sequences tailored to fold in the presence of a specific target. These synthetic sequences, termed aptamers, can be highly selective for a target ligand [50,54-57]. The rapid advancement of the field stems from the use of combinatorial library screening to select aptamer sequences based on binding affinity (K_d) response, resulting in new aptamers appearing in the literature for a wide range of small molecules including thrombin, ATP, cocaine, HIV-1 REV, Hg^{2+} , and prostate-specific membrane antigen (PSMA) [33-35,50,54-58,221]. Since their discovery, the use of aptamers to sense the binding of target molecules in solution or on cell surfaces has evolved rapidly for bioanalytical applications. Recently, the incorporation of gold nanoparticles (AuNPs) onto aptamers has further pushed aptamer technology into applications such as fluorescence, electrochemical, and plasmonic sensors to report binding [38,39,87,222-224].

It is well-known that the fluorescent quenching of a dye by a AuNP is well described within the nanometal surface energy transfer (NSET) model, and thus has attracted considerable attention as an optical ruler in biophysics [225]. NSET with longer R_0 values ($R_0 > 100 \text{ \AA}$) makes separation of the donor and acceptor more attainable than FRET studies, which can be advantageous for molecular beacon fluorescent sensors. In fact, earlier fluorescent biosensors utilizing pyrene-appended aptamers have shown perturbation of target binding due to interference of the binding site by dye-labeling in the binding pocket [226]. NSET allows the positioning of the donor and acceptor labels away from the binding pocket.

While the AuNP-based fluorescent assays are very sensitive, the difficulty in tuning the binding affinity to match the experimental conditions has limited their broader applicability. To increase the long-term applicability of nanoparticle-based aptamer sensors, the sensor response has to be generalizable to the experimental conditions in biophysics. The ability to systematically

tune a previously identified aptamer's binding affinity to better match experimental conditions (concentration range) without redesigning the aptamer or relying on single point mutations is not well developed [227]. When the aptamer is bound to a AuNP, the response of the aptamer can be influenced by the aptamer structure and any interaction with the AuNP surface, which can impact sensitivity as well as specificity of future sensors. The interaction of the AuNP with the aptamer can be minimized by surface passivation as previously demonstrated, but the effect of aptamer design on response is far less understood [179,228]. It has been observed in molecular beacon stem-loop architectures that the aptamer K_d values are affected by stem-loop size, stem length, stem composition, and single point mutations in and away from the target's binding site [48,227,229]. Several studies have also indicated that the aptamer binding affinity in optical sensors, including nonhairpin optical probes, is strongly impacted by the degree of duplex formation over the aptamer sequence. The higher K_d values are attributed to the thermodynamics associated with overcoming the duplexed regions or target accessibility to the binding sites on

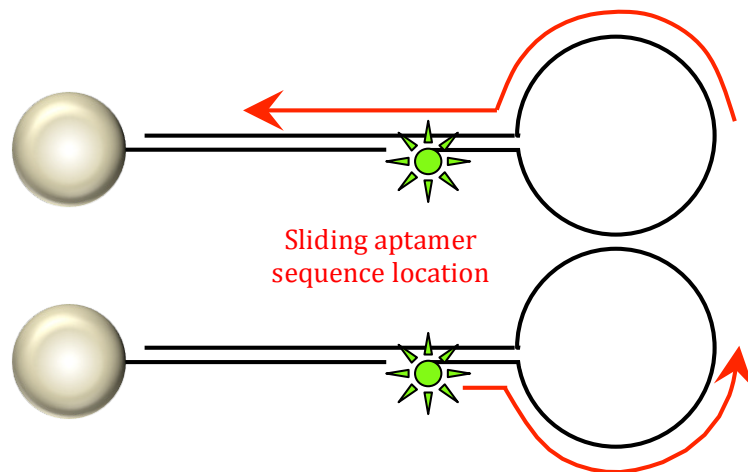


Figure 3.1: Illustration of the movement of the ATP aptamer sequence around the circumference of the NSET stemloop beacon, the effect of which on the binding affinity of ATP is studied in this chapter.

the aptamer [39,75]. Developing a deeper understanding of the underlying consequences of positioning the single-stranded aptamer sequence into a stem-loop molecular beacon framework could allow more judicious design of AuNP aptasensors.

In this chapter, the influence of a 25-mer single-stranded ATP DNA aptamer's location in the loop region of a 57-mer stem-loop molecular beacon on the aptamer's binding affinity for

ATP is described. The influence of target site exposure in the loop is investigated by sliding the aptamer sequence along the loop circumference as shown in Figure 3.1, resulting in a variable degree of single-stranded exposure for the ATP aptamer. The design allows the influence of ligand accessibility and duplex formation to be investigated. The chosen ATP aptamer is based upon the Huizenga and Szostak 25-mer ATP DNA aptamer sequence whose structure and ATP binding properties were previously analyzed by NMR [58,64]. The aptamer binds two ATP molecules per sequence and induces a folded structure. For the analysis of the influence of aptamer position within the loop, the aptamer beacon incorporates a 3 nm AuNP at the 3' end as an energy acceptor and a fluorescein dye (FAM) at the 5' end as an excited state donor. The use of the AuNP-FAM energy transfer pair allows the binding affinity to be measured and the change in distance following ATP binding to be monitored using Nanometal surface energy transfer techniques (NSET) [178]. The change in the photoluminescent (PL) intensity data with increasing ATP concentration allows the change in K_d and the change in aptamer sequence location in the loop to be correlated. The remainder of this chapter is divided into Experimental section (3.2), Results & discussion (3.3), and Conclusion (3.4).

3.2 Experimental section

3.2.1 Aptamer beacon construction

The 25-mer aptamer strand is incorporated into a 57-mer stem-loop construct with the aptamer sequence positioned sequentially around the structure. The sequences are listed in Table 3.1. The 57-mer DNA sequences contain a fluorescein dye label coupled to a C₆ phosphate spacer appended to the 5' terminus of the single-stranded, aptamer-encoded DNA. The complementary 15-mer ssDNA sequence contains a 5' C₆-NH₂ modification to allow coordination to the DHLA-AuNP through an EDC condensation reaction. The aptamer hairpin is annealed prior to appendage to the AuNP by heating to 95 °C for 4 min then snap cooling to 4 °C to ensure hairpin formation. The annealing is carried out in pH 7.5 phosphate buffer (20 mM phosphate, 50 mM NaCl). Coordination of the aptamer hairpin to the AuNP is accomplished through condensation of the C₆-NH₂ to the free acid group on the DHLA-AuNP by reaction of DHLA-AuNPs (1 nmol) with 10 µL of a stock EDC solution (10 mg/mL), and 100 µL of stock

Table 3.1: Stemloop aptamer beacon sequences used in this study. Red, italicized text is indicative of the conserved 25-base-pair ATP aptamer sequence. A dotted underline represents the loop portion in the stemloop structure while a bold underline represents the 6-base-pair stem. Amine-terminated 15-base-pair linkers are listed below the sequence, aligned at the appropriate complementary positions.

Seq <i>i.</i>	5 ⁻ -(FAM)- <u>CCTGGGGGAGTATTGCGGAGGAAGG</u> TTTTTTTTTCCAGGGGGGTGGAGGTGGAGG -3' 3 ⁻ - CCCACCTCCACCTCC(NH ₂) -5'
Seq <i>ii.</i>	5 ⁻ -(FAM)- <u>CACTGTCTGGGGGAGTATTGCGGAGGAAGG</u> TTTTTACAGTGGTGGAGGTGGAGGTG -3' 3 ⁻ - CACCTCCACCTCCAC(NH ₂) -5'
Seq <i>iii.</i>	5 ⁻ -(FAM)- <u>CCCTTCCGTTTATTTCTGGGGGAGTATTGCGGAGGAAGG</u> GGAGGTGGAGGTGGAG -3' 3 ⁻ - CTCCACCTCCACCTC(NH ₂) -5'
Seq <i>iv.</i>	5 ⁻ -(FAM)- <u>CTCCGCTTTTTTTTTTTTTTTTCTGGGGGAGTATTGCGGAGGAAGG</u> GTGGAGGTGG -3' 3 ⁻ - CTTCCACCTCCACC(NH ₂) -5'
Seq <i>v.</i>	5 ⁻ -(FAM)- <u>CAATACGTGAGTGAGTGAGTGATTTTTCTGGGGGAGTATTGCGGAGGAAGG</u> TTTTTC -3' 3 ⁻ - GCCTCCTTCCAAAAG(NH ₂) -5'
*Seq <i>vi.</i>	5 ⁻ -(FAM)- <u>CACTGTCTGGGGGAGTATTGCGGAGGAAGG</u> TTTTTACAGTGGTGGAGGTGGAGGTG -3' 3 ⁻ - AAAATGTCACCACCTCCACCTCCAC(NH ₂) -5'

NHSS solution (1 mg/mL) in 0.5 mL nanopure H₂O at RT (3 h) to form the NHS intermediate. The NHS intermediate is coupled by addition of the annealed aptamer (3 nmol) and reacted for 3h. Final concentrations obtained in the reaction are 1.3 μM and 3.8 μM for the AuNPs and aptamer, respectively. The AuNP–aptamer construct was purified via ethanol precipitation and analyzed by gel electrophoresis, UV–Vis, and TEM (Figure 3.2). The AuNP–aptamer construct is stored at 4 °C in the dark until use. Gel electrophoresis (2% agarose) on the hairpin aptamer appended to the AuNP exhibits a single band. TEM analysis shows a spherical, 3 ± 0.5 nm AuNP core, and absorption features consistent with the AuNP (520 nm) and duplex DNA (260 nm).

The FAM feature is obscured by the AuNP LSPR by comparison to the DNA aptamer absorption. The UV–Vis confirms a stochastic, ~1:1 coupling ratio for aptamer to AuNP. The aptamer loading is measured by UV–Vis absorption spectra by analyzing the ratio of the DNA absorption at 260 nm to the AuNP absorption at 520 nm using the Beer–Lambert law, as described below at 260nm

$$\begin{aligned}
 A(\text{total})_{260} &= A(\text{AuNP})_{260} + A(\text{DNA})_{260} \\
 &= b \{ \varepsilon(\text{AuNP})_{260}[\text{AuNP}] + \varepsilon(\text{DNA})_{260}[\text{DNA}] \}
 \end{aligned}$$

and at 520nm

$$A(\text{total}) = A(\text{AuNP})_{520} = b \{ \epsilon(\text{AuNP})_{520} [\text{AuNP}] \}$$

where A is the absorption value, ϵ is the extinction coefficient for the components and b is the pathlength of the cuvette ($b = 1 \text{ cm}$). Solving for the AuNP concentration at 520nm allows the DNA concentration to be calculated at 260 nm (and indirectly the FAM concentration since the ratio on the synthetic sequence is 1:1 FAM to DNA).

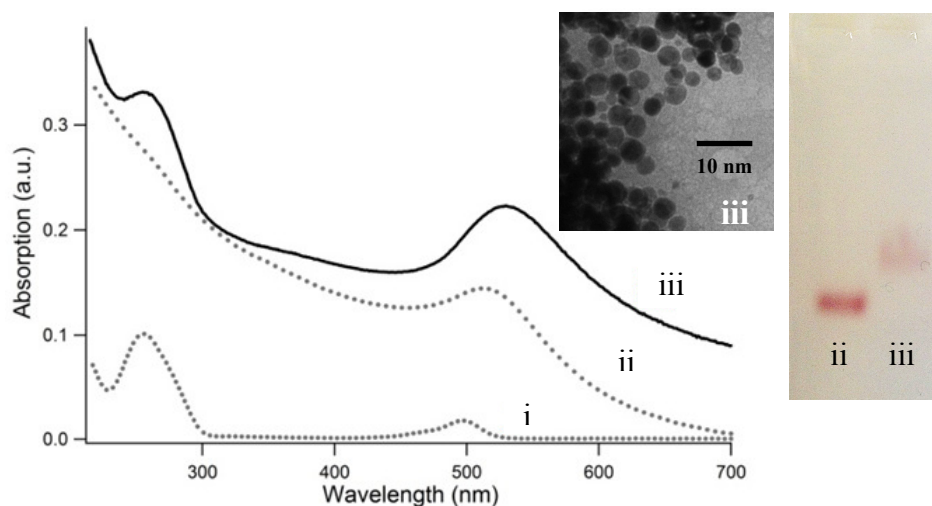


Figure 3.2: UV-Vis (left), TEM (middle) and gel electrophoresis (right) of the NSET stemloop beacons. Sample iii represents the final purified NSET beacon and contains features from its separate components, free FAM-labeled aptamer sequences (i) and free 3 nm AuNPs (ii). A DNA absorption peak at 260nm and FAM feature at 494nm are observed in sample i, though due to its low absorption cross-section relative to the AuNP, the FAM feature is not observed in the final purified NSET beacon (iii). TEM of the final NSET beacon indicates a size distribution of $3\text{nm} \pm 0.6$. Retardation of the NSET beacon's movement through the gel (iii) relative to the unlabeled DHLA-coated AuNPs (ii) is indicative of DNA attachment to the AuNP surface via EDC coupling reaction.

3.2.2 Absorption and photoluminescence measurements

Photoluminescence (PL) was measured in 0.3 cm quartz cuvettes on a Varian Eclipse fluorimeter in a thermostated optical cell holder ($20 \text{ }^\circ\text{C}$) by exciting the FAM at 494 nm and collecting the PL spectra from 505nm to 650nm. The aptamer beacon and ATP dilutions were dissolved in TRIS buffer (20 mM TRIS, 300 mM NaCl, and 5 mM MgCl_2). The AuNP-aptamer

concentration was ~1 nM and ATP concentrations were varied systematically from 5 nM to 97 mM. UTP, GTP, and AMP binding studies were carried out for selected aptamers identically to the ATP studies to analyze the impact on specificity and selectivity. Binding curves relating fluorescein intensity to target concentration are plotted as ΔPL vs. concentration, where ΔPL is the integrated fluorescein intensity.

3.3 Results & discussion

The stem-loop construct contains a 25-mer Huizenga-Szostak ATP aptamer, wherein the aptamer sequence is moved along the stem-loop region from the 5' toward the 3' end, resulting in partial blocking of the ATP target site due to base pairing when the loop is closed. The six individual 57-mer stem-loop constructs utilized in the study are shown in Figure 3.3 and Table 3.1. In Table 3.1, the 25-mer Huizenga-Szostak aptamer sequence in each of the six constructs is

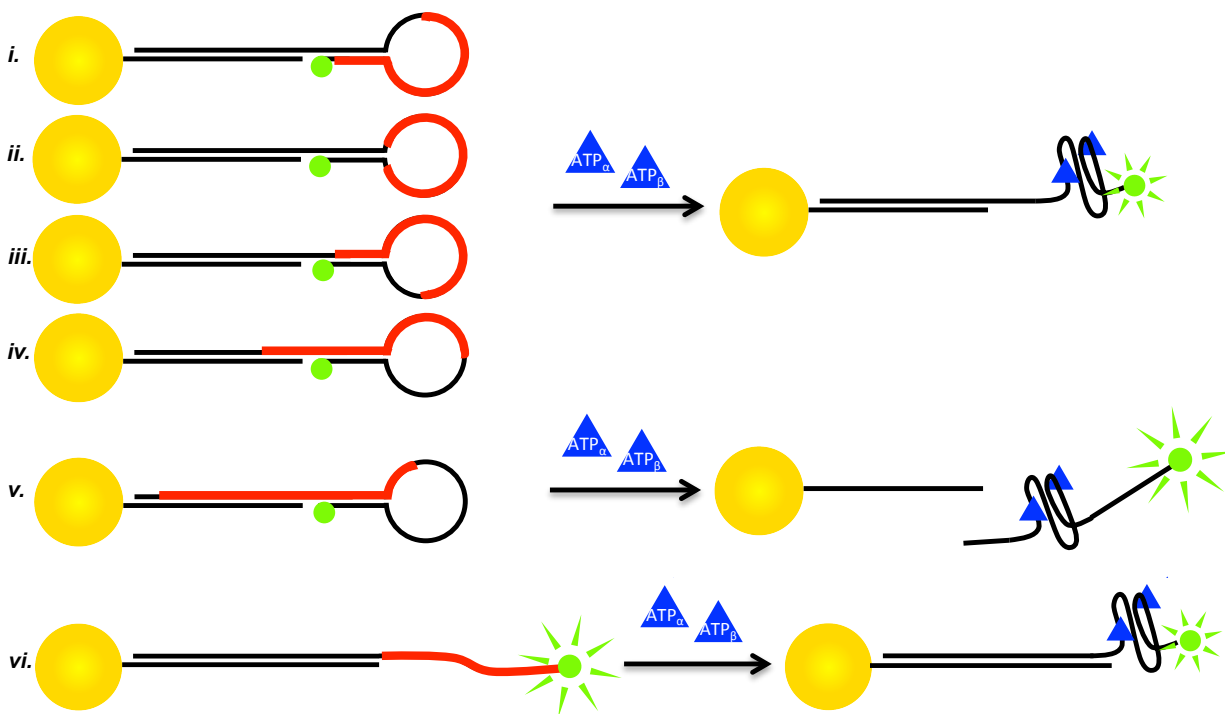


Figure 3.3: Scheme of the NSET stemloop beacons and their response to ATP. The red bars in the stemloop structures are indicative of the aptamer sequence location in the stemloop architecture. Sequences *i*, *ii*, *iii*, *iv*, and *vi* remain a single construct upon ATP binding whereas sequence *v* contains enough aptamer sequence overlap in the stem to induce displacement of the flare strand upon ATP binding.

red and italicized for clarity. To distinguish between the loop and stem region, the loop is highlighted by a dashed underline, while the stem is highlighted by a solid underline. As a control, the five stem-loop studies were compared to a single-stranded sequence containing the aptamer (sequence *vi*) that cannot form a stem-loop structure.

The stem-loop construct is designed (Figure 3.3) to detect the conformational changes in the ATP-induced aptamer binding by monitoring the change in the fluorescent intensity of the appended FAM when quenched in the vicinity of the AuNP. A 3 nm AuNP with low loading (1:1 AuNP:DNA) was chosen to promote high efficiency of the aptamer binding to ATP, as observed in previous studies where hybridization of DNA on AuNP surfaces was most efficient at low primer loading levels and on surfaces of high curvature [230,231]. The AuNP acts as a dark acceptor of the FAM excited state via a long-range NSET mechanism. The NSET method is similar to FRET techniques, wherein the separation distance between the fluorescein and AuNP are reported by the change in emission intensity of the fluorescein. The quenching can be described within an NSET model allowing the ensemble-averaged distances to be calculated by comparison to theoretical values. Unique to NSET, the R_0 (critical distance for 50% energy transfer) is a longer value of 110.6 Å for a 3 ± 0.5 nm AuNP-FAM acceptor donor pair, allowing the fluorescein (FAM) and AuNP to be bound distally from the aptamer site to minimize impact on the observed aptamer folding behavior [178].

The impact of small molecule dyes, quantum dots, and EPR tags on the folding of biopolymers is an area of open discussion in the biophysics community. Studies on AuNPs

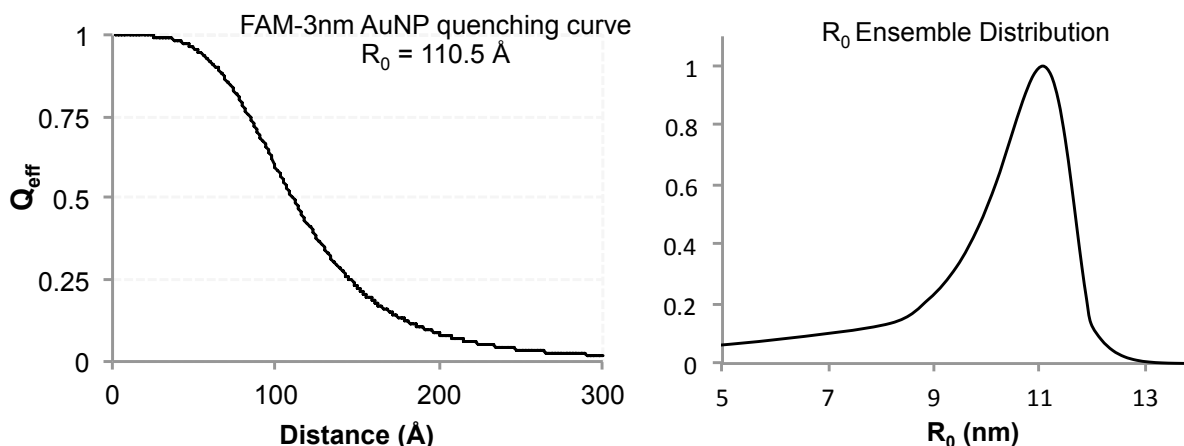


Figure 3.4: Quenching efficiency of FAM on a 3nm AuNP versus distance (left) and the calculated distribution in NSET R_0 values for FAM on a 3nm AuNP stemming from the distribution in AuNP diameter, $3.0\text{nm} \pm 0.6$ (right).

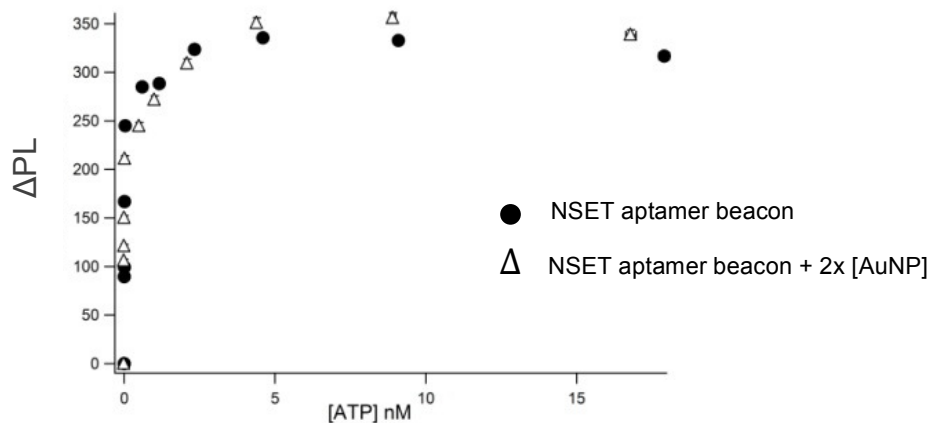


Figure 3.5: Binding curves of sequence *ii* without excess AuNPs (circles) and in the presence of 2x [AuNPs] (triangles) where ΔPL is the integrated FAM intensity. Similar saturation behavior indicates no adverse affects of free AuNPs in solution.

below 4 nm approach the size of the footprint of DNA. Earlier studies have shown that no impact on folding is observed for substrate induced folding of RNA or protein induced folding in DNA when bound to a small AuNP surface, presumably due to the increased distance of separation from the binding site allowable by NSET probes [179,198]. It is also important to note that nonspecific DNA interactions with the AuNP surface are not expected because previous groups report little to no DNA adsorption onto nanoparticle surfaces with a ligand-passivated, neutral surface [228,232]. Typical DNA adsorption studies that report high levels of single-stranded adsorption utilize citrate-capped AuNPs where the citrate molecule is displaced to accommodate DNA laying down on the surface [233]. The AuNPs used in this study are DHLA-capped, thus the surface is thiol-coated, and it is assumed that the small particle size and the stable ligand coating make these AuNPs resistant to nonspecific adsorption.

The PL NSET efficiencies and calculated distances for the aptamer sequences at I_0 (no ATP) and I_{max} (high ATP concentration) are listed in Table 3.2. In the absence of ATP, the aptamer forms a closed stem-loop hairpin conformation positioning the AuNP and the FAM in close proximity, resulting in partial quenching of the FAM in the AuNP near field. The intensity of the fluorescein emission in the absence of ATP for the closed stem-loop yields a separation distance of AuNP to FAM of 77 Å ($E = 19\%$) confirming loop formation in the absence of ATP. Exposure of the aptamer to ATP induces opening of the loop and formation of a folded DNA conformer that repositions the FAM and AuNP to cause the change in fluorophore emission,

Table 3.2: Intensity values and the extracted distance between the FAM moiety and the AuNP surface at I_0 (no ATP added) and I_{\max} (saturation with ATP) for each of the NSET beacon sequences.

	I_0	FAM-AuNP distance at I_0 (Å)	I_{\max}	FAM-AuNP distance at I_{\max} (Å)
Seq <i>i</i>	0.19	77 ± 7	0.41 ± 0.05	101 ± 9
Seq <i>ii</i>	0.19	77 ± 7	0.38 ± 0.06	98 ± 10
Seq <i>iii</i>	0.19	77 ± 7	0.38 ± 0.05	98 ± 9
Seq <i>iv</i>	0.19	77 ± 7	0.44 ± 0.05	104 ± 9
Seq <i>v</i>	0.19	77 ± 7	1.0	----
Seq <i>vi</i>	0.61	124 ± 8	0.41 ± 0.06	101 ± 10

tracking the binding of ATP. The fluorescein intensity at high concentrations of ATP yields a separation distance consistent with the NMR predicted folded structure, wherein the AuNP to FAM separation distance is 96–109 Å ($\sim \Delta 25\%$ E), confirming formation of the ATP induced folded aptamer in the presence of ATP [64]. A distal range is reported here because TEM analysis indicates a ± 0.6 nm Gaussian distribution in AuNP sizes, which results in an NSET R_0 that is better described as a weighted probability to account for the nanoparticle size (Figure 3.4). By incorporating the measured population distribution for particle size coupled to the change in extinction coefficient which scales as r^3 , the $R_{0\langle \text{avg} \rangle}$ value for the prepared AuNPs in the study is 110.6 Å. Although it should be noted that the correction to R_0 for the distribution results in only a minimal perturbation to the $R_{0\langle \text{calc}, 3 \text{ nm} \rangle}$ for the 3 nm average size ($R_{0\langle \text{calc}, 3 \text{ nm} \rangle} = 110.5$ Å). Moreover, while the ATP-bound NMR structure is available, its orientation to the surface could vary. Photoluminescent saturation is therefore used to establish the ATP saturation limit for ATP binding.

As a control and in an effort to ensure that free, unlabeled AuNPs in solution do not impact the conformation of the folded aptamer, analysis of the fluorescein intensity following the addition of free AuNP (up to 2 nM excess AuNP) in solution is provided (Figure 3.5). No change in PL saturation was observed from the binding curves. Binding assays for UTP and GTP on selected sequences are available in Figure 3.6 and demonstrate that specificity for ATP over

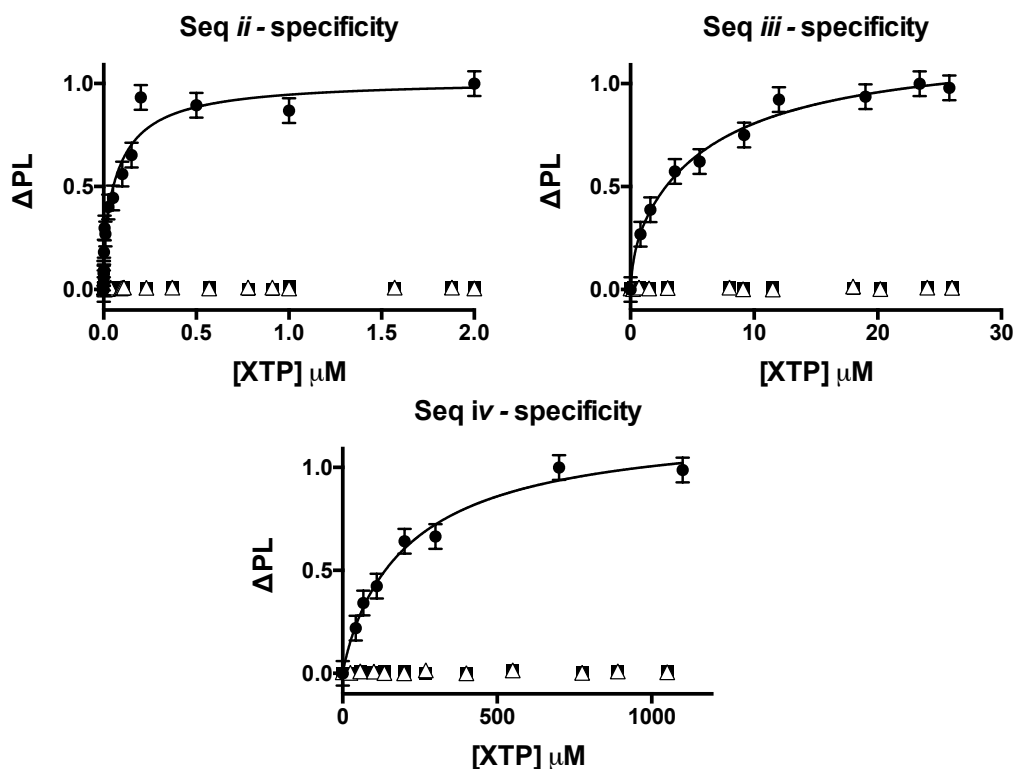


Figure 3.6: Binding curves of sequence *ii*, sequence *iii*, and sequence *iv* with ATP (circles), UTP (triangles), and GTP (squares.) The specificity of the aptamer for ATP is unchanged despite movement around the hairpin circumference.

other triphosphate nucleosides is not impacted by the binding of the AuNP or the position of the aptamer in the loop. Control studies on AMP binding relative to ATP were also performed and the extracted K_d values are listed in Table 3.3, wherein similar binding affinities between AMP and ATP are observed, consistent with literature results [41,226,234,235].

Table 3.3: K_{d1} and K_{d2} of AMP and ATP binding to sequence *iii* (circles) and sequence *iv*. Similarity in binding affinities indicate the NSET stemloop beacons have no effect on ATP and AMP's mechanism of binding to the aptamer sequence.

	AMP	ATP
	K_{d1} (2σ), K_{d2} (2σ)	K_{d1} (2σ), K_{d2} (2σ)
Seq iii	0.5 (1.6), 9.9 (10.8) μM	0.3 (0.6), 6.9 (12.0) μM
Seq iv	43.3 (19.9), 584.0 (389.0) μM	33.6 (4.5), 232.8 (333.4) μM

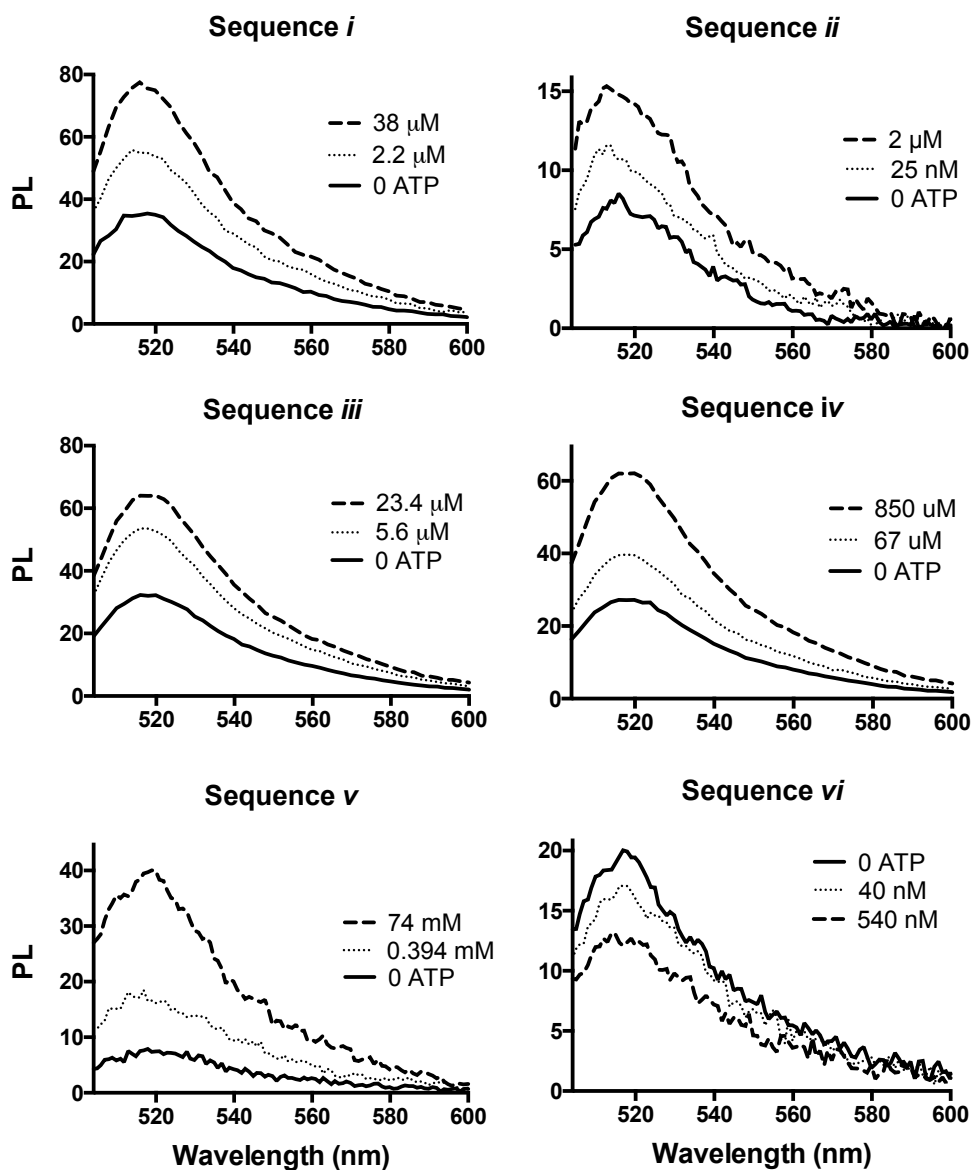


Figure 3.7. Raw PL data of the NSET stemloop beacons increasing ATP concentrations. Each sample is at a concentration of \sim 1nM beacon. Hairpin sequences (sequence *i*, *ii*, *iii*, *iv*, and *v*) increase in intensity with increasing ATP concentration whereas sequence *vi*, a non-hairpin structure, decreases in intensity with increasing ATP concentration.

The binding affinities for the five stem-loop constructs were measured by analyzing the ATP concentration-dependent change in integrated FAM photoluminescence (Δ PL) at 1 nM aptamer. The raw PL data is plotted in Figure 3.7, a binding curve of the data is plotted in Figure

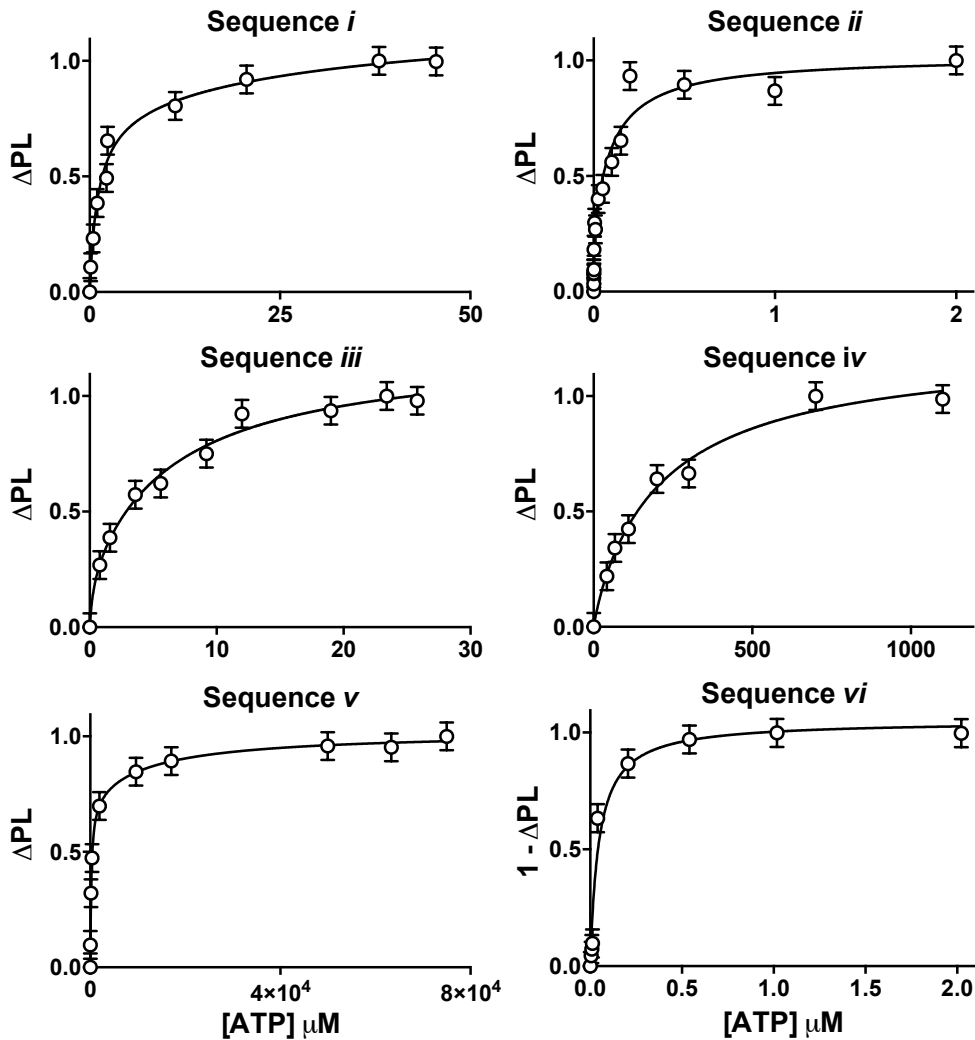


Figure 3.8: ATP binding curves of the five NSET stemloop beacons fit to equation 3.1. The curves display the relationship between ΔPL and micromolar ATP concentration. The sequence *vi* saturation curve is fit to a single-event model described in equation. 3.2.

3.8 (ΔPL vs $[\text{ATP}]$), and as a log plot of the binding curve (ΔPL vs $\log[\text{ATP}]$) is plotted in Figure 3.9. Consistent with the proposed structural folding of the aptamer following opening of the stem-loop upon ATP binding, the observed PL intensity increases asymptotically with increasing ATP concentration in sequences *i* through *v*. The maximum intensity change reflects the final conformation of the aptamer after ATP-induced folding. In sequence *vi*, the observed PL decreases with increasing ATP concentration, consistent with a shortened conformer forming in the ATP-bound aptamer state. The binding affinity for the ATP is extracted by fitting the ΔPL data to a two-site ATP binding curve

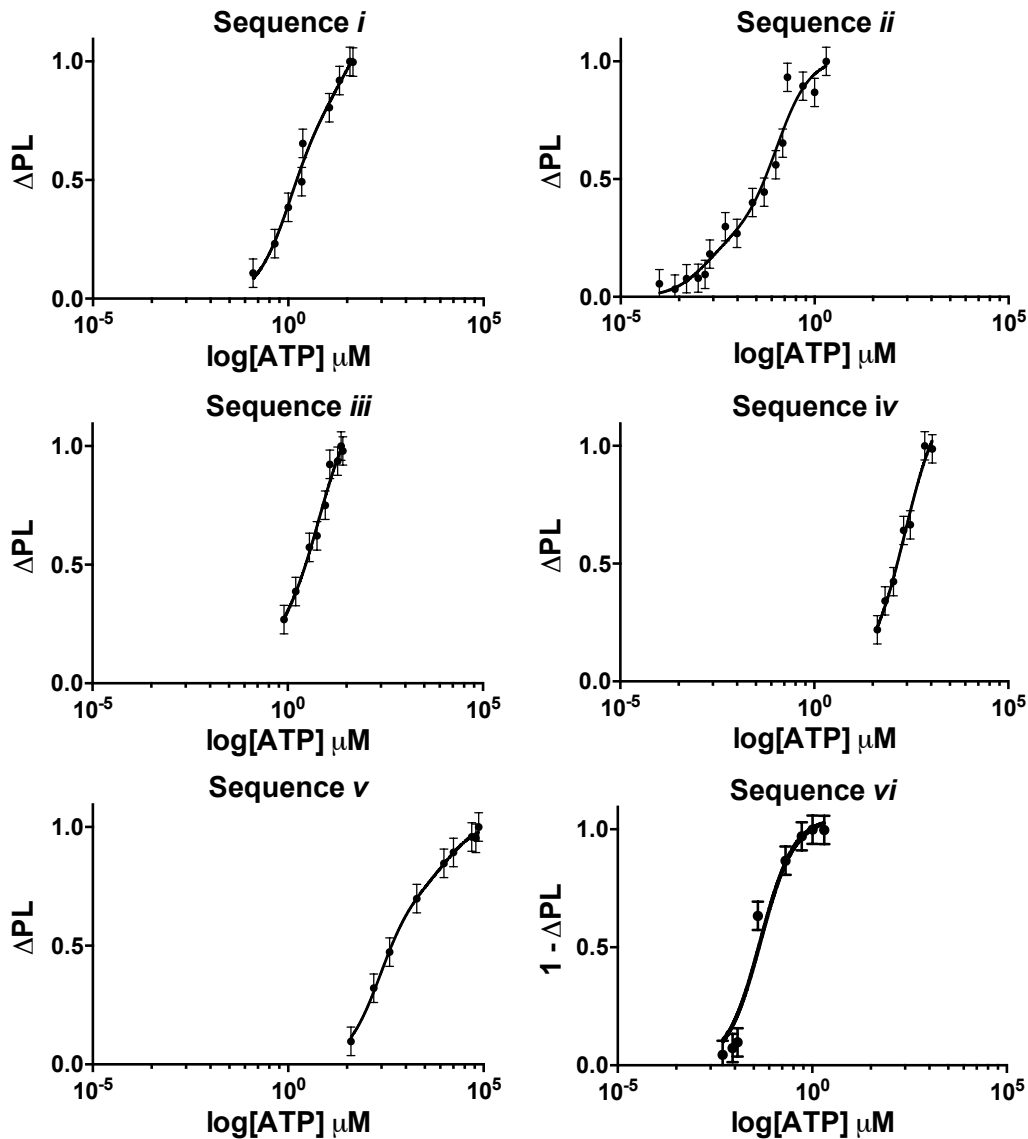


Figure 3.9: Log plot of the two-site binding model (one-site binding model is employed for sequence *vi*) fit to the NSET beacon saturation with ATP, demonstrating the range of detection for each sequence.

$$\Delta PL = \left(\frac{B_{max}^{(1)}[ATP]}{K_d^{(1)} + [ATP]} \right) + \left(\frac{B_{max}^{(2)}[ATP]}{K_d^{(2)} + [ATP]} \right) \quad \text{eqn. 3.1}$$

where $B_{max}^{(1)}$ represents the maximum ΔPL for the first binding site, $B_{max}^{(2)}$ represents the maximum ΔPL for the second binding site, and $K_d^{(1)}$ and $K_d^{(2)}$ are the binding affinities for the individual sites. NMR studies support the two-site model in that two ATP sites are observed in the NMR solution structure of this target-bound DNA aptamer [64]. The K_d values are listed in

Table 3.4 and the binding curves for sequences *i-v* are shown in Figure 3.8. Sequence *vi* was unable to be fit to a two-site binding model, as the two K_d values produced are ambiguous values. Thus, sequence *vi* is fit to a one-site binding curve described in eqn. 3.2 below,

$$\Delta PL = \left(\frac{[ATP]}{K_d + [ATP]} \right) \quad \text{eqn. 3.2.}$$

Despite confirmation of two ATP sites by NMR, previous groups employed a one-site binding curve in extracting the K_d of this DNA ATP aptamer, thus it was important to verify the use of the two-site binding curve in our studies. The degrees of freedom (DOF) and sum of squares (SS) from the one-site binding model (DOF_1 and SS_1) were statistically analyzed against the two-site binding model (DOF_2 and SS_2) using an F-test and an Akaike's (AIC) test. Details of the statistical equations are shown in eqn. 3.3 (a and b),

$$(a) F = \left[\frac{\left(\frac{SS_1 - SS_2}{SS_2} \right)}{\left(\frac{DOF_1 - DOF_2}{DOF_2} \right)} \right] \quad (b) A = N \left(\ln \left[\frac{SS_2}{SS_1} \right] \right) + 2(DOF_1 - DOF_2) \quad \text{eqn. 3.3}$$

where the F-test equation is denoted as (a) and the Akaike's (AIC) test as (b). F represents the F-test values, A is AIC test value, SS_1 and SS_2 are the sum of squares for the single-event and two-event models, respectively, DOF_1 and DOF_2 are the degrees of freedom for the respective models, and N is the number of points analyzed. Both approaches to comparing binding models, (a) and (b), relate the changes in the SS and DOF as the models become more complex (going from the one-site binding curve to the two-site binding curve). Values >1 for the F-test and negative values for the AIC test are indicative of the more complex model (two-site binding curve) being the statistically more appropriate fit. For the sequences *i* through *v*, F-test values of >1 with the Akaike's test values <0 are observed and are listed in Table 3.4. The F-test values of >1 coupled to negative AIC values confirms the validity of the more complex two-state model for the studied sequences. The control sequence, sequence *vi*, which cannot form a stem-loop structure, exhibits an F-test value of zero and a positive AIC value, and therefore is fit to the single-binding model in Figures 3.8 and 3.9.

Interestingly, NSET monitors two ATP binding sites consistent with the reported NMR

Table 3.4: Table of the K_d values with the reported 95% confidence limits (2σ) extracted from equation 3.1, the Hill coefficients (h) extracted from equation 3.4 and the F-test and AIC values extracted from equation statistical analyses described in equation 3.3.

	K_{d1} (2σ)	K_{d2} (2σ)	Hill (h)	F-test, AIC
Seq <i>i</i>	1.1 (1.2) μ M	35.3 (30.2) μ M	0.77	1.615, -0.307
Seq <i>ii</i>	1.3 (2.4) nM	102.3 (93.4) nM	0.55	8.754, -10.502
Seq <i>iii</i>	0.3 (0.6) μ M	6.9 (12.0) μ M	0.70	2.368, -1.818
Seq <i>iv</i>	33.6 (4.5) μ M	232.8 (333.4) μ M	0.49	1.498, -0.473
Seq <i>v</i>	203.0 (129.8) μ M	5486 (8248) μ M	0.73	7.940, -9.123
Seq <i>vi</i>	12.1 (10.2) nM	-----	2.07	0, 4

studies, but earlier FRET studies have been unable to distinguish separate sites [41,64]. The reasons for the FRET studies' shortcomings are not described and are possibly not well understood, but may stem from the ATP sites following a positively cooperative binding model, rendering the two-site binding curve unfittable. To analyze cooperativity between the ATP sites in our stem-loop aptamer constructs, the data from Figures 3.8 and 3.9 were analyzed by fitting to a cooperativity model

$$\Delta PL = \left(\frac{B_{max}[ATP]^h}{K_d^h + [ATP]^h} \right) \quad \text{eqn. 3.4}$$

where h is the Hill coefficient representative of positively cooperative ($h > 1$), negatively cooperative ($h < 1$), or noncooperative behavior ($h = 1$) between ATP binding sites. Fitting the ΔPL data to the cooperativity model (eq. 3.4) yields values for h between 0.4 and 0.8 for sequences *i* through *v* of the stem-loop constructs as shown in Table 3.4. A Hill value of < 1 indicates negative cooperativity between ATP sites for the sequences in Figure 3.3 and Table 3.1. A negative cooperativity can be understood in terms of the initial binding of one ATP obstructing the binding of the second ATP to the aptamer. A Hill coefficient value of 2.04 is measured for the sequence *vi*, which is indicative of positively cooperative or near-simultaneous

binding of the two ATP moieties. It is worth noting that a value of $h = 2.04$ in sequence vi would explain the inability to fit sequence vi data to a two-site binding model, as supported by the F-test and AIC statistical analyses.

Comparison of the K_d values in Table 3.3 for the sequences listed in Table 3.1 reveals that increasing single-stranded exposure in the loop decreases the K_d value. A decreasing K_d value indicates stronger binding affinity. No significant preference in K_d value is observed if the 5' or 3' end of the aptamer is partially blocked (sequence i vs. sequence iii). The measured K_d value of the fully exposed loop sequence (sequence ii) is consistent with the measured value for the single-stranded molecular beacon analogue (sequence vi). Likewise the sequence incorporated into the stem-loop configuration with significant duplex formation in the stem exhibits K_d values similar to previous reports in an analogous nanoflare design, supporting the effect of aptamer location on the observed K_d values [39,41,234]. The results of the binding curves imply that ATP accessibility to the single-stranded region is critical to the experimentally measured binding affinity with an observed tunability over 4 orders of magnitude.

It has been reported by molecular tweezer mechanical unfolding studies that the folded ATP-bound aptamer structure is energetically stable compared to the free, single-stranded aptamer, while separate groups have demonstrated ATP binding to the aptamer is hindered by duplexing across the aptamer sequence [236]. In addition, an aptamer embedded in the stem-loop conformations described here should reflect additional thermodynamic contributions from the innate stability of the hairpin structures. The sums of these duplex and hairpin structural stabilities undoubtedly act as competition to the ATP binding mechanism, which can be summed according to eqn. 3.5,

$$\Delta G_{duplex} + \Delta G_{hairpin} - \Delta G_{ATP-apt} = \Delta G_{NSETbeacon} \quad \text{eqn. 3.5}$$

where ΔG_{duplex} represents the change in free energy between the duplexed and denatured states of the double-stranded DNA region, $\Delta G_{hairpin}$ represents the change in free energy between the single-stranded and hairpin states, $\Delta G_{ATP-apt}$ is the change in free energy between the single-stranded and ATP-bound aptamer sequence, and $\Delta G_{NSETbeacon}$ represents the observed change in free energy between the ATP-unbound and ATP-bound states specific to the NSET stem-loop beacons in this study. Inspection of the individual thermodynamic contributions to ATP binding

Table 3.5: Percent double-stranded portion of the aptamer sequence (% d.s), the melting temperature of the hairpin (T_{hairpin}), the Gibbs free energy of the hairpin ($\Delta G_{\text{hairpin}}$), and the Gibbs free energy of the duplexed aptamer sequence (ΔG_{duplex}) in each NSET stemloop beacon. The ΔG values are calculated from IDT Oligoanalyzer software [237].

	% d.s	$\Delta G_{\text{hairpin}}$ kcal/mol	ΔG_{duplex} kcal/mol
Seq <i>i</i>	20%	-3.31	-9.69
Seq <i>ii</i>	0%	-1.79	-----
Seq <i>iii</i>	20%	-2.29	-8.19
Seq <i>iv</i>	44%	-4.18	-24.25
Seq <i>v</i>	60%	-1.34	-34.92
Seq <i>vi</i>	0%	-----	-----

to these stemloop beacons (Table 3.5) is informative. The ΔG_{duplex} and $\Delta G_{\text{hairpin}}$ values are calculated from IDT OligoAnalyzer software and, in the instance of the ΔG_{duplex} , the nick at the 5' end of the hairpin stem of the NSET beacon sequence is disregarded, as shown in Figure 3.10 [237]. The $\Delta G_{\text{ATP-apt}}$ is a constant value throughout these stem-loop beacon sequences, as the 25 basepair aptamer sequence itself does not change. Therefore, only the free energies of the duplex regions and the hairpin structure, listed in Table 3.5, are considered when determining the major contributions to the free energy of the NSET beacon, and subsequently the observed K_{ds} .

The values listed in Table 3.4 and Table 3.5 indicate that with increasing free energy stabilization of the duplexed region (decreasing ΔG_{duplex}), the K_{d} value also increases, while $\Delta G_{\text{hairpin}}$ does not appear to correlate. Furthermore, as ΔG_{duplex} appears to be the sole competitive contributor to ATP-aptamer binding, the values of ΔG_{duplex} and K_{d} should be logarithmically related based on the thermodynamic relationship between equilibrium constant and free energy change. A plot of $-\Delta G_{\text{duplex}}$ vs K_{d1} and K_{d2} on a logarithmic scale is shown in Figure 3.10. The graph demonstrates that a logarithmic correlation is observed consistent with thermodynamic

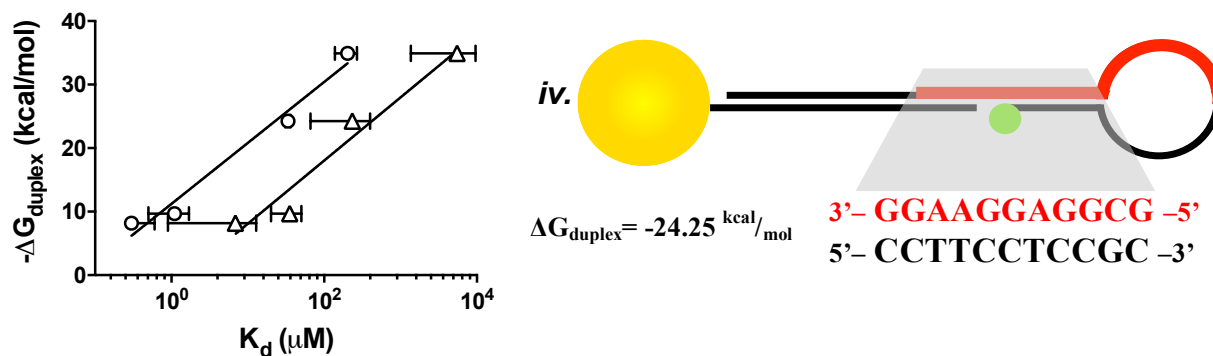


Figure 3.10: (Left) Correlation between the aptamer Gibbs free energy of the duplex region vs. experimentally measured K_{d1} (circles) and K_{d2} (triangles) values of the aptamer. (Right) The region of duplex sequence utilized for the $-\Delta G_{\text{duplex}}$ calculation, depicting sequence *iv* as an example.

expectations. Similar phenomena were observed previously in varying duplex lengths away from the aptamer sequence [238]. The results of the thermodynamic plot supports the observation that the ATP aptamer site location in the stem-loop architecture provides a strategy to systematically vary K_d by intentionally including duplexed regions without affecting selectivity or cooperative binding behavior.

3.4 Conclusion

For the Huizenga-Szostak ATP aptamer in this study, the results clearly indicate that increasing duplex formation by positioning the sequence in the stem allows the binding affinities for ATP to be tuned over four orders of magnitude with a seven order range of detection, as shown by the binding curves (Figure 3.11). The study shows a correlation between single-stranded exposure, lower K_d values, and a scaling with $-\Delta G_{\text{duplex}}$ in the DNA ATP aptamer. The advantage of using the stem-loop architecture and tuning the K_d values by positioning the aptamer target region in the loop is purely in the simplicity of the design parameters, not in adjusting the aptamer sequence itself. Earlier studies by Plaxco et al show similar results for control of metal ion sensors using allosteric inhibition, where distal DNA duplex sequences predictably tune the binding affinities of Hg^{2+} ions two orders of magnitude and across detection ranges of three orders [75]. This confirms an advantage in blocking portions of the aptamer sequence directly, as we see no change in ATP cooperative binding behavior while pushing the K_d 's and detection range to longer magnitudes. Another allosteric inhibition technique employed

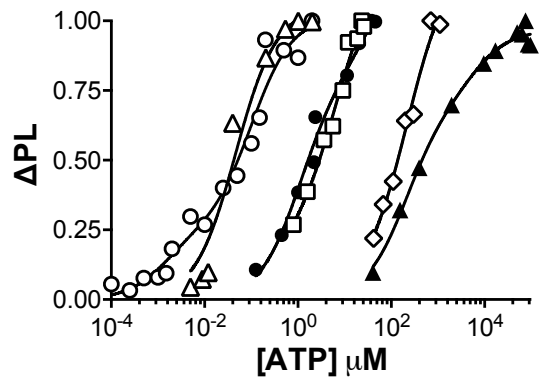


Figure 3.11: Log plots of the NSET beacon binding curves as a demonstration of their range of ATP detection across six orders of magnitude.

by Plaxco and colleagues tuned a cocaine aptamer with distal-site modifications where the K_d 's span three orders of magnitude and the detectable concentration range spans six [229]. Changing the aptamer sequence itself can be risky, as single-site modifications in nucleic acid strands capable of forming secondary structures can unpredictably impede secondary structure formation [73,74].

The observation of native biophysical constants for the NSET stem-loop designs indicates no perturbation of the ATP aptamer folding in the presence of the appended AuNP, which supports the utilization of NSET to monitor other complex biological events without manipulating native behavior. From a biophysical viewpoint the use of the NSET aptamer beacon allows multidimensional analysis of ATP aptamer binding. While previous optical studies have been unable to identify the cooperativity or distinguish individual ATP binding sites, the NSET hairpin probe method clearly observes two distinct binding sites.

The selection of aptamers against a target ligand leads to the aptamers with the lowest K_d values and, thus, aptamers are typically only useable in a narrow concentration range. The results of the study suggest that judiciously tuning the K_d value to expand the applicability of the aptamer can be achieved by site control of the aptamer in a stem-loop architecture without relying on mutation approaches or multiprobe platforms [48,229]. The ability to tune the K_d value by changing the duplex content in a stem-loop architecture provides clear design criteria that can be more widely implemented, the results of which may have an advantage in sensor design, namely, the ability to rationally extend the detectable concentration range for a ligand in a previously isolated aptamer from library screening.

CHAPTER 4

STRUCTURES OF TELOMERIC G-QUADRUPLEXES

4.1 Introduction

The realization that G-quadruplex repeats in the genome are ubiquitous and important in up-regulation of telomerase in non-senescent cells has resulted in a global effort to understand the structure and function of these simple G-tracts [136,145,146]. Telomeres are one example of many in the genome where quadruplex-protein interaction is coupled to genetic function [97,122,157,239-242]. The desire to gain structural insight into the possible folding landscapes of guanine repeats led the experimental focus towards telomeric G-quadruplexes, which have been observed to preferentially form mixed Hybrid-1 and Hybrid-2 structures in human telomere

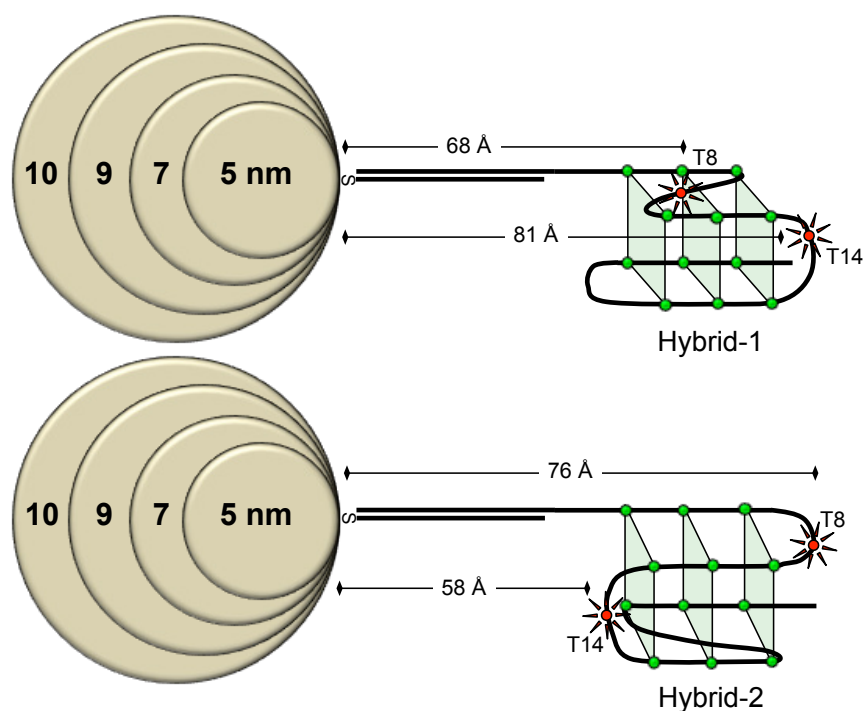


Figure 4.1: Scheme of Hybrid-1 and Hybrid-2 G-quadruplexes folded on AuNP surfaces of various sizes and the distinct position of thymine 14 (T14) between the two structures. Theoretical distances between the AuNP surface and the dye labels at T8 and T14 were extracted from proton NMR structures of the two conformers.

sequences (Figure 3.1)[105,142,143,166,167,243-245]. Several biophysical methods have been employed to investigate the folding of these structures. These methods, while effective in confirming structural folding, are widely carried out under non-biologically relevant conditions. NMR, for instance, is used for short contact measurements to deduce a global structure but requires highly concentrated samples and produces broadened line widths at high salt concentrations[141,166-168,243-248]. EPR is perhaps the most promising method for observing the G-quadruplex folding event at low concentration, but is incapable of measurements at room temperature[142,143,249]. Optical methods, like circular dichroism, are effective in recognizing the presence of a folded quadruplex, but fail to distinguish between the more relevant (3+1) hybrid structures in telomeres [182,250-253]. Förster resonance energy transfer (FRET) offers potential but the necessity for dyes to be within close proximity can limit their flexibility as long-range sensors [140,254,255]. Moreover, comparisons between folded and unfolded structures using FRET molecular rulers become difficult in scenarios where unfolding is contingent upon salt removal, as denaturing of complementary DNA is often a side effect of the desalting process. Accurately mapping telomere structure folding requires biophysical tools capable of monitoring structural formations at biologically relevant conditions without impacting the folding landscape.

Alternative optical rulers using resonance energy transfer principles hold potential for tracking these structures. Of these techniques, NSET has the largest dynamic range for mapping conformational space in biophysical settings [178]. Where other metal nanoparticle techniques, such as plasmonically-coupled probes, can attain distal coupling that rivals NSET, the use for these strictly plasmonic probes in biophysics is limited due to the required use of exceptionally large particles and overall lower resolution [256-259]. NSET allows long-range energy transfer ($d_0 > 100\text{\AA}$) from a dye to the AuNP through perturbation of the radiative and non-radiative rates for the dye when resonant with the metal localized surface plasmon (LSPR) [178]. NSET's inclusion of bioapplicable AuNP sizes (<20nm) permits observable dye emission to optically track structural biomolecular changes. The recent development of a mathematical model to predict the coupling distances achievable by NSET of AuNPs up to 16nm in diameter for the dyes emitting from 500 to 800nm allows the use of NSET rulers to unravel complicated folding events in biophysics [178]. Use of a AuNP molecular ruler, for instance, allows the fluorophore and AuNP quencher probes to be distally positioned, in order to minimize structural perturbation of the nucleic acid folding event [176,179,260]. More recently, NSET-based biological

applications using AuNPs larger than 2nm have appeared as payload delivery agents, molecular rulers, molecular flares, and even intracellular sensors [39,206,261-265].

Unfortunately, over the past two decades, observations of non-specific interactions for biopolymers with the surface of nanoparticles have been reported depending on surface passivation and experimental conditions, suggesting that while NSET is a viable toolset in biophysics, the potential for non-specific interactions perturbing the folding even is a real concern [228,232,233,266,267]. The possible impact of biomolecular function on the AuNP surface due to van der Waals, electrostatic, or molecular interactions has not been extensively studied with respect to AuNP nanoruler capabilities. In fact, the probability of non-specific interaction is likely to increase with increasing AuNP size reflecting the higher surface area on the nanoparticle [233,266-268]. The potential for interactions in single-stranded or overhang DNA sequences could be more significant, as other groups have reported variable surface adsorption behavior between duplex, single-stranded, kinked, and bent DNA strands [232,233]. Such unexpected interactions can produce significant error in measuring simple distances for ligand-induced folding events. This lack of predictability impacts the potential of NSET ruler use and more importantly can provide erroneous results if the interaction is not understood. For molecular ruler experiments based on NSET, quantifying the presence of non-specific interactions between the G-quadruplex and AuNP surface is critical to the mapping of the hybrid telomere structures. Specifically, surface interactions with nanosensor-relevant AuNP sizes (>2nm) need to be explored to determine NSET's applicability as a molecular ruler for future bioapplications.

In this chapter, to ascertain the impact of AuNPs on the folding of complex biomolecules, the folding of Hybrid-1 and Hybrid-2 telomere G-quadruplexes are mapped when assembled onto 5, 7, 9, and 10nm AuNPs. The folding event is visualized optically by monitoring the motion of two separate nucleotides in the telomere sequence, namely thymine 8 (T8) and thymine 14 (T14), labeled with DyLight680 fluorophore (DL680). The remainder of this chapter is divided into Experimental section (4.2), Results & discussion (4.3), and Conclusion (4.4)

4.2 Experimental section

4.2.1 NSET beacon construction

The NSET telomere beacons were constructed by appending a modified Tel26 or wtTel26 single stranded sequence to the surface of AuNPs of various sizes. Single-stranded sequences containing the Tel26 sequence (underlined), 5'-TATGTGTATGTGTAAAGGGT T(DL680)AGGGT T(DL680)AGGGTTAGGGAA-3,' or the wtTel26 sequence (underlined), 5'-TATGTGTATGTGTTTAGGGTT(DY680)AGGGTT(DL680)AGGGTTAGGGTT-3,' were annealed to a complementary 13mer linker, 5'-ACACATACACATA(C₃ thiol)-3,' with a terminal thiol modification for AuNP surface appendage. The flanked telomere sequences, Tel26 and wtTel26, were purchased with either a thymine 8 (T8) DL680 or thymine 14 (T14) DL680 internal dye modification as noted in the sequences by a bolded, italicized “T” followed by “(DL680).”

Spherical 5, 7, 9, and 10nm BSPP-coated AuNPs were prepared by modification of literature protocol [269]. Two reactions solutions were prepared and heated prior to mixing to induce a tannic acid/citrate reduction of a Au³⁺ salt. Solution 1 was prepared by purging 200uL of 1% (wt) HAuCl₄ in 16mL npH₂O with nitrogen and heating to 60°C. Solution 2, a solution of 1% (wt) tannic acid, 0.8mL of 1% (wt) sodium citrate, and npH₂O, contained a variable amount of tannic acid and npH₂O depending on the desired AuNP diameter. For a 5nm AuNP, 0.5mL tannic acid and 2.7mL npH₂O were required. For a 7nm AuNP, 0.1mL tannic acid and 3.1mL npH₂O were required. For a 9nm AuNP, 38uL tannic acid and 3.162mL npH₂O were required. And likewise, for a 10nm AuNP, 20uL tannic acid and 3.18mL npH₂O were required. Solution 2, with all three of its components, was heated to 60°C. Upon reaching 60°C, Solutions 1 and 2 were quickly mixed under high stirring and removed from heat upon a red color change indicative of AuNP formation. At room temperature, variable amounts of BSPP ligand were added (70mg for 5nm AuNPs and 60mg for larger AuNP sizes) and the reaction was stirred overnight. The AuNPs were collected by centrifugation after forced insolubility by addition of 0.5mL saturated NaCl. All samples were stored dry at 4°C until use.

Tel26 and wtTel26 sequences were annealed to the complement linker strand in 2 heat cycles (95°C for 4 minutes, RT for 10 minutes, ice for 4 minutes) and stored at 4°C in the dark until use. Appendage to the AuNPs was accomplished by DTT reduction of the linker's 3' thiol

by Sigma-Aldrich protocol. A 125 μ L aliquot of 100mM DTT solution (in pH 8, 50mM sodium phosphate buffer, 10mM NaCl) was added to 80pmoles of the annealed telomere linker complex and placed on the rotisserie for 35 minutes at RT. To remove the DTT after thiol reduction, the reaction was purified by Nap5 column washed with pH 6 sodium phosphate buffer (10mM) and the elutions were immediately added to a solution of AuNPs. The initial DNA:AuNP ratio was varied depending on AuNP size to accommodate the unequal surface area between the different sizes of AuNPs; 5:1 DNA to AuNP for 5nm, 7:1 DNA to AuNP for 7nm and 9nm, and 10:1 DNA to AuNP for 10nm. The AuNP-DNA ligand exchange reaction sat at RT for 1 hour and was then stored at 4°C for 1 day. All storage conditions involving the telomere sequence or telomere-AuNP conjugates were in the dark to avoid photobleaching of the DL680 dye. The telomere-AuNP conjugates were purified via EtOH precipitations without NaCl to avoid inadvertently high salt conditions in the optical quadruplex-folding experiments. Size distributions of the final AuNP products (after DNA appendage), 5.3 \pm 0.6 nm, 6.6 \pm 0.6 nm, 9.0 \pm 0.6 nm, and 10.0 \pm 1.1 nm, were determined by TEM. Appendage of the telomere sequences was also characterized by gel electrophoresis (2% agarose) and UV-Vis (Figure 3.2). Characteristic DNA absorption features are observed at 260nm, with DL680 absorption near

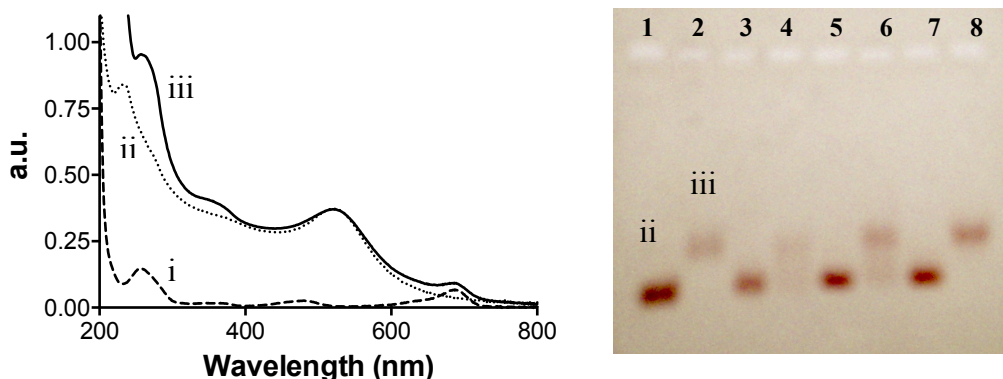


Figure 4.2: (Left) UV-Vis absorption spectra of DL680-labelled wtTel26 sequence (i), 5nm BSPP-coated AuNPs (ii), and a purified NSET wtTel26 beacon after appendage of the DNA to the AuNP surface via thiol reduction (iii). (Right) Gel electrophoresis of the BSPP-coated AuNPs prior to DNA appendage (lane 1: 5nm, lane 3: 7nm, lane 5: 9nm, and lane 7: 10nm), and after attachment of the wtTel26 beacon complex to the AuNP surface (lane 2: 5nm, lane 4: 7nm, lane 6: 9nm, and lane 8: 10nm.)

680nm, and a classic AuNP LSPR observed at 520nm. It should be noted that due to large differences in the AuNP, DNA, and DL680 extinction coefficients ($\text{AuNP } \epsilon_{520} = 9.70 \cdot 10^6 \text{ M}^{-1}$

$^1\text{mol}^{-1}$; DNA $\epsilon_{260} = 3.98 \times 10^5 \text{ M}^{-1}\text{mol}^{-1}$; DL680 $\epsilon_{680} = 1.40 \times 10^5 \text{ M}^{-1}\text{mol}^{-1}$) the DNA absorption features for loading levels used in this study are typically not observable. Thus, for the sole purpose of characterization, high loading levels of $\sim 15:1$ DNA to AuNP are shown in the UV-Vis absorption spectra.

4.2.2 Absorption and photoluminescence experiments

Photoluminescence (PL) was measured in 0.3cm quartz cuvettes on a Varian Eclipse fluorimeter in a thermostated optical cell holder (25°C) by exciting the DL680 at 620nm and collecting the PL spectra from 635 to 800nm. Samples were dissolved in 50 μL of nanopure H_2O and an initial (low-salt condition) PL was taken to represent the linearly extended DNA sequence value. Before salt additions, dilutions of the sample were made as needed to ensure the absence of the inner filter effect from high AuNP concentrations. Moreover, controls against DNA in solution with unappended AuNPs at comparable concentrations were also carried out. With DL680's red wavelength excitations, however, these inner filter adjustments were only required in the 10nm AuNP samples. The K^+ concentration was gradually increased with small aliquots of 3.4 M KCl every 5 minutes, along with intermittent sonication, until a $[\text{K}^+]$ of at least 75mM was reached. It was observed that 9 and 10nm AuNPs had a propensity for aggregation at high salt concentrations, thus sonication and gradual K^+ additions were employed to prevent AuNP precipitation. Because smaller AuNPs resist aggregation, the smaller AuNP sizes, 5 and 7nm, were brought to the goal K^+ concentration of 100mM. UV-Vis effectively monitored the solubility of the AuNPs throughout the salting process. After 6 hours at high KCl concentration, a final PL was taken, representative of the DL680 emission in the folded-quadruplex state. Slits were opened in the fluorimeter as needed to increase DL680 intensity on the larger AuNPs.

4.2.3 NSET distance calculations

The validity of the NSET molecular ruler is well-supported in the literature and has been demonstrated for identifying the folded structure of various nucleic acid structures [196,258,259]. The separation distance of the donor to the AuNP acceptor surface used in the NSET analysis is calculated using a Clegg model for the 13bp duplex and the predicted folding

of Hybrid-1 and Hybrid-2 structures from NMR for the appropriate telomere sequence (Figure 4.1) [105,165,244,262].

The quenching efficiency follows a R^{-4} distance dependent behavior leading to a functional ruler distances exceeding 130 Å for DL680 when coupled to a 10 nm AuNP. The predicted efficiency curves for a 5.3 ± 0.6 nm, 6.6 ± 0.6 nm, 9.0 ± 0.6 nm, and 10.0 ± 1.1 nm AuNP and DL680 are provided in Figure 3.3, indicating d_0 values (50% quenching efficiency, derived from eqn. 4.1) of 53.6 Å (5nm), 62.1 Å (7nm), 74.4 Å (9nm), and 78.4 Å (10nm), with an overall range of measurement from 40-130 Å [178]. Also shown in Figure 4.3 is the first derivative of the quenching efficiency curves for each of the AuNP sizes and DL680, where the peak maximum corresponds to the distance at which the greatest change in DL680 intensity per Å would be observed.

For an NSET ruler, the magnitude of PL quenching is extracted from the integrated intensity of the donor dye relative to the dye PL in the absence of an appended AuNP. The magnitude of quenching from the dye label is then a measure of the separation distance between the dye and the AuNP. Contact distance are extracted from the PL data via the NSET theorem using eqn. 3.1,

$$R_0 = \frac{\alpha\lambda}{n_m} (A\phi)^{1/4} \left[\frac{n_r}{2n_m} \left(\frac{1+\varepsilon_1^2}{\varepsilon_2^2} \right) \right]^{1/4} \quad \text{eqn. 4.1}$$

where α is the orientation of the donor to the metal which is assumed to be influenced only by the average vector, resulting in $\alpha = \frac{\left(\frac{9}{2}\right)^{1/4}}{4\pi}$, and A (eqn. 4.2) is the absorptivity of the AuNP.

$$A = 10^3 \ln 10 \left[\frac{\varepsilon_\lambda \left(2r_{cm} \left(\frac{2r_{cm}}{\gamma_{skin}} \right) \right)}{N_A V_{cm}^3} \right] \quad \text{eqn 4.2}$$

In equation 4.1, λ is the emission wavelength of DL680, n_m is the refractive index of water, n_r is the refractive index of gold, Φ is the quantum yield of DL680, ε_1 is the dielectric constant of water, and ε_2 is the dielectric constant of gold. In the subsequent equation (eqn. 4.2), N_A is Avogadro's number, ε_λ is the extinction coefficient as a function of λ , r_{cm} is the radius of the

Table 4.1: Variables used in this chapter to extract the appropriate d_0 values for a 5.3 ± 0.6 nm, 6.6 ± 0.6 nm, 9.0 ± 0.6 nm, and 10.0 ± 1.1 nm AuNP and DL680, as expressed in eqn. 3.1 and 3.2.

Variable	Symbol	Numerical Value
emission wavelength of DL680	λ	710nm
refractive index of water	n_m	1.33
refractive index of gold	n_r	0.13
quantum yield of DL680	ϕ	0.21
dielectric constant of water	ϵ_1	1.77
dielectric constant of gold	ϵ_2	$-18.3+(6.56*i)$
Avogadro's number	N_A	$6.02*10^{23}$
extinction as a function of λ	ϵ_λ	$6.6*10^5 \text{ LM}^{-1}\text{cm}^{-1}$
radius of the AuNP in centimeters	r_{cm}	$2.6*10^{-7} \text{ cm}$
skin depth of the AuNP	γ_{skin}	26.00 nm
volume of the AuNP	V_{cm}	$7.3*10^{-20} \text{ cm}^3$
orientation factor	α	0.123212

AuNP in centimeters, γ_{skin} is the skin depth of the AuNP, and V_{cm} is the volume of the AuNP in cm^3 [178]. The values for eqn. 4.1 and 4.2 are tabulated in Table 4.1.

4.3 Results & discussion

NSET methods utilizing AuNPs have emerged as a powerful tool in biophysics and structural biology [39,179,206,260,264,265,266]. Using the AuNP as the acceptor, NSET can be thought of as an analogue to a FRET molecular ruler, but operative over longer distances. The interaction between the Nanometal LSPR and a fluorescent dye in close proximity impacts the radiative and non-radiative rates of the dye and is described as a function of distance from the nanoparticle surface, nanoparticle size, and the dye emission frequency within the NSET theorem [178]. Until recently, NSET theory was restricted to 2nm AuNPs, limiting its range of applicability to below 200Å dye-AuNP donor-acceptor separation distances, but the development

of predictive theory to describe the interaction now allows distances greater than 400Å to be probed, expanding its potential applicability for addressing biophysical questions [178,225].

NSET molecular rulers on 5, 7, 9, and 10nm AuNPs were prepared with a Tel26 or wtTel26 sequence appendage and the folding behavior for the Hybrid-1 and Hybrid-2 telomeric G-quadruplexes under biologically relevant conditions were monitored using the NSET probes. The Hybrid-1 and Hybrid-2 constructs are schematically represented in Figure 4.1. The use of AuNP NSET molecular beacons allows desalting by centrifugation, permitting optically traceable folding of both the unfolded and folded G-quadruplex states. Duplexed FRET systems are not stable in low salt conditions, flawing the use of those systems to monitor nucleic acid folding on multiple DNA strands. The DNA quadruplex sequences employed in this chapter, Tel26 and wtTel26, are flanked sequences that contains the native telomere quadruplex sequence, Tel22. Tel26 and wtTel26 contains two additional basepairs at the 3' and 5' end, ensuring single population folding of Hybrid-1 in Tel26 and predictable 75%/25% Hybrid-2/Hybrid-1 folding in wtTel26 [244]. The sequences are synthesized with an additional 13 basepairs at the 5' end to accommodate a complementary 13mer 3'-thiol linker for AuNP attachment. Utilization of the flanked sequences is necessary to promote predictable Hybrid-1 or Hybrid-2 quadruplex populations, as Tel22 is known to form mixed conformer populations [105,141,143,244]. Estimation of the final DNA:AuNP ratio (~1-5:1) is calculated by DNA and AuNP UV-Vis absorption features. Multiple repeated trials where variation in loading levels

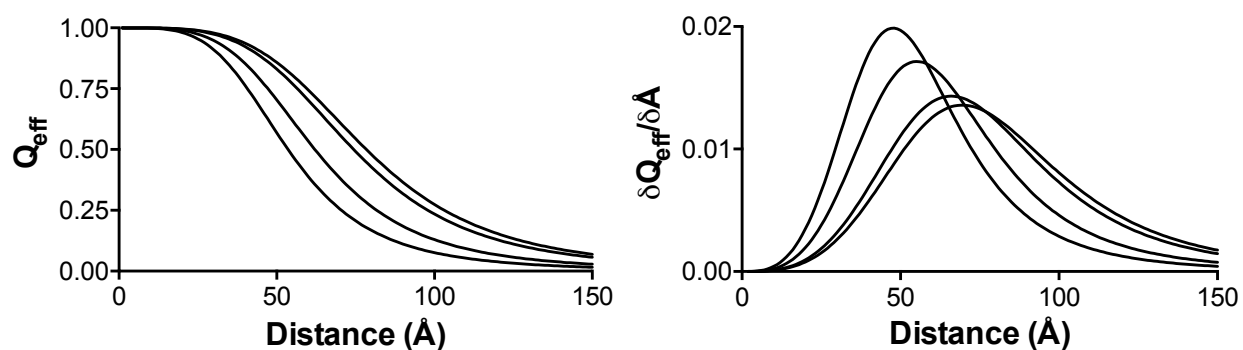


Figure 4.3: (Left) Theoretical NSET quenching efficiency versus distance of a 5.3 ± 0.6 nm, 6.6 ± 0.6 nm, 9.0 ± 0.6 nm, and 10.0 ± 1.1 nm AuNP (sliding from left to right) and DL680. (Right) First derivative of the quenching efficiency curve which depicts the distance at which the maximum slope of the quenching efficiency curve is incurred.

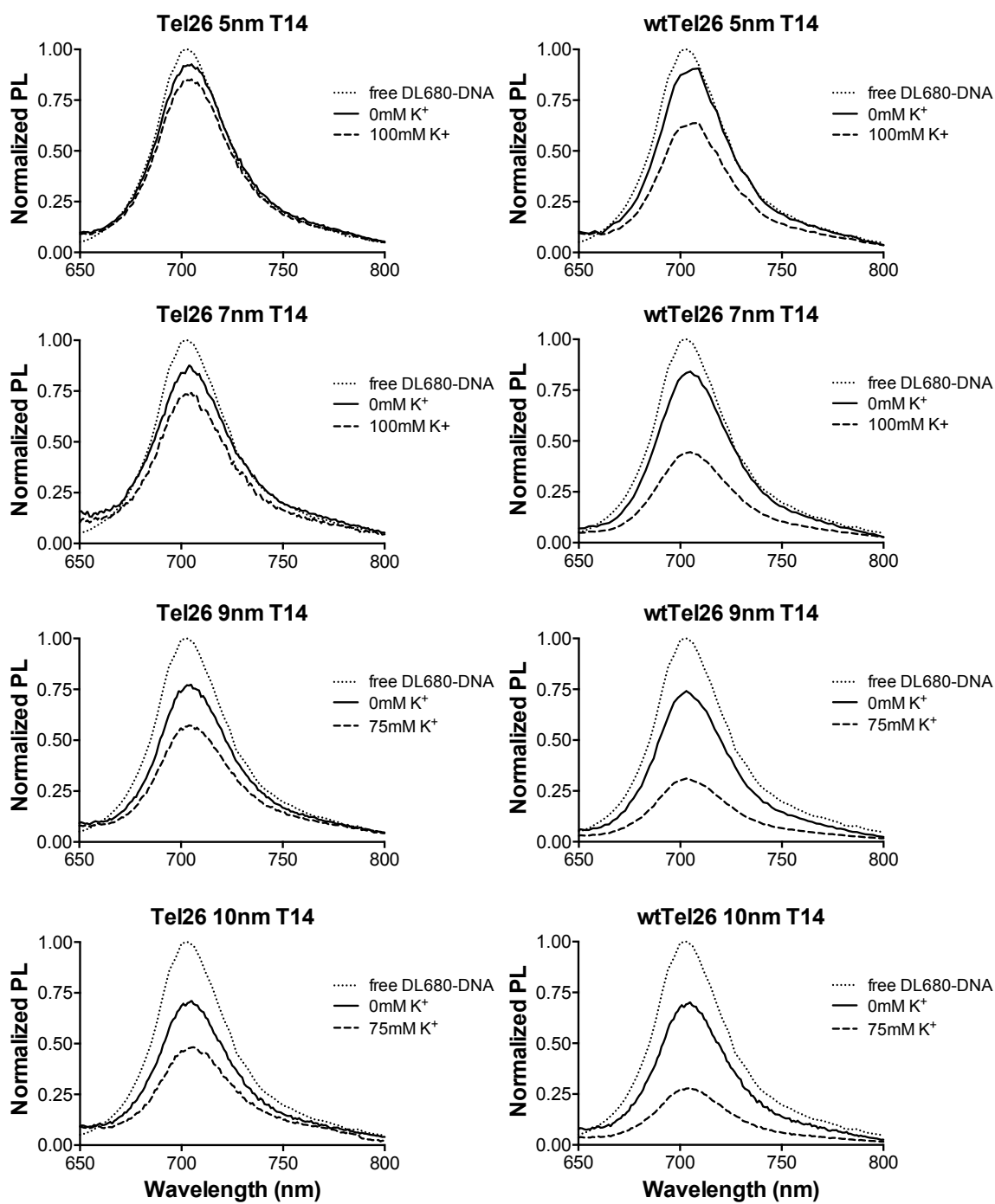


Figure 4.4: Normalized PL intensities of Tel26 (left column) and wtTel26 (right column) NSET beacons. The beacons are listed from top to bottom increasing in AuNP size. Each plot contains the normalized DL680 intensity of free DL680-DNA (dotted line), an initial, 0mM K^+ concentration (solid line), and at high 75-100mM K^+ concentration (dashed lined).

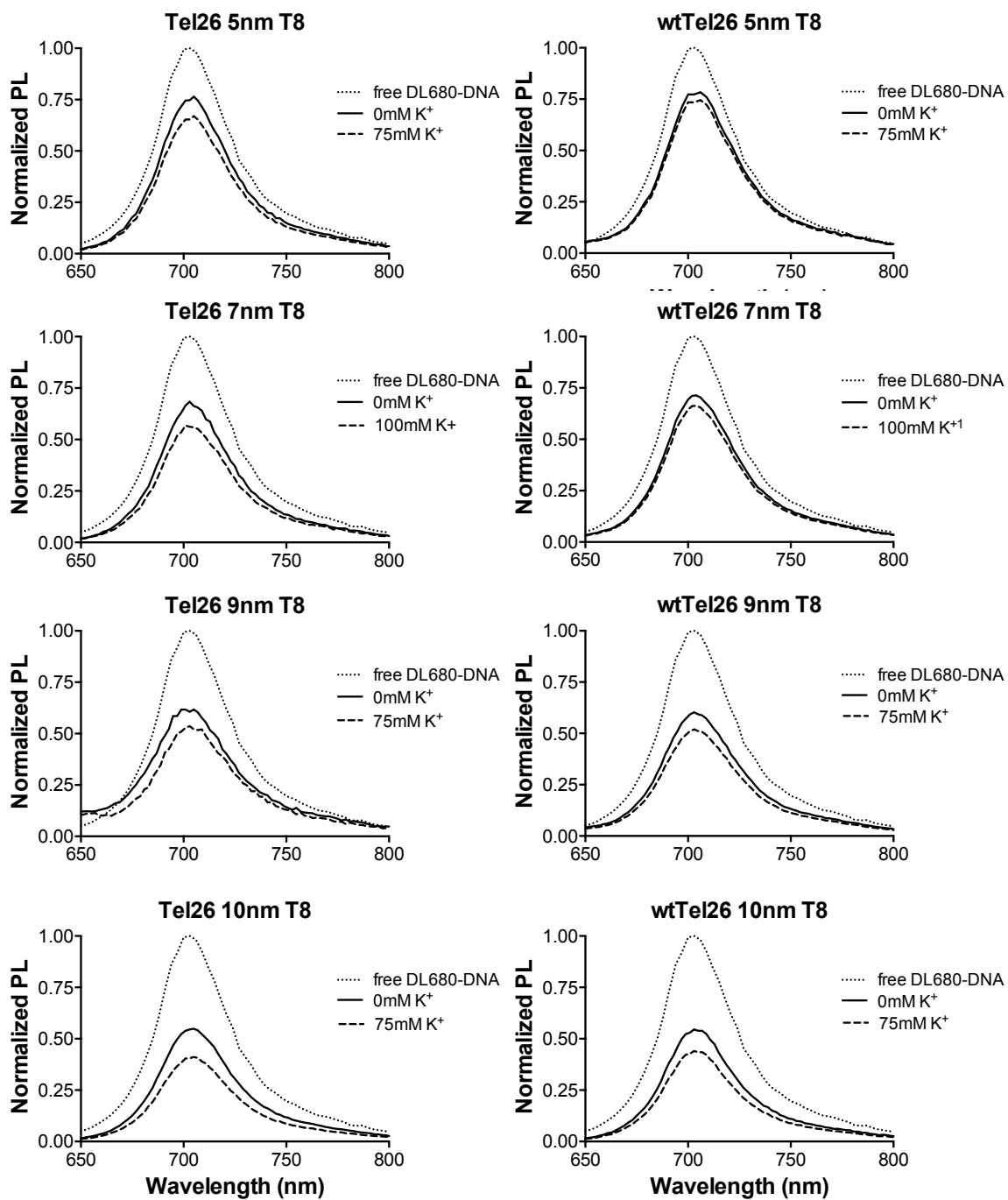


Figure 4.5: Normalized PL data of the T8 DL680 emission intensities for the 5nm, 7nm, 9nm, and 10nm NSET beacons upon K^+ addition. Each plot depicts the emission intensity of free DL680-DNA (dotted line), an initial, 0mM K^+ concentration (solid line), and at high 75-100mM K^+ concentration (dashed lined).

occurred produced identical changes in PL upon quadruplex folding and thus the small inconsistency in loading level between samples (~1-5 DNA per AuNP) is considered irrelevant. Low DNA loading levels are obtained to deter intermolecular DNA-DNA interactions on the surface that may affect the folded structures, as reported by previous AuNP-DNA sensors [191,192]. Evidence of the assembly of the molecular rulers is demonstrated by a shift in the gel electrophoresis (Figure 4.2) while the size of the AuNP-DNA assembly is determined by TEM images. Size distributions of the AuNPs used in this chapter as determined by TEM are 5.3 ± 0.6 nm, 6.6 ± 0.6 nm, 9.0 ± 0.6 nm, and 10.0 ± 1.1 nm.

In Figure 4.1, a schematic of the duplex modified telomere sequences folded into the Hybrid-1 and Hybrid-2 telomere structure when appended to an AuNP is shown. By inspection of Figure 4.1, it is clear that the two unique conformers can be optically identified by molecular ruler methods by monitoring the T14 to AuNP contact distances. Hybrid-1 ($r = 82 \text{ \AA}$) versus Hybrid-2 ($r = 58 \text{ \AA}$) folding will result in a measurable change in the separation distance for the T14 fluoro-label from the AuNP surface, and thus in the observed efficiency for NSET induced PL quenching of DL680. It is important to note that the wtTel26 flanked sequence has been shown via NMR studies to form a predictable 75%/25% ratio of Hybrid-2/Hybrid-1 [206]. Thus, the Hybrid-2 contribution from the wtTel26 K^+ -saturated spectra is extracted from equation 4.3,

$$\frac{[I_{wtTel26} - 0.25(I_{H-1})]}{0.75} = I_{H-2} \quad \text{eqn. 4.3}$$

where $I_{wtTel26}$ is the wtTel26 integral (after normalization), I_{H-1} is the Tel26 integral (from the corresponding AuNP size), and I_{H-2} is the subsequent Hybrid-2 contribution to the spectra.

In Figure 4.4, the normalized photoluminescence for the T14 fluoro-labeled Tel26 and wtTel26 ($\lambda_{ex} = 620\text{nm}$, 298K , $\text{pH}=6.0$, $<1\text{mM NaCl}$) are shown at $0\text{mM } K^+$ and at $75\text{mM } K^+$ or $100\text{mM } K^+$ for the NSET rulers measured at a concentration of 10nM . For the PL studies, the choice of NSET beacon concentration is chosen to minimize the inner-filter effect associated with the strong optical cross-section for an AuNP [232,233]. Although the changes in position for T8 are less significant, the T8 PL data is available in the Figure 4.5 for Tel26 and wtTel26. In all cases the intensity of the DL680 is decreased following addition of K^+ . Consistent with the projected structures, wtTel26 T14 exhibits the highest magnitude of PL signal loss following folding, while Tel26 T14 shows the smallest signal change.

Table 4.2: Table of the extracted distances from the NSET theorem based up the T14 DL680 emission intensities observed for the 5nm, 7nm, 9nm, and 10nm Tel26 and wtTel26 NSET beacons.

Tel26 T14	AuNP-DL680 distance (theory)	AuNP-DL680 distance (experimental)	DL680 % Emission (theory)	DL680 % Emission (experimental)
5nm AuNP	81 Å	85 Å ± 16	84%	86% ± 14
7nm AuNP	81 Å	78 Å ± 7	74%	72% ± 8
9nm AuNP	81 Å	78 Å ± 6	58%	55% ± 7
10nm AuNP	81 Å	79 Å ± 5	53%	51% ± 6
wtTel26 T14				
5nm AuNP	58 Å	59 Å ± 4	58%	59% ± 7
7nm AuNP	58 Å	54 Å ± 5	43%	35% ± 7
9nm AuNP	58 Å	54 Å ± 5	27%	22% ± 9
10nm AuNP	58 Å	56 Å ± 6	23%	21% ± 9

The experimental NSET data obtained for Tel26 and wtTel26 can be interpreted in terms of a folded structure by applying the NSET theorem and equation 4.3 for wtTel26. The experimental results confirm no observed structural perturbation occurs for AuNPs between 5 and 10 nm in size [234]. By application of the NSET equations (eqn. 4.1-4.2) to the quenching data in Figure 4.4, the observed PL data at 75 mM K⁺ ion (25°C) for T14 labelled Tel26 and wtTel26 can be converted to contact distances listed in Table 4.2. The observed PL data for Tel26 and wtTel26 confirm the prediction of exclusive Hybrid-1 and Hybrid-2 folding respectively for these sequences, as previously observed in NMR studies [145,146,206]. At 0mM K⁺, converting the PL data for Tel26, and wtTel26 to a contact distance yields a value of 95 ± 16 Å nm which is consistent with a fully extended sequence. The observation is consistent with previously reported results that show the single-stranded DNA persistence lengths >14 basepairs is observed at exceptionally low salt conditions [235,238].

4.4 Conclusion

This chapter demonstrates the capability of an NSET probe to optically track biologically relevant telomere G-quadruplexes and that no structural manipulation of the quadruplexes is

observed when bound to AuNP surfaces up to 10 nm in diameter. It is presumed that the long-range NSET labels, as well as a stable AuNP ligand coating, preserve the native folding behavior of the Hybrid-1 and Hybrid-2 structures in the flanked telomere sequences. As hybrid (3 + 1) quadruplexes have proven to be important conformations biology, new methods in identifying these structures under biologically relevant conditions are extremely desirable. The versatility in AuNP diameter of this NSET ruler exemplifies NSET's place as an impactful biomolecular probe.

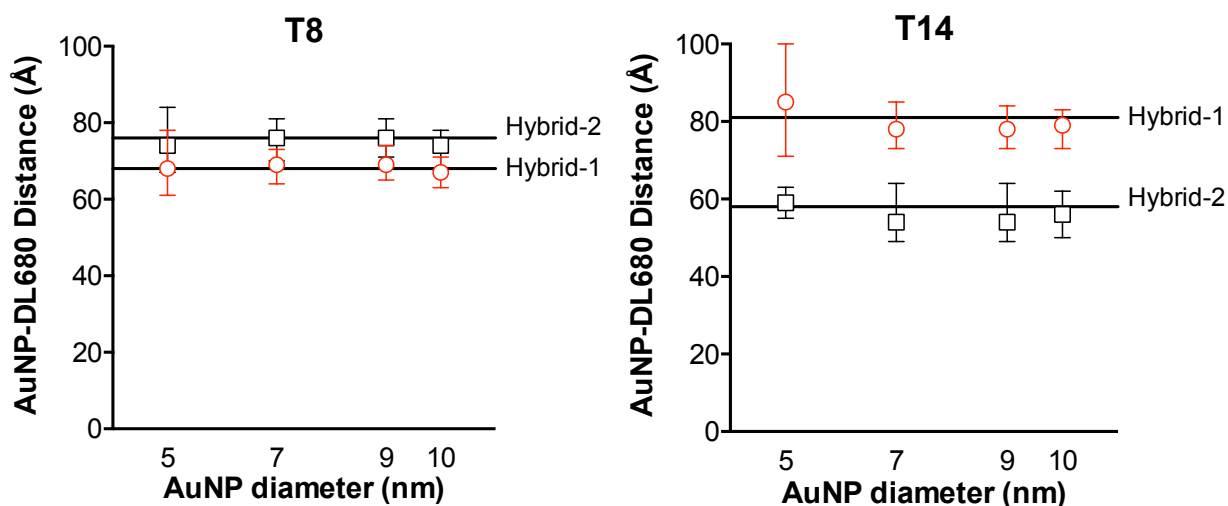


Figure 4.6: Plots of the AuNP-T8 (left) and AuNP-T14 (right) separation distances extracted from the DL680 emission intensities using the NSET theorem (eqn. 4.1, 4.2, and Table 4.1). Horizontal lines denote the theoretical separation distances exhibited by Hybrid-1 (Tel26) and Hybrid-2 (wtTel26) folding, as calculated from reported (3+1) Hybrid NMR structures.

While all sizes were capable in this instance of distinguishing Hybrid-1 and Hybrid-2 quadruplex folding, the 5 nm AuNP incurred more error (Table 4.1 and Figure 4.6), as the distal contacts observed lay far off the d_0 value for this sized particle (Figure 4.3). Inspection of the size-dependent AuNP sensitivity in these NSET-based, telomeric bioassays demonstrates the capability that NSET offers in optimizing the molecular ruler method. For a given distance of separation, merely selecting the appropriate AuNP size obtains the desired d_0 value for a specific dye–AuNP donor-acceptor pair.

CHAPTER 5

G-QUADRUPLEX POPULATIONS IN HUMAN TELOMERES

5.1 Introduction

The human telomere region contains a high number of repeats of the *six* mer nucleic acid sequence 5'-d(TTAGGG)-3'. Unique to G-tract sequences like the human telomere sequence, a minimum of four consecutive repeats can form a G-quadruplex secondary structure. The ubiquitous presence of G-runs in the telomere and their propensity to fold into a G-quadruplex has generated interest in the biomedical and biophysical fields [269]. The quadruplex comprises guanine-guanine hydrogen bonding through non-canonical Hoogsteen base pairing [260]. G-quadruplex forming sequences appear in both nuclear and mitochondrial genomes and evidence of G-quadruplex formation in cells has been reported [117,270]. The G-quadruplex sequence is implicated to play a role in helicase binding and replication [271-274]. In non-senescent cells up-regulation of telomerase occurs, regenerating telomere strand lengths, and is a proto-oncogenesis promoter [136-138,145-148]. The plethora of G-quadruplex sequences in the human genome, their unique structural forms, and their important role in biological processes have resulted in an intense effort to correlate theoretical and experimental results to understand the role of this unique sequence that is evolutionarily conserved in nature [101]. As the structural complexity of the G-quadruplex folding landscape is explored, the importance of the folding on regulatory function in biology is being revealed. The lack of unambiguous structural assignments of the folded conformer under physiological conditions have complicated the ability to understand the role of the G-quadruplex formation in biology. The folding landscape for the 5'-d(TTAGGG)-3' G-quadruplex sequence is quite complex and can exist in more than six possible folded intramolecular structures with similar thermodynamic stabilities [105,140,141,166,244]. Structural insights from NMR, EPR, and CD spectroscopy have revealed that telomeric G-quadruplex folds preferentially into the (3+1) Hybrid-1 or Hybrid-2 structures [105,140,141,166,181,182,244,249,251,275]. The structures are effectively inversions only differing in their DNA strand orientation (3' versus 5',) and as such the two hybrid forms are nearly thermodynamically equivalent. Based on NMR experiments, the native Tel22 sequence (5'-AGGGTTAGGGTTAGGGTTAGGG-3'), an in-vivo model oligomer, is believed to exist as

a mixture of Hybrid-1 and Hybrid-2 conformers, implying that Hybrid-1 and Hybrid-2 are in rapid equilibrium under physiological conditions [165]. Although alternative structures have been proposed for Tel22, including a basket form, the Hybrid-1 and Hybrid-2 form are the relevant physiological conformers [94,101,141,121,142]. The suggestion of an equilibrium for conformers in Tel22 is intriguing, as the population may impact the biological function of Tel22. It can be speculated the equilibrium may play a regulatory role due to the directionality of telomere-binding proteins and the opposing directionality of Hybrid-1 and Hybrid-2 [122,124,125,149]. Consistent with the speculation, studies have suggested that the structure of the quadruplex plays a role in binding of proteins, for example telomere-binding POT-1, TPP, UP1, Pif1, and helicases of the RecQ and ReG families [122-125,276-279]. The helicase, Pif1, has been reported to tightly bind to parallel intra-molecular G-quadruplexes with clear evidence that the rate of unfolding of the DNA is affected by the binding [276,277]. G-quadruplex-unfolding proteins, such as POT1, only traverse DNA in a single direction and therefore may be influenced by the quadruplex conformation, as strand directionality in the quadruplex is the primary determinant of the conformer [122-124].

The structural similarity of the Hybrid-1 and Hybrid-2 conformers have not allowed the most common quadruplex characterization methods to clearly distinguish the population of the

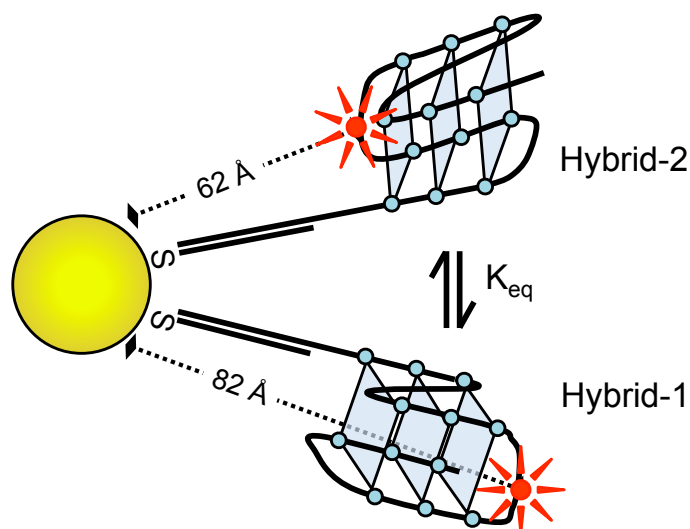


Figure 5.1: A schematic showing the two predicted G-quadruplex folding conformations and contact distances for Tel22 in an NSET ruler containing a T14 DyLight680 (DL680) fluorolabel on a 5.3 + 0.6 nm AuNP at the 5' end of the sequence. The structures are based upon calculations from previously reported NMR structures of Hybrid-1 and Hybrid-2 conformers [105,165,166].

conformers.[101,244] While single-molecule fluorescent studies of telomere-unwinding proteins have elucidated the denaturation process in a strand-by-strand fashion, it has failed to acknowledge the initial conformation of the G-quadruplex state as Hybrid-1 or Hybrid-2 [146-148]. Insight into the structural factors that are involved in the folding have been gained by application of flanked sequences, namely Tel26 and wtTel 26. Tel26 and wtTel26 are flanked sequences that contain the native telomere quadruplex sequence, Tel22 [155,206]. The Hybrid-1 and Hybrid-2 structure can be predictably isolated by sequence design and have been observed in NMR studies. The Tel26 (5'-AAAGGGTTAGGGTTAGGGTTAGGGAA-3') variant results in Hybrid-1 folding, while wtTel26 (5'-TTAGGGTTAGGGTTAGGGTTAGGG TT-3') produces a Hybrid-2 to Hybrid-1 ratio at 75%:25% [164]. Identifying the equilibrium condition, the percent population of the conformers, and the Gibbs free energy of interconversion in Tel22 can provide powerful insight into the regulatory function of the sequence in the genome. Further theoretical and experimental analysis is required to fully understand the structural polymorphism in Tel22, the equilibrium between structures that exist under biologically relevant conditions, and the impact on cell biology.

In Chapter 4, it was demonstrated that selective labeling of the nucleic acid by a fluorophore modification allowed the Hybrid-1 and Hybrid-2 folding to be distinguished on Tel26 and wtTel26 flanked sequences using an NSET ruler [260]. NSET utilizing AuNPs and a fluoro-label has emerged as a powerful tool in biophysics to measure distances for structural biology [176,178,179,269]. In this chapter, a Tel22 NSET beacon comprised of a 5nm AuNP and an internal base fluoro-label DL680 at T14 appended to the AuNP through a 5' end thiol linkage is designed to monitor the folded hybrid structure population from 4°C to 37°C. Additional studies utilizing a fluorescein-modified T14 sequence appended to a 5nm AuNP confirm the observed DL680 conformer results. By monitoring the quenching behavior with comparisons to Hybrid-1 and Hybrid-2 induced emission intensities in Chapter 4, the equilibrium of Hybrid-1 versus Hybrid 2 conformers in Tel22 as a function of temperature is extracted. The equilibrium ratio of the conformers (K_{eq}) as a function of temperature allows extraction of the free energy of the system, ΔG for inter-conversion at biological temperatures between the two folded conformers in Tel22. While the existence of the equilibrium was postulated from earlier NMR experiments, the optical ruler is capable of quantifying the equilibrium where other methods fall

short. The remainder of this chapter is divided into Experimental section (5.2), Results & discussion (5.3), and Conclusion (5.4).

5.2 Experimental section

5.2.1 Tel22 NSET beacon construction

The Tel22 NSET beacons were constructed by methods described previously in Chapter 4 with Tel26 and wtTel26 NSET beacons using the sequence 5'-TATGTGTATGTGTCC AGGGTTAGGGT***T***(DL680/FAM)AGGGTTAGGGTTA-3,' where the Tel22 sequence is underlined and the T14 basepair modified with a DL680 or fluorescein dye label is bold and italicized. DNA annealing to a 15mer complement sequence with a 3' C₆ alkyl-thiol is accomplished by heating at 95°C for 4 minutes then snap cooling to 4°C in phosphate buffer (20mM phosphate, 50mM NaCl, pH = 7.5). Appendage was subsequently carried out to the 5.3 ± 0.6 nm AuNP or 3.0 ± 0.6 nm AuNP in a 3:1 ratio of DNA to AuNP using the previously described place exchange methods in Chapter 4. In the Tel22 NSET beacons, the 5'-duplex modification to the telomere sequence involves the addition of a 15 base pair extension on the 5' end of the telomere sequence, which differs from the flanked sequences Tel26 and wtTel26

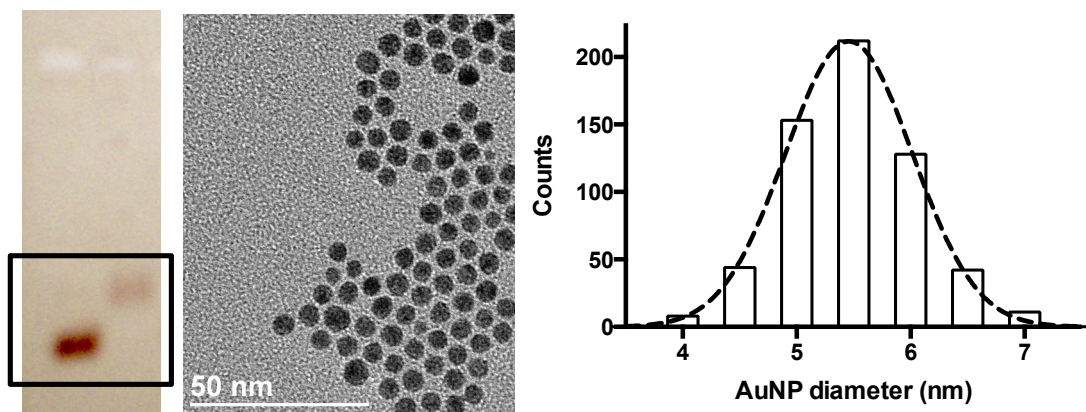


Figure 5.2: (Left) Gel electrophoresis of the NSET ruler versus BSPP-coated 5.3nm ± 0.6 AuNPs. Retardation of the NSET ruler band (left-hand well) in comparison to the BSPP-coated AuNPs (right-hand well) indicates appendage of DNA to the AuNP surface. (Center) TEM of the BSPP-coated 5.3nm ± 0.6 AuNPs and (Right) the AuNP size distribution. TEM size distribution analysis reports an AuNP size of 5.3nm ± 0.6.

which contain only a 13 basepair complement extension. The differences in linker length stem from the need to compensate for the flanked sequences' additional two basepairs at the 5' end to maintain an identical basepair length between the AuNP surface and the G-quadruplex folding event. Also, fluorescein-3nm AuNP conjugate differ slightly in that both the linker sequence and the fluorescein-modified Tel22 sequence contain terminal C₆ thiols for AuNP surface appendage. It has been demonstrated previously in Chapter 4 that neither the appendage of the duplex region

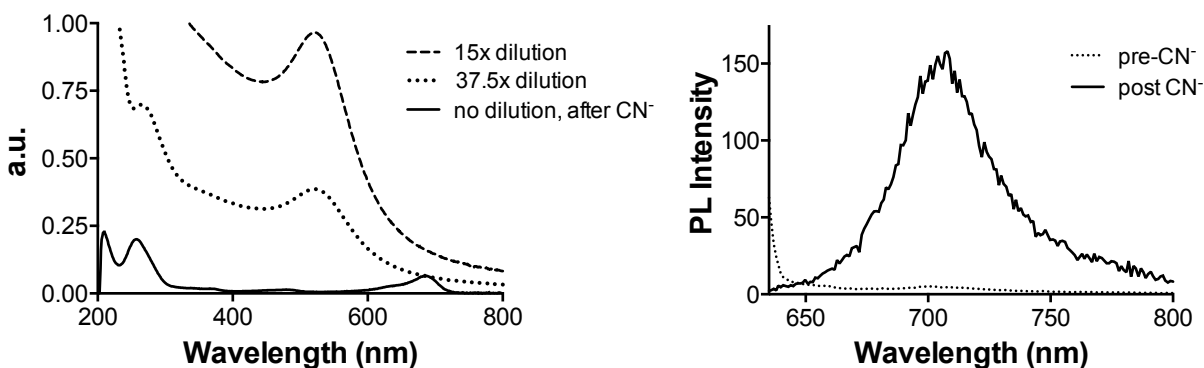


Figure 5.3: Dissolution of the AuNPs by NaCN and serial dilutions allow the measurement of DNA:AuNP ratios by UV-Vis absorption and Beer's Law correlation. A 10 μ L aliquot of 100mM NaCN was added to a concentrated (0.48 μ M) 50 μ L Tel26-AuNP construct. To track the disappearance of the AuNP features upon CN⁻ addition, dilutions of the sample are tracked via (A) UV-Vis and (B) PL spectroscopy. The concentrated sample blocks all incident light and is incapable of optical monitoring before dilutions. After 30 minutes, a UV-Vis and PL spectra (solid line) of the concentrated sample reveal complete digestion of the AuNP and a final [DNA] of 1.6 μ M. It should be noted that the absorption cross-sections of the DNA ($\epsilon_{260} = 3.97 \cdot 10^5 \text{ LM}^{-1} \text{ cm}^{-1}$) and DL680 ($\epsilon_{680} = 1.40 \cdot 10^5 \text{ LM}^{-1} \text{ cm}^{-1}$) are drastically lower than that of the AuNP ($\epsilon_{520} = 9.97 \cdot 10^7 \text{ LM}^{-1} \text{ cm}^{-1}$) and therefore the typical DNA:AuNP ratios utilized in the PL studies (~1-4:1) do not produce noticeable absorption features for the DL680-labeled DNA sequences, as observed in the 37.5x dilution (dotted line) spectra.

to the 5'-end of wtTel26 and Tel26 nor attachment to an AuNP impacts the observed quadruplex folding [260].

The NSET beacons are purified post-appendage by ethanol precipitation and stored in the dark at 4°C until use. The NSET beacon is characterized by gel electrophoresis and cyanide ion digestion of the AuNP (Figure 5.2 and Figure 5.3.) Cyanide ion digestion of the DL680 beacons

allows the labeling efficiency to be extracted from the optical data. The dye labeling is measured by monitoring the intensity of the absorption feature for DL680 at 680 nm relative to the AuNP absorption at 520 nm and the DNA absorption at 260 nm before and after AuNP digestion by addition of 10 μ L 100 mM NaCN. Assuming Beer's law behavior, the loading level is extracted from the optical data using the reported extinction coefficients. The results of the assay yields a DNA to AuNP labeling ratio of 3:1. The complete dissolution of the AuNP by addition of the CN⁻ ion is verified by the appearance of the DL680 PL intensity following CN⁻ ion addition (Figure 5.3.)

5.2.2 Temperature-dependent optical experiments

Dye labeling T14 allows optical tracking of conformational folding by monitoring the photoluminescence (PL) intensity for DL680 and fluorescein. Experimental data for T14-labelled and T8-labelled Tel26 and wtTel26 DL680 sequences is shown in Chapter 4. The PL change for T14 is more sensitive than T8 due to the larger magnitudes of structure change for the T14 position reflecting the larger change in distance and subsequent NSET efficiencies, therefore T8 data is not included for Tel22.

The PL measurements on the assembled Tel22 NSET beacon were measured at DL680 $\lambda_{\text{ex}} = 620$ nm (pH = 5.8 in nanopure water) and fluorescein $\lambda_{\text{ex}} = 488$ nm (pH = 8.0 in 20mM HEPES buffer, pHed with CsOH) in a 0.3cm quartz cuvette on a Varian Eclipse fluorimeter. The cuvette was sealed to prevent evaporation. Temperature-dependent PL studies were performed at 4°C, 15°C, 25°C, and 37°C following optical cell thermal equilibration for 6 hours in the spectrometer. The measured PL intensity for DL680 emission (650 to 800 nm) and for fluorescein emission (509 to 650 nm) utilized in the molecular ruler calculations are obtained from the integrated intensity for the NSET beacon at 0mM and 100mM KCl relative to a DL680 and fluorescein control PL measured under identical conditions without an appended AuNP to the terminal DNA thiols. Changes in Tel22 intensity with temperature is confirmed to be due to a reequilibration of Hybrid-1 and Hybrid-2 rather than a DL680 or fluorescein temperature-dependence, as the temperature range analyzed in this Chapter has no effect on the emission intensity of the dyes (Figure 5.4). To ensure the NSET beacon remains in solution as the salt concentration is raised, sequential aliquots (1 μ L) of 2M KCl were added every 5 minutes to

bring the final K^+ concentration to 100mM. The sample was gently sonicated and shaken to prevent aggregation with each salt addition. The PL following KCl addition is recorded 6h following of the salt to the sample. It is worth noting that maximum intensity change is observed within 1 hour as demonstrated in Figure 5.5 with the fluorescein-Tel22 beacons, but PL values are reported at 6 hours following addition of the last aliquot of K^+ ion to ensure the quadruplex-folded population is in equilibrium. To verify the change in intensity arises from the NSET beacon's expected quenching behavior upon quadruplex folding rather than a sensitivity of the dyes to changes in salt concentration, control studies of the free DNA strand in solution with unappended AuNPs were measured. No change in DL680's for fluorescein's emission is observed up to 200mM K^+ .

5.3 Results & discussion

In Figure 5.1, a schematic of the duplex modified Tel22 telomere sequence folded into the Hybrid-1 and Hybrid-2 telomere structure when appended to a AuNP is shown. Studies in Chapter 4 elucidated optimal NSET beacon conditions for tracking quadruplex folding when utilizing DL680 as the donor fluorophore. More specifically, larger particles, based upon the d_0 values for DL680-9nm AuNP and DL680-10nm AuNP, are ideal for tracking expected changes in distance between 50-90 Å. Unexpectedly, initial appendages of the Tel22 beacon sequence onto 9nm and 10nm AuNPs results in little to no DL680 emission intensity, contrary to appendage of similar Tel26 and wtTel26 NSET beacons. Gel electrophoresis confirms the modification of the AuNP surface upon Tel22 appendage (Figure 5.6), and emission intensity of DL680 is recovered when reduced dithiol small molecules (dihydrolipoic acid) are added to the NSET beacon solution. This suggests that appendage of the Tel22 beacon sequence is successful but that the DL680 emission intensity is quenched, until release of the telomere sequence is triggered by the dithiol replacement of the DNA-terminated monothiol at the AuNP surface. Moreover, this confirms the lack of DL680 intensity is not arising from a lack of DNA appendage, but rather a full quenching of DL680 when appended by adsorption to the AuNP surface.

While literature precedent suggests the susceptibility of DNA single strands to adsorb to AuNP surfaces, and that G-quadruplexes are also susceptible to surface adsorption, the flanked telomere sequences reported in Chapter 4 (Tel26 and wtTel26) are not observed to adhere to

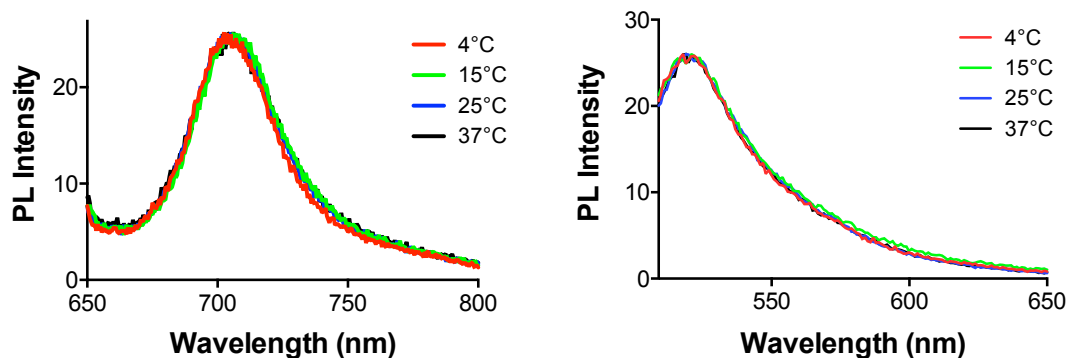


Figure 5.4: To ensure changes in Tel22 quenching arise from dynamic Hybrid-2/Hybrid-1 ratios, the temperature dependence in DL680 (left) and fluorescein (right) is shown. The photoluminescence of a Tel22 NSET beacon sample was divided into four 50 μ L aliquots, each taken to a different temperature, 4°C, 15°C, 25°C, and 37°C. It is clear the DL680 emission intensity is unchanged by the temperature range explored in this study.

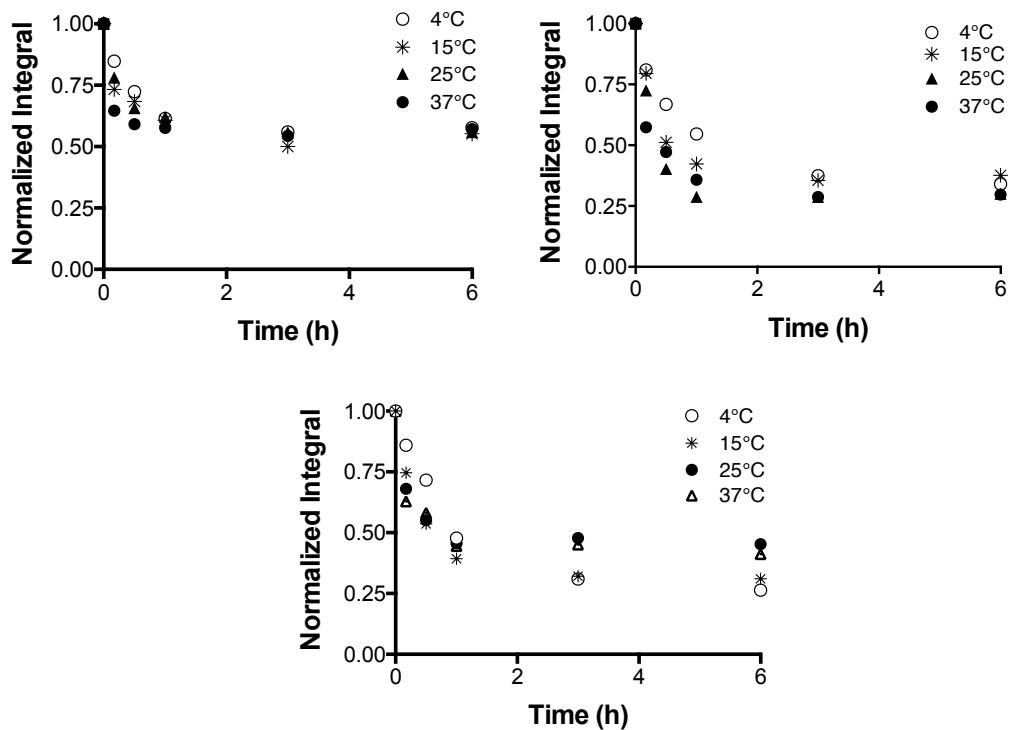


Figure 5.5: Time dependent quenching of Tel26, wtTel26, and Tel22, demonstrating an equilibrium is reached in each sequence within 2 hours of the K^+ addition.

AuNP surfaces up to 10nm in diameter [260,280,281]. The clear difference in the adsorption behavior of Tel22 versus the flanked sequences must arise from the susceptibility of Tel22 to unfold relative to the flanked sequences. Earlier groups have reported a precedent for AuNP surface adsorption in biosensors where certain G-quadruplexes are capable of withstanding attractive colombic surface forces and others succumb to AuNP surface adsorption, deeming those sequences unreliable for AuNP-based biosensors [280].

One would assume the propensity for one quadruplex sequence to adsorb to the AuNP surface while the other withstands adsorption stems from stability of the G-quadruplex in question. Computational analysis via hydrodynamic bead modeling from the Trent and Chaires groups indicate the stability of flanked sequences, Tel26 and wtTel26 ($\Delta G_{\text{Tel26}} = -5094.00$ kcal/mol, $\Delta G_{\text{wtTel26}} = -4933.18$ kcal/mol), is significantly greater than Tel22 ($\Delta G_{\text{Tel22}} = -4360.05$ kcal/mol) [101]. This confirms the notion that the native G-quadruplex sequence, Tel22, is more

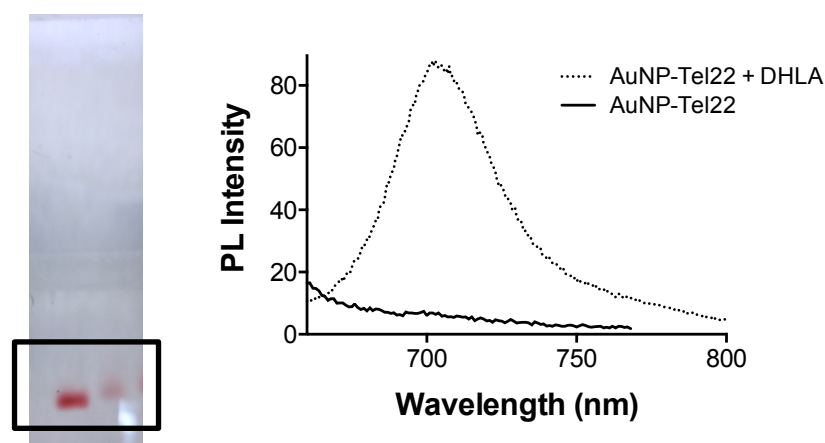


Figure 5.6: (Left) Gel electrophoresis of 10nm BSPP-coated AuNP (left lane) and 10nm AuNPs after Tel22 sequence appendage (right lane). (Right) PL monitoring DL680 emission intensity before (solid line) and after (dotted line) addition of excess reduced dihydrolipoic acid (DHLA).

likely to undergo AuNP surface adsorption via G-quadruplex unfolding as observed in this chapter. As it is reported that smaller metal nanoparticles (5nm) are less likely to induce DNA adsorption than larger particles, presumable due to surface curvature and surface area arguments, continuing temperature-dependent Tel22 NSET beacon studies were performed on 5nm AuNPs to resist adsorptive effects [228,233]. Because 5nm AuNP-quenching of DL680 is the least effective size regime explored in Chapter 4, additional studies with 3nm AuNPs and fluorescein-labeled Tel22 DNA are introduced here, as the R_0 of fluorescein for 3nm AuNPs is 110 Å, which

should result in a higher degree of fluorophore quenching upon quadruplex folding than with DL680.

The Tel22 sequence illustrates the predicted contact distances for a T14 fluoro-label to the surface of the AuNP based upon NMR predictions [105,165,166]. The validity of the predicted contact distances of Hybrid-1 and Hybrid-2 is verified in Chapter 4 using flanked Tel26 and wtTel26 [260]. From studies outlined in Chapter 4, it is clear that the two unique conformers can be optically identified by molecular ruler methods by monitoring the T14 to AuNP contact distances. Hybrid-1 ($r = 81 \text{ \AA}$) versus Hybrid-2 ($r = 62 \text{ \AA}$) folding will result in a measurable change in the separation distance for the T14 fluoro-label from the AuNP surface, and thus in the observed efficiency ($E_{\text{Hybrid-1}} = 86\%$, $E_{\text{Hybrid-2}} = 61\%$) for NSET induced PL

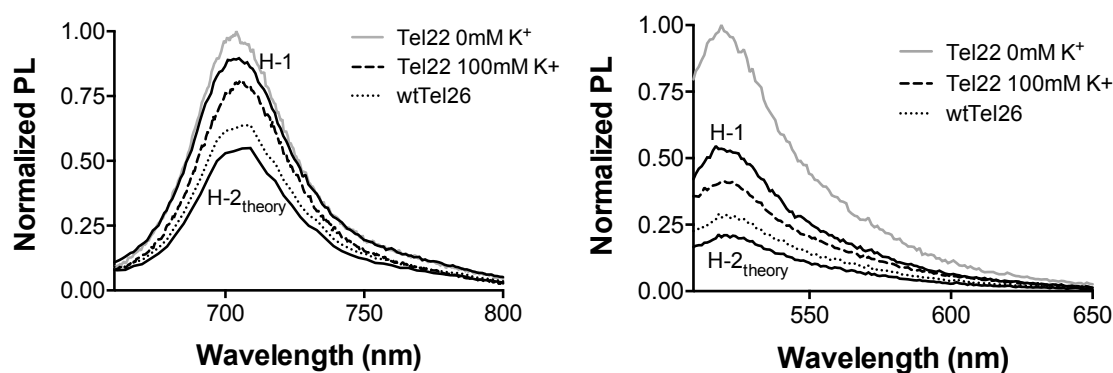


Figure 5.7: PL of T14 DL680 (left) and T14 fluorescein (right) emission intensities at 25°C for the Tel26 beacon (“H-1” solid line), the wtTel26 beacon (dotted line), the saturated (100mM K^+) Tel22 beacon (dashed line) and the pre-salt (0mM K^+) Tel22 beacon gray line. The “H-2_{theory}” solid line represents the theoretical 100% Hybrid-2 conformation, extracted from the wtTel26 data which is known to form 75% Hybrid-2 and 25% Hybrid-1.

quenching of DL680. An equilibrium population, as suggested in early NMR studies, will be reflected in an efficiency value that lies in between the two predicted conformers, and will be temperature dependent assuming an activation energy for conversion between the two conformers.

In Figure 5.7, the normalized photoluminescence for the T14 fluoro-labeled Tel22, Tel26, and wtTel26 for DL680 on 5nm AuNPs ($\lambda_{\text{ex}} = 620\text{nm}$, 298K, pH=5.8, <1mM NaCl) and for fluorescein on 3nm AuNPs ($\lambda_{\text{ex}} = 488\text{nm}$, 298K, pH=8.0, <1mM NaCl) are shown at 100mM K^+ (the G-quadruplex folded state) for the NSET rulers measured at a beacon concentration of 10nM. For the PL studies, the choice of NSET beacon concentration is chosen to minimize the

inner-filter effect associated with the strong optical cross-section for an AuNP [254,265]. As changes in position for T8 are less significant, the T14 PL data is utilized in the evaluation of a Hybrid-1/Hybrid-2 equilibrium. As expected, Tel22 T14 exhibits intermediate quenching relative to Tel26 T14 and wtTel26 T14, consistent with the earlier supposition that Tel22 is an equilibrium between Hybrid-1 and Hybrid-2 folded structures. In both the DL680 and fluorescein emission spectra in Figure 5.7, a theoretical peak for 100% Hybrid-2 is shown, as wtTel26 is presumed to have a maximum Hybrid-2 contribution of 75% [244]. Extraction of the Hybrid-2 contribution from the emission spectra is described in Chapter 4 with equation 4.3.

The experimental NSET data obtained for Tel22, Tel26 and wtTel26 can be interpreted in terms of a folded structure by applying the NSET theorem. By application of the NSET equations (eqn. 4.1-4.2) to the quenching data in Figure 5.5, the observed PL data at 100 mM K^+

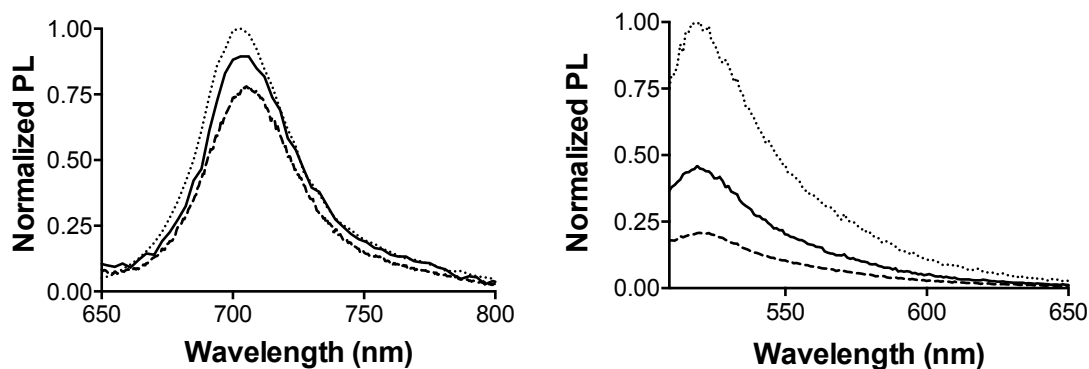


Figure 5.8: Tel22 T14 DL680 (left) and T14 fluorescein (right) emission intensity at 0mM K^+ (solid line) and at 100mM K^+ (dashed line). The dotted line is indicative of the emission intensity without appending the Tel22 sequence to an AuNP.

ion (25°C) for T14 labelled Tel22 sequence exhibits an emission value of $E_{DL680} = 78 \pm 6\%$ and $E_{fluor} = 23 \pm 6\%$ corresponds to a contact distance of $74 \pm 7 \text{ \AA}$ (DL680) and $78 \pm 8 \text{ \AA}$ (fluorescein). At 0mM K^+ (shown in Figure 5.8), converting the PL data for Tel 22 to a contact distance yields a value of $95 \pm 16 \text{ \AA}$ nm which is consistent with a fully extended sequence (just as the 0 mM K^+ PL data for Tel 26 and wtTel26 in Chapter 4 confirms). The predicted contact distance for the folded Tel22 state (100mM K^+) does not correlate to any reported theoretical distances for a single folded telomere conformer.

The inability to definitively assign Hybrid-1 or Hybrid-2 contact distances for the T14 dye label to the surface of the AuNP for Tel22 may arise from either the presence of an alternative structure (neither Hybrid-1 or -2) or more likely a population equilibrium between Hybrid-1 and Hybrid-2 structures for Tel22. Other groups have reported in Tel22 a parallel “propeller” conformation, however it was observed that appendage of additional basepairs to either the 5’ or 3’ end of the telomere eliminates the potential for the formation of the parallel structure [143]. Similarly, earlier reports of high concentrations of intermediate or unfolded states do not apply to these studies, as the observations of additional conformer states occur at short time scales (< 2 hours) and significantly lower salt concentration (35mM K⁺)

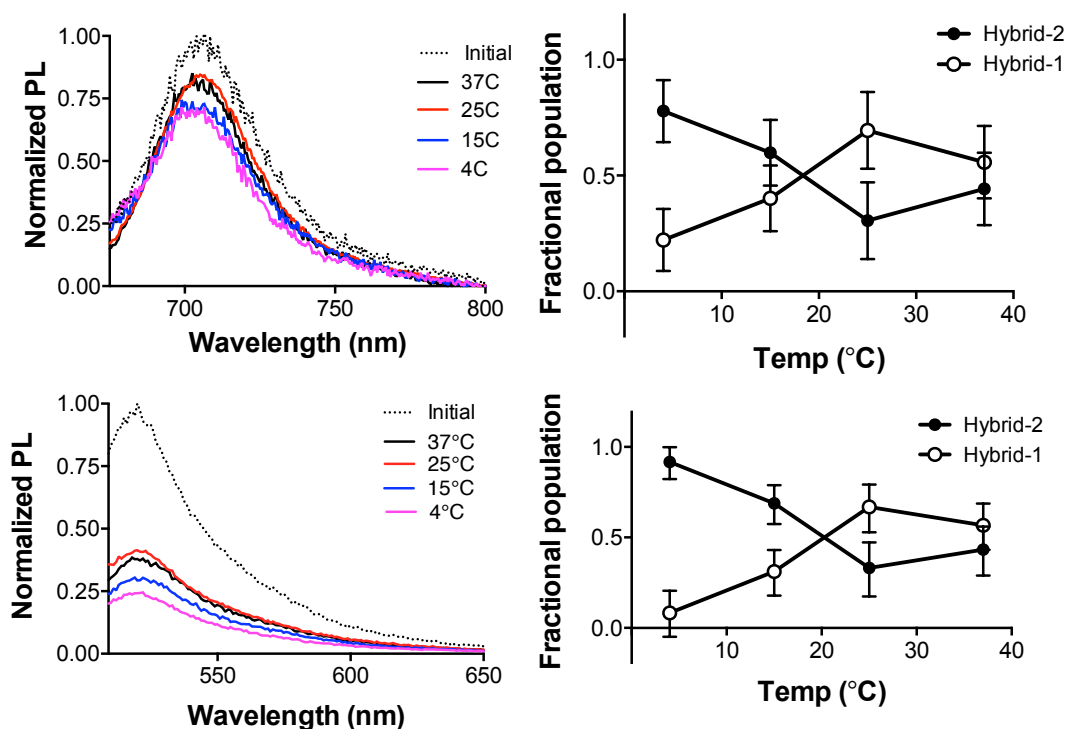


Figure 5.9: (Top left) Temperature-dependent PL measurements for the DL680 Tel22 beacon at 4°C (purple), 15°C (blue), 25°C (red), and 37°C (black). (Top right) The calculated fractional population of Hybrid-1 and Hybrid-2 as a function of temperature, extracted from NSET model calculations. (Bottom left) Temperature-dependent PL measurements for the fluorescein Tel22 beacon at 4°C (purple), 15°C (blue), 25°C (red), and 37°C (black). (Bottom right) The calculated fractional population of Hybrid-1 and Hybrid-2 as a function of temperature. The dotted line in both PL spectra represents the initial (0mM K⁺) state normalized to 1.

[275,282,283]. Therefore, it is reasonable to assume that the 5'-duplex modified Tel22 sequence used in this study will only form the Hybrid-1 or Hybrid-2 structures. The poor correlation with a known single population structure for Tel22 likely reflects the presence of an equilibrium population between the hybrid structures at room temperature. The presence of an equilibrium between Hybrid-1 and Hybrid-2 has been postulated previously from NMR data and reported for similar sequences (i.e. Tel24), although the equilibrium ratio specific for Tel22 has not been reported [141,165,244,275].

From the optical data, the ratio of Hybrid-2 to Hybrid-1 can be estimated by assuming no significant population of an intermediate unfolded species exists for the Tel22 structure. It should be noted that we are aware of reported intermediate steps between various folded quadruplex structures; however, we assume that their populations will be negligible after 6 hours at high salt concentration as demonstrated previously with NMR [100,101,166,175,275]. Assuming the two-state model, the observed PL intensity can be written as the combination of the independent structures, such that $I_{\text{Tel22}} = I_{\text{Tel26}}(1-x) + I_{\text{wtTel26}}(x)$, where I_{Tel22} , I_{Tel26} , and I_{wtTel26} represent the integrated PL intensities of T14-DY680 or T14-fluorescein on Tel22, and x represents the fractional population of Hybrid-2, attained by solving for the Hybrid-2 contribution in equation 4.3. Solving the expression yields a population equilibrium in Tel22_{DL680} of $31 \pm 16\%$ Hybrid-2 to $69 \pm 16\%$ Hybrid-1 and Tel22_{fluore} of $33 \pm 12\%$ Hybrid-2 to $67 \pm 12\%$ Hybrid-1 at 25°C. The equilibrium constant for the two conformers at 37°C is ~ 1.3 .

In Figure 5.9, the equilibrium population as a function of temperature is extracted and plotted for Hybrid-1 and Hybrid-2. The temperature dependent behavior for Tel26 and wtTel26 NSET beacons is shown in Figure 5.10 and verifies that these single-population flanked sequences exhibit the same folding behaviors across the temperature range used in this study. The temperature dependent change in the population percentage for the two hybrid structures is revealing. The signal at 4°C favors the Hybrid-2 folded structure implying Hybrid-2 is thermodynamically favored at low temperature. The temperature evolution of the population exhibits an asymptote in the population above 20°C indicative of a dynamic equilibrium for the two conformers, which has not been previously reported in Tel22. The appearance of a dynamic equilibrium between Hybrid-1 and Hybrid-2 allows the free energy parameters for Hybrid-1 to Hybrid-2 inter-conversion to be estimated, since $\Delta G = -RT\ln(K_{\text{eq}})$. The experimentally measured ΔG for interconversion at 37°C is -0.16 kcal/mol. The small activation energy is

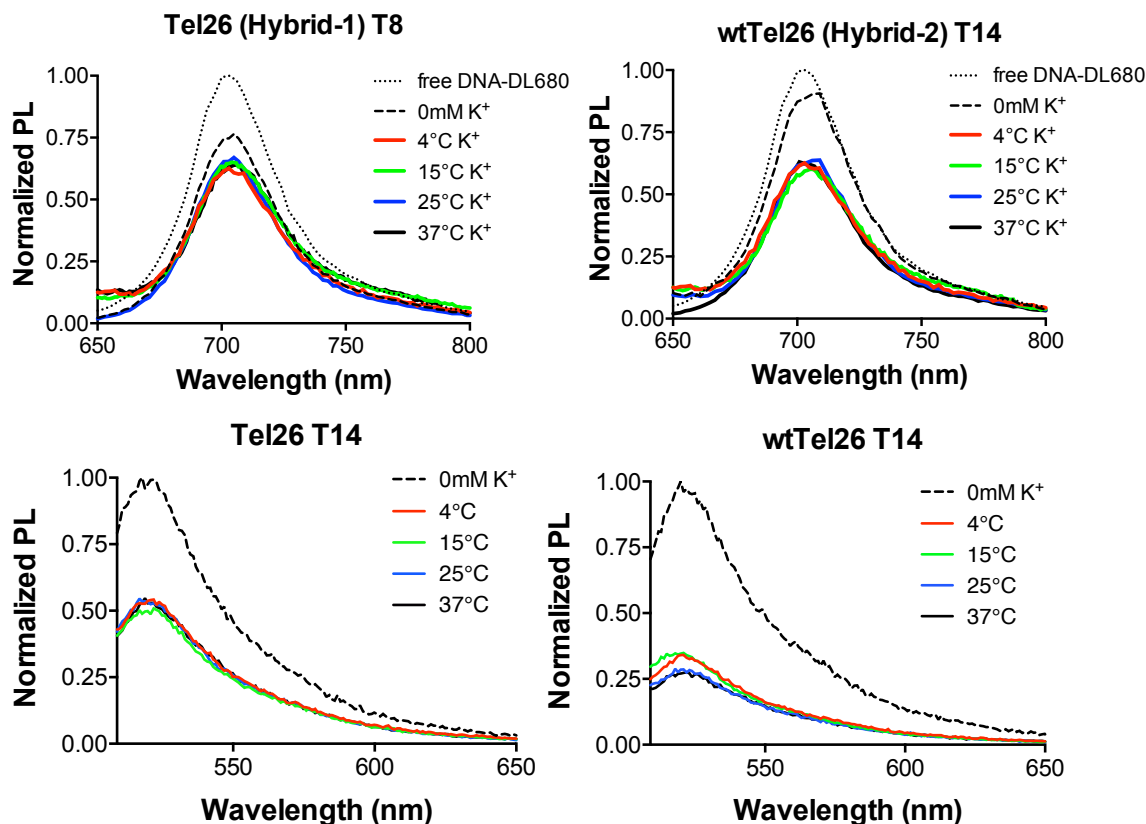


Figure 5.10: The observation of each flanked telomere sequence, Tel26 and wtTel26, to fold under the temperature range studied is essential to ensuring the observed quenching of Tel22 is due to a Hybrid-1/Hybrid-2 mixture, rather than an alternate temperature-dependent structure. (Top left) The DL680-T8 emission of Tel26 and (Top right) the DL680-T14 emission of wtTel26 are similarly quenched at all temperatures (4°C, 15°C, 25°C, and 35°C) at 100mM K^+ . (Bottom left) The fluorescein-T14 Tel26 emission and (Bottom right) the fluorescein-T14 wtTel26 emission are also similarly quenched at the temperature range studied. This is indicative of native folding behavior across the temperature range explored in this Tel22 study. For simplicity, the free-DNA fluorescein emission peak is not shown in the fluorescein-T14 (bottom) samples.

consistent with predictions of a low energy barrier for interconversion, as multiple conformers are observed in solution via NMR [165,244]. At 4°C, ΔG approaches -1.34 kcal/mol.

5.4 Conclusion

To our knowledge, this marks the first study in which Hybrid-1 and Hybrid-2 relative populations in Tel22 have been reported. Temperature dependent population measurements

reveal Hybrid-2 is thermodynamically favored and the ΔG for inter-conversion at 37°C is small. The ability to measure the population using low concentration telomere sequences via NSET methods is important, as it is known that protein binding can affect the thermodynamic energy of the folded structure and quadruplex-binding proteins often interact selectively with one structure. As such the low energy inter-conversion of Hybrid-1 and Hybrid-2 telomere structures may be an important regulator in biological activity and warrants further exploration. Specifically, telomere-denaturing proteins TPP, Pot1, and UP1 operate in a directionally relevant fashion, suggesting the directionality of the hybrid quadruplex contributes to the protein's biological mechanism [122-125]. Further studies are required to further support this postulate.

CHAPTER 6

COOPERATIVE BEHAVIOR IN ILPR QUADRUPLEXES

6.1 Introduction

The insulin-linked polymorphic region (ILPR) is a region of 14-basepair repeats (5'-ACAGGGGTGTGGGG-3') capable of folding into G-quadruplex structures and contains few single point mutations per ILPR region [121,151,284-286]. The healthy, wild-type ILPR allele (allele III) consists of 1900-2800 basepairs on average, whereas the common mutated, shortened form, allele I, is comprised of only 350-900 basepairs. Shortened alleles of the ILPR result in a 40% increased risk of late-onset Type I Diabetes (T1D) [152-157,287-292]. As T1D is an autoimmune disease, the malfunctions stemming from the large-scale ILPR deletion are localized within the thymus and not insulin-producing β -cells [155,157,158,291-294]. This is often overlooked within the biophysical community, as many of the ILPR G-quadruplex-protein studies under investigation by biophysicists include G-quadruplex-insulin interactions or studies with pancreatic cell extracts, which are not relevant to T1D [159,297,298]. The exact role of the genetic ILPR deletion in T1D development is unclear, though the ILPR is located only 365 basepairs upstream from the promoter and is known to be the regulator of the insulin gene (INS) transcription. Thymal cells in fetuses predisposed for late-onset T1D display low INS transcript levels (Figure 1.9) [152,153,155,239,289,293-296].

Corresponding with the significant drop in the number of basepairs from allele III to allele I is a simultaneous drop in the number of putative G-quadruplex sequences in the ILPR (~100 possible quadruplex formations in allele III down to ~32 possible formations in allele I) [122,153,162,248,294,295]. Though the exact role of the ILPR deletion in T1D development is unknown, two factors have demonstrated clear participation in low INS transcription levels: the presence of an allele I ILPR and low concentrations of autoimmune regulator protein (AIRE) [152,153,155,239,289,293-296]. Conveniently, AIRE is known to bind to ILPR G-quadruplexes, and thus, it is speculated that INS transcription is related to the degree of G-quadruplex formation in the ILPR and subsequent AIRE-quadruplex binding events [155,294].

Biophysical groups have focused on individual quadruplexes to elucidate 1) structures of folded ILPR quadruplexes, and 2) AIRE-quadruplex binding models [121,129,151,155,159,160,

239,284,285,299]. While information at the molecular level is important to the larger picture of deciphering the mechanism of ILPR's INS regulatory capabilities, the vast number of putative G-quadruplexes in the ILPR indicates that significant information lies in interactions between multiple quadruplexes as well. For instance, although single point mutations in individual ILPR quadruplex sequences demonstrate G-quadruplex structure inhibition, the low occurrence of this type of mutation found in the ILPR would result in a negligible number of G-quadruplexes lost, maintaining near normal INS transcription [121,151,285,286]. Thus, it is important to combine the views of biophysicists who investigate individual quadruplexes and the views of biologists who investigate the entire insulin genome by studying multiple quadruplex interactions to determine their contribution to the problem at hand.

In this chapter, the influence of sequential positioning of multiple quadruplexes on the individual quadruplex's ability to fold is studied using an NSET probe. The salt-induced folding of one and two ILPR quadruplexes is monitored by an NSET method using 5nm or 10nm AuNP quenchers attached to ILPR sequences with terminally-labeled fluorescein donor molecules (Figure 6.1). The ILPR NSET beacons are designed to decrease in emission intensity upon quadruplex folding, as G-quadruplexes would position the fluorescein dye closer to the AuNP relative to the unfolded, worm-like single-stranded DNA state.

Utilizing the saturation binding models and cooperativity models, the relationship between quadruplexes in the two-quadruplex system are explored by comparison to similar biophysical constants in the one-quadruplex system. Positive cooperativity between multiple quadruplexes is indicative of a potential force contributing to the regulation of the INS gene, as

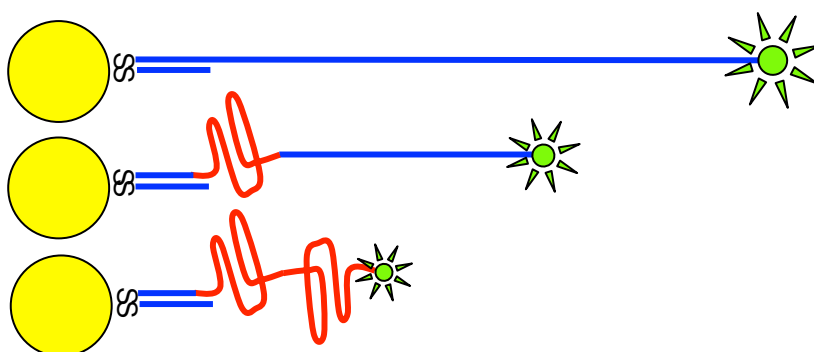


Figure 6.1: Scheme of the variable length (and variable quadruplex number) ILPR NSET beacons used in this chapter. The one, two, and non-quadruplex systems are named for the respective number of putative quadruplexes that can form from the ILPR 14mer repeats comprising the beacons' sequences.

Table 6.1: Table of the non-, one-, and two-quadruplex sequences, the universal 12mer linker, and the one- and two-quadruplex block sequences utilized in this chapter. ILPR G-quadruplex sequences are underlined in the one- and two-quadruplex sequences. The terminal 5' C₆ thiol and terminal 3' fluorescein modifications are shown in each sequence.

Non-Quad	5'-(C ₆ S-S) CAAAACAACAATGTATACTGAATTCGGTGTACTCTTGCCAACCTCGTG TATACTGAATTCACAGGT (fluorescein) -3'
One-Quad	5'-(C ₆ S-S) CAAAACAACAA <u>TGTGGGGACAGGGGTGTGGGGATAGGGGTGTCCTC</u> <u>GTGTATACTGAATTCACAGGT</u> (fluorescein) -3'
Two-Quad	5'-(C ₆ S-S) CAAAACAACAAT <u>TGTGGGGACAGGGGTGTGGGGATAGGGGTGTGGGG</u> <u>ACAGGGGTGTGGGGACAGGGGT</u> (fluorescein) -3'
linker	5'- TTGTTGTTTTTG (C ₆ S-S) -3'
block	5'- CCCCTATCCCATACCCCTGTCCCACATTGTTGTTTTTG (C ₆ S-S) -3'

preformation of the quadruplex may need to exist prior to AIRE binding [120,162,294]. In that instance, positive cooperativity of quadruplex formation is favorable towards AIRE binding, which in turn contributes to the promotion of INS transcription. The remainder of this chapter is divided into an Experimental section (6.2), Results & discussion (6.3), and Conclusion (6.4).

6.2 Experimental section

6.2.1 ILPR one-, two-, and non-quadruplex NSET beacon construction

The 69mer DNA sequences used in this chapter contain various degrees of potential G-quadruplex folding (one or two quadruplexes), as well as a control sequence that lacks guanine runs and subsequently lacks the capability to form a G-quadruplex structure. Additionally, complement sequences designed to inhibit quadruplex formation when annealed to the one and two quadruplex-forming sequences are employed. All sequences employed in the one- and two-quadruplex studies in this chapter are listed in Table 6.1.

The one-, two-, and non-quadruplex forming sequences are equipped with a 5' C₆-thiol modification and a 3' terminal fluorescein modification. The “block” sequence, designed to prevent quadruplex formation in the one-quadruplex sequence and prevent the 5' quadruplex from forming in the two-quadruplex sequence, contains a 3' C₆-thiol modification. The linker sequence, a 12mer complementary to the 5' end of the one-, two-, and non-quadruplex forming sequences, also contains a 3' C₆-thiol modification similar to the “block” sequence and is

utilized in experiments where monitoring the full quadruplex-forming capabilities is desired (i.e. when the “block” sequence is not used).

DNA annealing between the linker sequence and quadruplex sequences or between the “block” sequence and quadruplex sequences is accomplished by heating at 95°C for 4 minutes then snap cooling to 4°C in phosphate buffer (20mM phosphate, 50mM NaCl, pH = 7.5). To append to the AuNPs via ligand exchange of the two DNA 3' C₆-thiols, 25µL of 100mg/mL TCEP-HCl is added to 250 pmoles annealed DNA (~400µL volume). A total of 15pmol 5nm AuNP or 5pmol 10nm AuNP is added to the reaction and the reaction mixture is placed on the rotisserie in the dark overnight. Purification of free DNA and simultaneous desalting of the reaction is achieved by several rounds of saltless EtOH precipitations. Samples are stored in the dark to avoid photobleaching of the fluorescein dye and at 4°C until use.

6.2.2 Absorption and photoluminescence experiments

The PL measurements on the purified ILPR NSET beacons were measure in a sealed, 0.3cm quartz cuvette on a Varian Eclipse fluorimeter ($\lambda_{\text{ex}} = 465 \text{ nm}$) in a 20mM Hepes buffer brought to a pH of 8 with CsOH. It is necessary to work in slightly basic conditions to maximize the intensity of the fluorescein emission and, as Cs⁺ ions are too large to induce quadruplex folding, CsOH is an ideal candidate for buffer pH stabilization in this study [300,301].

Freshly purified ILPR samples were diluted and divided into equivalent samples at 2nM in concentration. Each sample was brought to a final desired [K⁺] using a 2µL aliquot of variable KCl concentrations. [K⁺] additions varied extremely from 10µM to 3M in these experiments depending the quadruplex sample under investigation. As shown in the Results & discussion (6.3), one-quadruplex and two-quadruplex sequences varied in saturation concentration and [K⁺] aliquots were adjusted to accommodate this variance. The PL following KCl addition is recorded 2h following of the salt to the sample. It is worth noting that maximum intensity change is observed within 30 minutes, but PL values are reported at 6 hours following addition of the last aliquot of K⁺ ion to ensure a fully quadruplex-folded population. Fluorescein intensity as a function of KCl concentration was monitored to ensure that changes in PL intensity arise from quadruplex conformer changes rather than adjustments in salt concentration. No change in fluorescein emission intensity is observed up to 200mM KCl.

6.2.3 Fluorescein-AuNP NSET distance calculations

As in Chapters 4 and 5, the separation distance of the fluorescein molecule to the AuNP surface used in the NSET analysis is calculated using a Clegg model for the 12 basepair duplex and the calculated single-stranded DNA persistence length at exceptionally low salt conditions for the extended 57mer. The Clegg model, originally monitored by FRET, accounts for the helical nature of DNA when measuring the separation distance of two labels appended via short alkyl linker molecules [262]. Previous uses of FRET to monitor DNA persistence lengths have proven to be effective in short single-stranded DNA sequences (< 40 bp) but the low R_0 values in FRET have limited this technique in longer single-stranded sequences [267,268]. Studies using AFM analysis under variable Na^+ conditions report maximum straightened gene-length DNA regions to be 91 Å at 0 mM NaCl, though the gene samples lie on a substrate prior to AFM imaging which is potentially non-native to DNA persistence length in salt-less solution conditions [302]. Therefore, the initial, salt-less distance value for the ILPR NSET beacons were calculated by a CN^- etch described similarly in Chapter 5 (Figure 5.3). The change in fluorescein intensity of the ILPR NSET beacons after concentrated CN^- additions is representative of the effective quenching (Q_{eff}) and correlated fluorescein-AuNP surface distance when appended to the AuNP surface. It should be noted that the addition of NaCN drastically increases the pH of

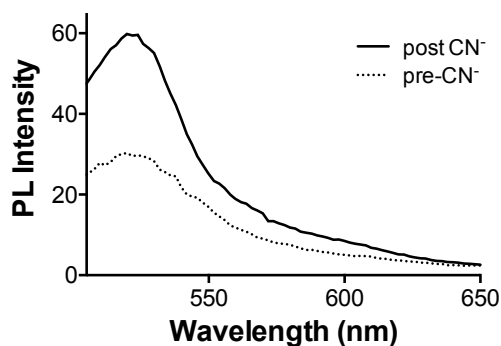


Figure 6.2: CN^- etch of the 5nm one-quadruplex ILPR NSET beacon. The relative change in intensity represents the degree of quenching in the initial, pre- K^+ state of the NSET beacons, where $Q_{\text{eff}} = 0.41$. Averaging of all three 5nm NSET beacons (one-, two-, and non-quadruplex) and conversion to a distance utilizing the NSET theorem results in an initial AuNP-fluorescein distance of 145 ± 19 Å prior to G-quadruplex folding. Identical distances were extracted in CN^- analysis of the 10nm ILPR NSET beacons.

the NSET beacon solution (even under buffered conditions) which results in an additional increase in fluorescein emission intensity due to fluorescein's sensitivity to pH [303,304]. Therefore, the final, CN⁻-etched fluorescein intensity is extracted from a control sample (*sans* CN⁻) comprised of identical concentrations, derived from UV-Vis monitoring of the NaCN etch study, of fluorescein and unappended AuNPs. An example of the change in intensity upon CN⁻ etching for the 5nm one-quadruplex ILPR NSET beacon is shown in Figure 6.2. The salt-less persistence length of the single-stranded DNA was calculated to $145 \pm 19 \text{ \AA}$ in the case of the 5nm and 10nm ILPR NSET beacon. Observation of the identical persistence lengths on the 5nm and 10nm AuNPs indicates a lack of influence by the AuNP on the single-stranded ILPR DNA system, also observed in Chapter 4 [266]. After asserting the initial extended value ($145 \pm 19 \text{ \AA}$), fluorescein intensity values at saturation are converted to distances using the NSET model where $d_0 = 136 \text{ \AA}$ for a fluorescein molecule on a 5nm AuNP, and $d_0 = 222 \text{ \AA}$ for a fluorescein molecule on a 10nm AuNP.

6.3 Results & discussion

G-quadruplex formation has been studied extensively on individual quadruplex models and quadruplex-quadruplex interactions in multi-quadruplex telomere chains have been examined via molecular tweezer studies [99,142]. The unwinding of up to six G-quadruplexes by molecular tweezer pulling forces demonstrates that, through statistical analysis of changing length scales per pulling event, quadruplex-quadruplex stabilizing interactions are present in long chain quadruplex biopolymers [121,162]. However, quantification of these inter-molecular stabilizing forces and observation of similar effects upon G-quadruplex folding (rather than forced unfolding) have not been reported.

Unique attachment elements, more specifically the use of two monothiol modifications, in the ILPR quadruplexes sequences were included in this study to enhance stability of the DNA at the AuNP surface even under low salt conditions [305,306]. It is observed that the ILPR quadruplexes in this chapter exhibit the highest propensity to undergo structural changes relative to the other nucleic acid sequences in this manuscript. Conditions to obtain the “extended” or “non-folded” must be exceptionally salt-free, and therefore an extra element of stability for DNA surface-appendage is incorporated. Previous groups have indicated significantly higher thermal

stability at the AuNP surface with a dual, monothiol system, than a dithiol or monothiol appendage [305,306].

In this chapter the salt-induced folding of multiple quadruplex sequences (non-quadruplex, one-quadruplex, and two-quadruplexes) as a function of $[K^+]$ concentration is evaluated to assess the cooperative effect of one quadruplex on the folding of a sequential quadruplex. The K_d value of the multi-quadruplex systems denote the propensity for a ILPR quadruplexes to form. Figure 6.3 and Figure 6.4 shows the raw fluorescein intensity data upon increasing potassium concentration for each of the 5nm and 10nm ILPR NSET beacons, respectively. Decreasing emission intensity for the ILPR quadruplexes is observed, as expected. The low-salt condition of the initial PL intensity relates to the extended DNA form whereas high salt concentration represents the fluorescein-quenched, G-quadruplex-folded, condensed structure.

Also shown in Figure 6.3 and Figure 6.4 are the normalized integrated fluorescein intensity peaks, fit to one-site binding models adjusted for a decreasing intensity system,

$$\frac{I}{I_0} = 1 - \left(\frac{B_{max}[K^+]}{K_d + [K^+]} \right) \quad \text{eqn. (6.1)}$$

where I is the fluorescein intensity, I_0 is the initial fluorescein intensity, B_{max} is the maximum binding at saturation, and K_d is the dissociation constant for the G-quadruplex folding event. Attempts to fit the sequences, even the multi-quadruplex ILPR sequences, to a two-site binding model, described similarly in Chapter 3 (eqn. 3.1), are unsuccessful in that ambiguous K_d values are extracted [260]. Similar observations of the inaccuracy of the two-site binding model are made in Chapter 3, where the non-hairpin, single-stranded ATP aptamer beacon is best fit to a one-site model reflecting the positively cooperative ATP relationship [260].

Even in the hairpin sequences described in Chapter 3 where a two-site binding curve is used to model ATP-induced saturation, positive cooperativity between ATP binding sites was observed via the cooperativity model ($h > 1$) [260]. Similarly in this chapter, the Hill coefficient is employed to assess the relationship between neighboring quadruplex folds. The two-quadruplex data from Figure 6.3 and Figure 6.4 was fit to a cooperativity model (eqn. 3.4) where it is observed that $h_{5nm} = 1.89$ and $h_{10nm} = 2.01$ for the 5nm and 10nm ILPR NSET beacons,

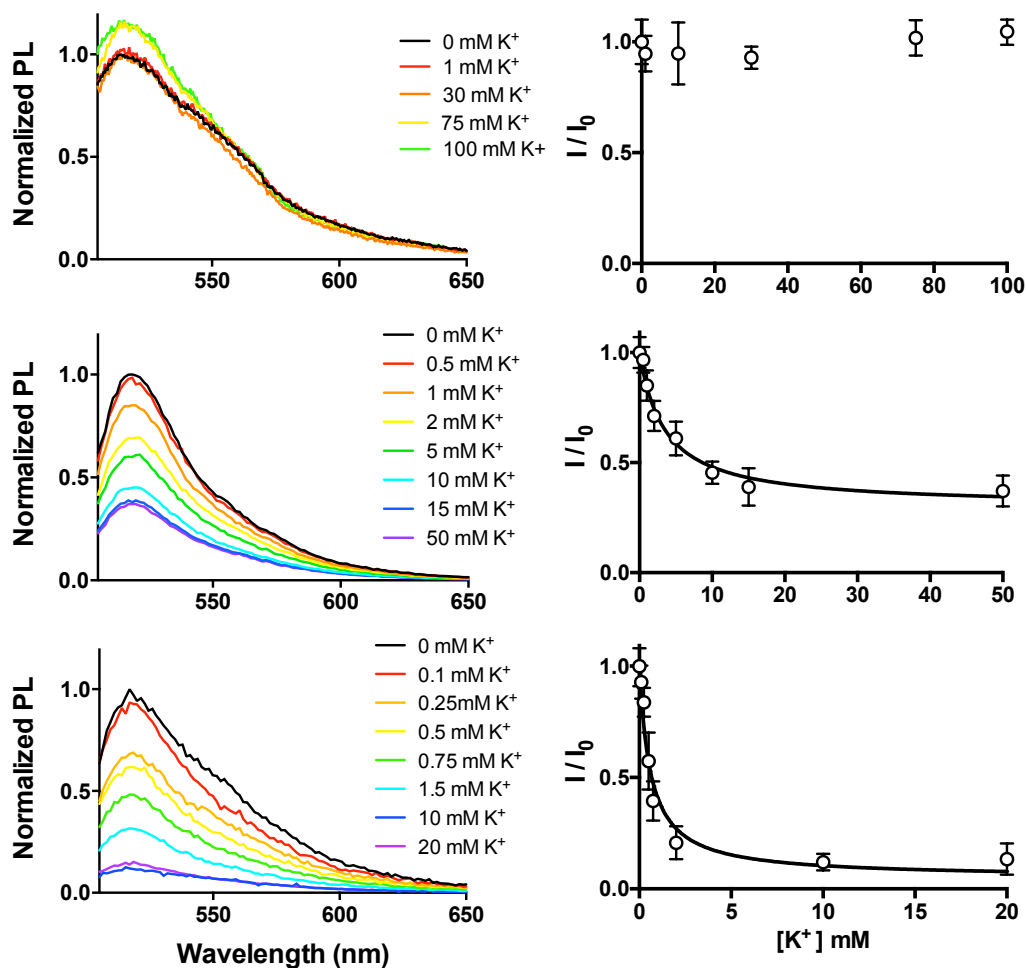


Figure 6.3: (Left column) Raw fluorescein PL data upon increase in [K⁺] of the 5nm NSET beacon non-, one-, and two-quadruplex strands (top to bottom). (Right column) Integration of the normalized fluorescein PL peaks with respect to [K⁺] concentration fit to a linear equation in the non-quadruplex system and eqn. 6.1 in the one- and two-quadruplex systems.

respectively. A Hill coefficient >1 correlates with a decreasing K_d and an increase in putative G-quadruplex content in the ILPR NSET beacon sequences, indicating increasing degrees of cooperativity as a sequential quadruplex sequence is added.

While the existence of cooperativity, described as “quadruplex-quadruplex interactions” by previous groups, has been noted before, this is the first report of a quantitative cooperative value, which conveniently corresponds to the number of quadruplexes under investigation in the sequence. The ability to first report positively cooperative values to multi-quadruplex sequences

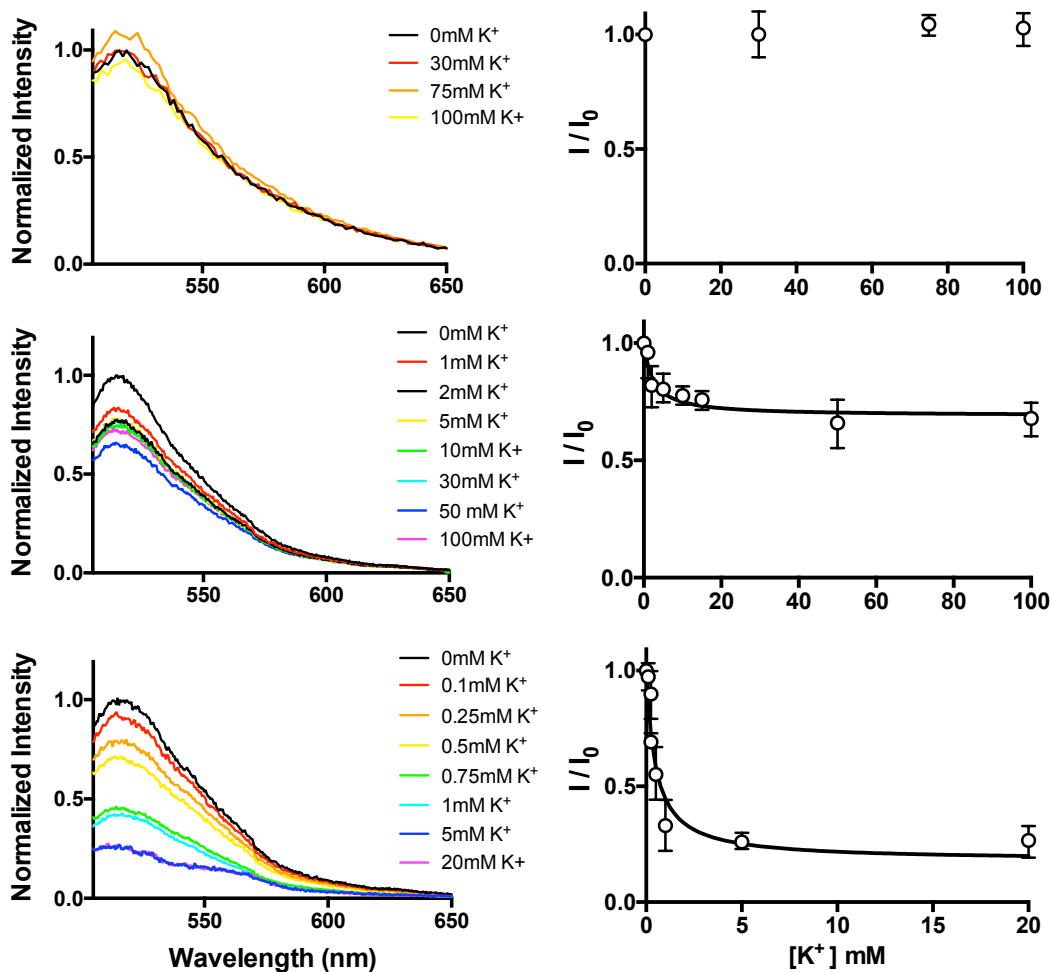


Figure 6.4: (Left column) Raw fluorescein PL data upon increase in $[K^+]$ of the 10nm NSET beacon one-, two-, and non-quadruplex strands (top to bottom). (Right column) Integration of the fluorescein PL peaks with respect to $[K^+]$ concentration fit to eqn. 6.1 in the one- and two-quadruplex system and fit to a linear equation in the non-quadruplex system.

in this chapter is attributed to the utilization of NSET, as earlier groups incorporate molecular tweezer techniques limited them to unwinding studies (rather than folding analysis) and FRET systems are unable to monitor the distances observed in these ILPR NSET beacon studies (90-150 Å).

The use of NSET also permits the extraction of distances upon K^+ saturation and G-quadruplex folding. The initial (0 mM K^+) donor-acceptor distance of the single-stranded DNA in all three, 69mer, ILPR systems studied in this chapter (one-, two-, and non-quadruplex) is 145

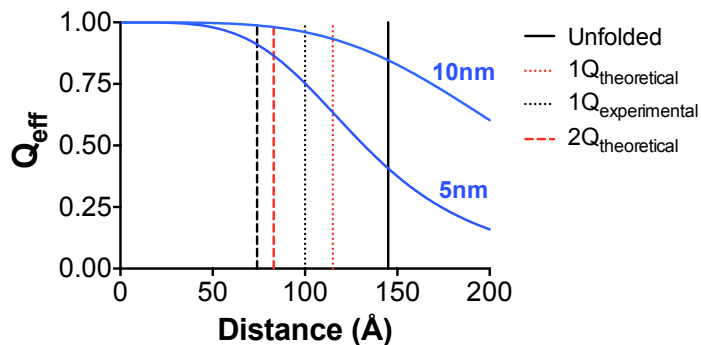


Figure 6.5: Quenching efficiency curve of 5nm and 10nm AuNPs with fluorescein (blue lines) which describes the fluorescein-AuNP separation distance relationship monitored in the ILPR quadruplex beacons. The d_0 values are 136 Å for the 5nm NSET beacon and 221 Å for the 10nm NSET beacon. The initial distance (calculated from the CN- etch experiments outlined in section 6.2 and Figure 6.2), $145 \pm 19\text{Å}$, is depicted as a black vertical solid line. Final saturated, G-quadruplex-folded distances extracted from the NSET theorem are shown as black dotted (one-quadruplex) and dashed (two-quadruplex) lines, at $100 \pm 9\text{Å}$ and $72 \pm 11\text{Å}$, respectively. Likewise the theoretical values are shown as red dotted (one-quadruplex) and dashed (two-quadruplex) lines, at 103Å and 70Å , respectively.

$\pm 19\text{Å}$. Distances in the folded quadruplex state in the one-, two-, and non-quadruplex sequence are extracted from the NSET model (for 5nm and 10nm AuNPs) from the fluorescein emission intensity at saturation (I) relative to the emission intensity at I_0 . In the 5nm NSET non-quadruplex beacon, the final non-quadruplex distance at saturation stems from an observed higher intensity upon K^+ addition (Figure 6.3) and is calculated to be $149 \pm 8\text{Å}$. No change in distance is observed at the highest $[K^+]$ for the 10nm NSET non-quadruplex beacon. In the one- and two-quadruplex ILPR systems where fluorescein emission intensities decrease upon increasing $[K^+]$, the distances extracted at saturation are $100 \pm 9\text{Å}$ and $72 \pm 11\text{Å}$, respectively, for the 5nm ILPR NSET beacon and $104 \pm 18\text{Å}$ and $80 \pm 22\text{Å}$, respectively, for the 10nm NSET beacon. Again, similar extracted values for the 5nm and 10nm AuNP system reflect no observed effect from the AuNPs on ILPR quadruplex folding [266]. Figure 6.5 displays the quenching efficiency curves (blue lines) of a fluorescein molecule appended to a 5nm AuNP ($d_0 = 136\text{Å}$) and 10nm AuNP ($d_0 = 222\text{Å}$). The black vertical line depicts the initial single-stranded DNA distance (145Å) prior to K^+ addition. The the experimental distances observed in the one- and two-quadruplex ILPR system extracted from the NSET model (eqn. 4.1) are represented by black

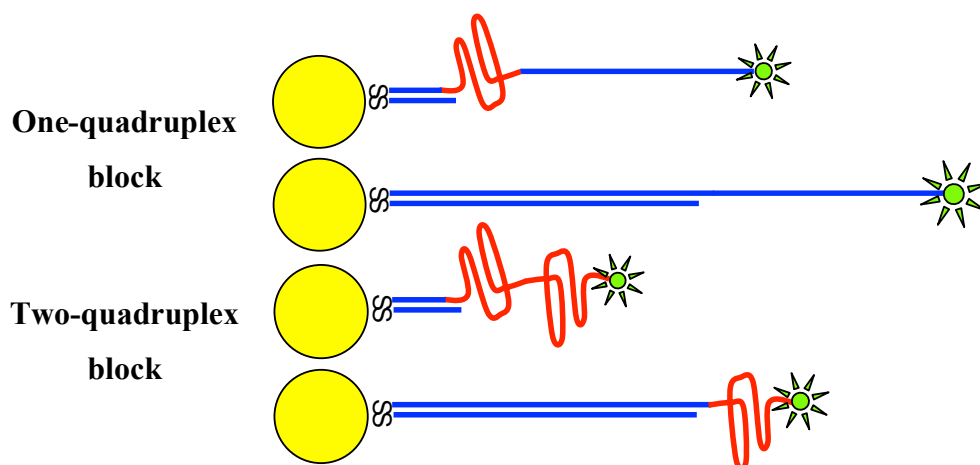


Figure 6.6: Scheme of the folded ILPR quadruplex behavior of the one- and two-quadruplex sequences with and without the pre-annealed 40mer “block” sequence.

dotted (one-quadruplex) and dashed (two-quadruplex) lines. Likewise, the red dotted (one-quadruplex) line at 103 Å and the dashed (two-quadruplex) line at 70 Å represent the theoretical distances in the ILPR beacons calculated using the Clegg model for the 12mer linker, C₆-thiol appendage to the AuNP, and a predicted folded-quadruplex length from similar solution NMR quadruplex structures [262]. In the case of the two-quadruplex system, a quadruplex end-to-end sequential folding model is assumed.

It should be noted that multiple quadruplexes could potentially form more complex intramolecular structures than an end-to-end formation and no crystal structure of this interaction has been reported. Thus, the experimental distance values of the folded two-quadruplex ILPR sequence extracted from Figure 6.4 are an ensemble representation of the most energetically favorable multi-quadruplex conformation, though that complex intramolecular conformation has yet to be fully mapped.

Chapter 4 describes the importance of selecting the appropriately-sized AuNP for optical NSET nanoruler measurements, as maximum changes in intensity per Ångstrom are observed at distances near the d_0 value [264]. An assessment of the observed distances, illustrated in Figure 6.6, in the ILPR NSET beacons indicates that the initial (prior to K⁺ additions) single-stranded DNA length, $145 \pm 19 \text{Å}$, is closer to the 5nm AuNP d_0 ($d_0 = 136 \text{Å}$) value than the 10nm AuNP observed in the 5nm ILPR NSET studies. The greater accuracy in the 5nm beacon is also apparent when comparing the error deviation for the 5nm and 10nm final saturation distances.

Therefore, the remaining studies in this chapter are performed solely with the 5nm AuNP as the quencher molecule, as it creates a system more apt for monitoring ILPR quadruplex folding.

To verify the enhancement in positive cooperativity stems from quadruplex-quadruplex interactions, inhibition of the one- and two-quadruplex ILPR systems in this chapter is accomplished by annealing to an 40mer “block” complement designed to prevent single quadruplex formation. The block sequence is listed in Table 6.1 and Figure 6.6 depicts the expected behavior of the block sequence on the one- and two-quadruplex system relative to the original (non-blocked) one- and two-quadruplex ILPR beacons. The $\Delta G = -81.6$ kcal/mol for Watson-Crick basepairing across the quadruplex and stability of the inhibitory complementary sequence is enhanced by a terminal 3' C₆-thiol modification designed to append to the AuNP surface upon reduction with the ILPR NSET sequences [307].

The raw PL and K_d binding curves of the one- and two-quadruplex block sequence of their quenching behavior with increasing potassium concentration are shown in Figure 6.8. The observed change in fluorescein PL of the one-quadruplex sequence when annealed to the “block” sequence resembles the non-quadruplex response to increasing salt concentration, as no significant change in intensity is observed (Figure 6.3 and Figure 6.7). Likewise, the two-quadruplex ILPR sequence, annealed to the “block” sequence, is similar in salt-dependent quenching behavior to the one-quadruplex (non-“block”) system in that $K_{d1Q} = 3.5$ mM and $K_{d2Qblock} = 4.7$ mM. Not surprisingly, with the “block” sequence preventing formation of the one-quadruplex system and preventing single-quadruplex formation of the two-quadruplex system, the newly quadruplex-inhibited ILPR sequences, perform identically to those with the same number of putative quadruplexes.

Utilizing the K_d of the unblocked, one-quadruplex sequence ($K_{d1Q} = 3.5$ mM) and the K_d of the blocked, two-quadruplex system ($K_{d2Qblock} = 3.1$ mM), a theoretical binding model for a two-quadruplex, two-site independent model (where $h = 1$) can be constructed (Figure 6.8). In this theoretical two-quadruplex system where quadruplex-folding is presumed to be independent of neighboring structures, the K_d of the unblocked one-quadruplex system is representative of the 5' quadruplex while the blocked, two-quadruplex K_d represents the 3' quadruplex, as described in eqn. 6.2 below,

$$\frac{I}{I_0} = 1 - \left[\left(\frac{[K^+]}{K_{d1Q} + [K^+]} \right) + \left(\frac{[K^+]}{K_{d2Qblock} + [K^+]} \right) \right] \quad \text{eqn 6.2.}$$

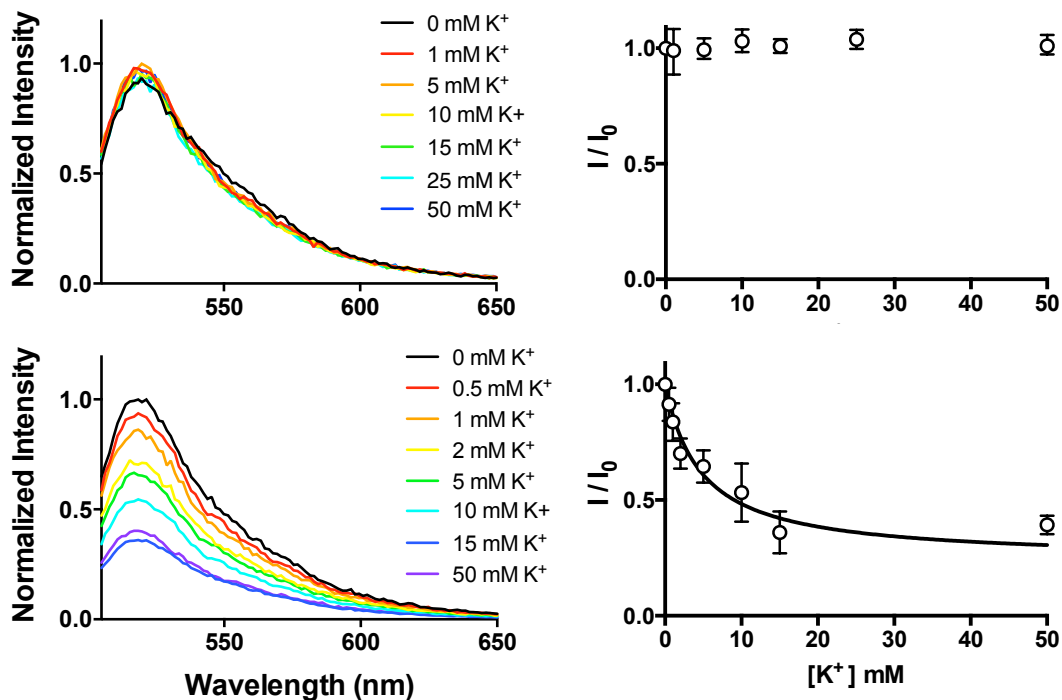


Figure 6.7: (Left column) Raw PL data of the one-quadruplex (top) and two-quadruplex block sequences with K⁺ additions. (Right column) Linear fit of the (top) one-quadruplex and K_d curve fit to eqn. 6.1 of the (bottom) two-quadruplex block sequence saturation extracted from the raw intensity data.

Figure 6.8 plots the theoretical uncoupled system (dotted line) using the individual quadruplex K_d values fit to eqn. 6.2, and the experimentally observed binding curve of the unblocked, two-quadruplex system (solid line) [260]. The x-axis of these plots are shown as the log of [K⁺] to better demonstrate the drastic difference in potassium ion saturations between the experimental and theoretical two-quadruplex systems. It is observed there is a decrease in K⁺ saturation as well as an inability to distinguish individual K_d values from the binding model in the two-quadruplex system, as it is best fit to a one-site model, indicating the two neighboring quadruplexes fold simultaneously rather than in distinct, individual motions. Therefore, the emergence of positively cooperative behavior in G-quadruplex formation is directly related to the inclusion of sequential, neighboring, putative quadruplexes in the ILPR sequences.

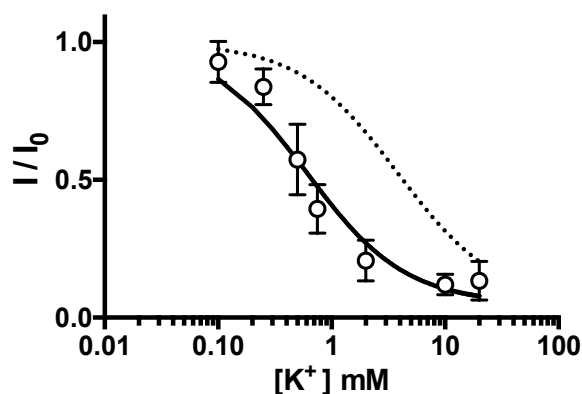


Figure 6.8: Plots of the theoretical two-quadruplex, two-site binding curve (dotted line) assuming a quadruplex-uncoupled system and the experimental two-quadruplex binding curve (solid line). The theoretical plot is fit to eqn. 6.2 where $K_{d1} = 3.5$ mM and $K_{d2block} = 4.7$ mM, and $B_{max(1)}$ and $B_{max(2)}$ are assumed to be 0.475 to match the maximum y-value in the experimental plot (0.95). The experimental plot is fit to a one-site binding model, eqn. 6.1, as the two-site model produces ambiguous values for K_{d1} and K_{d2} , commonly observed in highly positively cooperative systems [260].

6.4 Conclusion

The clear G-quadruplex formation stability under low-salt conditions in multi-quadruplex sequences confirms the suggestion by others that the quadruplex-folded ILPR state is most likely the resting conformation of the regulatory allele complex [129]. Nuclear conditions are reported to sustain high-salt conditions (250 mM K^+ , 10mM Na^+) which is far beyond the saturation limit of the lowest salt-induced quadruplex formation observed in this chapter [106-108]. Moreover, the incorporation of a long-strand complementary sequence to inhibit individual quadruplex formation demonstrates a method for potential ILPR manipulation. Using this blocked-quadruplex mechanism, it was observed that the positively cooperative behavior between quadruplexes in the two-quadruplex system is removed and the quadruplexes behave independently of each other.

If a decrease in quadruplex formation is responsible for the subsequent decrease in INS transcription, inhibition via complementary strand inhibition is a potential verification to the regulatory mechanism. Further studies are necessary to relate the degree of ILPR quadruplex folding to the complex, protein-binding regulatory mechanism of INS transcription [152,153,155,239,289,293-296].

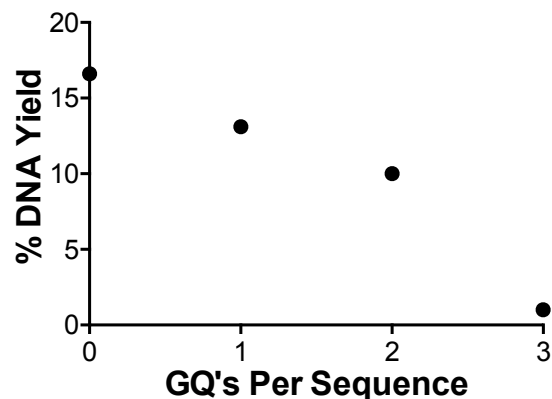


Figure 6.9: Graph of the synthetic disadvantage of G-quadruplex design plotted as a function of % yield (from a 200 nmole synthesis) vs. the number of putative quadruplexes incorporated into the sequence. It is worth noting that the terminal fluorescein and thiol modifications in the one-, two-, and non-quadruplex sequences are also detrimental to DNA yields when compared to unmodified DNA sequences of the same length (69mer). The three-quadruplex sequence contains more basepairs (111mer) to accommodate the inclusion of the third ILPR quadruplex sequence, which is also inhibitory to its synthesis.

Future studies increasing the number of quadruplex sequences in the ILPR beacons hinge upon overcoming obstacles to synthesizing quadruplex-dense DNA. Figure 6.9 denotes experiential evidence supporting the difficulty to synthesize putative G-quadruplex DNA by plotting the % yield of DNA synthesis versus inclusion of increasing putative G-quadruplex sequences. An obvious trend in synthetic inhibition with additional putative quadruplex sequences is observed. The three-quadruplex system, in particular, incurs a severe inability to attain high synthetic yields (1.0% yield) as noted in Figure 6.9. To counteract the overall synthetic limitations, the one-, two-, and non-quadruplex sequences were designed with high-yield modifications (3' thiols and terminal fluorescein modifications). Smaller, high yield DNA oligos containing the fluorescein and thiol modifications are the most promising route to a fully-constructed multi-quadruplex systems at sufficient yields to complete the appropriate biophysical studies.

CHAPTER 7

A MULTIFACETED OPTICAL ENERGY TRANSFER SYSTEM

7.1 Introduction

The biologically relevant conformations of biomolecules are classically constructed by measuring multiple local structural contacts. Methods such as NMR and X-ray crystallography easily achieve multiple length scales but require large quantities of materials, often negate the biologically native structure due to experimental conditions, and in the case of NMR, demand complex modeling to develop a map of the molecular structure in three dimensions [5,7,15,51, 61-65,180]. Optical methods offer a remedy to these downsides of X-ray crystallography and NMR, though at the loss of mapping entire biomolecules. However, in instances where determining the separation distance between biomolecular points is sufficient (such as the instance of telomere structure determination in Chapters 4 and 5), optical methods based upon energy transfer are potentially powerful tools measuring multiple length scales, and can even be used down to single molecule level [140,194,308,309].

The distance dependence of a donor molecule's optical emission and an acceptor molecule's absorption can be described by a variety of theoretical models, the most accurate and most prevalent in recent biophysical literature being NSET and FRET [191,193,198,176-178,201,254,272]. NSET and FRET differ in the absorptive properties of the acceptor (NSET employs metal nanoparticles while FRET utilizes organic fluorophores or other point dipole moieties) and subsequent coupling strength between donor and acceptor, resulting in individualities in measuring biopolymer distances [191,176-178].

Each has demonstrated successes in biophysical measurements. The capabilities of NSET to measure long-range biopolymer distances (up to 300Å) where FRET techniques fall short have been reported, as well as short-range FRET measurements reported to overcome NSET's resolution shortcomings [140,176-178,191,193,194,198,201,254,272,299,309]. Rarely are these optical techniques coupled to simultaneously monitor two different length scales, a capability that would be extremely advantageous in deciphering biological structures. For instance, FRET-resolvable distances would be those observed in protein binding pockets, where amino acid interactions across the protein chains occur [7,51,61,62,310,311]. On the other hand, large

structural changes in nucleic acid or protein conformations can occur at distances in the tens of nanometers, measurements of which would be far more attainable with metal nanoparticle-based NSET methods, as observed earlier in Chapter 6 [15,63,179]. Combining energy transfer systems with differing distal scales and deriving a useful theoretical model will improve experimental methods for researchers looking to explore more dynamic biological queries.

Other groups report the use of simultaneous NSET and FRET methods with large metal nanoparticles (>20nm) in an effort to 1) observe the near-field effects of the nanoparticle on the FRET process and 2) enhance the non-radiative FRET pathway thereby increasing the FRET R_0 value [196-198]. However, the extent of the observed enhancement effect is unpredictable by theory to date and has yet to be applied to biological molecules [196-198]. In this chapter, distance extraction measurements with a gold nanoparticle (AuNP)-based NSET system with FRET components on 10nm AuNPs are demonstrated. The smaller AuNPs (<20nm) ensure that near-field resonant enhancement effects are not impinging on the donor and acceptor dyes in the system. This system uniquely removes the radiative rate (k_r) manipulator (large AuNPs) from the system to leave the non-radiative (k_{nr}) decay pathway subject to the competitive NSET and FRET processes. Not only does a smaller AuNP result in a simpler, predictable model for deriving efficiency-based distances, but smaller AuNPs are also more advantageous for uses in biological systems, as the biopolymers under observation are less likely to interact with the AuNP surface [228,232,233,260].

In this study, measurements were obtained by tracking the radiative lifetime of a donor dye (5(6)-carboxy-X-rhodamine (ROX)) appended via basepair modifications on a double stranded DNA 60mer extending from the surface of the AuNP (Figure 7.1). The FRET acceptor

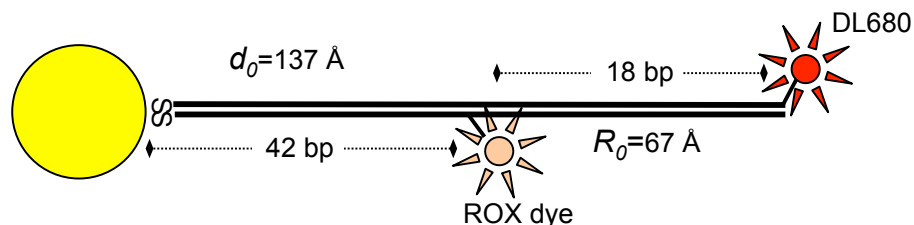


Figure 7.1: Scheme of the NSET-FRET beacon where a donor dye, ROX, is separated from a 10nm AuNP by 42 basepairs, and separated from an acceptor dye, DL680 by 18 basepairs. The NSET $d_0 = 137 \text{ \AA}$ for ROX with a 10nm AuNP and the $R_0 = 67 \text{ \AA}$ for an ROX-DL680 FRET pair.

(DL680 dye) is also appended to the dsDNA at the terminal end, opposite the AuNP. ROX acts as both the NSET and FRET donor in this dual energy transfer system.

Moreover, a theoretical model capable of describing the distal attributes of the NSET component (the ROX donor to the AuNP) and the FRET component (the ROX donor to the DL680 acceptor) of the system is proposed. The distances between the donor (ROX) and acceptors (AuNP and DL680) extracted from the donor lifetime and the theoretical model correlate well with expected dsDNA lengths based upon Clegg model predictions, which predicts helical DNA distances appended by a short alkyl linker at a nanoparticle surface [262]. This is the first report of a multi-faceted energy transfer system utilized to observe and predict biopolymer distances. Distal correlations between theory and experimental lifetimes demonstrate the advantage of merging common biophysical methods to elucidate unique or complex structures, where multiple length scales may be at play.

7.2 Experimental section

7.2.1 NSET-FRET beacon construction

Spherical BSPP-coated AuNPs of a 10nm diameter were synthesized via citrate/tannic acid reduction and ligand exchanged with BSPP prior to functionalization with DNA, as described in Chapter 4 (4.2.1) and in literature protocol [278].

The 60mer dsDNA sequence used in this study is comprised of two, modified, complementary 60mers, the donor strand, dROX, and the acceptor strand, aDL680, synthesized and purified by Midland Certified Reagent Company. When describing the ROX-modified DNA or the DL680-modified DNA in this chapter, the descriptors “dROX” and “aDL680” are used. When discussing the properties of the dyes themselves, however, they are references by their common “ROX” and “DL680” abbreviations. The full sequences used in the study are listed in the Table 7.1 and are written in the direction to which they anneal to each other for simplicity. The donor sequence, dROX, contains an ROX internal dye label via C₆ spacer on basepair #42 in the sequence (bold, italicized, and underlined in Table 7.1), with a terminal thiol modification at 5' end, also attached with a C₆ spacer linkage. The complementary acceptor sequence, aDL680, likewise, contains a terminal C₆ thiol modification at the 3' end and a terminal DL680 dye label at the 5' end. Each sequence also has a non-dye-labeled complement counterpart with a terminal

Table 7.1: Table listing the four sequences used in these energy transfer studies. The labeled basepair in the dROX donor strand is bold, italicized, and underlined. Sequences complementary to the dROX sequence, aDL680 and dROX-comp, are listed in the 3' to 5' direction.

Name	Sequence
dROX	5'-(C ₆ thiol) CAGTTACGCTAGATT <i><u>CGACATGCCGACAACAACGTCCAGTA</u></i> (ROX) CGACAATCCGACATTAAC-3'
aDL680	3'-(C ₆ thiol) GTCAATGCGATCTAAGCTGTACGGCTGTTGTTGCAGGTCATAG CTGTTAGGCTGTAATTG (DL680)-5'
dROX-comp	3'-(C ₆ thiol) GTCAATGCGATCTAAGCTGTACGGCTGTTGTTGCAGGTCATAG CTGTTAGGCTGTAATTG-5'
aDL680-comp	5'-(C ₆ thiol) CAGTTACGCTAGATT <i><u>CGACATGCCGACAACAACGTCCAGTA</u></i> CGACAATCCGACATTAAC-3'

C₆ spacer (at the 3' end for the ROX-complement and the 5' end for the DL680-complement) for control studies *sans* the donor or acceptor molecule.

DNA was annealed in two consecutive heat cycles (95°C for 4 minutes, cooling to RT for 10 minutes, and on ice for 4 minutes) with a 1.1:1 ratio of acceptor to donor to ensure no free donor is in the system. Appendage of the annealed sequences to the AuNPs was accomplished by a TCEP reduction of the terminal thiols and subsequent ligand exchange with BSPP ligand at the AuNP surface. In a ~1mL reaction volume of pH 7.2 phosphate buffer (50mM phosphate, 50mM NaCl, filtered), 12pmol 10nm BSPP-coated AuNPs was reacted with 500pmol annealed dsDNA complex. The final reaction volume was brought to a final TCEP concentration of 10mM with concentration TCEP aliquots (~20μL) in nanopure H₂O. A ligand exchange ratio of ~40:1 dsDNA to AuNP was used. The reaction was placed on the rotisserie overnight and the FRET-NSET beacons were purified with three rounds of EtOH precipitations, assisted with saturated NaCl additions. DNA appendage was confirmed by the beacons' hindered movement in 2% agarose gel electrophoresis when compared to the BSPP-coated AuNPs.

7.2.2 Absorption and photoluminescence experiments

Final concentrations of FRET-NSET beacons were extracted from UV-Vis absorption peaks for the DNA ($\epsilon_{260}=1.057*10^6 \text{ M}^{-1}\text{cm}^{-1}$) at 260nm and the AuNPs ($\epsilon_{520}=9.55*10^7 \text{ M}^{-1}\text{cm}^{-1}$)

at 520nm indicate a final coupled ratio of ~17:1 DNA to AuNP. Due to the drastic difference in extinction coefficients between the AuNPs and DNA sequences, it was necessary to perform CN⁻ etching studies on concentrated samples (as described in Chapter 5, section 5.2.1) to obtain the final DNA:AuNP ratio of ~17:1.

Quenching of ROX in the dROX-aDL680 FRET pair was first determined optically by relating the emission intensities of ROX in the dROX-aDL680 FRET pair to identical concentrations of free dROX-complement. The 10nm AuNP absorption spectrum, dROX absorption and emission spectra, and aDL680 absorption and emission spectra are shown in Figure 7.2. The aDL680 acceptor has a small absorption near the excitation wavelength (λ_{ex} =550 nm) and contributes additional, directly excited, emission intensity to the FRET acceptor emission in the FRET studies. Therefore, the emission intensity (at λ_{ex} =550 nm) of free aDL680 at a concentration identical to the dROX-aDL680 FRET pair is subtracted from the final FRET spectra. Concentrations for the DNA prior to annealing are [dROX]=0.4 μ M, [ROX complement]= 0.44 μ M, [aDL680]=0.44 μ M, and [DL680 complement]= 0.4 μ M.

Similarly, comparisons between the ROX emission intensity from the NSET-FRET beacon and a dROX-complement-AuNP conjugate were used to evaluate the NSET component of the NSET-FRET beacon. Differences in ROX emission intensity of the NSET-FRET beacon and dROX-complement-AuNP samples at 2nM were used to determine the E_{NSET} between ROX and the AuNP as well as the ROX-AuNP distance extracted from the NSET theorem, where d_0 =137 Å for a 10nm AuNP acceptor with an ROX donor. As in the FRET pair studies, direct-excitation emission from DL680 was accounted for by subtracting the DL680 emission (at

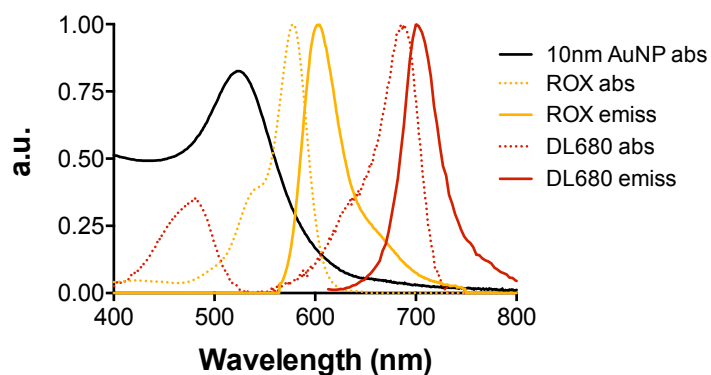


Figure 7.2: Absorption spectra of (black line) 10nm BSPP-AuNPs, (orange dotted line) dROX, (red dotted line) aDL680, and emission spectra of (orange solid line) aROX, and (red solid line) aDL680.

$\lambda_{\text{ex}}=550$ nm) in a 2nM aDL680-complement-AuNP sample from the NSET-FRET beacon sample.

7.2.3 Lifetime experiments

Lifetime measurements of the ROX donor, described similarly in previous publications, were measured by exciting at 560nm (<1 mW) using a Nd:VO₄-pumped (Spectra-Physics Vanguard, 2W, 532 nm, 76 MHz, 10 ps) cavity-dumped R6G fluorescent molecule laser (Coherent 702-1) as a source and collecting onto a Hamamatsu C5680 streak camera coupled to a Chromex 500 imaging monochromator. The intensity decay profiles are collected over a 20ns window to ensure ample time for fluorescent population decay, as well as a 200nm spectral window to observe the donor (ROX) as well as acceptor (DL680) emission.

7.3 Results & discussion

The FRET theorem, described in Chapter 2 (2.3.6), relates the degree of spectral overlap and strength of dipole coupling between a donor (ROX) and acceptor (DL680) dye with a value that describes the distance at which 50% energy transfer occurs (R_0) [178,191]. The R_0 value for an ROX-DL680 pair is 67 Å. Upon obtaining the R_0 value, the efficiency of energy transfer (E_{FRET}) is better described as,

$$E_{\text{FRET}} = \frac{1}{1 + \left(\frac{R}{R_0}\right)^6} \quad \text{eqn. 7.1}$$

where R is the distance between the coupled dipoles. Similarly, NSET's 50% efficiency value, d_0 , is described as

$$E_{\text{NSET}} = \frac{1}{1 + \left(\frac{d}{d_0}\right)^4} \quad \text{eqn. 7.2}$$

where d is the distance between the organic fluorophore and the AuNP surface. The full NSET theorem is outlined in further detail in Chapter 2 (2.4.1.) [176-178,191].

This NSET-FRET beacon is not the first to treat a FRET mechanism in the presence of a metal nanoparticle. Gersten, et al, treats the change in the FRET rate, k_{FRET} , in the near-field of a metal nanoparticle as a perturbation to the dipole interaction energy between donor and acceptor

dyes [312]. But in any energy transfer interaction (be it FRET, or NSET) the total rate of energy transfer, k_{ET} , must equal the sum of all pathways (including all radiative and non-radiative pathways), as expressed in equation 6.3,

$$k_{ET} = k_r + k_{nr(total)} \quad \text{eqn. 7.3}$$

where k_r and k_{nr} represent the radiative rates, respectively. Likewise, the lifetime of the donor, τ , is represented as the inverse of the energy transfer rate, or $1/(k_r + k_{nr})$ [176-178,201]. In this system where NSET, k_{NSET} , and FRET, k_{FRET} , non-radiative pathways are introduced as competitive donor relaxation pathways, the experimental lifetime of the ROX donor, τ' , is best represented as

$$\tau' = \frac{1}{k_{FRET} + k_{NSET} + k_r + k_{nr}} \quad \text{eqn. 7.4}$$

where k_r and k_{nr} represent the radiative rates, respectively. Written as an efficiency (E) relating the modified ROX lifetime in the presence of the NSET and FRET pathways, τ' , to its native lifetime, τ_0 , the value for E is shown as,

$$E = 1 - \frac{\tau'}{\tau_0} = \frac{k_{FRET} + k_{NSET}}{k_{FRET} + k_{NSET} + k_r + k_{nr}} \quad \text{eqn. 7.5.}$$

In this model, the energy transfer rates are unmodified from their FRET-only and NSET-only values. The nonradiative energy transfer pathways combine in a competitive manner with native decay rates and lead to a predictable decrease in ROX lifetime, τ' , in the NSET-FRET beacon. With this simple kinetic model, a system of equations can be generated, combining earlier expressions for E_{FRET} and E_{NSET} (eqn. 6.1 and 6.2, respectively,) to solve for the separation distances, d (ROX-AuNP) and R (ROX-DL680), in the FRET-NSET beacon:

$$d = d_0 \left[\left(\frac{\tau_0}{\tau'} - 1 \right) - \left(\frac{R}{R_0} \right)^{-6} \right]^{-1/4} \quad \text{eqn. 7.6}$$

$$R = R_0 \left[\left(\frac{\tau_0}{\tau'} - 1 \right) - \left(\frac{d}{d_0} \right)^{-4} \right]^{-1/6} \quad \text{eqn. 7.7.}$$

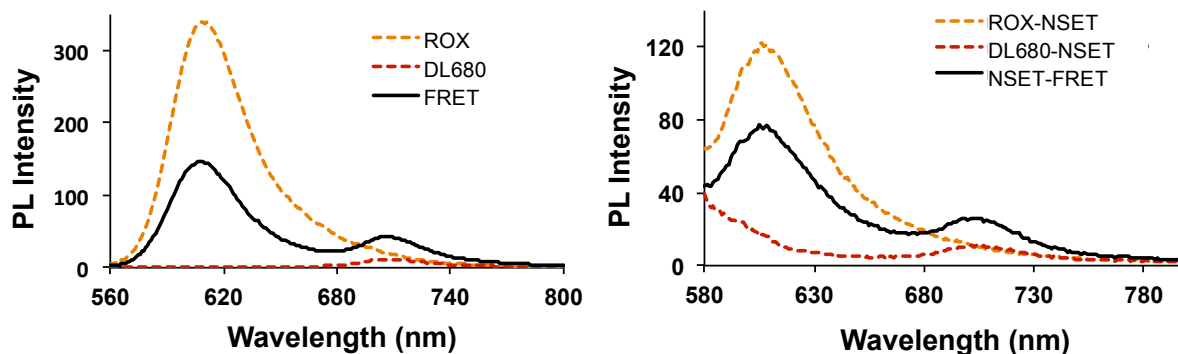


Figure 7.3: Raw PL data of the (Left) FRET-based beacons and the (Right) NSET-based beacons. (Left) The orange dotted line represents free dROX-complement strand, the red dotted line represents the small DL680 population directly excited by $\lambda_{ex}=550$ nm, and the solid black represents the FRET spectra after subtracting the directly excited DL680 contribution.

In this representation, the only experimental components required to obtain the donor-AuNP (NSET) and donor-acceptor (FRET) distances are the native donor lifetime, τ_0 , the modified donor lifetime, τ' , and one of the separation distances, d or R .

To exemplify this NSET-FRET mathematical model, a simple linear DNA duplex structure containing a short single contact FRET pair (ROX-DL680) with a single long-contact NSET pair (ROX-10nm AuNP) is examined by optical spectroscopy (photoluminescence and lifetime). A schematic of the NSET-FRET system under investigation is shown in Figure 7.1.

Initial photoluminescent studies of the control beacons (dROX-AuNP and aDL680-AuNP), the NSET-FRET beacon, the dROX-aDL680 FRET pair, and the free DNA controls (dROX and aDL680) were performed and are shown in Figure 7.3 (left). The FRET pair spectrum, with the subtraction of the directly excited emission contribution from aDL680, shows an E_{FRET} of 0.43 ± 0.10 . The dye-dye distance extracted from the FRET theorem, where ROX-DL680 $R_0=67$ Å value, of is 73 ± 7 Å. The theoretical distance between 18 basepairs in duplex DNA where 3.4 Å is allotted per basepair and C_6 dye linkers is 73 Å [253].

Photoluminescent NSET and NSET-FRET studies with dROX, were performed by comparing ROX emission intensity in an dROX-AuNP sample with that of the NSET-FRET beacon (Figure 7.3 - right). As loading with the dROX-complement duplex and the dROX-aDL680 consistently resulted in variable amounts of DNA on the AuNP surfaces, it was exceptionally difficult accurately quantify the degree of ROX quenching when dROX was

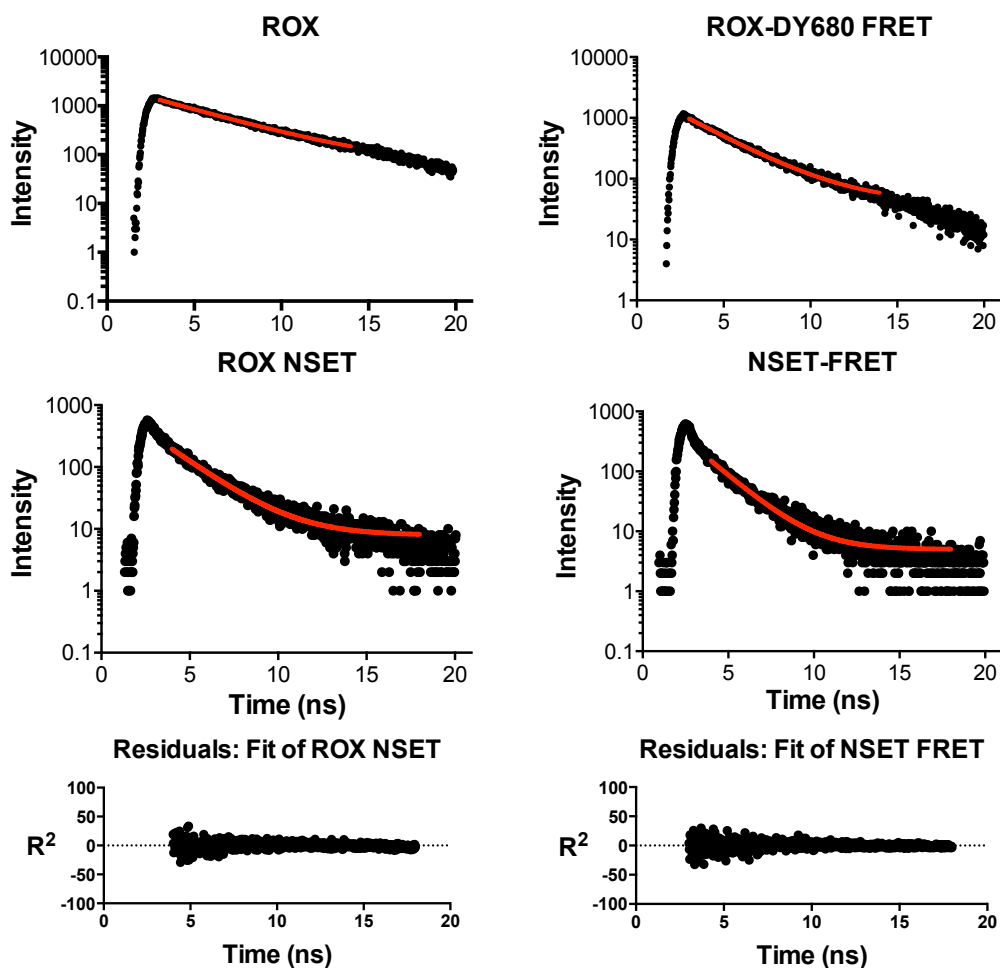


Figure 7.4: Lifetime decay data of the (top left) free dROX sequence ($\tau_0 = 4.4 \pm 0.1$ ns), (top right) the dROX-aDL680 FRET complex ($\tau' = 2.8 \pm 0.1$ ns), (bottom left) the dROX-complement-AuNP beacon ($\tau' = 2.1 \pm 0.1$ ns), and (bottom right) the NSET-FRET beacon ($\tau' = 1.9 \pm 0.1$ ns). Residuals of the AuNP-based fits (ROX NSET and FRET-NSET) are shown below the corresponding lifetime plots.

appended to the AuNP with an acceptor (aDL680) relative to quenching without an acceptor (dROX-complement). It is clear, however, that the ROX emission intensity *decreases* in the NSET-FRET beacon, relative to the dROX-AuNP conjugate; it is simply not easily quantifiable as to *how much* the ROX emission decreases. A decrease in emission intensity in the presence of an extra acceptor (aDL680) is not surprising, as another non-radiative pathway, k_{FRET} , is now presented to the ROX donor, decreasing the efficiency of the radiative rate, k_r . To properly

Table 7.2: Table of the extracted NSET, FRET, and FRET-NSET values using experimental ROX lifetimes (τ') and eqn. 7.6 and 7.7.

	τ_0 (ns)	τ' (ns)	τ'_{theo} (ns)	E'	E_{theo}	R_0 (Å)	$R_{0\text{-Clegg}}$ (Å)
ROX (free)	4.4 ± 0.1	----	----	----	----	----	----
ROX-DL680 FRET	----	2.8 ± 0.1	2.8	0.36	0.36	73 ± 7	73
ROX-NSET	----	2.1 ± 0.1	2.5	0.51	0.44	136 ± 7 (d_0)	146
NSET-FRET	----	1.9 ± 0.1	1.8	0.56	0.58	$75 \pm 7, 139 \pm 7$	73, 147

quantify the degree of increased ROX quenching in the NSET-FRET beacon, lifetime analysis the ROX donor, where the lifetimes obtained are independent of concentration, is essential.

The observed lifetimes of the ROX donor, extracted energy transfer rate components, and NSET-FRET beacon component separation distances are displayed in Table 7.2. The collected fluorescence decay curves for the ROX donor in the various beacons (dROX-complement-AuNP) as well as the residual fits for the AuNP-based ROX systems are shown in Figure 7.4. The lifetime for ROX in the absence of acceptors, τ_0 , was measured to be 4.4 ± 0.1 ns while the modified lifetime of ROX, τ' , in the NSET-FRET beacon (in the presence of both the AuNP and DL680 acceptors) is 1.9 ± 0.1 ns. In the modified NSET-FRET equations described earlier (eqn. 7.6), this lifetime correlates to an experimental ROX-AuNP separation distance of 139 ± 7 Å. Using the Clegg model for duplex DNA appended to a nanoparticle surface at these basepair lengths (146 Å), the theoretical lifetime for the ROX donor is $\tau'=1.8$ ns.

The experimental ROX lifetime in the dROX-aDL680 FRET pair is 2.8 ± 0.1 ns, which corresponds to an ROX-DL680 separation distance of 75 ± 7 Å following the FRET model ($R_0=67$ Å). Following the Clegg model for a 20 basepair separation, plus C_6 thiol linkers appending each dye, the theoretical dye-dye distance in the ROX-DL680 FRET pair is 73 Å, correlating well to the lifetime-derived experimental distance [262]. Little discrepancy is observed in the E_{FRET} values between the photoluminescent study (PL $E_{\text{FRET}}=0.43$) and the lifetime analysis ($\tau' E_{\text{FRET}}=0.36$). As lifetime measurements are concentration-independent, the simpler measurement in this NSET-FRET beacon study is undoubtedly lifetime analysis. In both energy transfer mechanisms taking place in this NSET-FRET beacon, the extraction of

separation distances from eqn. 7.6 and 7.7 (FRET distances and NSET distances) is possible from experimentally measured lifetimes.

7.4 Conclusion

Manipulation of common energy transfer components within the NSET and FRET models led to the experimental capability, and mathematical correlation, to track variable distance ranges in an example biomolecule, duplex DNA. Whereas previous groups have utilized large metal nanoparticles to enhance the FRET R_0 value to attain longer-range FRET measurements, a obvious lack of control over the extendable R_0 value is observed [196-198]. In this chapter, an additional, non-enhancing NSET component was added to the FRET-style complex in an effort to locate multiple contact points over variable distance ranges.

As biomolecular structures are comprised of individual units (molecules, basepairs, amino acids, etc.) as well as global structures built from the building-block units (nucleic acid secondary structures, peptides, proteins, etc.), a tool combining two separate, yet relevant distance skills is valuable to the biophysical community. In this chapter, demonstration of the NSET-FRET beacon's mathematical predictability provides immediate applicability.

REFERENCES

- (1) Watson, J.D.; Crick, F.H.C. Molecular structure of nucleic acids – A structure for deoxyribose nucleic acid. *Nature*. **1953**, *171*, 737-738.
- (2) Helmkamp, G.K.; Ts'o, P.O.P. The secondary structures of nucleic acids in organic solvents. *J. Am. Chem. Soc.* **1961**, *83*, 138-142.
- (3) Sukhorukov, B.I.; Moshkovskii, Y.S.; Birshtein, T.M.; Lystsov, V.N. Optical properties and molecular structure of nucleic acids and their components. *Biophys-USSR*. **1963**, *8*, 348-350.
- (4) Poltev, V.I.; Sukhorukov, B.I.; Mekler, L.B. Changes in pH solutions of nucleic acids in presence of configurational transitions. *Biophys-USSR*. **1967**, *12*, 617-620.
- (5) Hoogsteen, K. The crystal and molecular structure of a hydrogen-bonded complex between 1-methylthymine and 9-methyladenine. *Acta. Cryst.* **1963**, *16*, 907-916.
- (6) Sharp, S.J.; Schaack, J.; Cooley, L.; Johnson Burke, D.; Söll, D. Structure and transcription of eukaryotic tRNA genes. *CRC C.R. Rev. Bioch. Mol.* **1985**, *19*, 107-144.
- (7) Ishii, R.; Minagawa, A.; Takaku, H.; Takagi, M.; Nashimoto, M.; Yokoyama, S. Crystal structure of the tRNA 3' processing endoribonuclease tRNase Z from *Thermotoga maritima*. *J. Biol. Chem.* **2005**, *280*, 14138-14144.
- (8) Mustoe, A.M.; Brooks, C.L.; Al-Hashimi, H.M. Topological constraints are major determinants of tRNA tertiary structure and dynamics and provide basis for tertiary folding cooperativity. *Nucleic Acids Res.* **2014**, *42*, 11792-11804.
- (9) Kelly, N.J.; Morrow, C.D.; Structural elements of the tRNA T ψ C loop critical for nucleocytoplasmic transport are important for Human Immunodeficiency Virus Type 1 primer selection. *J. Virol.* **2005**, *79*, 6532-6539.
- (10) Yu, J.; Russell, J.E.; Structural and functional analysis of an mRNP complex that mediates the high stability of human β -globin mRNA. *Mol. Cell. Biol.* **2001**, *21*, 5879-5888.
- (11) Wells, S.E.; Hillner, P.E.; Vale, R.D.; Sachs, A.B. Circularization of mRNA by eukaryotic translation initiation factors. *Mol. Cell.* **1998**, *2*, 135-140.
- (12) Michael, D.; Manyuan, L. Intro-exon structures of eukaryotic model organisms. *Nucleic Acids Res.* **1999**, *27*, 3219-3228.
- (13) Noller, H.F. Structure of ribosomal RNA. *Ann. Rev. Biochem.* **1984**, *53*, 119-162.
- (14) Murray, H.D.; Schneider, D.A.; Gourse, R.L. Control of rRNA expression by small molecules is dynamic and nonredundant. *Mol. Cell.* **2003**, *12*, 125-134.

- (15) Yusupov, M.M.; Yusupova, G.Zh.; Baucom, A.; Lieberman, K.; Earnest, T.N.; Cate, J.H.D.; Noller, H.F. Crystal structure of the ribosome at 5.5 Å resolution. *Science*. **2001**, *292*, 883-896.
- (16) Mitsui, Y.; Langridge, R.; Shortle, B.E.; Cantor, R.C.; Kodama, M.; Wells, R.D. Physical and Enzymatic Studies on Poly d(I-C). Poly d(I-C), an Unusual Double-helical DNA. *Proc. Natl. Acad. Sci. U.S.A.*, **1970**, *228*, 1161-1169.
- (17) Patel, D.J.; Canuel, L.L.; Pohl, F.M. Alternating B-DNA" conformation for the oligo(dG-dC) duplex in high-salt solution. *Oncogene*. **1979**, *76*, 2508-2511.
- (18) Gosselin, G.; Imbach, J.L. B-DNA and Z-DNA - about the possible implication of B-reversible-Z transitions in carcinogenesis. *Eur. J. Med. Chem.* **1983**, *18*, 393-400.
- (19) Behe, M.; Felsenfeld, G. Effects of methylation on a synthetic polynucleotide: the B-Z transition in poly(dG-m5dC). *Proc. Natl. Acad. Sci. U.S.A.* **1981**, *78*, 1619-1623.
- (20) Borah, B.; Cohen, J.S.; Howard, F.B.; Miles, H.T. Poly(d2NH2A-dT): two-dimensional NMR shows a B to A conversion in high salt. *Biochemistry*. **1985**, *78*, 7456-7462.
- (21) Abdel-Monem, A.; Dürwald, H.; Hoffmann-Berling, H. Enzymic Unwinding of DNA 2. Chain Separation by an ATP-Dependent DNA Unwinding Enzyme. *Eur. J. Biochem.* **1976**, *65*, 441-449.
- (22) Lohman, T. Escherichia coli DNA helicases: mechanisms of DNA unwinding. *Mol. Microbiol.* **1992**, *6*, 5-14.
- (23) Lohman, T. Helicase-catalyzed DNA unwinding. *J. Biol. Chem.* **1993**, *268*, 2269-2272.
- (24) Bentley, D.R.; Balasubramanian, S.; Swerdlow, H.P.; Smith, G.P.; Milton, J.; Brown, C.G.; Hall, K.P.; Evers, D.J.; Barnes, C.L.; Bignell, H.R.; Boutell, J.M.; Bryant, J.; Carter, R.J.; Keira Cheetham, R.; Cox, A.J.; Ellis, D.J.; Flatbush, M.R.; Gormley, N.A.; Humphray, S.J.; Irving, L.J.; Karbelashvili, M.S.; Kirk, S.M.; Li, H.; Liu, X.; Maisinger, K.S.; Murray, L.J.; Obradovic, B.; Ost, T.; Parkinson, M.L.; Pratt, M.R.; Rasolonjatovo, I.M.; Reed, M.T.; Rigatti, R.; Rodighiero, C.; Ross, M.T.; Sabot, A.; Sankar, S.V.; Scally, A.; Schroth, G.P.; Smith, M.E.; Smith, V.P.; Spiridou, A.; Torrance, P.E.; Tzonev, S.S.; Vermaas, E.H.; Walter, K.; Wu, X.; Zhang, L.; Alam, M.D.; Anastasi, C.; Aniebo, I.C.; Bailey, D.M.; Bancarz, I.R.; Banerjee, S.; Barbour, S.G.; Baybayan, P.A.; Benoit, V.A.; Benson, K.F.; Bevis, C.; Black, P.J.; Boodhun, A.; Brennan, J.S.; Bridgham, J.A.; Brown, R.C.; Brown, A.A.; Buermann, D.H.; Bundu, A.A.; Burrows, J.C.; Carter, N.P.; Castillo, N.; Chiara, E.; Catenazzi, M.; Chang, S.; Neil Cooley, R.; Crake, N.R.; Dada, O.O.; Diakoumakos, K.D.; Dominguez-Fernandez, B.; Earnshaw, D.J.; Egbujor, U.C.; Elmore, D.W.; Etchin, S.S.; Ewan, M.R.; Fedurco, M.; Fraser, L.J.; Fuentes Fajardo, K.V.; Scott Furey, W.; George, D.; Gietzen, K.J.; Goddard, C.P.; Golda, G.S.; Granieri, P.A.; Green, D.E.; Gustafson, D.L.; Hansen, N.F.; Harnish, K.; Haudenschild, C.D.; Heyer, N.I.; Hims, M.M.; Ho, J.T.; Horgan, A.M.; Hoschler, K.; Hurwitz, S.; Ivanov, D.V.; Johnson, M.Q.; James, T.; Huw Jones, T.A.; Kang, G.D.; Kerelska, T.H.; Kersey, A.D.; Khrebtukova, I.; Kindwall, A.P.; Kingsbury, Z.; Kokko-Gonzales, P.I.; Kumar, A.; Laurent, M.A.; Lawley, C.T.;

Lee, S.E.; Lee, X.; Liao, A.K.; Loch, J.A.; Lok, M.; Luo, S.; Mammen, R.M.; Martin, J.W.; McCauley, P.G.; McNitt, P.; Mehta, P.; Moon, K.W.; Mullens, J.W.; Newington, T.; Ning, Z.; Ling Ng, B.; Novo, S.M.; O'Neill, M.J.; Osborne, M.A.; Osnowski, A.; Ostadan, O.; Paraschos, L.L.; Pickering, L.; Pike, A.C.; Pike, A.C.; Chris Pinkard, D.; Pliskin, D.P.; Podhasky, J.; Quijano, V.J.; Raczky, C.; Rae, V.H.; Rawlings, S.R.; Chiva Rodriguez, A.; Roe, P.M.; Rogers, J.; Rogert Bacigalupo, M.C.; Romanov, N.; Romieu, A.; Roth, R.K.; Rourke, N.J.; Ruediger, S.T.; Rusman, E.; Sanches-Kuiper, R.M.; Schenker, M.R.; Seoane, J.M.; Shaw, R.J.; Shiver, M.K.; Short, S.W.; Sizto, N.L.; Sluis, J.P.; Smith, M.A.; Sohna, E.; Sohna, J.; Spence, E.J.; Stevens, K.; Sutton, N.; Szajkowski, L.; Tregidgo, C.L.; Turcatti, G.; Vandevondele, S.; Verhovskiy, Y.; Virk, S.M.; Wakelin, S.; Walcott, G.C.; Wang, J.; Worsley, G.J.; Yan, J.; Yau, L.; Zuerlein, M.; Rogers, J.; Mullikin, J.C.; Hurler, M.E.; McCooke, N.J.; West, J.S.; Oaks, F.L.; Lundberg, P.L.; Klenerman, D.; Durbin, R.; Smith, A.J. Initial sequencing and analysis of the human genome. *Nature*. **2001**. *409*, 860-921.

(25) Feldmann, H.; Aigle, M.; Aljinovic, G.; André, B.; Baclet, M.C.; Barthe, C.; Baur, A.; Bécam, A.M.; Biteau, N.; Boles, E.; Brandt, T.; Brendel, M.; Brückner, M.; Bussereau, F.; Christiansen, C.; Contreras, R.; Crouzet, M.; Cziepluch, C.; Démolis, N.; Delaveau, T.; Doignon, F.; Domdey, H.; Düsterhus, S.; Dubois, E.; Dujon, B.; El Bakkoury, M.; Entian, K.D.; Feurmann, M.; Fiers, W.; Fobo, G.M.; Fritz, C.; Gassenhuber, H.; Glandsdorff, N.; Goffeau, A.; Grivell, L.A.; de Haan, M.; Hein, C.; Herbert, C.J.; Hollenberg, C.P.; Holmstrøm, K.; Jacq, C.; Jacquet, M.; Jauniaux, J.C.; Jonniaux, J.L.; Kallesøe, T.; Kiesau, P.; Kirchrath, L.; Kötter, P.; Korol, S.; Liebl, S.; Logghe, M.; Lohan, A.J.; Louis, E.J.; Li, Z.Y.; Maat, M.J.; Mallet, L.; Mannhaupt, G.; Messenguy, F.; Miosga, T.; Molemans, F.; Müller, S.; Nasr, F.; Obermaier, B.; Perea, J.; Piérard, A.; Piravandi, E.; Pohl, F.M.; Pohl, T.M.; Potier, S.; Proft, M.; Purnelle, B.; Ramezani Rad, M.; Rieger, M.; Rose, M.; Schaaff-Gerstenschläger, I.; Scherens, B.; Schwarzlose, C.; Skala, J.; Slonimski, P.P.; Smits, P.H.; Souciet, J.L.; Steensma, H.Y.; Stucka, R.; Urrestarazu, A. van der Aart, Q.J.; van Dyck, L.; Vassarotti, A.; Vetter, I.; Vierendeels, F.; Vissers, S.; Wagner, G.; de Wergifosse, P.; Wolfe, K.H.; Zagulski, M.; Zimmermann, F.K.; Mewes, H.W.; Kleine, K. Complete DNA sequence of yeast chromosome II. *EMBO J*. **1994**. *13*, 5795-5809.

(26) Venter, J.C.; Adams, M.D.; Myers, E.W.; Li, P.W.; Mural, R.J.; Sutton, G.G.; Smith, H.O.; Yandell, M.; Evans, C.A.; Holt, R.A.; Gocayne, J.D.; Amanatides, P.; Ballew, R.M.; Huson, D.H.; Wortman, J.R.; Zhang, Q.; Kodira, C.D.; Zheng, X.H.; Chen, L.; Skupski, M.; Subramanian, G.; Thomas, P.D.; Zhang, J.; Gabor Miklos, G.L.; Nelson, C.; Broder, S.; Clark, A.G.; Nadeau, J.; McKusick, V.A.; Zinder, N.; Levine, A.J.; Roberts, R.J.; Simon, M.; Slayman, C.; Hunkapiller, M.; Bolanos, R.; Delcher, A.; Dew, I.; Fasulo, D.; Flanigan, M.; Florea, L.; Halpern, A.; Hannenhalli, S.; Kravitz, S.; Levy, S.; Mobarry, C.; Reinert, K.; Remington, K.; Abu-Threideh, J.; Beasley, E.; Biddick, K.; Bonazzi, V.; Brandon, R.; Cargill, M.; Chandramouliswaran, I.; Charlab, R.; Chaturvedi, K.; Deng, Z.; Di Francesco, V.; Dunn, P.; Eilbeck, K.; Evangelista, C.; Gabrielian, A.E.; Gan, W.; Ge, W.; Gong, F.; Gu, Z.; Guan, P.; Heiman, T.J.; Higgins, M.E.; Ji, R.R.; Ke, Z.; Ketchum, K.A.; Lai, Z.; Lei, Y.; Li, Z.; Li, J.; Liang, Y.; Lin, X.; Lu, F.; Merkulov, G.V.; Milshina, N.; Moore, H.M.; Naik, A.K.; Narayan, V.A.; Neelam, B.; Nuskern, D.; Rusch, D.B.; Salzberg, S.; Shao, W.; Shue, B.; Sun, J.; Wang, Z.; Wang, A.; Wang, X.; Wang, J.; Wei, M.; Wides, R.; Xiao, C.; Yan, C.; Yao, A.; Ye, J.; Zhan, M.; Zhang, W.; Zhang, H.; Zhao, Q.; Zheng, L.; Zhong, F.; Zhong, W.; Zhu, S.; Zhao, S.;

Gilbert, D.; Baumhueter, S.; Spier, G.; Carter, C.; Cravchik, A.; Woodage, T.; Ali, F.; An, H.; Awe, A.; Baldwin, D.; Baden, H.; Barnstead, M.; Barrow, I.; Beeson, K.; Busam, D.; Carver, A.; Center, A.; Cheng, M.L.; Curry, L.; Danaher, S.; Davenport, L.; Desilets, R.; Dietz, S.; Dodson, K.; Doup, L.; Ferriera, S.; Garg, N.; Gluecksmann, A.; Hart, B.; Haynes, J.; Haynes, C.; Heiner, C.; Hladun, S.; Hostin, D.; Houck, J.; Howland, T.; Ibegwam, C.; Johnson, J.; Kalush, F.; Kline, L.; Koduru, S.; Love, A.; Mann, F.; May, D.; McCawley, S.; McIntosh, T.; McMullen, I.; Moy, M.; Moy, L.; Murphy, B.; Nelson, K.; Pfannkoch, C.; Pratts, E.; Puri, V.; Qureshi, H.; Reardon, M.; Rodriguez, R.; Rogers, Y.H.; Romblad, D.; Ruhfel, B.; Scott, R.; Sitter, C.; Smallwood, M.; Stewart, E.; Strong, R.; Suh, E.; Thomas, R.; Tint, N.N.; Tse, S.; Vech, C.; Wang, G.; Wetter, J.; Williams, S.; Williams, M.; Windsor, S.; Winn-Deen, E.; Wolfe, K.; Zaveri, J.; Zaveri, K.; Abril, J.F.; Guigó, R.; Campbell, M.J.; Sjolander, K.V.; Karlak, B.; Kejariwal, A.; Mi, H.; Lazareva, B.; Hatton, T.; Narechania, A.; Diemer, K.; Muruganujan, A.; Guo, N.; Sato, S.; Bafna, V.; Istrail, S.; Lippert, R.; Schwartz, R.; Walenz, B.; Yooseph, S.; Allen, D.; Basu, A.; Baxendale, J.; Blick, L.; Caminha, M.; Carnes-Stine, J.; Caulk, P.; Chiang, Y.H.; Coyne, M.; Dahlke, C.; Mays, A.; Dombroski, M.; Donnelly, M.; Ely, D.; Esparham, S.; Fosler, C.; Gire, H.; Glanowski, S.; Glasser, K.; Glodek, A.; Gorokhov, M.; Graham, K.; Gropman, B.; Harris, M.; Heil, J.; Henderson, S.; Hoover, J.; Jennings, D.; Jordan, C.; Jordan, J.; Kasha, J.; Kagan, L.; Kraft, C.; Levitsky, A.; Lewis, M.; Liu, X.; Lopez, J.; Ma, D.; Majoros, W.; McDaniel, J.; Murphy, S.; Newman, M.; Nguyen, T.; Nguyen, N.; Nodell, M.; Pan, S.; Peck, J.; Peterson, M.; Rowe, W.; Sanders, R.; Scott, J.; Simpson, M.; Smith, T.; Sprague, A.; Stockwell, T.; Turner, R.; Venter, E.; Wang, M.; Wen, M.; Wu, D.; Wu, M.; Xia, A.; Zandieh, A.; Zhu, X.; The sequence of the human genome. *Science*. **2001**. 291, 1304-1351.

(27) Hamilton, A.J.; Baulcombe, D.C. A Species of Small Antisense RNA in Posttranscriptional Gene Silencing in Plants. *Science*. **1999**. 286, 950-952.

(28) Harborth, J.; Elbashit, S.M.; Vandeburgh, K.; Manninga, H.; Scaringe, S.A.; Weber, K.; Tuschl, T. Sequence, Chemical, and Structural Variation of Small Interfering RNAs and Short Hairpin RNAs and the Effect on Mammalian Gene Silencing. *Antisense Nucleic A*. **2003**. 13, 83-105.

(29) Iyer, R.P. RNA interference: an exciting new approach for target validation, gene expression analysis and therapeutics. *Drug Future*. **2003**. 28, 51-59.

(30) Thompson, J.D. Applications of antisense and siRNAs during preclinical drug development. *Drug Discov. Today* **2002**. 7, 912-917.

(31) Vaucheret, H.; Béclin, C.; Fagard, M. Post-transcriptional gene silencing in plants. *J. Cell Sci*. **2001**. 114, 3083-3091.

(32) Wittrup, A.A. Knocking down disease: a progress report on siRNA therapeutics. *Nat. Rev. Genet*. **2015**. 16, 543-552.

(33) Bock, L.C.; Griffin, L.C.; Latham, J.A.; Vermaas, E.H.; Toole, J.J. Selection of single-stranded DNA molecules that bind and inhibit human thrombin. *Nature*. **1992**, 346, 564-566.

- (34) Stojanovic, M.N.; de Prada, P.; Landry, D.W. Aptamer-based folding fluorescent sensor for cocaine. *J. Am. Chem. Soc.* **2001**, *123*, 4928–4931.
- (35) Thomas, J.M.; Ting, R.; Perrin, D.M. High affinity DNAzyme-based ligands for transition metal cations - a prototype sensor for Hg²⁺. *Org. Biomol. Chem.* **2004**, *2*, 307–312.
- (36) Porchetta, A.; Valleé-Bélisle, A.; Plaxco, K.W.; Ricci, F. Allosterically-tunable, DNA-based switches triggered by heavy metals. *J. Am. Chem. Soc.* **2013**, *135*, 13238–13241.
- (37) *Aptamers selected by cell-SELEX for theranostics*; Tan, W., Fang, X. Eds.; Springer-Verlag: Berlin Heidelberg, **2015**.
- (38) Hamaguchi, N.; Ellington, A.; Stanton, M. Aptamer beacons for the direct detection of proteins. *Anal. Biochem.* **2001**, *294*, 126-131.
- (39) Zheng, D.; Seferos, D.S.; Giljohann, D.A.; Patel, P.C.; Mirkin, C.A. Aptamer nano-flares for molecular detection in living cells. *Nano Lett.* **2009**, *9*, 3258–3261.
- (40) Seferos, D.; Giljohann, D.A.; Hill, H.D.; Prigodich, A.E.; Mirkin, C.A. Nano-flares: probes for transfection and mRNA detection in living cells. *J. Am. Chem. Soc.* **2007**, *129*, 15477-15479.
- (41) Nutiu, R.; Li, Y. Structure-switching signaling aptamers. *J. Am. Chem. Soc.* **2003**, *125*, 4771-4778.
- (42) Liu, J.; Lu, Y. Fast colorimetric sensing of adenosine and cocaine based on a general sensor design involving aptamers and nanoparticles. *Angew. Chem.-Ger. Edit.* **2006**, *118*, 96-100.
- (43) Kawde, A.; Rodriguez, M.C.; Lee, T.M.H.; Wang, J. Label-free bioelectronics detection of aptamer protein interactions. *Electrochem. Commun.* **2005**, *7*, 537-540.
- (44) Fahlman, R.P.; Sen, D. DNA conformational switches as sensitive electronic sensors of analytes. *J. Am. Chem. Soc.* **2002**, *124*, 4610-4616.
- (45) Xiao, Y.; Piorek, B.D.; Plaxco, K.W.; Heeger, A.L. A reagentless signal-on architecture for electronic, aptamer-based sensors via target-induced strand displacement. *J. Am. Chem. Soc.* **2005**, *127*, 17990-17991.
- (46) Vallée-Bélisle, A.; Ricci, F.; Plaxco, K.W. Engineering biosensors with extended, narrowed, or arbitrarily edited dynamic range. *J. Am. Chem. Soc.* **2012**, *134*, 2875-2879.
- (47) Fernández de Ávila, B.E.; Watkins, H.M.; Pingarrón, J.M.; Plaxco, K.W.; Palleschi, G.; Ricci, F. Determinants of the detection limit and specificity of surface-based biosensors. *Anal. Chem.* **2013**, *85*, 6593-6597.

- (48) Kang, D.; Vallée-Bélisle, A.; Porchetta, A.; Plaxco, K.W.; Ricci, F. Re-engineering electrochemical biosensors to narrow or extend their useful dynamic range. *Angew. Chem.-Ger. Edit.* **2012**, *124*, 6821-6825.
- (49) Lao, Y.; Peck, K.; Chen, C. Enhancement of aptamer microarray sensitivity through spacer optimization and avidity effect. *Anal. Chem.* **2009**, *81*, 1747-1754.
- (50) Ellington, A.D.; Szostak, J.W. In vitro selection of RNA molecules that bind specific ligands. *Nature.* **1990**, *342*, 818-822.
- (51) Long, S.B.; Long, M.B.; White, R.R.; Sullenger, B.A. Crystal structure of an RNA aptamer bound to thrombin. *RNA.* **2008**, *14*, 2504-2512.
- (52) Oliphant, A.R.; Brandi, C.J.; Struhl, K. Defining the sequence specificity of DNA-binding proteins by selecting binding sites from random-sequence oligonucleotides: analysis of yeast GCN4 proteins. *Mol. Cell. Biol.* **1989**, *9*, 2944-2949.
- (53) Tuerk, C.; Gold, L. Systematic evolution of ligands by exponential enrichment: RNA ligands to bacteriophage T4 DNA polymerase. *Science.* **1990**, *249*, 505-510.
- (54) Crameri, A.; Stemmer, P. C. 10^{20} -Fold aptamer library amplification without gel purification. *Nucleic Acids Res.* **1993**, *21*, 4410.
- (55) Eaton, B.E.; Gold, L.; Hicke, B.J.; Nebojsa, J.; Jucker, F.M.; Sebesta, D.P.; Tarasow, T.M.; Willis, M.C.; Zichi, D.A. Post-SELEX combinatorial optimization of aptamers. *Bioorg. Med. Chem.* **1997**, *5*, 1087-1096.
- (56) Famulok, M.; Jenne, A. Oligonucleotide libraries - variatio delectat. *Curr. Opin. Chem. Biol.* **1998**, *2*, 320-327.
- (57) Wilson, D. S.; Szostak, J. W. Selection of functional nucleic acids. *Annu. Rev. Biochem.* **1999**, *68*, 611-647.
- (58) Huizenga, D.E.; Szostak, J.W. A DNA aptamer that binds adenosine and ATP. *Biochemistry.* **1995**, *34*, 656-665.
- (59) Giver, L.; Bartel, D.; Zapp, M.; Pawul, A.; Green, M.; Ellington, A. D. Selective optimization of the Rev-binding element of HIV- 1. *Nucleic Acids Res.* **1993**, *21*, 5509-5516.
- (60) Lupold, S.E.; Hicke, B.J.; Lin, Y. Identification and characterization of nuclease-stabilized RNA molecules that bind human prostate cancer cells via the prostate-specific membrane antigen. *Cancer Res.* **2002**, *62*, 4029-4033.
- (61) Convery, M.A.; Roswell, S.; Storehouse, N.J.; Ellington, A.D.; Hirao, I.; Murray, J.B.; Peabody, D.S.; Phillips, S.E.V.; Stockley, P.G. Crystal structure of an RNA aptamer-protein complex at 2.8 Å resolution. *Nat. Struct. Biol.* **1998**, *5*, 133-139.

- (62) Baugh, C.; Grate, D.; Wilson, C. 2.8 Å crystal structure of the malachite green aptamer. *J. Mol. Biol.* **2000**, *301*, 117-128.
- (63) Someya, T.; Baba, S.; Fujimoto, M.; Kawai, G.; Kumasaka, T.; Nakamura, K. Crystal structure of Hfq from *Bacillus subtilis* in complex with SELEX-derived RNA aptamer: insight into RNA-binding properties of bacterial Hfq. *Nucleic Acids Res.* **2012**, *40*, 1856-1867.
- (64) Lin, C.H.; Patel, D.J. Structural basis of DNA folding and recognition in an AMP-DNA aptamer complex: distinct architectures but common recognition motifs for DNA and RNA aptamers complexes to AMP. *Chem. Biol.* **1997**, *4*, 817-832.
- (65) Nomura, Y.; Sugiyama, S.; Sakamoto, T.; Miyakawa, S.; Adachi, H.; Takano, K.; Murakami, S.; Inoue, T.; Mori, Y.; Nakamura, Y.; Matsumura, H. Conformational plasticity of RNA for target recognition as revealed by the 2.15 Å crystal structure of a human IgG-aptamer complex. *Nucleic Acids Res.* **2010**, *38*, 7822-7829.
- (66) Sefah, K.; Shangguan, D.; Xiong, X.; O'Donoghue, M.B.; Tan, W. Development of DNA aptamers using cell-SELEX. *Nature Protoc.* **2010**, *5*, 1169-1185.
- (67) Ohuchi, S. Cell-SELEX technology. *Biores. Open Access.* **2012**, *1*, 265-272.
- (68) Barman, J. Targeting cancer cells using aptamers: cell-SELEX approach and recent advancements. *RSV Adv.* **2015**, *5*, 11724-11732.
- (69) Sun, H.; Zhu, X.; Lu, P.Y.; Rosato, R.R.; Tan, W.; Zu, Y. Oligonucleotide aptamers: new tools for targeted cancer therapy. *Mol. Ther. Nucleic Acids.* **2014**, *3*, e182.
- (70) Guo, K.; Paul, A.; Schichor, C.; Ziemer, G.; Wendel, H.P. Cell-SELEX: novel perspectives of aptamer-based therapeutics. *Int. J. Mol. Sci.* **2008**, *9*, 668-678.
- (71) Zhou, J.; Rossi, J.J. Cell-type-specific, aptamer-functionalized agents for targeted disease therapy. *Mol. Ther. Nucleic Acids.* **2014**, *3*, e169.
- (72) Zhou, J.; Rossi, J.J. Cell-specific aptamer-mediated targeted drug delivery. *Oligonucleotides.* **2011**, *21*, 1-10.
- (73) Siddiqui-Jain, A.; Grand, C.L.; Bearss, D.J.; Hurley, L.H. Direct evidence for a G-quadruplex in a promoter region and its targeting with a small molecule to repress c-MYC transcription. *Proc. Natl. Acad. Sci. U.S.A.* **2003**, *99*, 11593-11598.
- (74) Lee, J.Y.; Kim, D.S. Dramatic effect of single-base mutation on the conformational dynamics of human telomeric G-quadruplex. *Nucleic Acids Res.* **2009**, *37*, 3625-3634.
- (75) Porchetta, A.; Valleé-Bélisle, A.; Plaxco, K.W.; Ricci, F. Allosterically-tunable, DNA-based switches triggered by heavy metals. *J. Am. Chem. Soc.* **2013**, *135*, 13238-13241.

- (76) Jayasena, S.D. Aptamers: an emerging class of molecules that rival antibodies in diagnostics. *Clin. Chem.* **1999**, *45*, 1628-1650.
- (77) Dammer, U.; Hegner, M.; Anselmetti, D.; Wagner, P.; Dreier, M.; Huber, W.; Güntherodt, H.J. Specific antigen/antibody interactions measure by force microscopy. *Biophys. J.* **1996**, *70*, 2437-2441.
- (78) Simecka, J.W.; Ross, S.E.; Cassell, G.H.; Davis, J.K. Interactions of mycoplasmas with B cells: antibody production and nonspecific effects. *Clin. Infect. Dis.* **1993**, *17*, 176-182.
- (79) EMD Millipore Website. "SmartFlare™ Live Cell RNA Detection." <http://www.emdmillipore.com/US/en/life-science-research/genomic-analysis/SmartFlare-Live-Cell-RNA-Detection/ZdGb.qB.KCcAAAFLAQs0i.s1,nav> (Accessed August, 2015).
- (80) Lévy, R. "Localisation and properties of nanoparticle conjugates after cell entry...and why it matters." 250th National Meeting of the American Chemical Society, Boston, MA, August 16-20, 2015.
- (81) Swensen, J.S.; Xiao, Y.; Ferguson, B.S.; Lubin, A.A.; Lai, R.Y.; Heeger, A.J.; Plaxco, K.W.; Soh, H.T. Continuous, real-time monitoring of cocaine in the undiluted blood serum via a microfluidic, electrochemical aptamer-based sensor. *J. Am. Chem. Soc.* **2009**, *131*, 4262-4266.
- (82) Kirby, R.; Cho, E.J.; Gehrke, B.; Bayer, T.; Park, Y.S.; Neikirk, D.P.; McDevitt, J.T.; Ellington, A.D. Aptamer-based sensor arrays for the detection and quantification of proteins. *Anal. Chem.* **2004**, *76*, 4066-4075.
- (83) Willner, I.; Zayats, M. Electronic aptamer-based sensors. *Angew. Chem. Int. Edit.* **2007**, *46*, 6408-6418.
- (84) Baker, B.R.; Lai, R.Y.; Wood, M.S.; Doctor, E.H.; Heeger, A.J.; Plaxco, K.W. An electronic, aptamer-based small molecule sensor for the rapid label-free detection of cocaine in adulterated samples and biological fluids. *J. Am. Chem. Soc.* **2006**, *128*, 3138-3139.
- (85) So, H.; Won, K.; Kim, Y.H.; Kim, B.; Ryu, B.H.; Na, P.S.; Kim, H.; Lee, J. Single-walled carbon nanotube biosensors using aptamers as molecular recognition elements. *J. Am. Chem. Soc.* **2005**, *127*, 11906-11907.
- (86) Maehashi, K.; Katsura, T.; Kerman, K.; Takamura, Y.; Matsumoto, K.; Tamiya, E. Label-free protein biosensor based on aptamer-modified carbon nanotube field-effect transistors. *Anal. Chem.* **2007**, *79*, 782-787.
- (87) Xiao, Y.; Lubin, A.A.; Heeger, A.J.; Plaxco, K.W. Label-free electronic detection of thrombin in blood serum by using an aptamer-based sensor. *Angew. Chem.-Ger. Edit.* **2005**, *117*, 5592-5595.
- (88) Xiao, Y.; Lai, R.Y.; Plaxco, K.W. Preparation of electrode-immobilized, redox-modified

oligonucleotides for electrochemical DNA and aptamer-based sensing. *Nat. Protoc.* **2007**, *2*, 2875-2880.

(89) Yoshizumi, J.; Kumamoto, S.; Nakamura, M.; Yamana, K. Target-induced strand release (TISR) from aptamer-DNA duplex: a general strategy for electronic detection of biomolecules ranging from a small molecule to a large protein. *Analyst.* **2008**, *133*, 323-325.

(90) Lai, R.Y.; Seferos, D.S.; Keeger, A.J.; Bazan, G.C.; Plaxco, K.W. Comparison of the signaling and stability of electrochemical DNA sensors fabricated from 6- or 11-carbon self-assembled monolayers. *Langmuir.* **2006**, *22*, 10796-10800.

(91) Phares, N.; White, R.J.; Plaxco, K.W. Improving the stability and sensing of electrochemical biosensors by employing trithiol-anchoring groups in a six carbon self-assembled monolayer. *Anal. Chem.* **2009**, *81*, 1095-1100.

(92) Miller, J.R. *GraphPad Version 4.0 Step-by-Step Examples*, GraphPad Software Inc., San Diego, CA, **2003**.

(93) Gellert, M.; Lipsett, M.N.; Davies, D.R. Helix formation by guanylic acid. *Proc. Natl. Acad. Sci. U.S.A.* **1962**, *48*, 2013-2018.

(94) Zheng, K.; Wu, R.; He, Y.; Xiao, S.; Zhang, J.; Liu, J.; Hao, Y.; Tan, Z. A competitive formation of DNA:RNA hybrid G-quadruplex is responsible to the mitochondrial transcription termination at the DNA replication priming site. *Nucleic Acids Res.* **2014**, *42*, 10832-10844.

(95) Zhang, J.; Zheng, K.; Xiao, S.; Hao, S.; Tan, Z. Mechanism of manipulation of DNA:RNA hybrid G-quadruplex formation in transcription of G-rich DNA. *J. Am. Chem. Soc.* **2014**, *136*, 1381-1390.

(96) Wu, R.; Zheng, K.; Zhang, J.; Hao, Y.; Tan Z. Formation of DNA:RNA hybrid G-quadruplex in bacterial cells and its dominance of the intramolecular DNA G-quadruplex in mediating transcription termination. *Angew. Chem. Int. Edit.* **2015**, *54*, 2447-2451.

(97) Simonsson, T. G-quadruplex DNA structures variations on a theme. *Biol. Chem.* **2005**, *382*, 621-628.

(98) Burge, S.; Parkinson, G.N.; Hazel, P.; Todd, A.K.; Neidle, S. Quadruplex DNA: sequence, topology and structure. *Nucleic Acids Res.* **2006**, *34*, 5402-5415.

(99) Tran, P.L.T.; Mergny, J.; Alberti, P. Stability of telomeric G-quadruplexes. *Nucleic Acids Res.* **2011**, *39*, 3282-3292.

(100) Lane, A.N.; Chaires, J.B.; Gray, R.D.; Trent, J.O. Stability and kinetics of G-quadruplex structures. *Nucleic Acids Res.* **2008**, *36*, 5482-5515.

(101) Le, H.T.; Dean, W.L.; Buscaglia, R.; Chaires, J.B.; Trent, R.O. An investigation of G-

quadruplex structural polymorphism in the human telomere using a combined approach of hydrodynamic bead modeling and molecular dynamics simulation. *J. Phys. Chem. B.* **2014**, *118*, 5390-5405.

(102) Calculated from IDT OligoAnalyzer 3.1 for 5'-GGGG-3' annealed to its complement. www.idtdna.com/calc/analyzer.

(103) Sen, D.; Gilbert, W. Formation of parallel four-stranded complexes by guanine-rich motifs in DNA and its implications for meiosis. *Nature.* **1988**, *334*, 364-366.

(104) Šket, P.; Črnugelj, M.; Plavec, J. Identification of mixed di-cation forms of G-quadruplex in solution. *Nucleic Acids Res.* **2005**, *33*, 3691-3697.

(105) Ambrus, A.; Chen, D.; Dai, J.; Bialis, T.; Jones, R.A.; Yang, D. Human telomeric sequence forms a hybrid-type intramolecular G-quadruplex structure with mixed parallel/antiparallel strands in potassium solution. *Nucleic Acids Res.* **2006**, *34*, 2723-2735.

(106) Lodish, H.; Berk, A.; Zipursky, S.L. Intracellular ion environment and membrane electric potential. In *Molecular Cell Biology*; W.H. Freeman: New York; 2000, 4th Ed.

(107) Dick, D.A.T. The distribution of sodium, potassium and chloride in the nucleus and cytoplasm of *Bufo bufo* oocytes measured by electron microprobe analysis. *J. Physiol.* **1978**, *284*, 37-53.

(108) Aaronson, R.P.; Woo, E. Organization in the cell nucleus: divalent cations modulate the distribution of condensed and diffuse chromatin. *J. Cell Biol.* **1981**, *90*, 181-186.

(109) Keniry, M.A. Quadruplex structures in nucleic acids. *Biopolymers.* **2001**, *56*, 123-146.

(110) Huppert, J.L. Hunting G-quadruplexes. *Biochimie.* **2008**, *90*, 1140-1148.

(111) Lipps, H.J.; Rhodes, D. G-quadruplex structures: *in vivo* evidence and function. *Trends Cell Biol.* **2009**, *19*, 414-422.

(112) Simone, R.; Fratta, P.; Neidle, S.; Parkinson, G.N.; Isaacs, A.M. G-quadruplexes: emerging roles in neurodegenerative diseases and the non-coding transcriptome. *FEBS Lett.* **2015**, *589*, 1653-1668.

(113) Agarwala, P.; Pandey, S.; Maiti, S. The tale of RNA G-quadruplex. *Org. Biomol. Chem.* **2015**, *13*, 5570-5585.

(114) Patel, D.J.; Phan, A.T.; Kuryavyi, V. Human telomere, oncogenic promoter and 5'UTR G-quadruplexes: diverse higher order DNA and RNA targets for cancer therapeutics. *Nucleic Acids Res.* **2007**, *35*, 7429-7455.

(115) Gray, L.T.; Vallur, A.C.; Eddy, J.; Maizels, N. G-quadruplexes are genomewide targets of transcriptional helicases XPB and XPD. *Nat. Chem. Biol.* **2013**, *10*, 313-318.

- (116) Maizels, N.; Gray, L.T. The G4 genome. *PLOS Genet.* **2013**, *9*, e1003468.
- (117) Biffi, G.; Tannahill, D.; McCafferty, J.; Balasubramanian, S. Quantitative visualization of DNA G-quadruplex structures in human cells. *Nat. Chem.* **2013**, *5*, 182-186.
- (118) Biffi, G.; Di Antonio, M.; Tannahill, D.; Balasubramanian, S. Visualization and selective chemical targeting of RNA G-quadruplex structures in the cytoplasm of human cells. *Nat. Chem.* **2014**, *6*, 76-80.
- (119) Eddy, J.; Maizels, N. Gene function correlates with potential for G4 DNA formation in the human genome. *Nucleic Acids Res.* **2006**, *34*, 3887-3896.
- (120) Punnoose, J.A.; Cui, Y.; Koirala, D.; Yangyuoru, P.M.; Ghimire, C.; Shrestha, P.; Mao, H. Interaction of G-quadruplexes in the full-length 3' human telomeric overhang. *J. Am. Chem. Soc.* **2014**, *136*, 18062-18069.
- (121) Hammond-Kosack, M.C.; Dobrinski, B.; Lurz, R.; Docherty, K.; Kilpatrick, M.W. The human insulin gene linked polymorphic region exhibits an altered DNA structure. *Nucleic Acids Res.* **1992**, *20*, 231-236.
- (122) He, Q.; Zeng, P.; Tan, J.; Qu, T.; Gu, L.; Huang, Z. G-quadruplex-mediated regulation of telomere binding protein POT1 gene expression. *Biochim. Biophys. Acta* **2014**, *1840*, 2222–2233.
- (123) Hwang, H.; Buncher, N.; Opresko, P.L.; Myong, S. POT1- TPP1 regulates telomere overhang structural dynamics. *Structure* **2012**, *20*, 1872–1880.
- (124) Ray, S.; Bandaria, J.N.; Qureshi, M.H.; Yildiz, A.; Balci, H. G-quadruplex formation in telomere enhances POT1/TPP1 protection against RPA binding. *Proc. Natl Acad. Sci. USA* **2014**, *111*, 2990–2995.
- (125) Nagata, T.; Yusuke, T.; Ono, A.; Nagata, K.; Konishi, Y.; Nukina, T.; Ono, M.; Matsugami, A.; Furukawa, A.; Fujimoto, N.; Fukuda, H.; Nakagama, H.; Katahira, M. Elucidation of the mode of interaction in the UP1-telomerase RNA-telomeric DNA ternary complex which serves to recruit telomerase to telomeric DNA and to enhance the telomerase activity. *Nucleic Acids Res.* **2008**, *36*, 6816-6824.
- (126) Armas, P.; Nasif, S.; Calcaterra, N.B. Cellular nucleic acid binding protein binds G-rich single-stranded nucleic acids and may function as a nucleic acid chaperone. *J. Cell Biochem.* **2008**, *103*, 1013-1036.
- (127) Majello, B.; De Luca, P.; Suske, G.; Lania, L. Differential transcriptional regulation of c-myc promoter through the same DNA binding sites targeted by Sp1-like proteins. *Oncogene.* **1995**, *10*, 1841-1848.
- (128) Bugaut, A.; Balasubramanian, S. 5'-UTR RNA G-quadruplexes: translation regulation and

targeting. *Nucleic Acids Res.* **2012**, *40*, 4727-4741.

(129) Yu, Z.; Schonhofs, J.D.; Dhakal, S.; Bajracharya, R.; Hegde, R.; Soumitra, B.; Mao, H. ILPR G-quadruplexes formed in seconds demonstrate high mechanical stabilities. *J. Am Chem. Soc.* **2009**, *131*, 1876-1882.

(130) Tansey, W.P. Mammalian MYC proteins and cancer. *New J. Sci.* **2014**, *2014*, 1-27.

(131) Dang, C.V. C-Myc target genes involved in cell growth, apoptosis, and metabolism. *Mol. Cell. Biol.* **1999**, *19*, 1-11.

(132) González, V.; Hurley, L.H. The c-Myc NHE III₁: function and regulation. *Annu. Rev. Pharmacol. Toxicol.* **2010**, *50*, 111-129.

(133) Hurley, L.H. DNA and its associated processes as targets for cancer therapy. *Nat. Rev.* **2002**, *2*, 188-200.

(134) Onel, B.; Lin, C.; Yang, D. DNA G-quadruplex and its potential as anticancer drug target. *Sci. China.* **2014**, *57*, 1605-1614.

(135) Lemarteleur, T.; Gomez, D.; Paterski, R.; Mandine, E.; Mailliet, P.; Riou, J.F. Stabilization of the c-myc gene promoter quadruplex by specific ligands' inhibitors of telomerase. *Biochem. Biophys. Res. Commun.* **2004**, *323*, 802-808.

(136) Counter, C. M.; Avilion, A.A.; LeFeuvre, C.E.; Stewart, N.G.; Greider, C.W.; Harley, C.B.; Bacchetti, S. Telomere shortening associated with chromosome instability is arrested in immortal cells which express telomerase activity. *EMBO J.* **1992**, *11*, 1921-1929.

(137) Bearss, D.J.; Hurley, L.H.; Von Hoff, D.D. Telomere maintenance mechanisms as a target for drug development. *Oncogene.* **2009**, *19*, 6632-6641.

(138) Xu, Y. Chemistry in human telomere biology: structure, function and targeting of telomere DNA/RNA. *Chem. Soc. Rev.* **2010**, *40*, 2719-2740.

(139) Xu, X.; Ishizuka, T.; Kurabayashi, K.; Komiyama, M. Consecutive formation of G-quadruplexes in human telomeric-overhang DNA: a protective capping structure for telomere ends. *Angew. Chem. Int. Ed.* **2009**, *48*, 7833-7836.

(140) Ying, L.; Green, J.J.; Haitao, L.; Klenerman, D.; Balasubramanian, S. Studies on the structure and dynamics of the human telomeric G quadruplex by single-molecule fluorescence resonance energy transfer. *Proc. Natl Acad. Sci. USA* **2003**, *100*, 14629-14634.

(141) Li, J.; Correia, J.J.; Wang, L.; Trent, R.O.; Chaires, J.B. Not so crystal clear: the structure of the human telomere G-quadruplex in solution differs from that present in a crystal. *Nucleic Acids Res.* **2005**, *33*, 4649-4659.

- (142) Holder, I. T.; Drescher, M.; Hartig, J.S. Structural characterization of quadruplex DNA with in-cell EPR approaches. *Bioorg. Med. Chem.* **2013**, *21*, 6156–6161.
- (143) Singh, V.; Azarkh, M.; Drescher, M.; Hartig, J. Conformations of individual quadruplex units studied in the context of extended human telomeric DNA. *Chem. Commun.* **2012**, *48*, 8258–8260.
- (144) Kim, N.W.; Piatyszek, M.A.; Prowse, K.R.; Harley, C.B.; West, M.D.; Ho, P.L.C. Specific association of human telomerase activity with immortal cells and cancer. *Science.* **1994**, *266*, 2011–2015.
- (145) Counter, C.M.; Hirte, H.W.; Bachetti, S.; Harley, C.B. Telomerase activity in human ovarian carcinoma. *Proc. Natl Acad. Sci. USA.* **1998**, *91*, 2900–2904.
- (146) Fletcher, T.M.; Sun, D.; Salazar, M.; Hurley, L.H. Effect of DNA secondary structure on human telomerase activity. *Biochemistry.* **1998**, *37*, 5536–5541.
- (147) Ruden, M.; Puri, N. Novel anticancer therapeutics targeting telomerase. *Cancer Treat. Rev.* **2013**, *39*, 444-456.
- (148) Sekaran, V.; Soares, J.; Jarstfer, M.B. Telomere maintenance as a target for drug discovery. *J. Med. Chem.* **2014**, *57*, 521-538.
- (149) Hwang, H.; Buncher, N.; Opresko, P.L.; Myong, S. POT1-TPP1 regulates telomere overhang structural dynamics. *Structure* **2012**, *20*, 1872–1880.
- (150) Nakagawa, Y.; Kawaguchi, Y.; Twells, R.C.; Muxworthy, C.; Hunter, K.M.; Wilson, A.; Merriman, M.E.; Cox, R.D.; Merriman, T.; Cucca, F.; McKinney, P.A.; Shield, J.P.; Tuomilehto, J.; Tuomilehto-Wolf, E.; Ionesco-Tirgoviste, C.; Nisticò, L.; Buzzetti, R.; Pozzilli, P.; Joner, G.; Thorsby, E.; Undlien, D.E.; Pociot, F.; Nerup, J.; Rönningen, K.S.; Bain, S.C.; Todd, J.A. Fine mapping of the diabetes-susceptibility locus, IDDM4, on chromosome 11q13. *Am. J. Hum. Genet.* **1998**, *63*, 547-556.
- (151) Hanumantharao, P.; Firestine, S.M. Characterization of insulin ILPR sequences for their ability to adopt a G-quadruplex structure. *Nucleos. Nucleot. Nucl.* **2010**, *29*, 81-90.
- (152) Bennett, S.; Todd, J.A. Human type 1 diabetes and the insulin gene. Principles of mapping polygenes. *Annu. Rev. Genet.* **1996**, *30*, 343-370.
- (153) Undlien, D.E. Insulin gene region-encoded susceptibility to IDDM maps upstream of the insulin gene. *Diabetes.* **1995**, *44*, 620-625.
- (154) McGinnis, R.E. Insulin gene 5' flanking polymorphism. Length of class 1 alleles in number of repeat units. *Diabetes.* **1995**, *44*, 1296-1302.
- (155) Cai, C.Q.; Zhang, T.; Breslin, M.B.; Giraud, M.; Lan, M.S. Both polymorphic variable

number of tandem repeats and autoimmune regulator modulate differential expression of insulin in human thymic epithelial cells. *Diabetes*. **2011**, *60*, 336-344.

(156) Lucassen, A.M.; Julier, C.; Beressi, J.; Boitard, C.; Froguel, P.; Lathrop, M.; Bell, M.I. Susceptibility to insulin dependent diabetes mellitus maps to a 4.1 kb segment of DNA spanning the insulin gene and associated VNTR. *Nat. Genet.* **1993**, *4*, 305-310.

(157) Pugliese, A.; Zeller, M.; Fernandez, Jr., A.; Zalcborg, L.J.; Bartlett, R.J.; Ricordi, C.; Pietropaolo, M.; Eisenbarth, G.S.; Bennett, S.T.; Patel, D.D. The insulin gene is transcribed in the human thymus and transcription levels correlate with allelic variation at the *INS* VNTR-IDDM2 susceptibility locus for type 1 diabetes. *Nat. Genet.* **1997**, *15*, 293-297.

(158) Wang, Y.; Zhang, H.; Ligon, L.A.; McGown, L.B. Association of insulin-like growth factor 2 with the insulin-linked polymorphic region in cultured getal thymus cells. *Biochemistry*. **2009**, *48*, 8189-8194.

(159) Schonhoft, J.D.; Das, A.; Achamyelah, F.; Samdani, S., Sewell, A.; Mao, H.; Basu, S. ILPR repeats adopt diverse G-quadruplex conformations that determine insulin binding. *Biopolymers*. **2010**, *93*, 21-31.

(160) Lew, A.; Rutter, W.J.; Kennedy, G.C. Unusual DNA structure of the diabetes susceptibility locus IDDM2 and its effect on transcription by the insulin promoter factor Pur-1/MAZ. *Proc. Natl. Acad. Sci. U.S.A.* **2000**, *97*, 12508-12512.

(161) Ahmed, S.; Bennett, S.T.; Huxtable, S.J.; Todd, J.A.; Matthews, D.R.; Gough, S.C. *INS* VNTR allelic variation and dynamic insulin secretion in healthy adult non-diabetic caucasian subjects. *Diabetic Med.* **1999**, *16*, 910-917.

(162) Schonhoft, J.D.; Bajracharya, R.; Dhakal, S.; Yu, Z.; Mao, H.; Basu, S. Direct experimental evidence for quadruplex-quadruplex interaction within the human ILPR. *Nucleic Acids Res.* **2009**, *37*, 3310-3320.

(163) Smit, E.M.; Borst, P. LSD-25 does not intercalate in DNA. *Nature*. **1971**, *232*, 191-192.

(164) Mukundan, Jr., S.; Xu, Y.; Zon, G.; Marzilli, L.G. Heteronuclear carbon-13-protin NMR investigations of the effects on an oligodeoxyribonucleotide of intrastrand cross-linking by a platinum anticancer drug; a large shift of C3' accompanies an Sto N conformation change. *J. Am. Chem. Soc.* **1991**, *113*, 3021-3027.

(165) Dai, J.; Carver, M.; Punchihewa, C.; Jones, R.A.; Yang, D. Structure of the Hybrid-2 type intramolecular human telomeric G-quadruplex in K^+ solution: insights into structure polymorphism of the human telomeric sequences. *Nucleic Acids Res.* **2007**, *35*, 4927-4940.

(166) Wang, Z.; Li, M.; Hsu, S.D.; Chang, T. Structural basis of sodium-potassium exchange of a human telomeric DNA quadruplex without topological conversion. *Nucleic Acids Res.* **2014**, *42*, 4723-4733.

- (167) Heddi, B.; Phan, A.T. Structure of human telomeric DNA in crowded solution. *J. Am. Chem. Soc.* **2011**, *57*, 11–24.
- (168) Adrian, M.; Heddi, B.; Phan, A.T. NMR spectroscopy of G-quadruplexes. *Methods.* **2012**, *57*, 11–24.
- (169) Anderson, K.M.; Nguyen, D.; Esadze, A.; Zandrashvili, L.; Gorenstein, D.G.; Iwahara, J.; A chemical approach for site-specific identification of NMR signals from protein side chain NH_3^+ groups forming intermolecular ion pairs in protein-nucleic acid complexes. *J. Biomol. NMR.* **2015**, *62*, 1-5.
- (170) Sheperd, N.E.; Gamsjaeger, R.; Vandevenne, M.; Cubeddu, L.; Mackay, J.P. Site directed nitroxide spin labeling of oligonucleotides for NMR and EPR studies. *Tetrahedron.* **2015**, *71*, 813-819.
- (171) Crane, N.A.; Salzman, N.P. Density labeling of mammalian cell DNA and RNA with nitrogen-15. *Proc. Natl. Acad. Sci. U.S.A.* **1968**, *61*, 1356-1362.
- (172) Romainczyk, O.; Elduque, X.; Engels, J.W. Attachment of nitroxide spin labels to nucleic acids for EPR. *Curr. Protoc. Nucleic Acid Chem.* **2012**, Unit 7.17.
- (173) Jakobsen, U.; Shelke, S.A.; Vogel, S.; Sigurdsson, S.T. Site-directed spin-labeling of nucleic acids by click chemistry: detection of abasic sites in duplex DNA by EPR spectroscopy. *J. Am. Chem. Soc.* **2010**, *132*, 10424-10428.
- (174) Shevelev, G.Y.; Krumkacheva, O.A.; Lomzov, A.A.; Kuzhelev, A.A.; Rogoshnikova, O.Y.; Trukhin, D.V.; Troitskaya, T.I.; Tormushev, V.M.; Fedin, M.V.; Pyshnyi, D.P.; Bagryansjaya, E.G. Physiological-temperature distance measurement in nucleic acid using triarylmethyl-based spin labels and pulsed dipolar EPR spectroscopy. *J. Am. Chem. Soc.* **2014**, *136*, 9874-9877.
- (175) Dalaloyan, A.; Qi, M.; Ruthstein, S.; Vega, S.; Godt, A.; Feintuch, A.; Goldfarb, D. Gd(III)-Dg(III) EPR distance measurements – the range of accessible distances and the impact of zero field splitting. *Phys.Chem.Chem.Phys.* **2015**, *17*, 18464-18476.
- (176) Yun, C.S.; Javier, A.; Jennings, T.; Fisher, M.; Hira, S.; Peterson, S.; Hopkins, B.; Reich, N.O.; Strouse, G.F. Nanometal surface energy transfer in optical rulers, breaking the FRET barrier. *J. Am. Chem. Soc.* **2005**, *127*, 3115-3119.
- (177) Singh, M.P.; Jennings, T.L.; Strouse, G.F. Involvement of the LSPR spectral overlap for energy transfer between a dye and Au nanoparticle. *J. Am. Chem. Soc.* **2010**, *132*, 9383-9391.
- (178) Breshike, C.; Riskowski, R.; Strouse, G.F. Leaving Förster resonance energy transfer behind: nanometal surface energy transfer predicts the size-enhanced energy coupling between a metal nanoparticle and an emitting dipole. *J. Phys. Chem. C.* **2013**, *117*, 23942-23949.

- (179) Jennings, T.L.; Schlatterer, J.C.; Singh, M.P.; Greenbaum, N.L.; Strouse, G.F. NSET molecular beacon analysis of hammerhead RNA substrate binding and catalysis. *Nano Lett.* **2006**, *6*, 1318-1324.
- (180) Parkinson, G.N.; Lee, M.P.H.; Neidle, S. Crystal structure of parallel quadruplexes from human telomeric DNA. *Nature.* **2002**, *417*, 876-880.
- (181) Wiodarczyk, A.; Grzybowski, P.; Patkowski, A.; Dobek, A. Effect of ions on the polymorphism, effective charge, and stability of human telomeric DNA. Photon correlation spectroscopy and circular dichroism studies. *J. Phys. Chem. B.* **2005**, *109*, 3594–3605.
- (182) Paramasivan, S.; Rujan, I.; Bolton, P.H. Circular dichroism of quadruplex DNAs: applications to structure, cation effects and ligand binding. *Methods.* **2007**, *43*, 324–331.
- (183) Ashkin, A.; Dziedzic, J.M.; Bjorkholm, J.E.; Chu, S. Observation of a single-beam gradient force optical trap for dielectric particles. *Opt. Lett.* **1986**, *11*, 288-290.
- (184) Heller, I.; Hoekstra, T.P.; King, G.A.; Peterman, E.J.G.; Wuite, G.J.L. Optical tweezers analysis of DNA-protein complexes. *Chem. Rev.* **2014**, *114*, 3087-3119.
- (185) Moffitt, J.R.; Chemla, Y.A.; Smith, S.B.; Bustamante, C. Recent advances in optical tweezers. *Annu. Rev. Biochem.* **2008**, *77*, 205-228.
- (186) Ma, H.; Zhang, Y.; Ye, A. Single-cell discrimination based on optical tweezers Raman Spectroscopy. *Chin. Sci. Bull.* **2013**, *58*, 2594-2600.
- (187) Zhong, M.; Wei, X.; Zhou, J.; Wang, Z.; Li, Y. Trapping red blood cells in living animals using optical tweezers. *Nat. Commun.* **2012**, *4*, 1-7.
- (188) Zhang, H.; Liu, K. Optical tweezers for single cells. *J. R. Soc. Interface.* **2008**, *5*, 671-690.
- (189) Applied Photophysics Ltd. An introduction to circular dichroism (CD) spectroscopy. www.photophysics.com/tutorials/circular-dichroism-cd-spectroscopy (Accessed June 27th, 2015).
- (190) Lam, E.Y.N.; Beraldi, D.; Tannahill, D.; Balasubramanian, S. G-quadruplex structures are stable and detectable in human genomic DNA. *Nat. Commun.* **2012**, *4*, 1-7.
- (191) Förster, T. Zwischenmolekular Energiewanderung und Fluoreszenz. *Ann. Phys. (Berlin, Ger.)* **1948**, *437*, 55-75.
- (192) Lakowicz, J.R. Principles of fluorescence spectroscopy; Kluwer Academic; Plenum: New York, **1999**, 2nd Ed.
- (193) Didenko, V.L. DNA probes using fluorescence resonance energy transfer (FRET): designs and applications. *Biotechniques.* **2001**, *31*, 1106-1121.

- (194) Stein, I.S.; Steinhaur, C.; Tinnefeld, P. Single-molecule four-color FRET visualizes energy-transfer paths on DNA origami. *J. Am. Chem. Soc.* **2011**, *133*, 4193-4195.
- (195) Hu, R.; Zhang, X.; Zhao, Z.; Zhu, G.; Chen, T.; Fu, T.; Tan, W. DNA Nanoflowers for multiplexed cellular imaging and traceable targeted drug delivery. *Angew. Chem. Int. Ed.* **2014**, *53*, 5821-5826.
- (196) Kochuveedu, S.T.; Son, T.; Lee, Y.; Lee, M.; Kim, D.; Kim, D.H. Revolutionizing the FRET-based light emission in core-shell nanostructures via comprehensive activity of surface plasmons. *Scientific Reports.* **2014**, *4*, 4735.
- (197) Lunz, M.; Gerard, V.A.; Gun'ko, Y.K.; Lesnyak, V.; Gaponik, N.; Susha, A.S.; Rogach, A.L.; Bradley, A.L. Surface plasmon enhanced energy transfer between donor and acceptor CdTe nanocrystal quantum dot monolayers. *Nano Lett.* **2011**, *11*, 3341-3345.
- (198) Asselin, J.; Viger, M.; Boudreau, D. Metal-enhanced fluorescence and FRET in multilayer core-shell nanoparticles. *Adv. Chem.* **2014**, 1-16.
- (199) Chance, R.R.; Prock, A.; Silbey, R. Comments on the classical theory of energy-transfer. *J. Chem. Phys.* **1975**, *62*, 2245-2253.
- (200) Kuhn, H. Classical aspects of energy transfer in molecular systems. *J. Chem. Phys.* **1970**, *53*, 101-108.
- (201) Gersten, J.; Nitzan, A. Spectroscopic Properties of Molecules Interacting with Small Dielectric Particles. *J. Chem. Phys.* **1981**, *75*, 1139-1152.
- (202) Griffin, J.; Singh, A. K.; Senapati, D.; Rhodes, P.; Mitchell, K.; Robinson, B.; Yu, E.; Ray, P. Size- and distance-dependent nanoparticle surface-energy transfer (NSET) method for selective sensing of Hepatitis C virus RNA. *Chem. Eur. J.* **2009**, *15*, 342-351.
- (203) Ghosh, D.; Chattopadhyay, N. Gold nanoparticles: acceptors for efficient energy transfer from the photoexcited fluorophores. *Opt. Photon. J.* **2013**, *3*, 18-26.
- (204) Muroski, M.E.; Carnevale, K.F.; Riskowski, R.A.; Strouse, G.F. Plasmid transfection in mammalian cells spatiotemporally tracked by a gold nanoparticle. *ACS Nano.* **2015**, *9*, 124-133.
- (205) Singh, A.K.; Lu, W.; Senapati, D.; Khan, S.A.; Fan, Z.; Senapati, T.; Demeritte, L.B.; Ray, P.C. Long-range nanoparticle surface-energy-transfer ruler for monitoring photothermal therapy response. *Small.* **2011**, *7*, 2517-2525.
- (206) Chen, Y.; O'Donoghue, M.B.; Huang, Y.; Kang, H.; Phillips, J.A.; Chen, X.; Estevez, M.; Tan, W. A surface energy transfer nanoruler for measuring binding site distances on live cell surfaces. *J. Am. Chem. Soc.* **2010**, *132*, 16559-16570.
- (207) Jeschke, G. Conformational dynamics and distribution of nitroxide spin labels. *Prog. Nucl.*

Mag. Res. Sp. **2013**, 72, 42-60.

(208) Alexander, N.S.; Stein, R.A.; Koteiche, H.A.; Kaufmann, K.W.; Mchaourab, H.S.; Meiler, J. RosettaEPR: Rotamer library for spin label structure and dynamics. *PLoS ONE*, **2013**, 8, e72851.

(209) Tombolato, F.; Ferrarini, A. Dynamics of the nitroxide side chain in spin-labeled proteins. *J. Phys. Chem. B.* **2006**, 110, 26248-26259.

(210) Prisner, T.F.; Marko, A.; Sigurdsson, S.Th. Conformational dynamics of nucleic acid molecules studied by PELDOR spectroscopy with rigid spin labels. *J. Magn. Reson.* **2015**, 252, 187-198.

(211) Sale, K.; Song, L.; Liu, Y.; Perozo, E.; Fajer, P. Explicit treatment of spin labels in modeling distance constraints from dipolar EPR and DEER. *J. Am. Chem. Soc.* **2005**, 127, 9334-9335.

(212) Fajer, M.I.; Li, H.; Yang, W.; Fajer, P.G. Mapping electron paramagnetic resonances spin label conformations by the simulated scaling method. *J. Am. Chem. Soc.* **2007**, 129, 13840-13846.

(213) Qin, P.Z.; Warncke, K. *Methods in enzymology*, Vol 563. Elsevier; Oxford. **2015**, 1st Ed.

(214) Shevelev, G.Y.; Krumkacheva, O.A.; Lomzov, A.A.; Kuzhelev, A.A.; Trukhin, D.V.; Rogozhnikova, O.Y.; Tormyshev, V.M.; Pyshnyi, D.V.; Fedin, M.V.; Bagryanskaya, E.G. Triarylmethyl labels: toward improving the accuracy of EPR nanoscale distance measurements in DNAs. *J. Phys. Chem. B.* **2015**, 119, 11443-11458.

(215) Fielding, A.J.; Concilio, M.G.; Heaven, G.; Hollas, M.A. New developments in spin labels for pulsed dipolar EPR. *Molecules.* **2014**, 19, 16998-17025.

(216) Riskowski, R.; Armstrong, R.E.; Strouse, G.F. Triangulating nucleic acid conformations using multicolor surface energy transfer (McSET). *ACS Nano. In Review.*

(217) Sindbert, S.; Kalinin, S.; Nguyen, H.; Kienzler, A.; Clima, L.; Bannawarth, W.; Appel, B.; Müller, S.; Siedal, C.A. Accurate distance determination of nucleic acids via Förster resonances energy transfer: implications of dye linker length and rigidity. *J. Am. Chem. Soc.* **2011**, 133, 2463-2480.

(218) Søndergaard, S.; Asnauryan, M.; Hastrup, E.K.; Schøtt, B.; Birkedal, V.; Corry, B. Dynamics of fluorescent dyes attached to G-quadruplex DNA and their effect on FRET experiments. *ChemPhysChem.* **2015**, 16, 2562-2570.

(219) Unruh, J.R.; Gokulrangan, G.; Lushington, G.H.; Johnson, C.K.; Wilson, G.S. Orientational dynamics and dye-DNA interactions in a dye-labeled DNA aptamer. *Biophys. J.* **2005**, 88, 3455-3465.

- (220) Haller, A.; Rieder, U.; Aigner, M.; Blanchard, S.C.; Micura, R. Conformational capture of the saM-II riboswitch. *Nat. Chem. Biol.* **2007**, *7*, 393–400.
- (221) Yamamoto, R.; Kumar, P.K.R. Molecular beacon aptamer fluoresces in the presence of Tat protein of HIV-1. *Genes Cells.* **2000**, *5*, 389–396.
- (222) Ikebukuro, K.; Kiyohara, C.; Sode, K. Novel electrochemical sensor system for protein using the aptamers in sandwich manner. *Biosens. Bioelectron.* **2005**, *20*, 2168–2172.
- (223) Lu, W.; Arumugam, S.R.; Senapati, D.; Singh, A.K.; Arbnesi, T.; Khan, S.A.; Yu, H.; Ray, P.C. Multifunctional oval-shaped gold-nanoparticle-based selective detection of breast cancer cells using simple colorimetric and highly sensitive two-photon scattering assay. *ACS Nano.* **2010**, *4*, 1739–1749.
- (224) Pavlov, V.; Xiao, Y.; Shlyahovsky, B.; Willner, I. Aptamer-functionalized Au nanoparticles for the amplified optical detection of thrombin. *J. Am. Chem. Soc.* **2004**, *126*, 11768–11769.
- (225) Ray, P.C.; Fan, Z.; Crouch, R.A.; Sinha, S.S.; Pramanik, A. Nanoscopic optical rulers beyond the FRET distance limit: fundamentals and applications. *Chem. Soc. Rev.* **2014**, *43*, 6370–6404.
- (226) Yamanaa, K.; Ohtania, Y.; Nakanoa, H.; and Saitob, I. Bis- pyrene labeled DNA aptamer as an intelligent fluorescent biosensor. *Bioorg. Med. Chem. Lett.* **2003**, *13*, 3429–3431.
- (227) Porchetta, A.; Valleé-Bélisle, A.; Plaxco, K.W.; Ricci, F. Using distal site mutations and allosteric inhibition to tune, extend and narrow the useful dynamic range of aptamer-based sensors. *J. Am. Chem. Soc.* **2012**, *134*, 20601–20604.
- (228) Mahtab, R.; Rogers, J.P.; Singleton, C.P.; Murphy, C.J. Preferential adsorption of a 'kinked' DNA to a neutral curved surface: comparisons to and implications for nonspecific DNA-protein interactions. *J. Am. Chem. Soc.* **1996**, *118*, 7028–7032.
- (229) Ricci, F.; Valleé-Bélisle, A.; Porchetta, A.; Plaxco, K.W. The rational design of allosteric inhibitors and activators using the population-shift model: in vitro validation and application to an artificial biosensor. *J. Am. Chem. Soc.* **2012**, *134*, 15177–15180.
- (230) Nicewarner Peña, S.R.; Raina, S.; Goodrich, G.P.; Federoff, N.V.; Keating, C.D. Hybridization and enzymatic extension of Au nanoparticle-bound oligonucleotides. *J. Am. Chem. Soc.* **2002**, *124*, 7314–7323.
- (231) Bin, X.; Sargent, E.H.; Kelley, S.O. Nanostructuring of sensors determines the efficiency of biomolecular capture. *Anal. Chem.* **2010**, *82*, 5928–5931.
- (232) Mahtab, R.; Rogers, J.P.; Murphy, C.J. Protein-sized quantum dot luminescence can distinguish between "straight", "bent", and "kinked" oligonucleotides. *J. Am. Chem. Soc.* **1995**,

117, 9099–9100.

(233) Gearhart, L.A.; Ploehn, H.J.; Murphy, C.J. Oligonucleotide adsorption to gold nanoparticles: A surface-enhanced raman spectroscopy study of intrinsically bent DNA. *J. Phys. Chem. B.* **2001**, *105*, 12609–12615.

(234) Achenbach, J.C.; Nutiu, R.; Li, Y. Structure-switching allosteric deoxyribozymes. *Anal. Chim. Acta.* **2005**, *234*, 41–51.

(235) Arnaut, V.; Langecker, M.; Simmel, F. Nanopore force spectroscopy of aptamer-ligand complexes. *Biophys. J.* **2013**, *105*, 1199–1207.

(236) Yangyuoru, P.; Dhakal, S.; Yu, Z.; Koirala, D.; Mwongela, S.M.; Mao, H. Single-molecule measurements of the binding between small molecules and DNA aptamers. *Anal. Chem.* **2012**, *84*, 5298–5303.

(237) Calculated from IDT OligoAnalyzer 3.1. www.idtdna.com/calc/analyzer.

(238) Nakamura, I.; Shi, A.; Nutiu, R.; Yu, J.M.Y.; Li, Y. Kinetic modeling of designed signaling DNA aptamers. *Phys. Rev. E.* **2009**, *79*, 031906.

(239) Catasti, P.; Chen, X.; Moyzis, R.K.; Bradbury, E.M.; Gupta, G. Structure–function correlations of the insulin-linked polymorphic region. *J. Mol. Biol.* **1996**, *254*, 534–545.

(240) Cao, E.; Sun, X.; Zhang, X.; Li, J.; Bai, C. Fold-back tetraplex DNA species in DNase I-resistant DNA isolated from Hela cells. *J. Biomol. Struct. Dyn.* **2000**, *17*, 871–878.

(241) Rangan, A.; Fedoroff, O.Y.; Hurley, L.H. Induction of duplex to G-quadruplex transition in the c-Myc promoter region by a small molecule. *J. Biol. Chem.* **2001**, *276*, 4640–4646.

(242) Maizels, N. Dynamic roles for G4 DNA in the biology of eukaryotic cells. *Nat. Struct. Mol. Biol.* **2006**, *13*, 1055–1059.

(243) Hansel, R.; Lohr, F.; Trantirek, L.; Dotsch, V. High-resolution insight into G-overhang architecture. *J. Am. Chem. Soc.* **2013**, *135*, 2816–2824.

(244) Dai, J.; Carver, M.; Yang, D. Polymorphism of human telomeric quadruplex structures. *Biochimie.* **2008**, *90*, 1172–1183.

(245) Dai, J.; Punchihewa, C.; Ambrus, A.; Chen, D.; Jones, R.A.; Yang, D. Structure of the intramolecular human telomeric G-quadruplex in potassium solution: A novel adenine triple formation. *Nucleic Acids Res.* **2007**, *35*, 2440–2450.

(246) Patel, P.K.; Koti, A.S.; Hosur, R.V. NMR studies on truncated sequences of human telomeric DNA: Observation of a novel A-tetrad. *Nucleic Acids Res.* **1999**, *27*, 3836–3843.

- (247) Maradinata, H.; Phan, A.T. Structure of propeller-type parallel-stranded RNA G-quadruplexes, formed by human telomeric RNA sequences in K⁺ solution. *J. Am. Chem. Soc.* **2009**, *131*, 2570–2578.
- (248) Koirala, D.; Ghimire, C.; Bohrer, C.; Sannohe, Y.; Sugiyama, H.; Mai, H. Long-loop G-quadruplexes are misfolded population minorities with fast transition kinetics in human telomeric sequences. *J. Am. Chem. Soc.* **2013**, *135*, 2235–2241.
- (249) Singh, V.; Azarkh, M.; Exner, T.E.; Hartig, J.S.; Drescher, M. Human telomeric quadruplex conformations studied by pulsed EPR. *Angew. Chem. Int. Ed.* **2009**, *48*, 9728–9730.
- (250) Wiodarczyk, A.; Grzybowski, P.; Patkowski, A.; Dobek, A. Effect of ions on the polymorphism, effective charge, and stability of human telomeric DNA. Photon correlation spectroscopy and circular dichroism studies. *J. Phys. Chem. B.* **2005**, *109*, 3594–3605.
- (251) Gray, D.M.; Wen, J.; Gray, C.W.; Repges, R.; Repges, C.; Raabe, G.; Fleischhauer, J. Measured and calculated CD spectra of G-quartets stacked with the same or opposite polarities. *Chirality.* **2008**, *20*, 431–440.
- (252) Rujan, I.N.; Meleney, J.C.; Bolton, P.H. Vertebrate telomere repeat DNAs favor external loop propeller quadruplex structures in the presence of high concentrations of potassium. *Nucleic Acids Res.* **2005**, *33*, 2022–2031.
- (253) Zhou, J.; Wei, C.; Jia, G.; Wang, X.; Tang, Q.; Feng, Z.; Li, C. (2008) The structural transition and compaction of human telomeric G-quadruplex induced by excluded volume effect under cation-deficient conditions. *Biophys. Chem.* **2008**, *136*, 124–127.
- (254) Simonsson, T.; Sjobak, R. DNA tetraplex formation studied with fluorescence Resonance Energy Transfer. *J. Biol. Chem.* **1999**, *274*, 17379–17383.
- (255) Allain, C.; Monchaud, D.; Teulade-Fichou, M. FRET Templated by G-quadruplex DNA: A specific ternary interaction using an original pair of donor/acceptor partners. *J. Am. Chem. Soc.* **2006**, *128*, 11890–11893.
- (256) Sönnichsen, C.; Reinhard, B.M.; Liphardt, J.L.; Alivasatos, A.P. A molecular ruler based on plasmon coupling of single gold and silver nanoparticles. *Nat. Biotechnol.* **2005**, *23*, 741–745.
- (257) Jun, Y.W.; Sheikholeslami, S.; Hostetter, D.; Tajon, C.; Craik, C.; Alivasatos, A.P.; Continuous imaging of plasmon rulers in live cells reveals early stage caspase-3 activation at the single molecule level. *Proc. Natl Acad. Sci. U.S.A.* **2009**, *106*, 17735–17740.
- (258) Jain, P.K.; El-Sayed, M.A. Plasmonic coupling in noble metal nanostructures. *Chem. Phys. Lett.* **2010**, *487*, 153–164.
- (259) Hill, R.T.; Mock, J.J.; Hucknall, A.; Wolter, S.D.; Jokerst, N.M.; Smith, D.R.; Chilkoti, A. Plasmon ruler with Ångstrom length resolution. *ACS Nano.* **2012**, *6*, 9237–9246.

- (260) Armstrong, R.E.; Strouse, G.F. Rationally manipulating aptamer binding affinities in a stem-loop molecular beacon. *Bioconjugate Chem.* **2014**, *25*, 1769–1776.
- (261) Ding, Y.; Jiang, Z.; Saha, K.; Kim, C.S.; Kim, S.T.; Landis, R.F.; Rotello, V.M. Gold nanoparticles for nucleic acid delivery. *Mol. Ther.* **2014**, *22*, 1075–1083.
- (262) Clegg, R.M.; Murchie, A.I.H.; Zechel, A.; Lilley, D.M.J. Observing the helical geometry of double-stranded DNA in solution by fluorescence resonance energy transfer. *Proc. Natl. Acad. Sci. U.S.A.* **1993**, *90*, 2994–2998.
- (263) Webb, J. A.; Bardhan, R. Emerging advances in nanomedicine with engineered gold nanostructures. *Nanoscale.* **2014**, *2*, 2502–2530.
- (264) Cui, X.; Liu, M.; Li, B. Homogenous fluorescence-based immunoassay via inner filter effect of gold nanoparticles on fluorescence of CdTe quantum dots. *Analyst.* **2012**, *137*, 3293–3299.
- (265) Han, H.; Valle, V.; Maye, M.M. Probing energy transfer and inner filter effects in quantum dot-large metal nanoparticle clusters using a DNA-mediated quench and release mechanism. *J. Phys. Chem. C.* **2012**, *116*, 22996–23003.
- (266) Armstrong, R.E.; Riskowski, R.A.; Strouse, G.F. Nanometal Surface energy transfer optical ruler for measuring a human telomere structure. *Photochem. Photobiol.* **2015**, *91*, 732–738.
- (267) Kang, J.; Jung, J.; Kim, S.K. Flexibility of single-stranded DNA measured by single-molecule FRET. *Biophys. Chem.* **2014**, *195*, 49–52.
- (268) Murphy, M.; Rasnik, C.I.; Cheng, W.; Lohman, T.M.; Ha, T. Probing single-stranded DNA conformational flexibility using fluorescence spectroscopy. *Biophys. J.* **2004**, *86*, 2530–2537.
- (269) Wang, Y.; Patel, D.J. Guanine residues in d(T₂AG₃) and d(T₂G₄) for parallel-stranded potassium cation stabilized G-quadruplexes with anti-glycosidic torsion angles in solution. *Biochemistry*, **1992**, *31*, 8112–8119.
- (270) Bharti, S.K.; Sommers, J.A.; Zhou, J.; Kaplan, D.L.; Spelbrink, J.N.; Mergny, J.; Brosh Jr., R.M. DNA sequences proximal to human mitochondrial DNA deletion breakpoints prevalent in human disease form G-quadruplexes, a class of DNA structures inefficiently unwound by the mitochondrial replicative twinkle helicase. *J. Biol. Chem.* **2014**, *289*, 29975–29993.
- (271) Chen, M.C.; Murat, P.; Abecassis, K.; Ferré-D'Amaré, A.R.; Balasubramanian, S. Insights into the mechanism of a G-quadruplex-unwinding DEAH-box helicase. *Nucleic Acids Res.* **2015**, *43*, 2223–2231.
- (272) Wu, Y.; Shin-ya, K.; Brosh, Jr., R.M. FANCI helicase defective in Fanconi anemia and breast cancer unwinds G-quadruplex DNA to defend genomic stability. *Mol. Cell. Biol.* **2008**, *28*,

4116- 4128.

(273) Duan, X.; Liu, N.; Yang, Y.; Li, H.; Li, M.; Dou, S.; Xi, X. G-quadruplexes significantly stimulate Pif1 helicase-catalyzed duplex DNA unwinding. *J. Biol. Chem.* **2015**, *290*, 7722-7735.

(274) Paeschke, K.; Bochman, M.L.; Garcia, P.D.; Cejka, P.; Friedman, K.L.; Kowalczykowski, S.C.; Zakian, V.A. (2013) Pif1 family helicases suppress genome instability at G-quadruplex motifs. *Nature.* **2013**, *497*, 458-462.

(275) Bessi, I.; Jonker, H.R.A.; Richter, C.; Schwalbe, H. Involvement of long-lived intermediate states in the complex folding pathway of the human telomeric G-quadruplex. *Angew. Chem. Int. Ed.* **2015**, *54*, 8444-8448.

(276) Zhang, D.; Zhou, B.; Huang, Y.; Xu, L.; Zhou, J. The human Pif1 helicase, a potential *Escherichia coli* RecD homologue, inhibits telomerase activity. *Nucleic Acids Res.* **2006**, *34*, 1393- 1404.

(277) Byrd, A.K.; Raney, K.D. A parallel quadruplex DNA is bound tightly but unfolded slowly by Pif1 helicase. *J. Bio. Chem.* **2015**, *6*, 6482-6492.

(278) Budhathoki, J.B.; Ray, S.; Urban, V.; Janscak, P.; Yodh, J.G.; Balco, H. RecQ-core of BLM unfolds telomeric G-quadruplex in the absence of ATP. *Nucleic Acids Res.* **2014**, *42*, 11528-45.

(279) Chatterjee, S.; Zigelbaum, J.; Savitsky, P.; Sturzenegger, A.; Huttner, D.; Janscak, P.; Hickson, I.D.; Gileadi, O.; Rothenberg, E. Mechanistic insight into the interaction of BLM helicase with intra-strand G-quadruplex structures. *Nat. Commun.* **2014**, *5*, 1-12.

(280) Cheng, S.; Zheng, B.; Wang, M.; Ge, X.; Zhao, Q.; Liu, W. The unfolding of G-quadruplexes and its adverse effect on DNA-gold nanoparticles-based sensing system. *Biosens. Bioelectron.* **2014**, *53*, 479-485.

(281) Li, Z.; Mirkin, C.A. G-quartet induced nanoparticle assembly. *J. Am. Chem. Soc.* **2005**, *127*, 11568-11569.

(282) Bončina, M.; Lah, J.; Prislán, I.; Vesnaver, G. Energetic basis of human telomeric DNA folding into G-quadruplex structures. *J. Am. Chem. Soc.* **2012**, *134*, 9657-9663.

(283) Gray, R.D.; Buscaglia, R.; Chaires, J.B. Populated intermediates in the thermal unfolding of the human telomeric quadruplex. *J. Am. Soc. Chem.* **2012**, *134*, 16834-16844.

(284) Dhakal, S.; Yu, Z.; Konik, R.; Cui, Y.; Koirala, D.; Mao, H. G-Quadruplex and i-Motif Are Mutually Exclusive in ILPR Double-Stranded DNA. *Biophys. J.* **2012**, *102*, 2575–2584.

(285) Bauer, L.; Tlučková, K.; Tóthová, P.; Viglaský, V. G-Quadruplex Motifs Arranged in Tandem Occurring in Telomeric Repeats and the Insulin-Linked Polymorphic Region.

Biochemistry. **2011**, *50*, 7484–7492.

(286) Hammond-Kosack, M.C. A consensus repeat sequence from the human insulin gene linked polymorphic region adopts multiple quadruplex DNA structures in vitro. *FEBS Lett.* **1992**, *301*, 79-82.

(287) Paquette, J.; Varin, D.S.; Hamelin, C.E.; Hallgren, A.; Kämpe, O.; Carel, J.C.; Perheentupa, J.; Deal, C.L. Risk of autoimmune diabetes in APECED: association with short alleles of the 5'insulin VNTR. *Genes Immun.* **2010**, *11*, 590-597.

(288) Erligh, P.P.; Roep, B.O.; Giphart, M.J.; Koeleman, B.P. Insulin-like growth factor 1 promoter polymorphism influences insulin gene variable number of tandem repeat-associated risk for juvenile onset type 1 diabetes. *Tissue Antigens.* **2004**, *63*, 568-571.

(289) Bennett, S.T.; Lucassen, A.M.; Gough, S.C.L.; Powell, E.E.; Undlien, D.E.; Pritchard, L.E.; Merriman, M.E.; Kawaguchi, Y.; Dronsfield, M.J.; Pociot, F.; Nerup, J.; Bouzekri, N.; Cambon-Thomsen, A.; Rønningen, K.S.; Barnett, A.H.; Bain, S.C.; Todd, J.A. Susceptibility to human type 1 diabetes at IDDM2 is determined by tandem repeat variation at the insulin gene minisatellite locus. *Nat. Genet.* **1995**, *9*, 284-292.

(290) Bell, G.I.; Horita, S.; Karam, J.H. A polymorphic locus near the human insulin gene is associated with insulin-dependent diabetes mellitus. *Diabetes.* **1984**, *33*, 176-83.

(291) Desai, M.; Zeggini, E.; Horton, V.A.; Owen, K.R.; Hattersley, A.T.; Levy, J.C.; Hitman, G.A.; Walker, M.; Holman, R.R.; McCarthy, M.I.; Clark, A. The variable number of tandem repeats upstream of the insulin gene is a susceptibility locus for latent autoimmune diabetes in adults. *Diabetes.* **2006**, *55*, 1890-1894.

(292) Vafiadis, P.; Ounissi-Benkalha, H.; Palumbo, M.; Grabs, R.; Rousseau, M.; Goodyer, C.G.; Polychronakos, C. Class III alleles of the variable number of tandem repeat insulin polymorphism associated with silencing of thymic insulin predispose to type 1 diabetes. *J. Clin. Endocrinol. Metab.* **2001**, *86*, 3705-3710.

(293) Vafiadis, P.; Bennett, S.T.; Todd, J.A.; Nadeau, J.; Grabs, R.; Goodyer, C.G.; Wickramasinghe, S.; Colle, E.; Polychronakos, C. Insulin expression in human thymus is modulated by INS VNTR alleles at the IDDM2 locus. *Nat. Genet.* **1997**, *15*, 289 – 292.

(294) Sabatera, L.; Ferrer-Francesca, X.; Sospedra, M.; Caroa, P.; Juana, M.; Pujol-Borrell, R. Insulin alleles and autoimmune regulator (AIRE) gene expression both influence insulin expression in the thymus. *J. Autoimmun.* **2005**, *25*, 312–318.

(295) Kennedy, G.C.; German, M.S.; Rutter, W.J. The minisatellite in the diabetes susceptibility locus IDDM2 regulates insulin transcription. *Nat. Genet.* **1995**, *9*, 293–298.

(296) Melloul, D.; Marshak, S.; Cerasi, E. Regulation of insulin gene transcription. *Diabetologia.* **2002**, *45*, 309-326.

- (297) Xiao, J.; McGown, L.B. Mass spectrometric determination of ILPR G-quadruplex binding sites in insulin and IGF-2. *J. Am. Soc. Mass. Spectrom.* **2009**, *20*, 1974-1982.
- (298) Connor, A.C.; Frederick, K.A.; Morgan, E.J.; McGown, L.B. Insulin capture by an insulin-linked polymorphic region G-quadruplex DNA oligonucleotide. *J. Am. Chem. Soc.* **2008**, *128*, 4986-4991.
- (299) Dzubieli, D.; Ihmels, H.; Mahmoud, M.M.A.; Thomas, L. A comparative study of the interactions of cationic heteroarenes with quadruplex-DNA forming oligonucleotide sequences of the insulin-linked polymorphic region (ILPR). *Beilstein J. Org. Chem.* **2014**, *10*, 2963-2974.
- (300) Cho, M.; Kim, Y.; Min, K.; Rahman, M.A.; Shim, Y.B.; Ban, C. Detection for folding of the thrombin binding aptamer using label-free electrochemical methods. *BMB Reports.* **2008**, *29*, 126-131.
- (301) Shim, J.W.; Tan, Q.; Gu, L. Single-molecule detection of folding and unfolding of the G-quadruplex aptamer in a nanopore nanocavity. *Nucleic Acids Res.*, **2009**, *37*, 972-982.
- (302) Mantelli, S.; Muller, P.; Harlepp, S.; Maaloum, M. Conformational analysis and estimation of the persistence length of DNA using atomic force microscopy in solution. *Soft Matter.* **2011**, *7*, 3412-3416.
- (303) Chen, A.K.; Cheng, Z.; Behlke, M.A.; Tsourkas, A. Assessing the sensitivity of commercially available fluorophores to the intracellular environment. *Anal. Chem.* **2008**, *80*, 7437-7444.
- (304) Shu, H.; Derksen, R.C.; Krause, C.R.; Fox, R.D.; Brazee, R.D.; Ozkan, H.E. Fluorescent intensity of dye solutions under different pH conditions. *J. ASTM. Int.* **2005**, *2*, 1-7.
- (305) Li, Z.; Jin, R.; Mirkin, C.A.; Letsinger, R.L. Multiple thiol-anchor capped DNA-gold nanoparticle conjugates. *Nucleic Acids Res.* **2002**, *30*, 1558-1562.
- (306) Li, F.; Zhang, H.; Dever, B.; Li, X.; Le, X.C. Thermal stability of DNA functionalized gold nanoparticles. *Bioconjugate Chem.* **2013**, *24*, 1790-1797.
- (307) Calculated from IDT OligoAnalyzer 3.1 for 5'-CCCCTATCCCCATACCCCTGTC CCCACATTGTTGTTTTTG-3' annealed to its complement. www.idtdna.com/calc/analyzer.
- (308) Joo, C.; Balci, H.; Ishitsuka, Y.; Buranachai, C.; Ha, T. Advances in single-molecule fluorescence methods for molecular biology. *Ann. Rev. Biochem.* **2008**, *77*, 51-76.
- (309) Persson, F.; Barkefors, I.; Elf, J. Single molecule methods with applications in living cells. *Curr. Opin. Biotechnol.* **2013**, *24*, 737-744.
- (310) Alguel, Y.; Meng, C.; Terán, W.; Krell, T.; Ramos, J.L.; Gallegos, M.; Zhang, X. Crystal structures of multidrug binding protein TtgR in complex with antibiotics and plant

antimicrobials. *J. Mol. Biol.* **2007**, *369*, 829-840.

(311) Banfield, M.J.; Barker, J.J.; Perry, A.C.F.; Brady, R.L.; Function from structure? The crystal structure of human phosphatidylethanolamine-binding protein suggests a role in membrane signal transduction. *Structure*. **1998**, *6*, 1245-1254.

(312) Gersten, J.I.; Nitzan, A. Accelerated energy transfer between molecules near a solid particle. *Chem. Phys. Lett.* **1984**, *104*, 31-37.

BIOGRAPHICAL SKETCH

EDUCATION

PhD Inorganic Chemistry Graduation November 2015

Florida State University, Tallahassee, FL

Thesis: Structural Elucidation in Biomolecules by Nanometal Surface Energy Transfer

Contact Points

Advisor: Dr. Geoffrey F. Strouse

Bachelor of Science – Chemistry, Spanish (Minor in Biology) May 2008

Randolph-Macon College, Ashland, VA

Thesis: Synthesis of Water-Soluble Platinum Complexes and their Interactions with 5'-GMP

Advisor: Dr. Serge Schreiner

Foreign exchange student – studied Spanish and Latin American civilization Summer 2006

Centros de Estudios Interamericanos (CEDEI), Cuenca, Ecuador

RESEARCH EXPERIENCE

Florida State University Dept. of Chemistry & Biochemistry August 2009 - present

Advisor: Dr. Geoffrey F. Strouse

- Implemented gold nanoparticle nano-beacons with energy transfer mechanisms and target-specific surface chemistry to monitor biological events, elucidate nucleic acid structures, and construct effective biosensors. Examples of these nano-beacons include aptamer sensors and genetic G-quadruplex probes that utilize SET to monitor changing DNA conformations.

Analytix Corporation, Ashland, VA July 2008 - May 2009

- Worked as a wet chemist in an industrial hygiene laboratory employing various analytical techniques to detect toxin levels in factory samples. Analytical techniques included total Kjeldahl nitrogen distillations, nitrate columns, and surfactant extractions.

Randolph-Macon College Chemistry Department, Ashland, VA June 2007 - May 2008

Advisor: Dr. Serge Schreiner

- Synthesized, and characterized with ^{31}P -NMR and ^{195}Pt -NMR, a family of novel, platinum-based compounds using water-soluble phosphine ligands. Analyzed by proton NMR the DNA-binding activity of these compounds as compared to the DNA-binding capabilities in commercial platinum anticancer agents, such as cisplatin and carboplatin.

PUBLICATIONS

1. “Rationally manipulating aptamer binding affinities in a stem-loop molecular beacon.” Armstrong, RE, Strouse, GF. (2014) *Bioconjugate Chemistry*, 25,1769-1776. DOI: **10.1021/bc500286r**
2. “NSET optical ruler for measuring a human telomere structure.” Armstrong, RE, Riskowski, RA, Strouse, GF. (2015) (M. Kasha edition – invited submission) *Photochemistry and Photobiology*, 91, 732-738. DOI: **10.1111/php.12423**
3. “Evidence for a dynamic equilibrium G-quadruplex population in the human Tel22 telomere.” Armstrong, RE, Riskowski, RA, Strouse, GF. *Bioconjugate Chemistry*. ***In preparation***
4. “Coopertivity in the quadruplex-dense ILPR.” Armstrong, RE, Strouse, GF. *ChemBioChem*. ***In preparation***
5. “Triangulating Nucleic Acid Conformations Using Multicolor Surface Energy Transfer (McSET).” Riskowski, RA, Armstrong, RE, Strouse, GF. *ACS Nano*. ***Accepted***

AWARDS

- Outstanding Teaching Assistant Award* April 2015
Florida State University Department of Chemistry & Biochemistry, Tallahassee, FL
- Award given to outstanding TAs in the department nominated by their students
- 3MT – The Three Minute Thesis Competition Finalist* November 2014
Florida State University, Tallahassee, FL
- Selected as a finalist in a university-wide 3-minute research communication competition
- Ermine M. Owenby, Jr. Fund to Promote Excellence Travel Award* October 2012, 2014
Florida State University College of Arts and Sciences, Tallahassee, FL
- Fellowship awarded to a female graduate student presenting at a conference in her field
- Lindau Nobel Laureate Meetings Attendee Nominee* December 2012
Florida State University Department of Chemistry & Biochemistry, Tallahassee, FL
- Nominated by the department for consideration to attend the Lindau Meetings in Germany
- ACS Division of Colloid and Surface Chemistry Poster Award* August 2012
Philadelphia Conference Center, Philadelphia, PA

- Top division poster award at the 244th ACS national meeting
The Florida Annual Meeting & Exposition (FAME) Top Poster Award April 2011
Innisbrook Golf Resort and Spa, Palm Harbor, FL
 - 1st Place Graduate Poster Award at FAME 2011
- Hoffman Fellowship Recipient* August 2009
Florida State University, Tallahassee, FL
- Fellowship presented to academically eligible incoming graduate students
- Senior Chemistry Award* May 2008
Randolph-Macon College Chemistry Department, Ashland, VA
- Award given to the top senior chemistry major
- Schapiro Undergraduate Research Fellowship* Summer 2007
Randolph-Macon College, Ashland, VA
- Summer research fellowship awarded to students with outstanding research proposals
- Jackson Fellowship Recipient* Fall 2004 – Spring 2008
Randolph-Macon College Chemistry Department, Ashland, VA
- Fellowship awarded to incoming freshmen with notable high school science credentials

PRESENTATIONS

1. *NanoFlorida 2015 – Nanoscience Technology Institute, Tallahassee, FL – May 2015*
Oral “Utilizing SET to monitor hybrid-1 and hybrid-2 G-quadruplex interconversion in a human telomere sequence”
2. *248th ACS National Meeting, San Francisco, CA – August 2014*
Oral “Utilizing size-dependent NSET as an optical probe for human telomere conformations”
3. *The FSU Life Sciences Symposium, Tallahassee, FL – February 2014*
Poster “Utilizing size-dependent NSET to monitor human telomere conformations”
4. *246th ACS National Meeting, Indianapolis, IN – September 2013*
Oral “Optically calculating quantities of hybrid-1 and hybrid-2 G-quadruplexes in telomeric sequences using NSET”
5. *244th ACS National Meeting, Philadelphia, PA – August 2012*
Poster “Measuring biophysical constants with an NSET torque wrench”

6. *The Florida Annual Meeting & Exposition (FAME), Palm Harbor, FL – May 2012*
Oral “Measuring biophysical constants with an NSET torque wrench”
7. *The Southeast Regional Meeting of the ACS (SERMACS), Richmond, VA – October 2011*
Oral “Interfacing nano- and biotechnology for the detection of small molecules”
8. *The Florida Annual Meeting & Exposition (FAME), Palm Harbor, FL – May 2011*
Poster “A single construct aptamer-NP conjugate for the sensitive optical detection of ATP”
9. *235th ACS National Meeting, New Orleans, LA – April 2008*
Poster “Synthesis of water-soluble platinum complexes and their interactions with 5'-GMP”

TEACHING EXPERIENCE

Florida State University Dept. of Chemistry & Biochemistry Fall 2009 – Spring 2015

- General Chemistry I Recitation (CHM1045-R), Head Teaching Assistant
- Survey of Organic Chemistry Lab (CHM2200-L), Teaching Assistant
- Chemistry I&II Recitation and Lab (CHM1045/6-R/L), Teaching Assistant
- Liberal Studies Chemistry (CHM1020), Teaching Assistant
- Survey of General Chemistry (CHM1032), Teaching Assistant

Johns Hopkins Center for Talented Youth (CTY) Residential Camps Summer 2008, 2009

- Biotechnology (Puebla, Mexico – 2008; Bethlehem, PA – 2009), Teaching Assistant